

# Oscillatory Dynamics for PDE Models Coupling Bulk Diffusion and Dynamically Active Compartments:

Theory, Numerics and Applications

by

Jia Gou

B.Sc., Beijing Normal University, China, 2009

A THESIS SUBMITTED IN PARTIAL FULFILLMENT OF  
THE REQUIREMENTS FOR THE DEGREE OF

DOCTOR OF PHILOSOPHY

in

The Faculty of Graduate and Postdoctoral Studies

(Mathematics)

THE UNIVERSITY OF BRITISH COLUMBIA

(Vancouver)

April 2016

© Jia Gou 2016

# Abstract

We formulate and investigate a relatively new modeling paradigm by which spatially segregated dynamically active units communicate with each other through a signaling molecule that diffuses in the bulk medium between active units. The modeling studies start with a simplified setting in a one-dimensional space, where two dynamically active compartments are located at boundaries of the domain and coupled through the feedback term to the local dynamics together with flux boundary conditions at the two ends. For the symmetric steady state solution, in-phase and anti-phase synchronizations are found and Hopf bifurcation boundaries are studied using a winding number approach as well as parameter continuation methods of bifurcation theory in the case of linear coupling. Numerical studies show the existence of double Hopf points in the parameter space where center manifold and normal form theory are used to reduce the dynamics into a system of amplitude equations, which predicts the configurations of the Hopf bifurcation and stability of the two modes near the double Hopf point. The system with a periodic chain of cells is studied using Floquet theory. For the case of a single active membrane bound component, rigorous spectral results for the onset of oscillatory dynamics are obtained and in the finite domain case, a weakly nonlinear theory is developed to predict the local branching behavior near the Hopf bifurcation point. A previously developed model by Gomez et al.[23] is analyzed in detail, where the phase diagrams and the Hopf frequencies at onset are provided analytically with slow-fast type of local kinetics. A coupled cell-bulk system, with small signaling compartments, is also studied in the case of a two-dimensional bounded domain using the method of asymptotic expansions. In the very large diffusion limit we reduce the PDE cell-bulk system to a finite dimensional dynamical system, which is studied both analytically and numerically. When the diffusion rate is not very large, we show the effect of spatial distribution of cells and find the dependence of the quorum sensing threshold on influx rate.

# Preface

This thesis is an original work of the author, Jia Gou. This research project was originally initiated under the supervision of Dr. Yuexian Li and later under the supervision of Dr. Michael Ward all the way to the completion of the thesis.

The work in chapter 2 has been submitted for publication along with my supervisor Dr. Michael Ward, Dr. Yuexian Li and co-authors Dr. Pik-Yin Lai, Wei-Yin Chiang[24]. Dr. Yuexian Li was involved in the stage of model formulation and gave useful suggestions on design of biological models. Dr. Pik-Yin Lai provided helpful comments on numerical simulations and manuscript edits. I conducted all computational work and derivations. Dr. Ward was the supervisory author on this project and was involved throughout this project in project design, concept formation and manuscript revision.

A version of chapter 3 has been submitted for publication with Dr. Wayne Nagata and Dr. Yuexian Li[25]. I conducted all computational work. Dr. Nagata was the supervisory author on this project and was involved throughout this project in conception and manuscript edits.

A version of chapter 4 is published in *SIAM J. Appl. Dyn. Sys.* along with Dr. Michael Ward, Dr. Wayne Nagata and Dr. Yuexian Li[26]. Dr. Nagata provided valuable suggestions in the developing of the weakly non-linear theory. I conducted all computational work. Dr. Ward was the supervisory author on this project and was involved throughout this project in project design, concept formation and manuscript revision.

The materials in chapter 5 and chapter 6 has been submitted with Dr. Michael Ward[27, 28]. I conducted all computational work. Dr. Ward was the supervisory author on this project and was involved throughout this project in project design, concept formation and manuscript revision.

# Table of Contents

<b>Abstract</b> . . . . .	ii
<b>Preface</b> . . . . .	iii
<b>Table of Contents</b> . . . . .	iv
<b>List of Figures</b> . . . . .	vii
<b>Acknowledgements</b> . . . . .	xi
<b>Dedication</b> . . . . .	xii
<b>1 Introduction</b> . . . . .	1
1.1 Background and Motivation . . . . .	1
1.2 Thesis Outline . . . . .	3
<b>2 Two Coupled Sel'kov Oscillators</b> . . . . .	7
2.1 Formulation of the Coupled Compartment-Bulk Model . . . . .	8
2.2 Linear Coupling Between the Compartments and the Bulk . . . . .	10
2.2.1 Linear Stability Analysis of the Steady State . . . . .	11
2.2.2 The Winding Number Analysis . . . . .	17
2.3 A Periodic Chain of Active Units Coupled by Bulk Diffusion . . . . .	21
2.3.1 The Steady-State Solution . . . . .	23
2.3.2 The Linear Stability Analysis . . . . .	24
2.3.3 Hopf Bifurcation Boundaries, Global Branches and Numerics . . . . .	26
2.3.4 Large $D$ Analysis for the Hopf Bifurcation Boundaries . . . . .	29
2.4 Nonlinear Coupling Between Compartments and Bulk . . . . .	34
2.4.1 Compartmental Dynamics Neglecting Bulk Diffusion . . . . .	37
<b>3 Nonlinear Analysis Near the Double Hopf Bifurcation Point</b> . . . . .	40
3.1 The Coupled Compartment-Bulk Diffusion Model . . . . .	41
3.2 Linearized Stability . . . . .	42

*Table of Contents*

---

3.3	Double Hopf Bifurcation . . . . .	48
<b>4</b>	<b>Generalized Model in One Dimensional Space . . . . .</b>	<b>58</b>
4.1	Model Formulation . . . . .	61
4.2	The Steady-State Solution and the Formulation of the Linear Stability Problem . . . . .	61
4.3	One-Component Membrane Dynamics . . . . .	65
4.3.1	Theoretical Results for a Hopf Bifurcation: The Infinite- Line Problem . . . . .	66
4.3.2	A Finite Domain: Numerical Computations of the Winding Number . . . . .	74
4.4	Examples of the Theory: One-Component Membrane Dy- namics . . . . .	75
4.4.1	A Class of Feedback Models . . . . .	76
4.4.2	A Phase Diagram for an Explicitly Solvable Model . . . . .	79
4.4.3	A Model of Kinase Activity Regulation . . . . .	83
4.4.4	Two Biologically-Inspired Models . . . . .	84
4.5	Two-Component Membrane Dynamics: Extension of the Ba- sic Model . . . . .	89
4.6	Weakly Nonlinear Theory for Synchronous Oscillations . . . . .	94
4.6.1	Numerical Validation of the Weakly Nonlinear Theory With the Explicitly Solvable Model . . . . .	106
4.6.2	Numerical Validation of the Weakly Nonlinear Theory With the <i>Dictyostelium</i> Model . . . . .	110
<b>5</b>	<b>A Model of Bulk-Diffusion Coupled to Active Membranes With Slow-Fast Kinetics . . . . .</b>	<b>113</b>
5.1	Coupled Membrane-bulk Model With Activator-Inhibitor Dy- namics . . . . .	113
5.2	The Steady-State Solution and the Formulation of the Linear Stability Problem . . . . .	116
5.2.1	Formulation of the Linear Stability Problem . . . . .	119
5.3	One Diffusive Species in the Bulk . . . . .	122
5.3.1	Stability Analysis for the $\epsilon \rightarrow 0$ Limiting Problem . . . . .	125
5.3.2	Stability Analysis for the $\epsilon = \mathcal{O}(1)$ Problem . . . . .	139
5.4	Two Diffusive Species in the Bulk . . . . .	142
<b>6</b>	<b>Models in a Two-Dimensional Domain . . . . .</b>	<b>149</b>
6.1	Formulation of a 2-D Coupled Cell-Bulk System . . . . .	151
6.2	Analysis of the Dimensionless 2-D Cell-Bulk System . . . . .	155

*Table of Contents*

---

6.2.1	The Steady-State Solution for the $m$ Cells System . . .	157
6.2.2	Formulation of the Linear Stability Problem . . . . .	161
6.3	The Distinguished Limit of $D = \mathcal{O}(\nu^{-1}) \gg 1$ . . . . .	165
6.4	Examples of the Theory: Finite Domain With $D = \mathcal{O}(\nu^{-1})$ . .	170
6.4.1	Example 1: $m$ Cells; One Local Component . . . . .	170
6.4.2	Example 2: $m$ Cells; Two Local Components . . . . .	172
6.5	Finite Domain: Reduction to ODEs for $D \gg \mathcal{O}(\nu^{-1})$ . . . .	183
6.5.1	Large D Theory: Analysis of Reduced Dynamics . . . . .	188
6.6	The Effect of the Spatial Configuration of the Small Cells: The $D = \mathcal{O}(1)$ Regime . . . . .	195
6.6.1	Example: The Sel'kov Model . . . . .	200
6.7	Infinite Domain: Two Identical Cells . . . . .	212
6.7.1	The Steady-State Solution . . . . .	214
6.7.2	Linear Stability Analysis . . . . .	216
<b>7</b>	<b>Conclusion and Future Work</b> . . . . .	<b>221</b>
7.1	Future Work . . . . .	222
	<b>Bibliography</b> . . . . .	<b>225</b>
 <b>Appendices</b>		
<b>A</b>	<b>Formulation of the PDE-ODE System for a Periodic Chain</b>	<b>232</b>
<b>B</b>	<b>An Alternative PDE-ODE Formulation for a Periodic Chain</b>	<b>234</b>
<b>C</b>	<b>Calculation of Normal Form Coefficients</b> . . . . .	<b>236</b>
<b>D</b>	<b>Two Specific Biological Models</b> . . . . .	<b>241</b>
D.1	The Dictyostelium Model . . . . .	241
D.2	The GnRH Model . . . . .	242

# List of Figures

2.1	Schematic plot of the geometry for the coupled model in 1-D	10
2.2	Phase diagram with $D$ and $\beta$	14
2.3	Bifurcation diagram of $V$ with respect to $D$ and $\beta$ with linear coupling	15
2.4	Full numerical simulation of (2.1.1)	16
2.5	Trace of the counterclockwise contour	17
2.6	Plot of the characteristic function	20
2.7	Schematic diagram of a periodic chain of four cells	22
2.8	Phase diagram showing Hopf bifurcation boundaries for the case of three cells in the $D$ versus $\kappa$ plane	27
2.9	Global bifurcation diagram and plot of $\mathcal{F}(i\lambda_I)$	28
2.10	Full numerical results showing in-phase and anti-phase synchronous oscillations	30
2.11	Plot of $p_1 p_2 - p_3$ versus $\kappa$ for the <i>Routh-Hurwitz criterion</i>	32
2.12	Bifurcation diagram with respect to $D$ and $\beta$ with nonlinear coupling	36
2.13	Numerical simulation of the coupled PDE-ODE system (2.1.1) with nonlinear coupling	37
2.14	Bifurcation diagram of the ODE system (2.4.6) versus $\beta$	38
3.1	Parameteric portrait in the $(\mu_1, \mu_2)$ and the $(\beta, D)$ plane	53
3.2	Bifurcation diagram with parameters near the double-Hopf point	55
3.3	Full numerical simulation shows unstable torus bifurcation and two frequencies	57
4.1	Phase diagram in the $(\kappa, \gamma)$ plane	80
4.2	Two typical bifurcation diagrams for $u$ versus $\gamma$ with different value of $\kappa$	81
4.3	Full numerical simulations of the PDE-ODE system for (4.4.6) for the finite-domain problem shows synchronized oscillations of the two membranes	82

*List of Figures*

---

4.4	Full numerical simulations of the PDE-ODE system for (4.4.6) for the finite-domain problem shows phase-locking of the two membranes . . . . .	82
4.5	Numerical simulation on the GnRH model and the winding number criterion . . . . .	85
4.6	Numerical simulation on the <i>Dict</i> model and winding number criterion . . . . .	87
4.7	Bifurcation diagram with respect to $D$ of the <i>Dict</i> model . .	88
4.8	Heterogeneous cells: bifurcation diagram and numerical simulation . . . . .	92
4.9	Winding number computation indicates the synchronous and asynchronous modes . . . . .	94
4.10	Numerical simulation of the heterogeneous membranes shows different behaviors . . . . .	95
4.11	Bifurcation diagrams with respect to $D$ for different values of $\gamma$	107
4.12	Comparison of bifurcation diagrams near a subcritical Hopf bifurcation point . . . . .	108
4.13	Comparison of bifurcation diagrams near a supercritical Hopf bifurcation . . . . .	109
4.14	Delayed Hopf bifurcation behavior . . . . .	110
4.15	Comparison of numerical and theoretical calculated bifurcation diagram for the <i>Dictyostelium</i> model . . . . .	112
5.1	Plot of nullclines of the isolated membrane model . . . . .	115
5.2	Stability boundary with different value of $\epsilon$ . . . . .	119
5.3	Winding number calculation of the membrane-bulk coupling model . . . . .	127
5.4	Phase diagram in the $(l_1/l_0, L/l_0)$ plane . . . . .	131
5.5	Winding number calculation for $\tau = 200$ and $\tau = 1$ . . . . .	132
5.6	Spectrum near the boundary of different region in phase diagram . . . . .	134
5.7	Bifurcation diagram with respect to $k_v$ and numerical simulation near asymmetric equilibrium solution . . . . .	136
5.8	Bifurcation diagram with respect to $k_v$ and plot of periods . .	137
5.9	Numerical simulation shows in-phase and anti-phase synchronization of two membranes . . . . .	138
5.10	Phase diagram in the $(l_1/l_0, L/l_0)$ plane and bifurcation diagram for fixed $L$ . . . . .	140
5.11	Full numerical simulation of (5.3.1) shows unequal amplitude of oscillations on two membranes . . . . .	141

*List of Figures*

---

5.12	Phase diagram on $(l_1/l_0, L/l_0)$ plane and bifurcation diagram for fixed $L$ with two diffusive molecule . . . . .	144
5.13	Numerical simulation of (5.1.1) shows in-phase oscillation . . . . .	145
5.14	Numerical simulation shows two periods oscillation and correspond bifurcation diagram . . . . .	146
6.1	Schematic diagram showing the model setup in 2D . . . . .	155
6.2	Hopf bifurcation boundaries for the Sel'kov model in $d_1$ versus $d_2$ plane . . . . .	177
6.3	Hopf bifurcation boundaries for the Sel'kov model in $\tau$ versus $D_0$ plane . . . . .	178
6.4	Comparison of the Hopf bifurcation boundaries in $D = \mathcal{O}(\nu^{-1})$ and $D \gg \mathcal{O}(\nu^{-1})$ regime . . . . .	180
6.5	Hopf bifurcation boundaries for the FN system in the $d_1$ versus $d_2$ plane . . . . .	182
6.6	Hopf bifurcation boundaries for the FN system in the $\tau$ versus $D_0$ plane . . . . .	183
6.7	Comparison of $D = \mathcal{O}(\nu^{-1})$ and $D \gg \mathcal{O}(\nu^{-1})$ regime for the Hopf boundaries for the Sel'kov model; Numerical simulation of the reduced system . . . . .	191
6.8	Plot of $u_1, u_2$ and $U_0$ versus time for the reduced system; Plot of $u_1$ versus $u_2$ for the uncoupled system . . . . .	192
6.9	Bifurcation diagram of $u_1$ with respect to $d_2$ for the reduced system . . . . .	193
6.10	Comparison of $D = \mathcal{O}(\nu^{-1})$ and $D \gg \mathcal{O}(\nu^{-1})$ regime for the Hopf boundaries for the FN system; Numerical simulation of the reduced system . . . . .	194
6.11	Bifurcation diagram of $u_1$ versus $d_1$ . . . . .	195
6.12	Schematic diagram showing five cells on a 2D ring . . . . .	196
6.13	Hopf bifurcation boundaries in the $\tau$ versus $D$ plane for $m = 2, r_0 = 0.25$ . . . . .	203
6.14	Hopf bifurcation boundaries for the synchronous mode and the asynchronous mode in the $\tau$ versus $D$ plane . . . . .	205
6.15	Hopf bifurcation boundaries in the $\tau$ versus $D$ plane for the synchronous mode in the case of three cells . . . . .	206
6.16	Hopf bifurcation boundaries in the $\tau$ versus $D$ plane for the synchronous mode for five cells . . . . .	207
6.17	Hopf bifurcation boundaries for the two distinct asynchronous modes for two radius $r_0$ values . . . . .	208
6.18	Global bifurcation diagram of $u_{1e}$ versus $\tau$ for the Sel'kov model	210

*List of Figures*

---

6.19 Quorum sensing threshold as a function of  $d_1$  . . . . . 211

6.20 Schematic plot of the geometry of two cells on the infinite plane 212

# Acknowledgements

Foremost, I would like to express my deepest gratitude to my supervisor, Dr. Michael Ward, whose expert guidance, patience and continuous support helped me in all of time of studies and the completion of this thesis. His passion for Mathematics always inspires me and will keep encouraging me in my future career.

I am grateful to my co-supervisor Dr. Yuexian Li, who introduced me to the field of Mathematical Modeling in Biology, helped me understand concepts in this interdisciplinary field and construct the model system used in Chapter 2.

My sincere thanks goes to Dr. Wayne Nagata for his various forms of support during my graduate study. I benefit a lot from many valuable comments from Wayne. I would like to thank the Dr. Rachel Kuske and Dr. Anthony Peirce for their insightful comments and encouragements. I am also thankful to Dr. Leah Keshet, Dr. Daniel Coombs and Dr. Eric Cytrynbaum for their support.

Thanks to my friend Vincent Zhai, Jing Dong and Tara Cai. Without their precious support this would be an impossible task.

Last but not the least, I would like to thank my family especially my parents and my brother for their love and support throughout all of these years.

# Dedication

*To my mother and father*

# Chapter 1

## Introduction

### 1.1 Background and Motivation

Individuals in a large network communicate with each other to engage and coordinate their activities. This happens at almost all levels of the living world ranging from a colony of unicellular amoebae to highly sophisticated social networks of people. For instance, the synchronous rhythmic flashing of fireflies is revealed to be an critical component of the mating process of adult fireflies [4]. In neuronal systems, synchrony between different regions of the brain, communicating through synaptic connections, is thought to be the basis of many cognitive activities [75]. Among a variety of communication methods, a common scenario is where the communication is carried out through diffusive chemicals. Examples of such kind of systems range from the signalling of the amoebae *Dictyostelium discoideum* through the release of cAMP into the medium [19] where it diffuses and act on each individual, to some endocrine neurons that secrete a hormone to the extracellular medium where it influences the secretion of this hormone from a pool of such neurons [35, 40], and to girls sharing a dormitory room getting their periods synchronized [51] presumably through the secretion of a pheromone [66, 72] in the shared space. Further examples where this kind of signalling occurs are related to quorum sensing behavior (cf. [12], [54], [55], [53], [13]). In many of these systems, the individual cells or localized units, can, under appropriate conditions, exhibit sustained temporal oscillations. In this way, signalling through a diffusive chemical often can switch on and/or off the oscillations and to synchronize the oscillations among all the individuals.

Biological rhythms are ubiquitous in living organisms, especially in mammals including human being, with periods ranging from seconds to years. Examples include cardiac and respiratory rhythms, which are crucial for the maintenance of normal function of life, and the ultradian rhythms, which refers to a rhythm with period much shorter than the circadian rhythm, observed in the blood level of most hormones in mammals including human being, which often plays a fundamental role in their physiological function. The creation of those periodic phenomena involve chemical reactions and

cooperations of individuals which might not be directly connected.

The modeling paradigm we are interested in and will be studied in this thesis includes spatially segregated dynamically active compartments, like cells or membranes, and coupling among those local units through diffusive signals. This coupling can induce periodicities to the local compartments, which otherwise would not be present. The biological phenomenon that initially inspired our study is the pulsatile variation in the concentration of gonadotropin-releasing hormone (GnRH) in the portal blood that circulates from the hypothalamus to the pituitary gland. This periodic signal of about one pulse per hour has been shown to be crucial in maintaining the normal reproductive activities in mammals [73]. In order to generate pulsatile GnRH signals observed in the portal blood, synchronization in the secretory activities among the hundreds to thousands GnRH neurons is essential. A synchronization mechanism was proposed in [47], whereby neurons are coupled through GnRH secreted into the extracellular space. Results from this model were shown to be consistent with *in vivo* experiments. However the key limitation of this model of [47] is that it assumed that extracellular space was continuously stirred so as to average out any spatial effects resulting from any chemical secretions. In the real experimental settings, when the diffusion rate of chemicals in the extracellular space is small, it is unavoidable to introduce spatial ingredients into the model system. In this way, one should consider the diffusion of GnRH in the bulk, which couples localized secretory activity of individual neurons.

In addition to the wide variety of cellular examples, the coupling of local compartments to bulk diffusion arises in many applications, such as surface science, the effect of catalyst particles, etc. It was shown numerically in [23] that a two-component membrane-bulk dynamics on a 1-D spatial domain can trigger synchronous oscillatory dynamics in the two membranes. Models of the multistage adsorption of viral particles trafficking across biological membranes are studied in (cf. [10]). In the modeling of catalytic reactions occurring on solid surfaces, it was shown in [38] that oscillations in the surface kinetics are triggered by the effect of spatial bulk diffusion in the gas phase near the catalytic surface. The models of the effect of the coupling of diffusion to localized chemical reactions are given in [71] and [64]. Other applications include the analysis of Turing patterns arising from coupled bulk and surface diffusion (cf. [44]). In the study of cellular signal transduction, the survey [33] emphasizes the need for developing detailed models of cell signaling that are not strictly ODE based, but that, instead, involve spatial diffusion processes coupled with bio-chemical reactions occurring within localized signaling compartments. A related class of models,

referred to here as quasi-static models, consist of linear bulk diffusion fields that are coupled solely through nonlinear fluxes defined at specific spatial lattice sites. Such systems arise in the modeling of signal cascades in cellular signal transduction (cf. [45], [11]), and in the study of the effect of catalyst particles and defects on chemically active substrates (cf. [59], [56]). In [56] it was shown numerically that one such quasi-static model exhibits an intricate spatial-temporal dynamics consisting of a period-doubling route to chaotic dynamics.

## 1.2 Thesis Outline

Motivated by the prior studies, the goal of this thesis is to formulate a relatively new modeling paradigm by which spatially segregated dynamically active units, such as cells or localized signalling compartments, communicate with each other through a signalling molecule that diffuses in the bulk medium between the active units. We will give a detailed analysis of the possibility of the triggering of synchronous oscillations for the coupled system. The outline of this thesis is as follows.

In chapter §2, we construct and analyze a coupled compartment-bulk diffusive model with a one-dimensional domain. The coupling between each compartment and the bulk is due to both feedback terms to the compartmental dynamics and flux boundary conditions at the interface between the compartment and the bulk. The coupled model consists of dynamically active compartments located at the two ends  $x = 0$  and  $x = 2L$  of a 1-D bulk region of spatial extent  $2L$ . The two compartments are assumed to be identical chemical *conditional oscillators*, which is a term used to refer to a dynamical system that stays at a stable steady state when isolated from others, but is capable of generating sustained oscillations with some other parameter values. The local dynamics is modeled by Sel'kov kinetics, which is originally used to model glycolytic oscillations that occur in yeast and muscle cells. Glycolysis is the metabolic pathway that breaks down glucose to provide the energy for cellular metabolism. However, we emphasize that the particular choice of the local kinetics is not essential. The signalling molecule between the two compartments is assumed to undergo both diffusion, with diffusivity  $D$ , and constant bulk degradation. For the resulting PDE-ODE system, we construct a symmetric steady-state solution and analyze the stability of this solution to either synchronous(in-phase mode, where the two compartments oscillate at identical frequencies with no phase difference) or asynchronous(anti-phase mode, where the two compartments

oscillate at identical frequencies with a phase difference of half a period) perturbations about the midline  $x = L$ . The conditions for the onset of oscillatory dynamics, as obtained from a linearization of the steady-state solution, are studied using a winding number approach. Global branches of either in-phase or anti-phase periodic solutions, and their associated stability properties, are determined with numerical bifurcation and continuation methods. For the case of a linear coupling between the compartments and the bulk, with coupling strength  $\beta$ , a phase diagram showing the Hopf bifurcation boundaries in the parameter space  $D$  versus  $\beta$  is constructed that shows the existence of a rather wide parameter regime where stable synchronized oscillations can occur between the two compartments. It also shows that there are parameter regions where bistability occurs, where both in-phase and anti-phase synchronizations exist and both are stable. In addition, the double Hopf (or Hopf-Hopf) points, parameter values where the Hopf bifurcations of the in-phase and anti-phase modes coincide, are found in the model with certain parameter values, and will be studied in detail in chapter §3. By using a Floquet-based approach, the analysis with linear coupling is then extended to determine Hopf bifurcation thresholds for a periodic chain of evenly-spaced dynamically active units. For one particular case of nonlinear coupling between the compartments and the bulk, stable in-phase or anti-phase oscillations are also shown to occur in certain parameter regimes, but as isolated solution branches that are disconnected from the steady state solution branch.

In chapter §3 we consider the double Hopf bifurcation point that is found through numerical study of the model system in chapter §2 with linear coupling. We use a center manifold approach and normal form theory to reduce the local dynamics of the model system to a system of two amplitude equations, which determines the patterns of Hopf bifurcation and stability of the two modes near the double Hopf point. The normal form also shows the existence of an unstable invariant torus in the dynamics of the model system, and the location of the torus can be approximated from the normal form near the double Hopf point. Numerical simulations and continuation-bifurcation computations with the spatially discretized model are used to verify these predictions.

We extend our study to a general class of coupled membrane-bulk dynamics in the one-dimensional space in chapter §4. Firstly, we formulate a general model system that describes two dynamically active membranes, where  $n$  species are assumed to interact with each other, separated spatially by a distance  $2L$ , that are coupled together through a linear bulk diffusion field, with a fixed bulk decay rate. With this model setting, the algebraic

system of equations that the steady state solutions should satisfy are derived and the linear stability problem is also formulated. For this class of models, it is shown both analytically and numerically that bulk diffusion can trigger a synchronous oscillatory instability in the temporal dynamics associated with the two active membranes. For the case of a single active component on each membrane, and in the limit  $L \rightarrow \infty$ , rigorous spectral results for the linearization around a steady-state solution, characterizing the possibility of Hopf bifurcations and temporal oscillations in the membranes, are obtained. For finite  $L$ , a weakly nonlinear theory, accounting for eigenvalue-dependent boundary conditions appearing in the linearization, is developed to predict the local branching behavior near the Hopf bifurcation point. The analytical theory, together with numerical bifurcation results and full numerical simulations of the PDE-ODE system, are undertaken for various coupled membrane-bulk systems, including two specific biologically relevant applications. In addition, in the case of two heterogeneous membranes, numerical simulations show the possibility of two sustained oscillations with distinct amplitudes on the two membranes, which serves as a modeling verification of the phenomenon observed in laboratory experiments where one cell exhibits oscillatory dynamics and the other one is essentially quiescent.

In chapter §5, we consider a coupled membrane-bulk PDE-ODE model proposed by Gomez et al. [23]. A detailed analysis using a combination of asymptotic analysis, linear stability theory, and numerical bifurcation software is given. The mathematical model consists of two dynamically active membranes with Fitzhugh-Nagumo kinetics, which is often used to model spike generation of excitable neurons, separated spatially by a distance  $L$ , that are coupled together through a diffusion field that occupies the bulk region  $0 < x < L$ . The flux of the diffusion field on the membranes at  $x = 0$  and  $x = L$  provides feedback to the local dynamics on the membranes. In the absence of membrane-bulk coupling the membrane kinetics has a stable fixed point. The effect of bulk diffusion is to trigger either synchronous and asynchronous oscillations in the two membranes. In the singular limit of slow-fast membrane dynamics, and with only one diffusing species in the bulk, phase diagrams in parameter space showing where either synchronous or asynchronous oscillations occur, together with the corresponding Hopf frequencies at onset, are provided analytically. When the membrane kinetics is not of slow-fast type, a numerical study of the stability problem together with numerical bifurcation software is used to construct global bifurcation diagrams of steady-states and the bifurcating periodic solution branches for the case of either one or two diffusing species in the bulk. Predictions from the analytical and bifurcation theory are confirmed with full

numerical simulations of the PDE-ODE system.

In chapter §6, we formulate and analyze a class of coupled cell-bulk ODE-PDE models in a two-dimensional domain, which is relevant to studying quorum sensing behavior on thin substrates. In this model, spatially segregated dynamically active signaling cells of a common small radius  $\epsilon \ll 1$  are coupled through a passive bulk diffusion field. For this coupled system, the method of matched asymptotic expansions is used to construct steady-state solutions and to formulate a spectral problem that characterizes the linear stability properties of the steady-state solutions, with the aim of predicting whether temporal oscillations can be triggered by the cell-bulk coupling. Phase diagrams in parameter space where such collective oscillations can occur, as obtained from our linear stability analysis, are illustrated for two specific choices of the intracellular kinetics. In the limit of very large bulk diffusion, it is shown that solutions to the ODE-PDE cell-bulk system can be approximated by a finite-dimensional dynamical system. This limiting system is studied both analytically, using a linear stability analysis, and globally, using numerical bifurcation software. For one illustrative example of the theory it is shown that when the number of cells exceeds some critical number, i.e. when a quorum is attained, the passive bulk diffusion field can trigger oscillations that would otherwise not occur without the coupling. Moreover, for two specific models for the intracellular dynamics, we show that there are rather wide regions in parameter space where these triggered oscillations are synchronous in nature. Unless the bulk diffusivity is asymptotically large, it is shown that a clustered spatial configuration of cells inside the domain leads to larger regions in parameter space where synchronous collective oscillations between the small cells can occur. Additionally, the linear stability analysis for these cell-bulk models is shown to be qualitatively rather similar to the linear stability analysis of localized spot patterns for activator-inhibitor reaction-diffusion systems in the limit of long-range inhibition and short-range activation.

The chapter §7 is the conclusion chapter, where we summarize the main results and contributions of this thesis. Also we list several open problems for further explorations.

## Chapter 2

# Two Coupled Sel'kov Oscillators

The goal of this chapter is to formulate and investigate a simple cell-bulk coupled model in a 1-D domain with two types of coupling. The symmetric steady state and its linear stability are studied both analytically and numerically. The remainder of this chapter proceeds as follows.

In §2.1 we formulate a 1-D model on the interval  $0 < x < 2L$ , which consists of a PDE-ODE system that couples diffusion in the bulk  $0 < x < 2L$ , with constant diffusivity  $D$ , to compartmental dynamics with Sel'kov kinetics on the boundaries  $x = 0$  and  $x = 2L$ . The particular choice of Sel'kov kinetics is not essential, as the qualitative behavior of bulk-mediated oscillatory dynamics will also occur for other, more general, compartmental kinetics. In particular, the numerical study of [23] has revealed the possibility of stable synchronous dynamics under Fitzhugh-Nagumo reaction-kinetics in the compartments and an detailed analysis of the model in [23] is provided in §5.

In §2.2 we consider the case where there is a linear coupling between the two compartments at  $x = 0$  and  $x = 2L$  and the bulk, where  $\beta$  represents the strength of this coupling. For this linearly coupled model, we construct a steady-state solution that is symmetric about the midline  $x = L$ . In §2.2.1 we then derive a transcendental equation for the eigenvalue parameter  $\lambda$  associated with the linearization of the coupled compartment-bulk model around the symmetric steady-state solution. In our stability theory, we must allow for perturbations that are either symmetric or anti-symmetric about the midline, which leads to the possibility of either synchronous (in-phase) or asynchronous (out-of-phase) instabilities in the two compartments. To determine unstable eigenvalues of the linearization, in §2.2.2 we use the winding number of complex analysis to determine the number of roots in  $Re(\lambda) > 0$  to the transcendental equation for the eigenvalue. Branches of periodic solutions, either in-phase or anti-phase, that bifurcate from the symmetric steady-state solution branch, together with their stability properties, are determined using the numerical bifurcation software package XPPAUT

[16] after first spatially discretizing the PDE-ODE system into a relatively large system of ODEs. In this way, a phase-diagram in the  $D$  versus  $\beta$  parameter space, characterizing the region where stable synchronous and asynchronous oscillations between the two compartments can occur is obtained. Our results show that there is a rather large parameter range where either stable synchronous or asynchronous oscillations occur. Full numerical computations of the PDE-ODE system of coupled compartmental-bulk dynamics, undertaken using a method-of-lines approach, are used to validate the theory.

In §2.3, we extend the simple two-compartment case of §2.2 to allow for a periodic chain of evenly-spaced dynamically active units that are linearly coupled to a bulk diffusion field. By using an approach based on Floquet theory, we analyze the linear stability problem to determine Hopf bifurcation thresholds associated with the various possible modes of oscillation. Comparisons of predictions from the linear stability theory with full numerical simulations are performed.

In §2.4 we illustrate oscillatory compartmental dynamics for a specific type of nonlinear coupling between the bulk and the two compartments. Although this nonlinearly coupled system possesses the same steady-state as that of the uncoupled compartmental dynamics, we show using XPPAUT [16] that it can still generate compartment-bulk oscillations. In particular, our numerical computations show, in contrast to the case of a linear coupling between the compartments and the bulk, that the branches of synchronous and asynchronous periodic solutions are disconnected and do not bifurcate off of the symmetric steady-state solution branch. Our global bifurcation diagram also shows that there is a parameter range of bistability where either stable synchronous oscillations or stable asynchronous oscillations can co-exist with the stable symmetric steady-state solution branch. In §2.4.1 we study an extended ODE compartmental dynamics model, closely related to the nonlinear coupled compartment-bulk model, but where bulk diffusion is neglected.

## 2.1 Formulation of the Coupled Compartment-Bulk Model

We begin by formulating a simple model that describes the diffusion and degradation of a signalling particle in a 1-D spatial domain. The concentration/density of the particle is represented by  $C(x, t)$ , defined on the bulk  $x \in [0, 2L]$  at time  $t$ . Two identical compartments are introduced at the two

## 2.1. Formulation of the Coupled Compartment-Bulk Model

---

ends of the interval. These compartments can either be regarded as two cells or two dynamically active membranes, which can interact with the diffusive signalling particle in the bulk. The dynamical process in each compartment, be it biochemical reactions inside a cell or other chemical reactions on the membrane, is described by a system of nonlinear ODEs. However, the dynamical process in each compartment is modulated by the concentration of the diffusive particle near each boundary. Thus, the dynamics in the compartment at the left end depends on  $C(0, t)$ , while the one at the right end is modulated by  $C(2L, t)$ . The release of signalling particles from the compartments into the bulk is modeled as a flux boundary condition at each of the two compartments. In the bulk, we model the diffusion process as

$$\begin{aligned} \frac{\partial C}{\partial t} &= DC_{xx} - kC, & 0 < x < 2L, & \quad t > 0, \\ -DC_x(0, t) &= \kappa(V_0(t) - C(0, t)), & DC_x(2L, t) &= \kappa(V_1(t) - C(2L, t)). \end{aligned} \tag{2.1.1a}$$

Here  $D > 0$  and  $k > 0$  are the constant diffusion and degradation rates, respectively, while  $V_i(t)$  ( $i = 0, 1$ ) are the concentrations of the particle in the two compartments. In our model, we assume the efflux of particles out of each compartment is proportional to the difference between the concentration inside each compartment and that outside of it in the bulk. Therefore, the influence of each compartment on the diffusive particles is described by the linear flux boundary condition of (2.1.1a).

The dynamics governing the time evolution of the concentration  $V_i(t)$  and another variable  $W_i(t)$  inside each compartment is described by the following system of nonlinear ODEs:

$$\frac{dV_i}{dt} = f(V_i, W_i) + \beta P(C(2Li, t), V_i(t)), \quad \frac{dW_i}{dt} = g(V_i, W_i); \quad \text{for } i = 0, 1. \tag{2.1.1b}$$

For simplicity, we assume that the compartment kinetics  $f(V, W)$  and  $g(V, W)$ , as well as the coupling term  $\beta P(C, V(t))$  to the bulk, are identical for the two compartments. We assume that this system, when isolated (i.e. when  $\beta = 0$ ), and given favourable choices of parameter values, is capable of generating sustained oscillations of limit cycle type. In addition, we further assume that, when isolated, the compartmental dynamics has a unique stable steady-state. In Fig. 2.1 we give a schematic plot of the geometry for (2.1.1).

To illustrate the new behavior that can be induced by compartment-bulk

## 2.2. Linear Coupling Between the Compartments and the Bulk

---

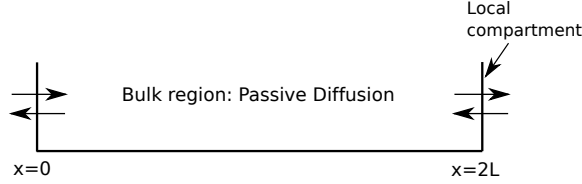


Figure 2.1: Schematic plot of the geometry for (2.1.1) showing the bulk region  $0 < x < 2L$ , where passive diffusion occurs, and the two local compartments at  $x = 0$  and  $x = 2L$ . One of the local species can be exchanged between the compartment and the bulk.

coupling, we will use Sel’kov model, for which the kinetics are

$$f(V, W) = \alpha W + WV^2 - V, \quad g(V, W) = \epsilon \left[ \mu - (\alpha W + WV^2) \right], \quad (2.1.1c)$$

where  $0 < \epsilon < 1$  is a parameter. We remark that the qualitative conclusions derived in the present study do not depend on the specific forms of the reaction kinetics, provided that limit cycle type oscillations in the dynamics can occur. In later chapters, we will show modeling studies using other form of local kinetics. In our model, the influence of the concentration of particles near each boundary on the compartment dynamics is described by the coupling term  $\beta P(C, t, V)$ , where  $\beta$  represents the coupling strength. Two types of coupling will be considered. In §2.2 we consider a linear coupling term, while in §2.4 we consider a specific form of nonlinear coupling.

For this Sel’kov model, when each compartment is isolated, i.e. when  $\beta = 0$ , there is a unique steady state solution given by  $V_0 = \mu$  and  $W_0 = \mu/(\alpha + \mu^2)$ , which is stable. In other words, the two compartments are “conditional oscillators” when decoupled from each other. Therefore, when oscillations occur in the present study, they are caused by the coupling between the two compartments induced by the diffusive signalling particles.

## 2.2 Linear Coupling Between the Compartments and the Bulk

We first consider (2.1.1) with a linear coupling term  $P(C(2Li, t), V)$  where  $i = 0, 1$ . We specify that

$$P(C(2Li, t), V) = C(2Li, t) - V(t), \quad i = 0, 1. \quad (2.2.1)$$

## 2.2. Linear Coupling Between the Compartments and the Bulk

---

With this choice, all interactions between the compartments and the diffusive particles are linear.

We first determine a steady-state solution to (2.1.1), with (2.2.1), that is symmetric about the midline  $x = L$ . To construct this steady-state solution we solve (2.1.1) on  $0 < x < L$ , while imposing a no-flux boundary condition for  $C$  at  $x = L$ . Since only the compartment at the left boundary  $x = 0$  is considered, we drop the subscripts for the compartmental variables  $V$  and  $W$ . We readily calculate that there is a unique symmetric steady-state solution  $C_e(x)$ ,  $V_e$ , and  $W_e$ , given by

$$C_e(x) = C_e^0 \frac{\cosh(\omega(L-x))}{\cosh(\omega L)}, \quad C_e^0 = \frac{\kappa\mu}{\kappa + D\omega \tanh(\omega L)(1+\beta)}, \quad \omega \equiv \sqrt{k/D},$$

$$V_e = \frac{\mu}{1+\beta} + \frac{\beta C_e^0}{1+\beta}, \quad W_e = \frac{\mu}{\alpha + V_e^2}.$$
(2.2.2)

We observe that the steady-state solution in the compartment for the coupled system differs from that of the uncoupled problem, and reduces to  $V_e = V_0 \equiv \mu$  and  $W_e = W_0 \equiv \mu/(\alpha + \mu^2)$  in the absence of coupling.

### 2.2.1 Linear Stability Analysis of the Steady State

To analyze the linear stability of the symmetric steady-state solution, we introduce the perturbation

$$C(x, t) = C_e(x) + e^{\lambda t} \eta(x), \quad V(t) = V_e + e^{\lambda t} \varphi, \quad W(t) = W_e + e^{\lambda t} \phi,$$
(2.2.3)

into (2.1.1). Upon linearizing the resulting system, we obtain the following eigenvalue problem for the eigenvalue parameter  $\lambda$ :

$$\lambda \eta = D \eta_{xx} - k \eta, \quad 0 < x < L; \quad -D \eta_x(0) = \kappa(\varphi - \eta_0), \quad (2.2.4a)$$

$$\lambda \varphi = f_V^e \varphi + f_W^e \phi + \beta (P_C^e \eta_0 + P_V^e \varphi), \quad \lambda \phi = g_V^e \varphi + g_W^e \phi. \quad (2.2.4b)$$

Here we have defined  $\eta_0 \equiv \eta(0)$ ,  $f_V^e \equiv f_V(V_e, W_e)$ ,  $f_W^e \equiv f_W(V_e, W_e)$ ,  $P_C^e \equiv P_C(C_e^0, V_e)$ , etc.

The formulation of the linear stability problem is complete after imposing a boundary condition for  $\eta(x)$  on the midline  $x = L$ . We will consider two distinct choices. The choice  $\eta(L) = 0$  corresponds to an asynchronous, or anti-phase, perturbation, while the condition  $\eta_x(L) = 0$  corresponds to an in-phase synchronization of the two compartments. We will consider both possibilities in our analysis below.

## 2.2. Linear Coupling Between the Compartments and the Bulk

---

For either choice of the boundary condition, we can readily solve (2.2.4) to derive that  $\lambda$  must be a root of the transcendental equation  $\mathcal{F}(\lambda) = 0$ , where  $\mathcal{F}(\lambda)$  is defined by

$$\mathcal{F}(\lambda) \equiv \frac{1}{p_{\pm}(\lambda)} - \frac{g_W^e - \lambda}{\det(J_e - \lambda I)}, \quad J_e \equiv \begin{pmatrix} f_V^e & f_W^e \\ g_V^e & g_W^e \end{pmatrix}. \quad (2.2.5a)$$

Here  $J_e$  is the Jacobian matrix of the uncoupled compartmental dynamics evaluated at the steady-state (2.2.2) for the coupled system. In (2.2.5a),  $p_{\pm}(\lambda)$  are defined by

$$p_+(\lambda) \equiv \frac{\beta D \Omega_\lambda \tanh(\Omega_\lambda L)}{\kappa + D \Omega_\lambda \tanh(\Omega_\lambda L)}, \quad p_-(\lambda) \equiv \frac{\beta D \Omega_\lambda \coth(\Omega_\lambda L)}{\kappa + D \Omega_\lambda \coth(\Omega_\lambda L)},$$

$$\Omega_\lambda \equiv \sqrt{\frac{k + \lambda}{D}}, \quad (2.2.5b)$$

where  $p_+$  corresponds to synchronous (in-phase) perturbations, while  $p_-$  corresponds to asynchronous (anti-phase) perturbations. In (2.2.5b), we must specify the principal branch of the square root to ensure that  $\eta(x)$  is analytic in  $\text{Re}(\lambda) > 0$ .

To classify any instabilities that can occur with compartment-bulk coupling we need to determine the number of roots of (2.2.5a) and their distribution in the right-half of the complex  $\lambda$ -plane (i.e.  $\text{Re}(\lambda) > 0$ ). We will approach this problem in two ways. One method is to numerically implement a winding number approach, as done below in §2.2.2. The second method, which we discuss here, is to use the bifurcation software XPPAUT[16]. First we spatially discretize (2.1.1) into a relatively large system of ODEs, and then we use XPPAUT to path-follow solution branches that bifurcate off the steady-state solution (2.2.2). In this way, in Fig. 2.3 we show two typical bifurcation diagrams with respect to the diffusivity  $D$  and the coupling strength  $\beta$ , for fixed values of the other parameters as shown in the figure caption. As seen from these plots, there are Hopf bifurcation points at which the steady-state solution loses its stability to either synchronous or asynchronous oscillatory instabilities in the two compartments. Moreover, in some regions of the  $(\beta, D)$  parameter space only either the synchronous or asynchronous mode is present. In the left panel of Fig. 2.3, where we plot the bifurcation diagram for  $V$  versus  $D$  when  $\beta = 0.8$ , we observe that the synchronous and asynchronous periodic solution branches change stability at  $D \approx 0.25$  and  $D \approx 0.55$ , respectively. These bifurcation points correspond

## 2.2. Linear Coupling Between the Compartments and the Bulk

---

to Torus bifurcations. By tuning the parameter  $\beta$ , these bifurcation points can occur at a common value of  $D$ , and correspond to the intersection of the black and magenta curves in Fig. 2.2. For this co-dimension-2 case, such double Hopf bifurcations were analyzed in detail using normal form theory in §3. For  $\beta = 0.8$ , we further observe from the left panel of Fig. 2.3 that both the synchronous and asynchronous oscillations are stable on the range  $0.25 < D < 0.55$ . A similar bifurcation diagram, but with fixed  $D = 0.4$  and  $\beta$  a parameter, is shown in the right panel of Fig. 2.3.

By varying the values of  $D$  and  $\beta$ , we can obtain a series of bifurcation diagrams, representing slices through the  $(\beta, D)$  phase space. By amalgamating these slices, we generate the phase diagram in the  $(\beta, D)$  parameter plane as shown in Fig. 2.2. We remark that the diffusivity  $D$  effectively represents the length scale of this system. When  $D$  is small, effectively the distance between the two cells is large. However, when  $D$  is large, effectively one can consider that the two cells are close together. Therefore, changing  $D$  is equivalent to changing the distance between the two cells. Variations in the coupling strength  $\beta$  determine the importance of the feedback in the compartment-bulk interactions.

The phase diagram in Fig. 2.2 shows the region of stability of the steady-state solution, and regions where either synchronous or asynchronous oscillations, or both, can occur as the diffusivity  $D$  and the coupling strength  $\beta$  are varied. From this plot, we observe that when  $D$  is relatively small, then as the coupling strength  $\beta$  is increased it is the anti-phase mode that becomes unstable first. This phenomenon is also plausible biologically, since when  $D$  and  $\beta$  are both small the communication between the two cells is not very efficient, and so it is hard to synchronize their dynamics with a common phase.

From Fig. 2.2, we also observe that when  $D$  is relatively large, only the in-phase synchronized oscillation can occur. In the region of Fig. 2.2 bounded by the blue solid curve, the steady-state solution is unstable to the in-phase mode, but it is only above the black solid curve where a stable synchronized oscillation between the two compartments can occur. Similarly, inside the red dashed curve, the steady-state solution is unstable to the anti-phase mode, but it is only under the magenta dashed curve where the asynchronous mode is stable. Therefore, in the region of Fig. 2.2 bounded by the black and magenta curves, stable synchronous and stable asynchronous periodic oscillations can co-exist. The determination which mode would result from numerical computations of the initial value problem (2.1.1) should depend on the initial conditions at time  $t = 0$ .

To confirm predictions obtained from the bifurcation analysis, full time-

## 2.2. Linear Coupling Between the Compartments and the Bulk

---

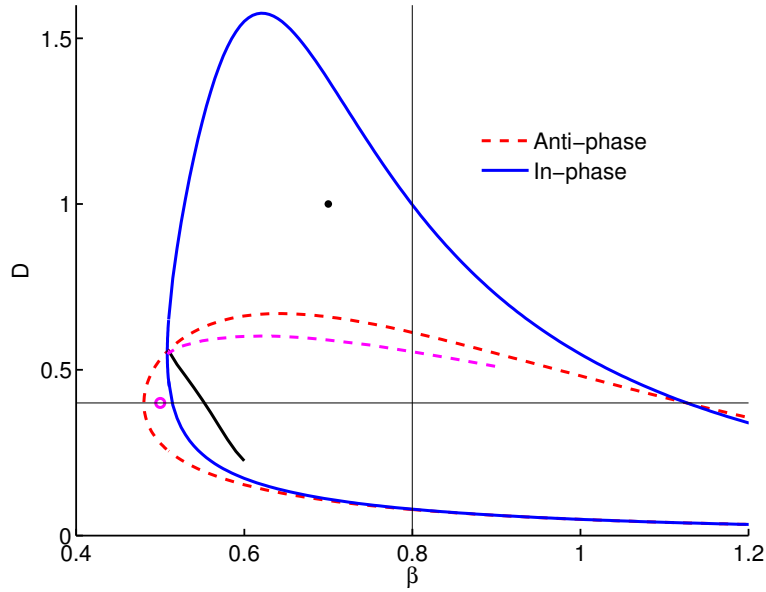


Figure 2.2: Phase diagram in the  $D$  versus  $\beta$  parameter plane, for the Sel'kov model (2.1.1) with linear coupling (2.2.1) for both the synchronous (in-phase) and asynchronous (anti-phase) modes. The other fixed parameters in (2.1.1) are  $\mu = 2$ ,  $\alpha = 0.9$ ,  $\epsilon = 0.15$ ,  $\kappa = 1$ ,  $k = 1$ , and  $L = 1$ . The parameter regime where compartment oscillations occur is within the blue solid curve (in-phase synchronization) and the red dashed curve (anti-phase synchronization). Above the black solid line, the in-phase periodic solution is stable, while below the dashed magenta curve the anti-phase periodic solution is stable. The horizontal and vertical slices at  $D = 0.4$  and  $\beta = 0.8$ , respectively, through the phase diagram are discussed in Fig. 2.3.

## 2.2. Linear Coupling Between the Compartments and the Bulk

---

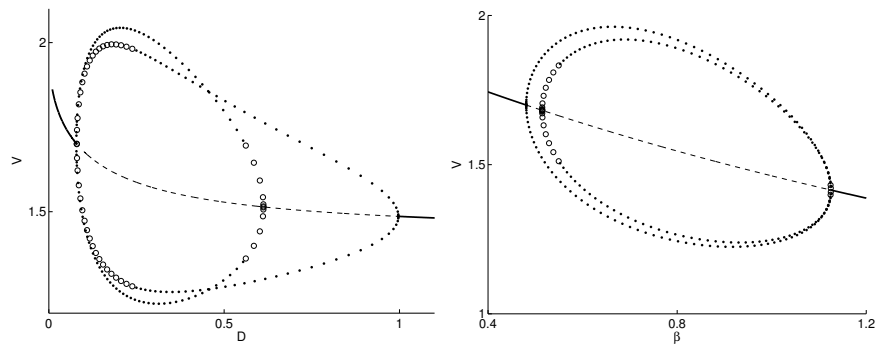


Figure 2.3: Bifurcation diagram of  $V$  corresponding to the vertical and horizontal slices through the phase diagram of Fig. 2.2, as computed using XPPAUT [16]. Left panel:  $V$  versus  $D$  for  $\beta = 0.8$  (vertical slice). Right panel:  $V$  versus  $\beta$  for  $D = 0.4$  (horizontal slice). In these panels the solid and dashed lines denote linearly stable and unstable branches of steady-state solutions, respectively. The two closed loops correspond to branches of synchronous and asynchronous periodic solutions. In the left panel, the branch that bifurcates from the steady-state near  $D = 1$  is the synchronous branch and in the right panel, the outer loop is the asynchronous branch. The solid/open circles on these loops denote linearly stable/unstable periodic solutions, respectively.

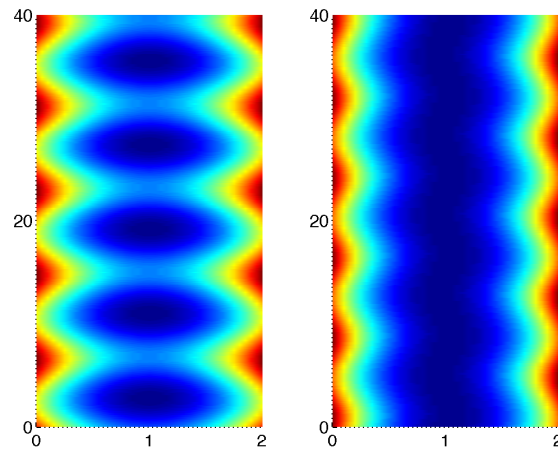


Figure 2.4: Full numerical solutions of the ODE-PDE system (2.1.1) demonstrating either in-phase or anti-phase oscillations of the two compartments. Time increases from bottom to top and the horizontal axis indicate the bulk region where  $L = 1$ . Left panel: synchronous oscillations for  $D = 1$  and  $\beta = 0.7$  (black dot in Fig 2.2). Right panel: asynchronous oscillations for  $D = 0.4$  and  $\beta = 0.5$  (magenta open circle in Fig. 2.2.) The other parameter values are the same as in the caption of Fig.2.2.

dependent numerical solutions of the coupled ODE-PDE system (2.1.1) were computed using a method of lines approach based on a second-order spatial discretization of the bulk diffusion operator. In our computation, we picked two points in the phase diagram in Fig. 2.2 indicated in the figure by the black solid dot and the magenta open circle. For these parameter sets, full numerical solutions of the ODE-PDE system (2.1.1) are shown in Fig. 2.4 starting with the initial value  $C(x, 0) = 0.2$ , and with randomly generated initial values for  $V_i$  and  $W_i$  for  $i = 0, 1$  at  $t = 0$ . The plots in Fig. 2.4 for  $t$  large confirm the theoretical predictions of the phase diagram by showing synchronous in-phase oscillations for  $D = 1$  and  $\beta = 0.7$  (left panel), and asynchronous anti-phase oscillations for  $D = 0.4$  and  $\beta = 0.5$  (right panel).

### 2.2.2 The Winding Number Analysis

In this section, we show how to use the winding number criterion of complex analysis to determine the number of roots of  $\mathcal{F}(\lambda) = 0$  in  $\text{Re}(\lambda) > 0$ , where  $\mathcal{F}(\lambda)$  is defined in (2.2.5). The analysis below is similar to that used in [57] to analyze the stability of localized pulse solutions to reaction-diffusion systems.

To determine the number  $N$  of roots of  $\mathcal{F}(\lambda) = 0$  in  $\text{Re}(\lambda) > 0$  of the spectral plane, we calculate the winding number of  $\mathcal{F}(\lambda)$  over the contour consisting of the imaginary axis  $-iR \leq \text{Im}\lambda \leq iR$ , decomposed as  $\Gamma_{I_+} = i\lambda_I$  and  $\Gamma_{I_-} = -i\lambda_I$  where  $0 < \lambda_I < R$ , together with the semi-circle  $|\lambda| = R$ , with  $|\arg \lambda| \leq \pi/2$ , which we denote by  $\Gamma_R$ , as shown in Fig. 2.5.

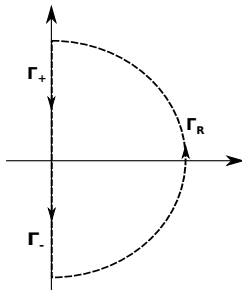


Figure 2.5: Counterclockwise contour consisting of the imaginary axis  $-iR \leq \text{Im}\lambda \leq iR$ , denoted by  $\Gamma_- \cup \Gamma_+$ , and the semicircle  $\Gamma_R$ , given by  $|\lambda| = R > 0$ , for  $|\arg \lambda| \leq \pi/2$ .

Assuming that there are no roots of  $\mathcal{F}(\lambda) = 0$  on the imaginary axis, we

## 2.2. Linear Coupling Between the Compartments and the Bulk

---

use the argument principle of complex analysis to determine  $N$  as

$$N = \frac{1}{2\pi} \left( \lim_{R \rightarrow \infty} [\arg \mathcal{F}]_{\Gamma_R} + 2 \lim_{R \rightarrow \infty} [\arg \mathcal{F}]_{\Gamma_{I_+}} \right) + P, \quad (2.2.6)$$

where  $P$  is the number of poles of  $\mathcal{F}(\lambda)$  in  $\text{Re}(\lambda) > 0$ . Here  $[\arg \mathcal{F}]_{\Gamma}$  denotes the change in the argument of  $\mathcal{F}(\lambda)$  over the contour  $\Gamma$  oriented in the counterclockwise direction. In deriving (2.2.6), we have used  $\overline{\mathcal{F}(\lambda)} = \mathcal{F}(\bar{\lambda})$  to obtain the relation  $\lim_{R \rightarrow \infty} [\arg \mathcal{F}]_{\Gamma_{I_-}} = \lim_{R \rightarrow \infty} [\arg \mathcal{F}]_{\Gamma_{I_+}}$ .

To determine  $P$ , we first observe from (2.2.5) that the choice of the principal branch of the square root for  $\Omega_\lambda$  ensures that  $1/p_\pm(\lambda)$  is analytic in  $\text{Re}(\lambda) > 0$ . Therefore,  $P$  is determined by the number of zeros of the quadratic function  $\det(J_e - \lambda I) = \lambda^2 - \text{tr}(J_e)\lambda + \det(J_e)$  in  $\text{Re}(\lambda) > 0$ . By using the specific forms of the nonlinearities  $f(V, W)$  and  $g(V, W)$  in (2.1.1c), we readily calculate  $\det(J_e) = \epsilon(\alpha + V_e^2) > 0$ . Therefore, in terms of the trace of  $J_e$ , which we have denoted by  $\text{tr}(J_e)$ , we have that  $P = 2$  if  $\text{tr}(J_e) > 0$  and  $P = 0$  if  $\text{tr}(J_e) < 0$ .

Next, we determine the change in the argument of  $\mathcal{F}(\lambda)$  over  $\Gamma_R$  as  $R \rightarrow +\infty$ . Since  $\det(J_e - \lambda I)$  is a quadratic function of  $\lambda$  and  $1/p_\pm(\lambda) \sim \beta^{-1} + \mathcal{O}(\Omega_\lambda^{-1/2})$  as  $|\lambda| \rightarrow +\infty$  in  $\text{Re}(\lambda) > 0$ , we estimate from (2.2.5a) and (2.2.5b) that, for either the synchronous or asynchronous modes,

$$\mathcal{F}(\lambda) \sim \frac{1}{\beta} + \frac{\kappa}{D\Omega_\lambda\beta} + \mathcal{O}\left(\frac{1}{\lambda}\right), \quad \text{as } |\lambda| = R \rightarrow +\infty, \quad (2.2.7)$$

where  $|\arg \lambda| \leq \pi/2$ . Hence, we have  $\lim_{R \rightarrow \infty} [\arg \mathcal{F}]_{\Gamma_R} = 0$ , so that (2.2.6) becomes

$$N = \frac{1}{\pi} \lim_{R \rightarrow \infty} [\arg \mathcal{F}]_{\Gamma_{I_+}} + P, \quad (2.2.8)$$

where  $P = 2$  if  $\text{tr}(J_e) > 0$  and  $P = 0$  if  $\text{tr}(J_e) < 0$ .

In this way, the problem of determining  $N$  is reduced to the simpler problem of calculating  $[\arg \mathcal{F}]_{\Gamma_{I_+}}$  where  $\Gamma_{I_+}$  is traversed in the downwards direction. On  $\Gamma_{I_+}$ , we let  $\lambda = i\lambda_I$  for  $0 < \lambda_I < \infty$ , and decompose  $\mathcal{F}(i\lambda_I)$  in (2.2.5a) into real and imaginary parts as  $\mathcal{F}(i\lambda_I) = \mathcal{F}_R(\lambda_I) + i\mathcal{F}_I(\lambda_I)$ . As  $\lambda_I$  decreases from  $+\infty$  to 0, we use (2.2.5a) to determine how many times  $\mathcal{F}(i\lambda_I)$  wraps around the origin in the  $(\mathcal{F}_R, \mathcal{F}_I)$  plane. By using (2.2.5b) to calculate the asymptotics of  $p_\pm$  as  $\lambda_I \rightarrow +\infty$ , we conclude that  $\mathcal{F}_R \rightarrow 1/\beta > 0$  and  $\mathcal{F}_I \rightarrow 0$  as  $\lambda_I \rightarrow +\infty$ . This shows that  $\arg \mathcal{F}(i\lambda_I) \rightarrow 0$  as  $\lambda_I \rightarrow \infty$ .

## 2.2. Linear Coupling Between the Compartments and the Bulk

---

In contrast, as  $\lambda_I \rightarrow 0$ , we further calculate from (2.2.5a) and (2.2.5b) that

$$\mathcal{F}(0) = \frac{1}{p_{\pm}(0)} - \frac{g_W^e}{\det(J_e)}, \quad \text{where} \quad \frac{1}{p_{\pm}(0)} = \begin{cases} \frac{1}{\beta} + \frac{\kappa}{\beta D \omega \tanh(\omega L)} > 0, \\ \frac{1}{\beta} + \frac{\kappa}{\beta D \omega \coth(\omega L)} > 0, \end{cases} \quad (2.2.9)$$

and  $\omega \equiv \sqrt{k/D}$ . Then, from the specific form of  $g(V, W)$  in (2.1.1c), we get that  $g_W^e = -\epsilon(\alpha + V_e^2) < 0$ . Upon recalling that  $\det(J_e) = \epsilon(\alpha + V_e^2) > 0$ , we conclude from (2.2.9) that  $\mathcal{F}(0) = [p_{\pm}(0)]^{-1} + 1 > 0$ .

This indicates that as we traverse  $\Gamma_{I_+}$ , the path of  $\mathcal{F}(i\lambda_I)$  both starts and ends on the positive real axis of the  $(\mathcal{F}_R, \mathcal{F}_I)$  plane. It follows that the change in the argument of  $\mathcal{F}(\lambda)$  on  $\Gamma_{I_+}$  can only be an integer number of  $2\pi$ , so that

$$[\arg \mathcal{F}] \Big|_{\Gamma_{I_+}} = 2m\pi, \quad m = 0, \pm 1, \pm 2, \dots$$

Consequently, we have from (2.2.8) that

$$N = 2m + P, \quad P = \begin{cases} 2, & \text{when } \text{tr}(J_e) > 0, \\ 0, & \text{when } \text{tr}(J_e) < 0. \end{cases} \quad (2.2.10)$$

Although we cannot, in general, determine  $m$  analytically, it is readily calculated numerically from (2.2.5a). To illustrate the numerical computation of the winding number, we consider (2.1.1) with the linear coupling (2.2.1) for the parameter value  $D = 1$  and  $\beta = 0.7$ , corresponding to the marked black dot in Fig. 2.2. The other parameter values for (2.1.1) are given in the caption of Fig. 2.2. For this parameter set we calculate that  $\text{tr}(J_e) > 0$  so that  $P = 2$  from (2.2.10). In the right panel of Fig. 2.6, we plot the path of  $\mathcal{F}(i\lambda_I)$  in the  $(\mathcal{F}_R, \mathcal{F}_I)$  parameter plane for both the in-phase synchronous mode (solid curve) and the anti-phase asynchronous mode (dashed curve). For the asynchronous mode we observe that as  $\lambda_I$  decreases from a very large initial value,  $\mathcal{F}(\lambda)$  wraps around the origin once in clockwise direction, so that  $[\arg \mathcal{F}] \Big|_{\Gamma_{I_+}} = -2\pi$ . Therefore, since  $m = -1$ , we get  $N = 0$  from (2.2.10). In contrast, for the synchronous mode we observe from Fig. 2.6 that  $[\arg \mathcal{F}] \Big|_{\Gamma_{I_+}} = 0$ , so that  $m = 0$  and  $N = 2$  from (2.2.10). These winding number computations show that, at this parameter set, the steady-state solution is unstable only to synchronous perturbations.

To determine the location of the two unstable eigenvalues for the synchronous mode when  $D = 1$  and  $\beta = 0.7$  we look for roots of  $\mathcal{F}(\lambda)$  on the

## 2.2. Linear Coupling Between the Compartments and the Bulk

---

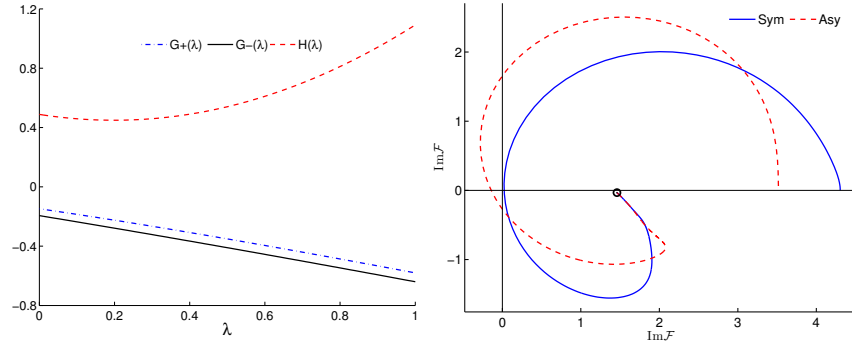


Figure 2.6: Left panel:  $G_+(\lambda)$ ,  $G_-(\lambda)$ , and  $H(\lambda)$ , as defined in (2.2.11), are plotted on  $\lambda > 0$  real for  $D = 1$  and  $\beta = 0.7$ , with the other parameters as in the caption of Fig. 2.2. There is no intersection between  $G_{\pm}(\lambda)$  and  $H(\lambda)$ , which shows that  $\mathcal{F}(\lambda)$  has no real roots  $\lambda$  for either the synchronous and asynchronous modes. Right panel:  $\mathcal{F}_I(\lambda_I) = \text{Im}(\mathcal{F}(i\lambda_I))$  is plotted versus  $\mathcal{F}_R(\lambda_I) = \text{Re}(\mathcal{F}(i\lambda_I))$  for both the synchronous and asynchronous modes as  $\lambda_I$  is decreased from 1000 to 0. The open circle represents the starting point at  $\lambda_I = 1000$ . For the asynchronous mode (dashed curve), we have  $m = -1$  in (2.2.10) since the trajectory wraps around the origin once in the clockwise direction. For the synchronous mode (solid curve), the plot shows that  $m = 0$  in (2.2.10).

### 2.3. A Periodic Chain of Active Units Coupled by Bulk Diffusion

---

positive real axis  $\lambda > 0$ . To do so, it is convenient to rewrite  $\mathcal{F}$  as

$$\mathcal{F}(\lambda) = \frac{H(\lambda) - G_{\pm}(\lambda)}{p_{\pm}(\lambda) \det(J_e - \lambda I)}, \quad (2.2.11a)$$

where

$$H(\lambda) \equiv \det(J_e - \lambda I), \quad G_{\pm}(\lambda) \equiv p_{\pm}(\lambda)(g_W^e - \lambda). \quad (2.2.11b)$$

In the left panel of Fig. 2.6 we plot  $H(\lambda)$  and  $G_{\pm}(\lambda)$  on  $\lambda > 0$  real for  $D = 1$  and  $\beta = 0.7$ . This plot shows that there are no intersections between  $H(\lambda)$  and  $G_{\pm}(\lambda)$ . Since, consequently, there is no real positive root to  $\mathcal{F}(\lambda) = 0$ , we conclude that the initial instability associated with the in-phase-mode is a synchronous oscillatory instability of the compartmental dynamics. A bifurcation diagram (not shown) similar to that in Fig. 2.3 predicts that this initial instability leads to a large-scale stable synchronous oscillation. The full numerical results of the ODE-PDE system (2.1.1) shown in the left panel of Fig. 2.4, as computed using a method of lines approach, confirms this prediction of a stable synchronous oscillation in the two compartments.

We remark that this strategy of computing the winding number, and then using (2.2.10) to determine  $N$ , was used for mapping out the regions in the phase diagram of Fig. 2.2 characterizing the linear stability properties of the steady-state solution to either in-phase or anti-phase perturbations.

### 2.3 A Periodic Chain of Active Units Coupled by Bulk Diffusion

In this section we extend the analysis in §2.2 to the case where  $m$  identical compartments, or cells, are evenly-spaced, with spacing  $2L$ , on a 1-D ring. These cells are then coupled by a bulk-diffusion field. A schematic diagram of this periodic arrangement of active cells is shown in the left panel of Fig. 2.7. Equivalently, we consider a 1-D domain on the interval  $[-L, (2m - 1)L]$ , with cells located at  $2jL$  for  $j = 0, \dots, m - 1$ , with the imposition of periodic boundary conditions for the bulk diffusion field at the endpoints. A schematic plot of four such cells is shown in the right panel of Fig. 2.7.

With the same notation used in §2.1, we model the system with  $m$  identical cells on a 1-D structure as follows. Firstly, the bulk diffusion process

### 2.3. A Periodic Chain of Active Units Coupled by Bulk Diffusion

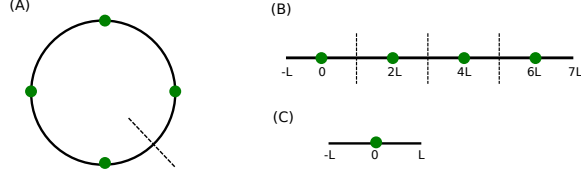


Figure 2.7: Left panel: Schematic diagram of four identical cells on a ring structure. The green solid dots represent cells. Top right panel: Schematic diagram of four identical cells on the domain  $[-L, 7L]$  with periodic boundary conditions at the two ends. Bottom right panel: schematic of one cell on  $[-L, L]$ .

is modeled by

$$\begin{aligned}
 C_t &= DC_{xx} - kC, \quad t > 0, \quad x \in (-L, (2m-1)L), \\
 &\quad \text{with } x \neq 2jL, \quad j = 0, \dots, m-1, \\
 C(-L, t) &= C(2mL - L, t), \quad C_x(-L, t) = C_x(2mL - L, t).
 \end{aligned}
 \tag{2.3.1a}$$

Inside each cell, we suppose that there are  $n$  locally interacting chemicals species. As shown in Appendix A, the local dynamics in each cell, with the linear coupling to the bulk diffusion field, is governed by

$$\frac{d\mathbf{u}_j}{dt} = \mathbf{F}(\mathbf{u}_j) + \mathbf{e}_1 \left[ \frac{\kappa}{2} \left( C(2jL^+, t) + C(2jL^-, t) \right) - \kappa u_{1j} \right], \quad j = 0, \dots, m-1,
 \tag{2.3.1b}$$

where  $\mathbf{u}_j = (u_{1j}, u_{2j}, \dots, u_{nj})^T$  denotes the  $n$  species inside the  $j$ -th cell,  $\mathbf{e}_1 \equiv (1, 0, \dots, 0)^T$ , with  $u_{1j}$  being the first chemical species inside the  $j^{\text{th}}$  cell. Moreover,  $\mathbf{F}$  is the common local reaction kinetics, since the cells are assumed to be identical. Here  $C(2jL^-, t)$  and  $C(2jL^+, t)$  represent the bulk concentration field at the left and right boundary of the  $j$ -th cell. As shown in Appendix A, the boundary conditions for the bulk concentration  $C$  at the cell boundaries, where  $j = 0, \dots, m-1$ , are

$$\begin{aligned}
 DC_x(2jL^+, t) &= \kappa \left( C(2jL^+, t) - u_{1j}(t) \right), \\
 DC_x(2jL^-, t) &= \kappa \left( u_{1j}(t) - C(2jL^-, t) \right),
 \end{aligned}
 \tag{2.3.1c}$$

where  $\kappa > 0$  is the common cell permeability parameter.

We remark that in our formulation, we have only assumed that  $C(x, t)$  is piecewise continuous on the ring, and so in general  $C(2jL^+, t) \neq C(2jL^-, t)$ .

An alternative, but simpler formulation, would be to impose that  $C$  is continuous on the ring, and that there is a jump in the flux  $DC_x$  across each cell. Although we do not pursue this simpler problem here, the linear stability analysis associated with this problem is discussed briefly in Appendix B.

### 2.3.1 The Steady-State Solution

We first calculate the symmetric steady-state solution of (2.3.1). For this steady-state, the bulk concentration is symmetric with respect to the midline of every two cells, and the local cell variables are the same for each cell. Although there might be other asymmetric steady-state solutions for the full system (2.3.1) of  $m$  coupled cells, we focus only on the symmetric steady-state solution and its linear stability properties.

To construct the symmetric steady-state, we need only consider the domain  $[-L, L]$ , as shown in Fig. 2.7, with a cell located at  $x = 0$  and with periodic boundary conditions at  $x = \pm L$ . We denote this steady-state solution by  $C^e(x)$  and the corresponding local steady-state cell variables as  $\mathbf{u}^e$ . Then the symmetric steady-state solution for  $C$  in the full system (2.3.1) is constructed by a simple period extension of this basic solution. Hence, focusing on the interval  $[-L, L]$ , the steady-state solution  $C^e(x)$  satisfies

$$\begin{aligned} C_{xx}^e &= \frac{k}{D}C^e, \quad x \in (-L, 0) \cup (0, L); \quad C^e(-L) = C^e(L), \quad C_x^e(-L) = C_x^e(L), \\ DC_x^e(0^+) &= \kappa \left( C^e(0^+) - u_1^e \right), \quad DC_x^e(0^-) = \kappa \left( u_1^e - C^e(0^-) \right). \end{aligned} \quad (2.3.2)$$

The steady-state solution for the compartmental variable  $\mathbf{u}^e$  satisfies

$$\mathbf{F}(\mathbf{u}^e) + \mathbf{e}_1 \left[ \frac{\kappa}{2} \left( C^e(0^+) + C^e(0^-) \right) - \kappa u_1^e \right] = 0. \quad (2.3.3)$$

On each subinterval, we can calculate the steady state solution  $C^e(x)$  separately as

$$C^e(x) = \begin{cases} A \cosh((x - L)\omega), & 0 < x < L, \\ A \cosh((x + L)\omega), & -L < x < 0, \end{cases} \quad (2.3.4a)$$

where  $A$  and  $\omega$  are given by

$$\omega \equiv \sqrt{\frac{k}{D}}, \quad A = \frac{\kappa u_1^e}{\kappa \cosh(L\omega) + D\omega \sinh(L\omega)}. \quad (2.3.4b)$$

As expected this steady-state is continuous across the cells.

For the special case where the local cell variable  $\mathbf{u}$  has two components  $\mathbf{u} = (V, W)^T$  with local reaction term  $\mathbf{F} = (f, g)^T$ , where  $f$  and  $g$  are the Sel'kov kinetics given in (2.1.1c), we can use (2.3.3) and (2.3.4) to explicitly identify a unique steady-state  $V^e$  and  $W^e$  as

$$V^e = \frac{\mu(\kappa + D\omega \tanh(L\omega))}{\kappa + (1 + \kappa)D\omega \tanh(L\omega)}, \quad W^e = \frac{\mu}{\alpha + (V^e)^2}. \quad (2.3.4c)$$

### 2.3.2 The Linear Stability Analysis

Next, we study the linear stability of the steady-state solution (2.3.4) for the case of Sel'kov kinetics. By introducing the perturbation (2.2.3) into (2.3.1) and linearizing, we obtain the eigenvalue problem

$$\begin{aligned} \eta'' &= \frac{(k + \lambda)}{D} \eta, \quad x \in (-L, (2m - 1)L), \text{ with } x \neq 2jL, \quad j = 0, \dots, m - 1, \\ D\eta'(2jL^+) &= \kappa(\eta(2jL^+) - \varphi), \\ D\eta'(2jL^-) &= \kappa(\varphi - \eta(2jL^-)), \quad j = 0, \dots, m - 1, \end{aligned} \quad (2.3.5a)$$

subject to the periodic boundary conditions

$$\eta(-L) = \eta(2mL - L), \quad \eta'(-L) = \eta'(2mL - L). \quad (2.3.5b)$$

Upon linearizing the reaction kinetics we have that

$$\lambda\varphi = f_V^e\varphi + f_W^e\phi - \kappa\varphi + \frac{\kappa}{2}(\eta(0^+) + \eta(0^-)), \quad \lambda\phi = g_V^e\varphi + g_W^e\phi, \quad (2.3.5c)$$

where  $f_V^e$ ,  $f_W^e$ ,  $g_V^e$ , and  $g_W^e$  are evaluated at the steady-state (2.3.4c).

Instead of considering (2.3.5a) with periodic boundary condition (2.3.5b), we make use of Floquet theory and consider (2.3.5a) on the fundamental interval  $[-L, L]$  with the Floquet boundary conditions

$$\eta(L) = z\eta(-L), \quad \eta'(L) = z\eta'(-L). \quad (2.3.6)$$

The solution can then be extended to the interval  $[L, 3L]$  by defining  $\eta(x) \equiv z\eta(x - 2L)$  for  $x \in [L, 3L]$  and using translation invariance. Since the  $m$  cells are identical, it is clear that  $\eta(x)$  satisfies (2.3.5a). By iterating this process, we construct the solution of (2.3.5a) on the whole domain  $[-L, (2m - 1)L]$

### 2.3. A Periodic Chain of Active Units Coupled by Bulk Diffusion

---

provided that  $\eta(2mL - L) = z^m \eta(-L)$ . Therefore, we obtain that  $z$  must be one of the  $m$ -th roots of unity

$$z \equiv e^{2\pi il/m}, \quad \text{where } l = 0, \dots, m-1. \quad (2.3.7)$$

In this way we have recovered the periodic solution to (2.3.5a) on  $[-L, (2m-1)L]$ .

Next, we solve (2.3.5a) on  $[-L, L]$  subject to the Floquet boundary conditions (2.3.6). The solution to (2.3.5a) and (2.3.6) is

$$\eta(x) = \begin{cases} [zA \cosh((x-L)\Omega_\lambda) + zB \sinh((x-L)\Omega_\lambda)] \varphi, & 0 < x < L, \\ [A \cosh((x+L)\Omega_\lambda) + B \sinh((x+L)\Omega_\lambda)] \varphi, & -L < x < 0, \end{cases} \quad (2.3.8)$$

where  $A$ ,  $B$ , and  $\Omega_\lambda$  are defined by

$$\begin{aligned} A &\equiv \frac{\kappa(z+1)/z}{2D\Omega_\lambda \sinh(L\Omega_\lambda) + 2\kappa \cosh(L\Omega_\lambda)}, \\ B &\equiv \frac{\kappa(z-1)/z}{2D\Omega_\lambda \cosh(L\Omega_\lambda) + 2\kappa \sinh(L\Omega_\lambda)}, \quad \Omega_\lambda \equiv \sqrt{\frac{k+\lambda}{D}}, \end{aligned} \quad (2.3.9)$$

and where we choose the principal branch of  $\Omega_\lambda$  if  $\lambda$  is complex. From this solution we then calculate

$$\eta(0^+) + \eta(0^-) = A(z+1) \cosh(\Omega_\lambda L) + B(1-z) \sinh(\Omega_\lambda L). \quad (2.3.10)$$

Upon substituting these expressions into (2.3.5c), we obtain a homogeneous linear system for  $\varphi$  and  $\phi$  given by

$$\begin{aligned} (f_V^e + \Delta_\lambda)\varphi + f_W^e\phi &= \lambda\varphi, \quad g_V^e\varphi + g_W^e\phi - \lambda\phi = 0, \\ \Delta_\lambda &\equiv \frac{\kappa}{2} [A(1+z) \cosh(\Omega_\lambda L) + B(1-z) \sinh(\Omega_\lambda L)] - \kappa. \end{aligned} \quad (2.3.11)$$

By writing (2.3.11) in matrix form, and then using (2.3.9) together with (2.3.7) for  $z$ , we readily derive, after some algebra, that the discrete eigenvalues  $\lambda$  satisfy the transcendental equation  $\mathcal{F}(\lambda) = 0$ , where

$$\mathcal{F}(\lambda) \equiv \frac{1}{\Delta_\lambda} + \frac{g_W^e - \lambda}{\det(J_e - \lambda I)}, \quad (2.3.12a)$$

and where for each possible mode  $l$  of instability, with  $l = 0, \dots, m-1$ , we have

$$\begin{aligned} \Delta_\lambda &\equiv \frac{\kappa^2 \Omega_\lambda D [\operatorname{Re}(z_l) - \cosh(2\Omega_\lambda L)] - \kappa \Omega_\lambda^2 D^2 \sinh(2\Omega_\lambda L)}{(\Omega_\lambda^2 D^2 + \kappa^2) \sinh(2\Omega_\lambda L) + 2\kappa D \Omega_\lambda \cosh(2\Omega_\lambda L)}, \\ \operatorname{Re}(z_l) &= \cos\left(\frac{2\pi l}{m}\right). \end{aligned} \quad (2.3.12b)$$

### 2.3. A Periodic Chain of Active Units Coupled by Bulk Diffusion

---

Here  $J_e$  is the Jacobian of the reaction kinetics, as defined in (2.2.5a), evaluated at the steady-state (2.3.4).

Our goal below is to determine Hopf bifurcation thresholds for which  $\mathcal{F}(\pm i\lambda_I) = 0$  in (2.3.12a), for some  $\lambda_I > 0$ . Such pure imaginary eigenvalues depend on  $\text{Re}(z)$  through  $\Delta_\lambda$ , as defined in (2.3.12b). To examine the possible modes of instability, we observe that if  $z_l$  is one of the  $m$ -th roots of unity, then

$$z_l = \bar{z}_{m-l}, \quad l = 1, \dots, \lfloor \frac{m}{2} \rfloor, \quad (2.3.13)$$

where the floor function  $\lfloor x \rfloor$  is defined as the largest integer not greater than  $x$ . Therefore, if  $m$  is odd, there are  $(m+1)/2$  different values of  $\text{Re}(z)$ , and thus  $(m+1)/2$  different possible modes of linear instability. Alternatively, if  $m$  is even, there are  $\frac{m}{2} + 1$  different possible modes of linear instability. The eigenvalue of multiplicity one corresponds to  $z = 1$  (and also  $z = -1$  if  $m$  is even). The remaining eigenvalues always have multiplicity two. In other words, the eigenvalue corresponding to  $z_l$  is also an eigenvalue for  $z = z_{m-l}$ . Therefore, if we find a Hopf bifurcation point for  $z \neq \pm 1$ , then there are always two possible spatial modes of oscillation for that specific pair of purely imaginary eigenvalues. Finally, to determine the predicted spatial pattern of any Hopf bifurcation point  $\lambda = i\lambda_I$ , we observe that at the midpoint between the cells the perturbation  $\text{Re}(e^{\lambda t} \eta [(2j-1)L])$  to the bulk diffusion field  $C(x, t)$  is

$$\text{Re} \left( e^{i\lambda_I t} \eta [(2j-1)L] \right) = \cos \left( \lambda_I t + \frac{2\pi l j}{m} \right), \quad j = 0, \dots, m. \quad (2.3.14)$$

#### 2.3.3 Hopf Bifurcation Boundaries, Global Branches and Numerics

Next, we use (2.3.12) to compute the Hopf bifurcation boundaries for the different possible modes of instability in the  $D$  versus  $\kappa$  parameter plane. We remark that the choice  $l = 0$  in (2.3.12) corresponds to in-phase synchronous perturbations across the cells, whereas the  $\lfloor \frac{m}{2} \rfloor$  other eigenvalues correspond to the various anti-phase modes across the  $m$  cells. For  $m = 3$ , and for one particular parameter set for the Sel'kov model (2.1.1c), in Fig. 2.8 we plot the Hopf bifurcation thresholds in the  $D$  versus  $\kappa$  plane.

Next, for the  $m = 3$  cell problem with  $\kappa = 1$ , we use XPPAUT [16] to compute the global bifurcation diagram, as a function of  $D$ , for the in-phase synchronous periodic solution branch, which bifurcates from the symmetric steady-state solution in (2.3.4) at the two distinct values of  $D$  shown in the

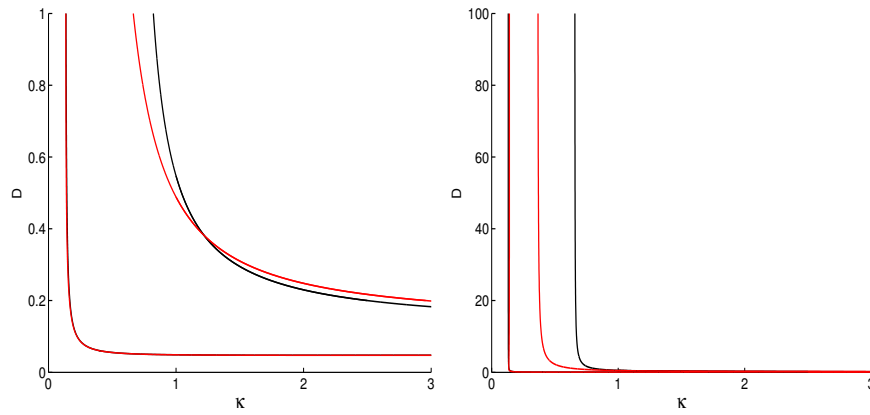


Figure 2.8: Left: Phase diagram showing Hopf bifurcation boundaries for the case of three ( $m = 3$ ) cells in the  $D$  versus  $\kappa$  plane for  $k = 1$ ,  $L = 1$ , and where the Sel'kov parameters in (2.1.1c) are  $\epsilon = 0.15$ ,  $\mu = 2$  and  $\alpha = 0.9$ . The black curves corresponds to  $l = 0$  and the red curves corresponds to  $l = 1, 2$ . The black and red curves almost coincide on the lower boundary. In the region bounded by the two black and two red curves the symmetric steady-state is linearly unstable to the  $l = 0$  and  $l = 1, 2$  modes, respectively. Right: Same as the left panel, but with a larger range of  $D$  for the vertical axis. For these parameter values we observe that the region of instability is unbounded in the  $D$  versus  $\kappa$  plane.

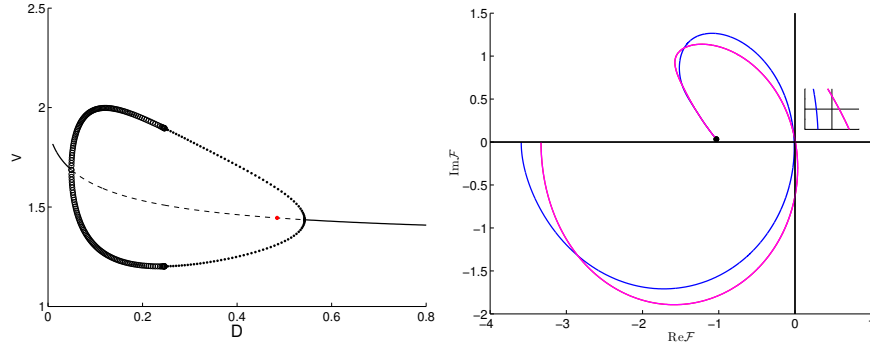


Figure 2.9: Left: Global bifurcation diagram with  $m = 3$  cells on the domain  $[-1, 5]$  for  $\kappa = 1$ , with the other parameters as in the caption of Fig. 2.8. The solid and dashed lines denote linearly stable and unstable branches of steady-state solutions, respectively. The closed loop is the global branch of in-phase synchronous periodic solutions. The upper Hopf bifurcation value  $D \approx 0.54299$  is for the  $l = 0$  in-phase mode. The solid/open circles on this loop denotes a linearly stable/unstable periodic solution, respectively. The red dot at  $D \approx 0.48482$  corresponds to the Hopf bifurcation point for the degenerate  $l = 1, 2$  mode. Right panel: Plot of  $\mathcal{F}(i\lambda_I)$  as  $\lambda_I$  decreases from 1000 to 0 with  $D = 0.5$ . The blue curve corresponds to  $l = 0$ , and the magenta curve is for  $l = 1, 2$ . The inner panel shows the curves near the origin. The trace and determinant of  $J_e$  are  $\text{tr}J_e = 0.4879$  and  $\det J_e = 0.4474$ , so that  $P = 2$  in (2.3.15). We obtain  $N = 2$  unstable eigenvalues for  $l = 0$ , and  $N = 0$  for  $l = 1, 2$  from (2.3.15).

left panel of Fig. 2.8. The computations, done by first discretizing (2.3.1), are displayed in the left panel of Fig. 2.9. From this figure we observe that for larger values of  $D$  the in-phase synchronous periodic solution branch is linearly stable, but it then destabilizes as  $D$  is decreased towards the lower Hopf bifurcation threshold.

To verify the linear stability properties of the steady-state solution for the  $l = 0$  and  $l = 1, 2$  modes off of the Hopf bifurcation boundaries, we can use a similar winding number criterion for  $\mathcal{F}(\lambda)$ , defined in (2.3.12), as was developed in §2.2.2. With the same notation as in §2.2.2, the number  $N$  of unstable eigenvalues of the linearization of the symmetric steady-state for the periodic cell problem is

$$N = \frac{1}{\pi} [\arg \mathcal{F}] \Big|_{\Gamma_{I_+}} + P, \quad P = \begin{cases} 2, & \text{when } \text{tr}(J_e) > 0, \\ 0, & \text{when } \text{tr}(J_e) < 0. \end{cases} \quad (2.3.15)$$

For  $\kappa = 1$  and  $D = 0.5$ , a numerical computation of the winding number shown in the right panel of Fig. 2.9 yields  $[\arg \mathcal{F}] \Big|_{\Gamma_{I_+}} = 0$  for  $l = 0$  and  $[\arg \mathcal{F}] \Big|_{\Gamma_{I_+}} = -2\pi$  for  $l = 1, 2$ . Therefore,  $N = 2$  for  $l = 0$  and  $N = 0$  for  $l = 1, 2$ . These results agree with those predicted from the phase diagram in the left panel of Fig. 2.8, since it is only the in-phase  $l = 0$  mode that is within the region of instability.

Finally, to confirm predictions obtained from the linear stability analysis and the global bifurcation diagram, full time-dependent numerical solutions of the coupled PDE-ODE system (2.3.1) were computed for two values of  $D$  when  $\kappa = 1$  by using a method of lines approach based on a second-order spatial discretization for the bulk diffusion. In the upper row in Fig. 2.10 for  $D = 0.5$  we observe, as expected, a stable in-phase synchronous periodic solution. In the lower row of Fig. 2.10 where  $D = 0.2$ , the full numerical simulations show a stable asynchronous oscillation where the dynamics in the cells are phase-shifted. The phase-shifting observed in the lower row of Fig. 2.10 is consistent with the  $l = 2$  mode (with  $m = 3$ ) in the result (2.3.14) from the linear stability analysis, in that the bulk diffusion field at the midpoint of the cells and the cell dynamics  $V_1, V_2, V_3$  have the form  $\cos(\lambda_I t)$ ,  $\cos(\lambda_I t + 4\pi/3)$ , and  $\cos(\lambda_I t + 8\pi/3)$ .

### 2.3.4 Large $D$ Analysis for the Hopf Bifurcation Boundaries

In this subsection, we examine analytically some qualitative aspects of the region in the  $D$  versus  $\kappa$  phase diagram shown in Fig. 2.8 where the sym-

2.3. A Periodic Chain of Active Units Coupled by Bulk Diffusion

---

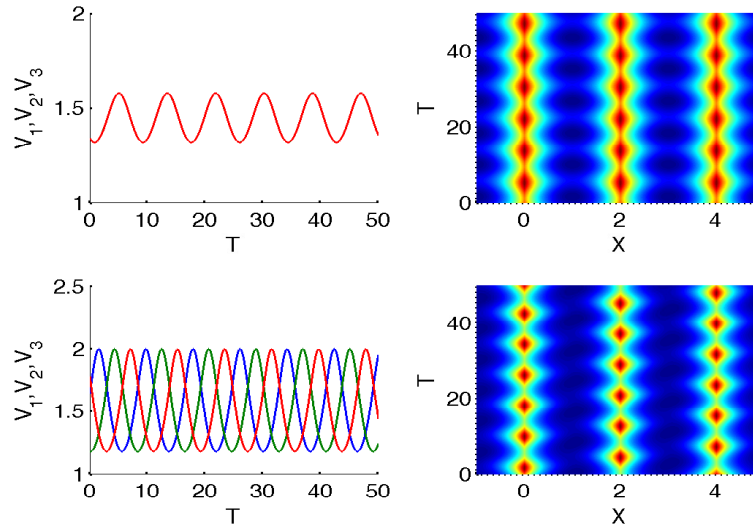


Figure 2.10: Full numerical results computed from (2.3.1) with  $D = 0.5$  (upper row) and  $D = 0.2$  (lower row). Other parameters are the same as in Fig. 2.8 with  $\kappa = 1$ . The initial conditions for  $D = 0.5$  are  $V_0 = [0.5, 1.5, 0.5]$ ,  $W_0 = [1, 1, 1]$ , and  $C_0(x) = 1$ . For  $D = 0.2$  the initial conditions are  $V_0 = [0.5, 1.5, 0.5]$ ,  $W_0 = [1, 1, 1]$ , and  $C_0(x) = 1$  if  $x > 0$ ,  $C_0(x) = \sin(x) + 1$  if  $x < 0$ . The  $V_1$ ,  $V_2$  and  $V_3$  curves are in blue, green and red respectively. For  $D = 0.5$  there are stable in-phase synchronous oscillations, whereas for  $D = 0.2$  stable phase-shifted synchronous oscillations occur. The phase shift among  $V_1$ ,  $V_2$  and  $V_3$ , is consistent with the mode  $l = 2$  in the linear stability analysis (2.3.14). The right panel in each row is a contour plot of  $C(x, t)$ .

### 2.3. A Periodic Chain of Active Units Coupled by Bulk Diffusion

---

metric steady-state is linearly unstable. In particular, we will study the large  $D$  behavior of the Hopf bifurcation boundaries in this plane. From this analysis we will also formulate a simple criterion that can be used to predict whether the lobe of instability in the  $D$  versus  $\kappa$  plane is bounded in  $D$  for other domain lengths  $L$  and bulk degradation parameter  $k$ . For the choice  $L = k = 1$  the instability regions were unbounded as  $D \rightarrow \infty$  (see the right panel of Fig. 2.8).

Firstly, we determine the limiting behavior of  $\mathcal{F}(\lambda)$  in (2.3.12) as  $D \rightarrow \infty$ . Upon using  $\Omega_\lambda D \sinh(2\Omega_\lambda L) \sim 2\Omega_\lambda^2 L D = 2(k + \lambda)L$  and  $\cosh(2\Omega_\lambda L) \sim 1$ , we obtain from (2.3.12b) that

$$\lim_{D \rightarrow \infty} \Delta_\lambda = \Delta_{\lambda, \infty} \equiv \frac{\kappa^2(\text{Re}(z_l) - 1) - 2\kappa L(k + \lambda)}{2L(k + \lambda) + 2\kappa}. \quad (2.3.16)$$

Therefore,  $\mathcal{F}(\lambda)$  in (2.3.12a) has the following limiting form as  $D \rightarrow \infty$ :

$$\lim_{D \rightarrow \infty} \mathcal{F}(\lambda) \equiv \mathcal{F}_\infty(\lambda) \equiv \frac{1}{\Delta_{\lambda, \infty}} + \frac{g_W^e - \lambda}{\det(J_e - \lambda I)}. \quad (2.3.17)$$

In addition, for  $D \rightarrow \infty$ , we can also find an approximate expression for the steady state  $V^e$  from (2.3.4c), which is needed to calculate the terms in (2.3.17). By using  $D\omega \tanh(\omega L) \sim D\omega^2 L \sim kL$ , we obtain from (2.3.4c), that for  $D \rightarrow \infty$ ,

$$\lim_{D \rightarrow \infty} V^e = V_\infty^e \equiv \frac{\mu(\kappa + Lk)}{\kappa + (1 + \kappa)kL}, \quad \lim_{D \rightarrow \infty} W^e = W_\infty^e \equiv \frac{\mu}{\alpha + (V_\infty^e)^2}. \quad (2.3.18)$$

We observe from (2.3.16), (2.3.17) and (2.3.18), that upon setting  $\mathcal{F}_\infty(\lambda) = 0$ , and rearranging the resulting expression, we obtain a cubic equation in  $\lambda$  of the form

$$\lambda^3 + \lambda^2 p_1 + \lambda p_2 + p_3 = 0, \quad (2.3.19a)$$

where we have identify  $p_1$ ,  $p_2$  and  $p_3$  by

$$\begin{aligned} p_1 &\equiv \frac{a}{2L} + \kappa - \text{tr}(J_e), \\ p_2 &\equiv \det(J_e) - \kappa g_W^e - \frac{(a \text{tr}(J_e) + b)}{2L}, \\ p_3 &\equiv \frac{(a \det(J_e) + b g_W^e)}{2L}, \end{aligned} \quad (2.3.19b)$$

and where we have defined  $a$  and  $b$  by

$$a \equiv 2(\kappa + kL), \quad b \equiv \kappa^2(\text{Re}(z_l) - 1) - 2L\kappa k. \quad (2.3.19c)$$

### 2.3. A Periodic Chain of Active Units Coupled by Bulk Diffusion

Next, we simplify (2.3.19b) for the Sel'kov kinetics (2.1.1c), for which

$$\det(J_e) = \epsilon \left( \alpha + (V_\infty^e)^2 \right) = -g_W^e > 0, \quad \text{tr}(J_e) = 2V_\infty^e W_\infty^e - 1 - \det(J_e). \quad (2.3.20)$$

By substituting (2.3.20) into (2.3.19b), we readily calculate that

$$\begin{aligned} p_1 &\equiv \kappa \left( 1 + \frac{1}{L} \right) + k + 1 + \det(J_e) - \frac{2\mu V_\infty^e}{\left( \alpha + (V_\infty^e)^2 \right)}, \\ p_2 &\equiv \left( 1 + \kappa \left( 1 + \frac{1}{L} \right) + k \right) \det(J_e) + \frac{\xi}{2L} - \frac{2(\kappa + kL)\mu V_\infty^e}{L \left( \alpha + (V_\infty^e)^2 \right)}, \\ p_3 &\equiv \frac{\xi}{2L} \det(J_e), \quad \xi \equiv a - b = 2kL(1 + \kappa) + 2\kappa + \kappa^2(1 - \text{Re}(z_l)) > 0. \end{aligned} \quad (2.3.21)$$

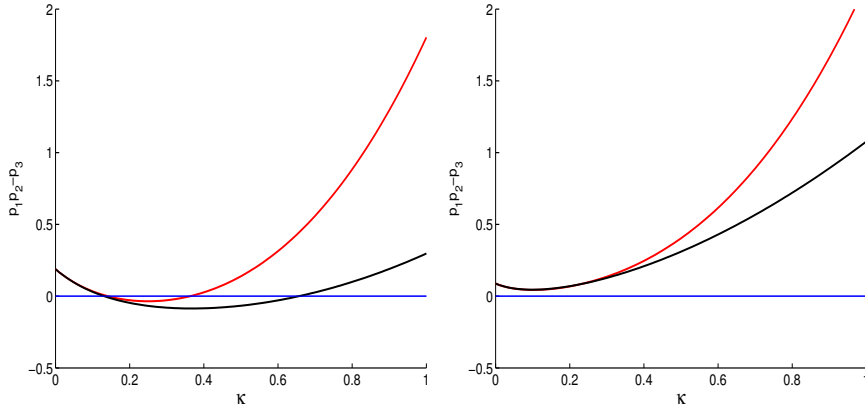


Figure 2.11: Plot of  $p_1 p_2 - p_3$  versus  $\kappa$  for  $l = 0$  (black) and  $l = 1$  (red) for a ring of  $m = 3$  cells. The blue horizontal line is the threshold  $p_1 p_2 = p_3$ . Any intersections of the black (red) curve with the blue line yields the bifurcation points for  $\kappa$  for  $l = 0$  ( $l = 1$ ). Left panel: the parameter values as given in Fig. 2.8. Between the two bifurcation points, the black (red) curve lies below the threshold  $p_1 p_2 = p_3$ , and so by the Routh-Hurwitz criterion there are unstable eigenvalues. Numerically we verify  $p_1 > 0$ . Right panel: same parameters except that now the bulk decay is smaller at  $k = 0.3$ . There are now no Hopf bifurcation values of  $\kappa$  in the  $D \rightarrow \infty$  regime.

For the Sel'kov model with  $\epsilon = 0.15$ ,  $\mu = 2$ , and  $\alpha = 0.9$ , we now use the

### 2.3. A Periodic Chain of Active Units Coupled by Bulk Diffusion

---

cubic (2.3.19a) with coefficients (2.3.21) to calculate the the limiting Hopf bifurcation values of  $\kappa$ , valid as  $D \rightarrow \infty$ , when  $k = 1$  and  $L = 1$ . By the *Routh-Hurwitz* criterion, a necessary and sufficient condition for all of the roots of (2.3.19a) to satisfy  $Re(\lambda) < 0$  is that the following three inequalities hold:

$$p_1 > 0, \quad p_3 > 0, \quad p_1 p_2 > p_3. \quad (2.3.22)$$

From (2.3.21), we have  $p_3 > 0$  for any parameter set. Moreover, the Hopf bifurcation boundary satisfies

$$p_1 p_2 = p_3. \quad (2.3.23)$$

provided that  $p_1 > 0$  and  $p_3 > 0$ .

Our numerical computations, from enforcing (2.3.23) for  $m = 3$ , predict that there is a Hopf bifurcation for  $D \gg 1$  when

$$\begin{aligned} l = 0, \quad \kappa &\approx 0.1313 \text{ and } 0.6564, \\ l = 1, \quad \kappa &\approx 0.1407 \text{ and } 0.3633. \end{aligned} \quad (2.3.24)$$

This is shown in Fig. 2.11. In contrast, from the phase diagram of  $D$  versus  $\kappa$ , as seen in the right panel of Fig. 2.8, we obtain for  $D = 100$  that the Hopf bifurcation values for  $\kappa$  are

$$\begin{aligned} l = 0, \quad \kappa &\approx 0.1314 \text{ and } 0.6579, \\ l = 1, \quad \kappa &\approx 0.1405 \text{ and } 0.3665, \end{aligned} \quad (2.3.25)$$

which are remarkably close to the values calculated in (2.3.24) from the  $D \rightarrow \infty$  theory.

Finally, to obtain a bounded lobe of instability in the  $D$  versus  $\kappa$  plane, rather than the unbounded region as  $D \rightarrow \infty$  shown in Fig 2.8, all that is needed is to seek conditions on the domain length  $L$  and bulk parameter  $k$  such that the Routh-Hurwitz stability condition (2.3.22) holds for all  $\kappa$ . This can be achieved by decreasing either  $L$  or  $k$ . We remark that if we decrease either the domain length  $L$  or bulk decay parameter  $k$ , then the black and red curves in Fig. 2.11 move up, and so there no longer any Hopf bifurcation points for the  $D \rightarrow \infty$  regime. An example of this is shown in the right panel of Fig. 2.11 for the same parameters as in the left panel of Fig 2.11 except that now  $k = 0.3$ . In this case, the instability lobe in the phase diagram of  $D$  versus  $\kappa$  would be bounded in  $D$  for both the  $l = 0$  and  $l = 1, 2$  modes.

## 2.4 Nonlinear Coupling Between Compartments and Bulk

In the previous section, we considered the case where there is a linear coupling between the compartment and the bulk. Such a linear coupling term shifts the steady-state of the original ODE system from  $V_e = \mu$  to a new value that depends on the coupling strength  $\beta$ .

In this section, we will study a nonlinear coupling between the compartments and the bulk that possesses the same stable steady-state as that of the uncoupled ODE system in the compartment, but that still has the effect of generating compartment-bulk oscillations. To illustrate such a possibility, we consider the coupling term  $P(C(2Li, t), V)$ , for  $i = 0, 1$  with the form

$$\begin{aligned} P(C(2Li, t), V) &= \beta h(C(2Li, t))q(V(t)), \\ h(C(2Li, t)) &= \frac{C(2Li, t)(C(2Li, t) - c_0)}{K_c + C(2Li, t)^2}, \quad q(V) = \frac{V(V - \mu)}{L_v + V^2}, \quad i = 0, 1, \end{aligned} \quad (2.4.1)$$

where  $L_v > 0$ ,  $K_c > 0$ , and where we have defined  $c_0$  by

$$c_0 = \gamma\mu, \quad \gamma \equiv \frac{\kappa}{\kappa + D\omega \tanh(\omega L)}, \quad \omega \equiv \sqrt{k/D}. \quad (2.4.2)$$

As in §2.2 we will determine the symmetric steady-state solution to (2.1.1) with (2.4.1) and analyze its linear stability. Upon solving the time-independent problem for (2.1.1) on the domain  $[0, L]$ , with no-flux boundary condition for  $C$  at  $x = L$ , we readily obtain that

$$\begin{aligned} C_e(x) &= C_e^0 \frac{\cosh(\omega(L-x))}{\cosh(\omega L)}, \quad C_e^0 = \frac{\kappa V_s}{\kappa + D\omega \tanh(\omega L)}, \\ W_e &= \frac{\mu}{\alpha + V_e^2}, \end{aligned} \quad (2.4.3)$$

where  $V_e$  satisfies the following fifth order polynomial:

$$(V_e - \mu)Q(V_e) = 0, \quad Q(V_e) \equiv (V_e^4 - \beta V_e^3 + V_e^2(\frac{K_c}{\gamma^2} + L_v + \beta\mu) + \frac{K_c L_v}{\gamma^2}). \quad (2.4.4)$$

Here  $\gamma, \omega$  are defined in (2.4.2). We observe that with the nonlinear coupling function (2.4.1), the steady state solution of the uncoupled ODE compartmental dynamics is still a steady-state of the coupled ODE system. Specifically, we have the uncoupled steady-state

$$V_e = \mu, \quad W_e = \frac{\mu}{\alpha + \mu^2}, \quad C_e^0 = c_0, \quad (2.4.5)$$

## 2.4. Nonlinear Coupling Between Compartments and Bulk

---

where corresponds to setting  $\beta = 0$  in (2.2.2). In addition, there can be at most four other steady-state solutions, corresponding to the roots of  $Q(V_e) = 0$  in (2.4.4). However, since  $Q(\mu) > 0$ , none of these additional steady-state solution branches bifurcate from the uncoupled steady-state branch (2.4.5).

To examine the stability of the steady state (2.4.5), we introduce the same perturbation as in (2.2.3). Upon linearizing (2.1.1), we obtain, after some algebra, that the associated eigenvalue  $\lambda$  satisfies

$$\lambda^2 - \lambda(g_W^e + f_V^e + \beta(P_V^e + \delta P_C^e)) + (g_W^e f_V^e - g_V^e f_W^e + \beta g_W^e (P_V^e + \delta P_C^e)) = 0,$$

where

$$\begin{aligned} \delta &\equiv \frac{\kappa}{\kappa + D\Omega_\lambda \tanh(\Omega_\lambda L)} && \text{(in-phase),} \\ \delta &\equiv \frac{\kappa}{\kappa + D\Omega_\lambda \coth(\Omega_\lambda L)} && \text{(anti-phase).} \end{aligned}$$

We observe that with the special choice (2.4.1) of nonlinear coupling  $P(C(0, t), V)$ , we have  $P_C^e = 0$  and  $P_V^e = 0$ , so that the characteristic equation for  $\lambda$  becomes

$$\lambda^2 - \lambda(g_W^e + f_V^e) + (g_W^e f_V^e - g_V^e f_W^e) = 0,$$

which is the same as that for the uncoupled problem. Since we assumed that the uncoupled problem has stable dynamics, we have  $\text{Re}(\lambda) < 0$ . Thus, our linear stability analysis predicts that the steady-state (2.4.5) can never be destabilized by the nonlinear coupling (2.4.1).

To determine whether, nevertheless, there can be any compartment-bulk oscillations, we used XPPAUT[16] to compute global bifurcation diagrams after first spatially discretizing (2.1.1) with the coupling (2.4.1). In Fig. 2.12 we show two typical bifurcation diagrams of the compartmental variable  $V$ . In the left panel of Fig. 2.12 we plot  $V$  versus the coupling strength  $\beta$  for the fixed diffusivity  $D = 0.1$  showing the stable steady-state solution and the branch of synchronous periodic oscillations. There is also a branch of asynchronous periodic solutions (not shown), that essentially overlaps the synchronous branch. This overlap occurs since for  $D = 0.1$ , the bulk diffusion field decays rather quickly away from  $x = 0$  and  $x = 2L$ , which leads to a rather weak coupling between the two compartments. The key feature from the left panel of Fig. 2.12 is that there is some parameter regime in  $\beta$ , with  $D = 0.1$ , where stable synchronous time-periodic solutions co-exist with the stable steady-state solution (2.4.5). This phenomenon cannot be revealed from a local linear stability analysis along the solution branch (2.4.5). For  $\beta = 4$ , in the right panel of Fig. 2.12 we plot a bifurcation diagram of  $V$  versus  $D$  showing the stable steady-states together with disconnected branches

## 2.4. Nonlinear Coupling Between Compartments and Bulk

---

of synchronous and asynchronous periodic solutions. Both the asynchronous and synchronous branches have a saddle-node bifurcation point at  $D \approx 0.57$  and  $D \approx 0.67$ , respectively. The synchronous branches are always unstable. Stable asynchronous time-periodic solutions co-exist with the stable steady-state solution (2.4.5) when  $D < 0.57$ .

To confirm predictions from the bifurcation diagram, we computed full numerical solutions of the PDE-ODE system (2.1.1) with nonlinear coupling (2.4.1) for  $D = 0.5$  and  $\beta = 4$ , with the other parameter values as given in the caption of Fig. 2.13. From Fig. 2.12, we observe for these parameter values that the asynchronous mode is stable. The full numerical results shown in Fig. 2.13 confirm this prediction of stable asynchronous oscillatory dynamics.

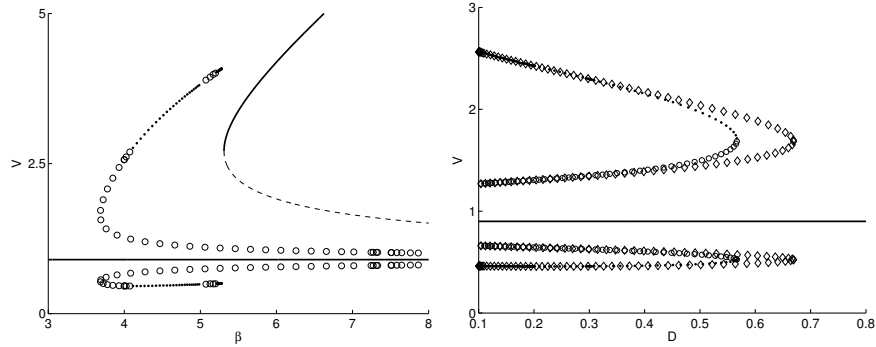


Figure 2.12: Bifurcation diagram of the local variable  $V$  with respect to the coupling strength  $\beta$  and diffusivity  $D$  for the parameter set  $L = 1$ ,  $k = 2$ ,  $\kappa = 3$ ,  $\epsilon = 0.15$ ,  $\mu = 0.9$ ,  $\alpha = 0.55$ ,  $K_c = 1$  and  $L_v = 0.8$ . The solid/dashed line represents stable/unstable steady state solution of  $V$ , open/solid circle indicates unstable/stable periodic solution, respectively. The steady-state (2.4.5) is the solid horizontal line. Left panel:  $V$  versus  $\beta$  for  $D = 0.1$ . The periodic solution branches shown correspond only to the synchronous oscillations. Stable synchronous oscillations and stable steady-states will coexist only for some range of  $\beta$ . Right panel:  $V$  versus  $D$  for  $\beta = 4$ . The periodic solution branch that is unstable, with a saddle-node point at  $D \approx 0.67$ , is the synchronous branch. The other periodic solution branch, with a saddle-node point at  $D \approx 0.57$  represents asynchronous oscillations. This plot shows that synchronous oscillations are unstable for  $\beta = 4$ , but that stable asynchronous oscillations and stable steady-state solutions will co-exist in some range of  $D$  when  $\beta = 4$ .

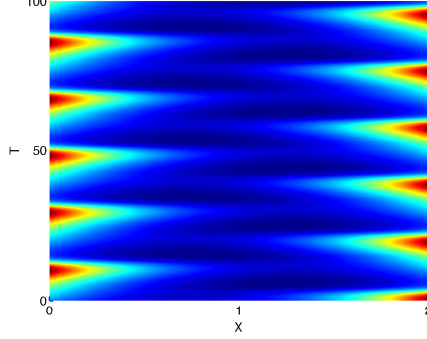


Figure 2.13: Numerical simulation of the coupled PDE-ODE system (2.1.1) with nonlinear coupling (2.4.1) for  $D = 0.5$ ,  $\beta = 4$ , and  $L = 1$ . The other parameter values are the same as in the caption of Fig. 2.12. The initial conditions are  $C(x, 0) = 2$ ,  $v_1 = 1$ ,  $w_1 = 0.3$ ,  $v_2 = 0.2$ , and  $w_2 = 0.3$ . Stable asynchronous oscillations for  $C(x, t)$  are observed.

#### 2.4.1 Compartmental Dynamics Neglecting Bulk Diffusion

As shown above, a local stability analysis around the steady-state (2.4.5) does not provide any insight into the occurrence of oscillatory behavior of the coupled ODE-PDE system (2.1.1) with coupling (2.4.1). In this subsection, we consider an ODE model in the compartment, where we have neglected the bulk diffusion process, and simply set  $P(C, V) = q(V)$  in (2.4.1). The resulting ODE model is written as

$$\begin{aligned} \frac{dV}{dt} &= f_0(V, W) - V + \beta q(V), & \frac{dW}{dt} &= \epsilon(\mu - f_0(V, W)), \\ f_0(V, W) &\equiv \alpha W + WV^2, & q(V) &\equiv \frac{V(V - \mu)}{L_v + V^2}. \end{aligned} \quad (2.4.6)$$

A typical bifurcation diagram of this ODE system is shown in Fig. 2.14. From this numerically calculated bifurcation diagram we observe that there are three types of critical points; three Hopf bifurcation (HB) points, the saddle node (SN) point, and the transcritical point where two steady-state branches intersect (IS).

To determine the location of these points we first determine the steady-states of (2.4.6), which satisfy

$$(V_e - \mu)(V_e^2 - \beta V_e + L_v) = 0. \quad (2.4.7)$$

## 2.4. Nonlinear Coupling Between Compartments and Bulk

---

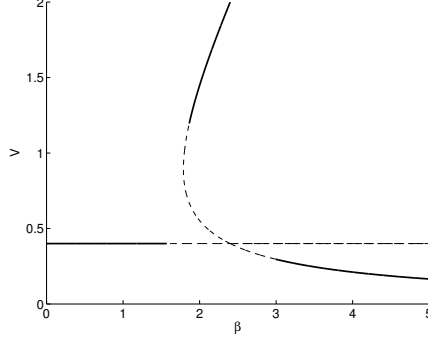


Figure 2.14: Bifurcation diagram of the ODE system (2.4.6) versus  $\beta$  for the parameter set  $\epsilon = 0.15$ ,  $\mu = 0.4$ ,  $\alpha = 0.55$ , and  $L_v = 0.8$ . The solid/dashed line represents stable/unstable steady state solution of  $V$ .

Therefore,  $V_e = \mu$  is a steady-state, and there are two additional steady-state solutions given by

$$V_e^\pm = \frac{\beta}{2} \pm \sqrt{\left(\frac{\beta}{2}\right)^2 - L_v}, \quad (2.4.8)$$

when  $L_v < \beta^2/4$ . At the SN point, we have  $V_e^+ = V_e^-$ , which gives

$$\beta_{\text{SN}} = 2\sqrt{L_v}, \quad \text{and} \quad V_e^\pm = \sqrt{L_v}. \quad (2.4.9)$$

For the parameter values in Fig. 2.14 we get  $\beta_{\text{SN}} \approx 1.789$ .

At the IS point, since one of  $V_e^\pm$  must equal  $\mu$ , we obtain that

$$\frac{\beta}{2} \pm \sqrt{\left(\frac{\beta}{2}\right)^2 - L_v} = \mu, \quad (2.4.10)$$

which yields  $\beta = \mu + L_v/\mu$ . Since,  $\mu - \beta/2 = (\mu^2 - L_v)/(2\mu)$ , we conclude that  $V_e^- = \mu$  when  $L_v > \mu^2$ , and  $V_e^+ = \mu$  when  $L_v < \mu^2$ . The parameter set in the caption of Fig. 2.14 corresponds to this first possibility. The IS point occurs at  $\beta_{\text{IS}} = (0.4^2 + 0.8)/0.4 = 2.4$ .

To determine the HB points, we calculate the trace and the determinant of the Jacobian matrix  $J_e$  associated with (2.4.6) as

$$\text{tr}(J_e) = f_{0V}^e - 1 + \beta q'(V_e) - \epsilon f_{0W}^e, \quad \det(J_e) = -\epsilon f_{0W}^e (\beta q'(V_e) - 1).$$

The Hopf bifurcation occurs when  $\text{tr}(J_e) = 0$  and  $\det(J_e) > 0$ , which gives

$$\beta q'(V_e) = 1 + \epsilon f_{0W}^e - f_{0V}^e, \quad (2.4.11a)$$

provided that

$$\det(J_e) = -\epsilon f_{0W}^e (\epsilon f_{0W}^e - f_{0V}^e) = \epsilon \left[ 2V_e \mu - \epsilon (\alpha + V_e^2)^2 \right] > 0. \quad (2.4.11b)$$

To determine the HB point off of the  $V_e = \mu = 0.4$  steady-state branch in Fig. 2.14, we set  $V_e = \mu$  in (2.4.11b) to calculate that  $\det(J_e) \approx 0.0367 > 0$ . By using (2.4.6) for  $q(V)$  to calculate  $q'(\mu)$ , we obtain from (2.4.11a) that the HB point  $\beta_{\text{HB}}$  is

$$\beta_{\text{HB}} = \frac{(L_v + \mu^2)}{\mu(\alpha + \mu^2)} \left[ \alpha - \mu^2 + \epsilon(\alpha + \mu^2)^2 \right]. \quad (2.4.12)$$

For the parameter set of Fig. 2.14 this yields  $\beta_{\text{HB}} \approx 1.574$ . The other two HB points in Fig. 2.14, corresponding to bifurcations from the  $V_e^\pm$  steady-states, are also readily calculated from (2.4.11). We find that the Hopf bifurcation on the  $v_+$  branch is at  $\beta_{\text{HB}} \approx 1.8641$  with  $\det(J_e) \approx 0.0554 > 0$ , while the Hopf bifurcation on the  $v_-$  branch occurs at  $\beta_{\text{HB}} \approx 2.9884$  with  $\det(J_e) \approx 0.0265 > 0$ .

We conclude that the bifurcation diagram of the ODE system (2.4.6) does share only a few of the characteristics observed in the bifurcation diagram of Fig. 2.12 for the fully coupled compartmental-bulk problem (2.1.1) with (2.4.1). For both the ODE model and the fully coupled model, new branches of steady-state solutions, other than the base-state  $V_e = \mu$ , are possible. However, for the fully coupled problem, the branches of periodic solutions are isolated in the sense that they do not arise from bifurcations off of the steady-state solution branches.

## Chapter 3

# Nonlinear Analysis Near the Double Hopf Bifurcation Point

In the previous chapter, parameter study of the cell-bulk coupled system with linear coupling shows the existence of a double Hopf bifurcation point in the  $\beta$  versus  $D$  plane. In the following chapter, we provide an extensive analyze near such point with the full PDE-ODE coupled system. The analysis explains and predicts certain features of the parameter study of the system regarding the interaction of in-phase and anti-phase modes. For example, in parameter regions of bistability near the double Hopf point, there is an unstable invariant torus in the dynamics whose stable manifold forms a boundary in phase space between the stable in-phase and anti-phase modes. We express the coupled compartment-bulk system as an evolution equation in an infinite-dimensional space, and use center manifold theory to reduce the evolution to a four-dimensional local invariant manifold in the infinite-dimensional space. This latter evolution is further reduced to a normal form, which is then used to make predictions about the in-phase and anti-phase modes and their nonlinear interaction near the double Hopf bifurcation.

In the following section §3.1, we restate the model system that describes the two diffusively coupled cells. Then in section §3.2 we find in parameter space the location of the double Hopf point, and calculate associated eigenvalues and eigenvectors. In section §3.3 we describe the double Hopf bifurcation analysis and its results, and describe tests of its predictions using AUTO and simulations.

### 3.1 The Coupled Compartment-Bulk Diffusion Model

The model we consider describes chemical reactions in two cells, and the diffusion of a signalling chemical in the extracellular space between the cells. We will take a one-dimensional spatial domain, and let  $C(x, t)$  denote the concentration of the signalling chemical, where  $x$  denotes the spatial location in the interval  $-L \leq x \leq +L$  representing the extracellular space, and  $t$  is time. We assume the signalling chemical diffuses and degrades while in the extracellular space, and model this with the linear partial differential equation

$$\frac{\partial C}{\partial t}(x, t) = D \frac{\partial^2 C}{\partial x^2}(x, t) - kC(x, t), \quad -L < x < +L, \quad (3.1.1)$$

where  $D > 0$  and  $k > 0$  are the diffusion and degradation constants. Two cells, or compartments, are located at each of the boundaries of the extracellular space  $x = -L$  and  $x = +L$ . Inside each cell, the signalling chemical is involved in chemical reactions. We assume chemicals are well-mixed inside each cell, and let  $V_-(t)$  and  $V_+(t)$  denote the concentration of the signalling chemical inside the cell at  $x = -L$  and the cell at  $x = +L$ , respectively. The cells can exchange the signalling chemical with the extracellular space, and we model this with a flux condition at each boundary of the extracellular space,

$$\begin{aligned} -D \frac{\partial C}{\partial x}(-L, t) &= \kappa [V_-(t) - C(-L, t)], \\ +D \frac{\partial C}{\partial x}(+L, t) &= \kappa [V_+(t) - C(+L, t)], \end{aligned} \quad (3.1.2)$$

where  $\kappa$  is a positive flux constant. Thus, if the concentration  $V_{\pm}$  of the signalling chemical inside a cell is higher than the concentration  $C(\pm L, \cdot)$  at the corresponding boundary, there is a positive flux of the chemical out of the cell, into the extracellular space.

Inside each cell, at  $x = -L$  and at  $x = +L$ , the signalling chemical reacts with some intermediate chemical product, whose concentrations are denoted  $W_-(t)$  and  $W_+(t)$ , respectively. The reactions are governed by ordinary differential equations

$$\begin{aligned} \frac{dV_-}{dt}(t) &= f(V_-(t), W_-(t)) + \beta [C(-L, t) - V_-(t)], \\ \frac{dW_-}{dt}(t) &= \epsilon g(V_-(t), W_-(t)), \end{aligned} \quad (3.1.3)$$

### 3.2. Linearized Stability

---

inside the cell at  $x = -L$ , and

$$\begin{aligned}\frac{dV_+}{dt}(t) &= f(V_+(t), W_+(t)) + \beta [C(+L, t) - V_+(t)], \\ \frac{dW_+}{dt}(t) &= \epsilon g(V_+(t), W_+(t)),\end{aligned}\tag{3.1.4}$$

inside the cell at  $x = +L$ , where  $\epsilon$  is a positive constant. The influence of the outside concentration of the signalling chemical on the reaction dynamics inside each cell is described by the coupling terms  $\beta[C(\pm L, \cdot) - V_{\pm}]$ , with a positive constant  $\beta$  that represents the coupling strength. We take identical cells, so  $\epsilon$  and  $\beta$  are the same for each cell, and the functions  $f$  and  $g$  representing the reaction kinetics inside each cell are the same. For specific kinetics, we take the Sel'kov model

$$\begin{aligned}f(V, W) &= -V + \alpha W + V^2 W, \\ g(V, W) &= \mu - \alpha W - V^2 W,\end{aligned}\tag{3.1.5}$$

where  $\alpha$  and  $\mu$  are positive constants. These kinetics have the property that when the cells are isolated ( $\beta = 0$ ) there is a unique steady state  $V_0 = \mu$ ,  $W_0 = \mu/(\alpha + V_0^2)$  which is stable, but when the cells are coupled there can be stable oscillating solutions, so in this sense, oscillations are ‘‘conditional’’. Our model system is (3.1.1)–(3.1.5), which in more mathematical terms can be described as a pair of identical, diffusively coupled, conditional oscillators. Since the cells are identical, the model system (3.1.1)–(3.1.5) has a reflection symmetry, under spatial reflection  $x \rightarrow -x$  and exchange of cells.

## 3.2 Linearized Stability

In this section we study the eigenvalue problem that gives the linearized stability of the steady state solution of the model system. From this we obtain parameter values that give Hopf points for two types of marginally stable synchronized linear oscillations, which we call anti-phase and in-phase eigenvectors. In particular, we obtain parameter values for a double Hopf point, where both the anti-phase and in-phase eigenvectors are marginally stable.

We find the steady state, or equilibrium, of the model system (3.1.1)–(3.1.5) as

$$C(x, t) = C^e(x), \quad V_-(t) = V^e, \quad V_+(t) = V^e, \quad W_-(t) = W^e, \quad W_+(t) = W^e,\tag{3.2.1}$$

### 3.2. Linearized Stability

---

where

$$C^e(x) = C_0^e \frac{\cosh(\Omega_0 x)}{\cosh(\Omega_0 L)}, \quad V^e = \frac{\mu + \beta C_0^e}{1 + \beta}, \quad W^e = \frac{\mu}{1 + (V^e)^2},$$

and

$$\Omega_0 = \sqrt{\frac{k}{D}}, \quad C_0^e = \frac{\kappa \mu}{\kappa + D \Omega_0 (1 + \beta) \tanh(\Omega_0 L)}.$$

Then defining deviations from the steady state by

$$C(x, t) = C^e(x) + c(x, t), \quad V_{\pm}(t) = V^e + v_{\pm}(t), \quad W_{\pm}(t) = W^e + w_{\pm}(t),$$

from (3.1.1)–(3.1.4) we obtain the corresponding differential equations for the deviations

$$\begin{aligned} \frac{\partial c}{\partial t} &= D \frac{\partial^2 c}{\partial x^2} - kc, \\ \frac{dv_-}{dt} &= f(V^e + v_-, W^e + w_-) - f(V^e, W^e) + \beta [c(-L, \cdot) - v_-], \\ \frac{dw_-}{dt} &= \epsilon [g(V^e + v_-, W^e + w_-) - g(V^e, W^e)], \\ \frac{dv_+}{dt} &= f(V^e + v_+, W^e + w_+) - f(V^e, W^e) + \beta [c(+L, \cdot) - v_+], \\ \frac{dw_+}{dt} &= \epsilon [g(V^e + v_+, W^e + w_+) - g(V^e, W^e)], \end{aligned} \quad (3.2.2)$$

with boundary conditions

$$\begin{aligned} -D \frac{\partial c}{\partial x}(-L, \cdot) &= \kappa [v_- - c(-L, \cdot)], \\ +D \frac{\partial c}{\partial x}(+L, \cdot) &= \kappa [v_+ - c(+L, \cdot)], \end{aligned} \quad (3.2.3)$$

We linearize (3.2.2)–(3.2.3) about the origin (which now corresponds to the steady state) and obtain

$$\begin{aligned} \frac{\partial c}{\partial t} &= D \frac{\partial^2 c}{\partial x^2} - kc, \\ \frac{dv_{\pm}}{dt} &= f_V^e v_{\pm} + f_W^e w_{\pm} + \beta [c(\pm L, \cdot) - v_{\pm}], \\ \frac{dw_{\pm}}{dt} &= \epsilon [g_V^e v_{\pm} + g_W^e w_{\pm}], \end{aligned} \quad (3.2.4)$$

with the same boundary conditions

$$\pm D \frac{\partial c}{\partial x}(\pm L, \cdot) = \kappa [v_{\pm} - c(\pm L, \cdot)], \quad (3.2.5)$$

### 3.2. Linearized Stability

---

where  $f_V^e$ ,  $g_V^e$ ,  $f_W^e$  and  $g_W^e$  are the partial derivatives of  $f$  and  $g$ , evaluated at the steady state (3.2.1).

To study the linearized stability of the steady state, we make the usual ansatz  $c(x, t) = e^{\lambda t} \eta(x)$ ,  $v_{\pm} = e^{\lambda t} \varphi_{\pm}$  and  $w_{\pm} = e^{\lambda t} \psi_{\pm}$  in (3.2.4)–(3.2.5), and obtain the eigenvalue problem

$$\begin{aligned} \lambda \eta &= D\eta'' - k\eta, \\ \lambda \varphi_{\pm} &= f_V^e \varphi_{\pm} + f_W^e \psi_{\pm} + \beta [\eta(\pm L) - \varphi_{\pm}], \\ \lambda \psi_{\pm} &= \epsilon [g_V^e \varphi_{\pm} + g_W^e \psi_{\pm}], \end{aligned} \quad (3.2.6)$$

with boundary conditions

$$\pm D\eta'(\pm L) = \kappa [\varphi_{\pm} - \eta(\pm L)]. \quad (3.2.7)$$

If  $\text{Re } \lambda < 0$  for all eigenvalues  $\lambda$ , then the steady state is asymptotically stable. We seek parameter values where the steady state is marginally stable:  $\text{Re } \lambda = 0$  for finitely many eigenvalues, called critical eigenvalues, and  $\text{Re } \lambda < 0$  for all remaining eigenvalues. Near such parameter values, we expect the nonlinear system (3.2.2)–(3.2.3) will have bifurcations of solutions near the steady state.

Due to the reflection symmetry of (3.2.6)–(3.2.7), the eigenvectors come in two types, odd or “anti-phase” with

$$\eta(-x) = -\eta(x), \quad v_- = -v_+, \quad w_- = -w_+,$$

and even or “in-phase” with

$$\eta(-x) = \eta(x), \quad v_- = v_+, \quad w_- = w_+,$$

Solving the eigenvalue problem for anti-phase eigenvectors, we have

$$\eta_-(x) = \eta_1^0 \frac{\sinh(\Omega_{\lambda} x)}{\sinh(\Omega_{\lambda} L)}$$

for some constant  $\eta_1^0$ , where

$$\Omega_{\lambda} = \sqrt{\frac{k + \lambda}{D}},$$

and the boundary condition at  $x = +L$  gives

$$[\kappa + D\Omega_{\lambda} \coth(\Omega_{\lambda} L)] \eta_1^0 = \kappa \varphi_-.$$

### 3.2. Linearized Stability

---

Therefore the  $\varphi_-$  and  $\psi_-$  components of an anti-phase eigenvector satisfy the homogeneous system of linear equations

$$\begin{aligned} [f_V^e - p_-(\lambda) - \lambda]\varphi_- + f_W^e\psi_- &= 0, \\ \epsilon g_V^e\varphi_- + (\epsilon g_W^e - \lambda)\psi_- &= 0, \end{aligned} \quad (3.2.8)$$

where

$$p_-(\lambda) = \frac{D\Omega_\lambda \coth(\Omega_\lambda L)}{\kappa + D\Omega_\lambda \coth(\Omega_\lambda L)}.$$

Taking the determinant of the coefficient matrix of (3.2.8) we obtain a transcendental equation for any eigenvalue  $\lambda$  for anti-phase eigenvectors

$$[f_V^e - p_-(\lambda) - \lambda](\epsilon g_W^e - \lambda) - \epsilon f_W^e g_V^e = 0. \quad (3.2.9)$$

Similarly, for in-phase eigenvectors we have

$$\eta_+(x) = \eta_+^0 \frac{\cosh(\Omega_\lambda x)}{\cosh(\Omega_\lambda L)}$$

and  $\lambda$  must satisfy

$$[f_V^e - p_+(\lambda) - \lambda](\epsilon g_W^e - \lambda) - \epsilon f_W^e g_V^e = 0, \quad (3.2.10)$$

where

$$p_+(\lambda) = \frac{D\Omega_\lambda \tanh(\Omega_\lambda L)}{\kappa + D\Omega_\lambda \tanh(\Omega_\lambda L)}.$$

We solve the eigenvalue equations (3.2.9) and (3.2.10) numerically, using the mathematical software package Maple. We put

$$k = 1, \quad L = 1, \quad \alpha = 0.9, \quad \epsilon = 0.15, \quad \kappa = 1, \quad \mu = 2, \quad (3.2.11)$$

and seek parameter values (“Hopf points”) that give purely imaginary eigenvalues

$$\lambda = i\omega_1 \quad \text{or} \quad \lambda = i\omega_2$$

with anti-phase or in-phase eigenvectors, respectively. With  $D$  and  $\beta$  as free parameters, we solve (3.2.9) to find a curve of Hopf points for anti-phase eigenvectors, and solve (3.2.10) to obtain another curve of Hopf points, for in-phase eigenvectors. These curves intersect, at a double Hopf point, and this intersection can be found by simultaneously solving (3.2.9) and (3.2.10), using starting values from the preliminary explorations with AUTO on the finite-difference approximation. We obtain, for the double Hopf point, parameter values

$$D = 0.555509 \quad \beta = 0.508394, \quad (3.2.12)$$

### 3.2. Linearized Stability

---

with

$$\omega_1 = 0.811618, \quad \omega_2 = 0.794334.$$

We checked, using spatially discretized finite-difference approximations of the eigenvalue problem (3.2.6)–(3.2.7), for parameter values at the double Hopf point (3.2.11)–(3.2.12), that (allowing for small discretization errors) there are four critical, purely imaginary simple eigenvalues  $\lambda = \pm i\omega_{1,2}$ , and all remaining eigenvalues have negative real parts bounded away from 0.

If parameters are varied continuously, the eigenvalues change continuously. Therefore, if parameters are near the double Hopf point, there are four simple eigenvalues near  $\pm i\omega_{1,2}$ , near the imaginary axis, which we still call critical eigenvalues. Near the double Hopf point, by continuity the remaining eigenvalues still have negative real parts bounded away from 0.

We conclude this section by introducing a vector notation, which makes the subsequent bifurcation calculations more convenient. We let

$$X(t) = \begin{bmatrix} c(x, t) \\ v_-(t) \\ w_-(t) \\ v_+(t) \\ w_+(t) \end{bmatrix}, \quad (3.2.13)$$

where for each  $t$ ,  $X(t)$  belongs to a real infinite-dimensional function space  $H$  consisting of vectors  $X(t)$  whose components satisfy the boundary conditions (3.2.5). We define the linear differential operator  $M$  by

$$MX = \begin{bmatrix} D \frac{\partial^2 c}{\partial x^2} - kc \\ f_V^e v_- + f_W^e w_- + \beta[c(-L, \cdot) - v_-] \\ \epsilon g_V^e v_- + \epsilon g_W^e w_- \\ f_V^e v_+ + f_W^e w_+ + \beta[c(+L, \cdot) - v_+] \\ \epsilon g_V^e v_+ + \epsilon g_W^e w_+ \end{bmatrix}, \quad (3.2.14)$$

for all  $X(t)$  belonging to  $H$ . Then the linearized system (3.2.4)–(3.2.5) can be written as

$$\dot{X} = MX, \quad (3.2.15)$$

### 3.2. Linearized Stability

---

for  $X(t)$  belonging to  $H$ , where the dot denotes differentiation with respect to  $t$ . Setting  $X(t) = e^{\lambda t}q$ , where

$$q = \begin{bmatrix} \eta(x) \\ \varphi_- \\ \psi_- \\ \varphi_+ \\ \psi_+ \end{bmatrix}$$

belongs to  $H$ , the eigenvalue problem (3.2.6)–(3.2.7) is expressed as

$$Mq = \lambda q, \quad (3.2.16)$$

For complex eigenvalues  $\lambda$ , we seek the corresponding eigenvectors  $q$  in the complexification of  $H$ . In particular, at the double Hopf point (3.2.11)–(3.2.12) we have

$$Mq_1 = i\omega_1 q_1, \quad Mq_2 = i\omega_2 q_2.$$

The complex eigenvectors (up to multiplication by an arbitrary complex scalar) are

$$q_1 = \begin{bmatrix} \eta_1^0 \sinh(\Omega_1 x) / \sinh(\Omega_1 L) \\ -1 \\ -\epsilon g_V^e / (i\omega_1 - \epsilon g_W^e) \\ 1 \\ \epsilon g_V^e / (i\omega_1 - \epsilon g_W^e) \end{bmatrix}, \quad q_2 = \begin{bmatrix} \eta_2^0 \cosh(\Omega_2 x) / \cosh(\Omega_2 L) \\ 1 \\ \epsilon g_V^e / (i\omega_2 - \epsilon g_W^e) \\ 1 \\ \epsilon g_V^e / (i\omega_2 - \epsilon g_W^e) \end{bmatrix}, \quad (3.2.17)$$

where

$$\Omega_1 = \sqrt{\frac{k+i\omega_1}{D}}, \quad \Omega_2 = \sqrt{\frac{k+i\omega_2}{D}}, \quad \eta_1^0 = \frac{\kappa}{\kappa + D\Omega_1 \coth(\Omega_1 L)}, \quad \eta_2^0 = \frac{\kappa}{\kappa + D\Omega_2 \coth(\Omega_2 L)}.$$

Generally, the critical eigenspace (or center subspace)  $T^c$  is the real subspace consisting of the span of the real and imaginary parts of the (generalized) eigenvectors corresponding to all eigenvalues  $\lambda$  with  $\text{Re } \lambda = 0$ . In our case it is the four-dimensional subspace

$$T^c = \text{span} \{ \text{Re } q_1, \text{Im } q_1, \text{Re } q_2, \text{Im } q_2 \}.$$

### 3.3. Double Hopf Bifurcation

---

For later computational convenience we express the critical eigenspace in complex notation as

$$T^c = \{z_1 q_1 + \bar{z}_1 \bar{q}_1 + z_2 q_2 + \bar{z}_2 \bar{q}_2 : z_1, z_2 \in \mathbb{C}\}.$$

Since all eigenvalues other than the four critical ones  $\pm i\omega_{1,2}$  have negative real parts, the complementary subspace to  $T^c$  in  $H$  is  $T^s$ , the infinite-dimensional stable subspace. If parameters changes smoothly, then all the eigenvalues change continuously, and simple eigenvalues change smoothly. Therefore, if parameters are near a double Hopf point, there are four simple eigenvalues near  $\pm i\omega_{1,2}$ , near the imaginary axis, which we still call critical eigenvalues, and the remaining eigenvalues still have negative real parts bounded away from 0.

### 3.3 Double Hopf Bifurcation

In the previous section, we found a double Hopf point, i.e. parameter values where the critical eigenvalues for the linearization of the model system are two pairs of purely imaginary eigenvalues  $\pm i\omega_1, \pm i\omega_2$ . In the nonlinear model system itself, for parameter values near the double Hopf point, we expect bifurcations of nonlinear modes of oscillations that resemble the linear anti-phase and in-phase eigenvectors. This is confirmed by a bifurcation analysis, which also tells us the stabilities of the nonlinear anti-phase and in-phase modes, and how the modes interact near the double Hopf point. Key to this analysis is the reduction of the infinite-dimensional model system near the steady state to a four-dimensional normal form whose dynamics can be more easily determined.

We extend the vector notation introduced in the previous section to the nonlinear problem, and write the model system (3.1.1)–(3.1.5) as

$$\dot{X} = MX + \frac{1}{2!}B(X, X) + \frac{1}{3!}C(X, X, X), \quad (3.3.1)$$

for  $X(t)$  belonging to  $H$ , where  $X(t)$  is given by (3.2.13) and the linear differential operator  $M$  is given by (3.2.14). The operators  $B$  and  $C$  are

### 3.3. Double Hopf Bifurcation

---

symmetric bilinear and trilinear forms, respectively, given by

$$B(X^a, X^b) = \begin{bmatrix} 0 \\ b_1 \\ -\epsilon b_1 \\ b_2 \\ -\epsilon b_2 \end{bmatrix}, \quad C(X^a, X^b, X^c) = \begin{bmatrix} 0 \\ c_1 \\ -\epsilon c_1 \\ c_2 \\ -\epsilon c_2 \end{bmatrix}.$$

where

$$\begin{aligned} b_1 &= 2W^e v_-^a v_-^b + 2V^e (v_-^a w_-^b + v_-^b w_-^a), & b_2 &= 2W^e v_+^a v_+^b + 2V^e (v_+^a w_+^b + v_+^b w_+^a), \\ c_1 &= 2v_-^a v_-^b w_-^c + 2v_-^b v_-^c w_-^a + 2v_-^c v_-^a w_-^b, & c_2 &= 2v_+^a v_+^b w_+^c + 2v_+^b v_+^c w_+^a + 2v_+^c v_+^a w_+^b, \end{aligned}$$

Then

$$\frac{1}{2!}B(X, X) = \begin{bmatrix} 0 \\ W^e v_-^2 + V^e v_- w_- \\ -\epsilon(W^e v_-^2 + V^e v_- w_-) \\ W^e v_+^2 + V^e v_+ w_+ \\ -\epsilon(W^e v_+^2 + V^e v_+ w_+) \end{bmatrix}, \quad \frac{1}{3!}C(X, X, X) = \begin{bmatrix} 0 \\ v_-^2 w_- \\ -\epsilon v_-^2 w_- \\ v_+^2 w_+ \\ -\epsilon v_+^2 w_+ \end{bmatrix}.$$

are the quadratic and cubic terms, respectively, of the model system.

At the double Hopf point (3.2.11)–(3.2.12), we recall that the linear operator  $M$  has the four critical eigenvalues  $\pm i\omega_{1,2}$  on the imaginary axis in the complex plane, and the remaining eigenvalues of  $M$  are in the left complex half-plane, bounded away from the imaginary axis. In this situation, for parameter values near the double Hopf point, the nonlinear evolution equation (3.3.1) possesses a four-dimensional invariant local center manifold  $W_{loc}^c$  in the function space  $H$ , that is tangent to the critical eigenspace  $T^c$  at the double Hopf point. Furthermore, all solutions of (3.3.1) near the steady state decay exponentially rapidly, as  $t$  increases, to the local center manifold  $W_{loc}^c$ . Therefore, the local long-term dynamics of the entire system (3.3.1) is governed by a four-dimensional system of ordinary differential equations that describes the dynamics restricted to  $W_{loc}^c$ . In fact, only low-order terms in the Taylor series expansion of this system are required. Finally, a standard procedure of introducing coordinate changes reduces the system of

### 3.3. Double Hopf Bifurcation

---

differential equations to a simpler but equivalent one, called a normal form. This normal form is easier to analyze, and predicts the local dynamics of the entire infinite-dimensional system (3.3.1).

In the Appendix, we give some details of the reduction of the evolution equation (3.3.1) to the normal form. The computations are analytical, assisted by the mathematical software package Maple. Near the double Hopf point, the normal form is a four-dimensional system of ordinary differential equations, written in complex notation as

$$\begin{aligned}\dot{\zeta}_1 &= \lambda_1 \zeta_1 + G_{2100} \zeta_1^2 \bar{\zeta}_1 + G_{1011} \zeta_1 \zeta_2 \bar{\zeta}_2 + O(\|\mu\| \|\zeta\|^3 + \|\zeta\|^5), \\ \dot{\zeta}_2 &= \lambda_2 \zeta_2 + H_{1110} \zeta_1 \bar{\zeta}_1 \zeta_2 + H_{0021} \zeta_2^2 \bar{\zeta}_2 + O(\|\mu\| \|\zeta\|^3 + \|\zeta\|^5),\end{aligned}\tag{3.3.2}$$

whose solutions  $\zeta_1(t)$ ,  $\zeta_2(t)$  are complex numbers that, to leading order, represent the evolving amplitudes and phases of the anti-phase and in-phase oscillatory modes in the nonlinear system (3.3.1). The critical eigenvalues of the linearization  $M$  near the double Hopf point are  $\lambda_1$  and  $\lambda_2$ , so at the double Hopf point itself we have  $\lambda_1 = i\omega_1$ ,  $\lambda_2 = i\omega_2$ . Near the double Hopf point, the real parts of the critical eigenvalues  $\mu_j = \text{Re } \lambda_j$  serve as “unfolding” parameters that usefully quantify small deviations from the double Hopf point. The higher-order Taylor series terms in the expansions  $O(\|\mu\| \|\zeta\|^3 + \|\zeta\|^5)$ , where  $\mu = (\mu_1, \mu_2)$  and  $\zeta = (\zeta_1, \bar{\zeta}_1, \zeta_2, \bar{\zeta}_2)$ , are not explicitly needed for our work. The four coefficients  $G_{jklm}$  and  $H_{jklm}$  of the cubic terms in the normal form are calculated with the help of Maple, and we evaluate them at the double Hopf point,

$$\begin{aligned}G_{2100} &= -3.07849 + i0.00166, & G_{1011} &= -5.89627 + i2.80222, \\ H_{1110} &= -6.00121 - i0.14896, & H_{0021} &= -2.90063 + i1.38790.\end{aligned}\tag{3.3.3}$$

The analysis of the normal form (3.3.2) is described in several textbooks on bifurcation theory. Here we briefly summarize the relevant parts of the treatment in [39]. If we take polar representations  $\zeta_1 = r_1 e^{i\phi_1}$ ,  $\zeta_2 = r_2 e^{i\phi_2}$ , and truncate higher-order terms, then in polar coordinates  $(r_1, r_2, \phi_1, \phi_2)$  the normal form (3.3.2) can be written as

$$\begin{aligned}\dot{r}_1 &= r_1(\mu_1 + p_{11}r_1^2 + p_{12}r_2^2), \\ \dot{r}_2 &= r_2(\mu_2 + p_{21}r_1^2 + p_{22}r_2^2), \\ \dot{\phi}_1 &= \omega_1, \\ \dot{\phi}_2 &= \omega_2,\end{aligned}\tag{3.3.4}$$

where

$$p_{11} = \text{Re } G_{2100}, \quad p_{12} = \text{Re } G_{1011}, \quad p_{21} = \text{Re } H_{1110}, \quad p_{22} = \text{Re } H_{0021}.$$

### 3.3. Double Hopf Bifurcation

---

We point out that the truncated normal form (3.3.4) is an approximation of the normal form (3.3.2) due to missing higher-order terms in the Taylor series expansions, but the approximation turns out to be sufficiently accurate to predict the existence and stability of bifurcating solutions.

We see in the truncated normal form (3.3.4) that the first pair of equations is independent of the second pair and thus the bifurcations of (3.3.4) are completely determined by the two equations in  $r_j$ , where  $r_j$  represent the amplitudes of the anti-phase and in-phase modes:

$$\begin{aligned} \dot{r}_1 &= r_1(\mu_1 + p_{11}r_1^2 + p_{12}r_2^2), \\ \dot{r}_2 &= r_2(\mu_2 + p_{21}r_1^2 + p_{22}r_2^2). \end{aligned} \quad (3.3.5)$$

Since we have  $p_{11} = -3.07849$  and  $p_{22} = -2.90063$ , the normal form falls into the “simple” case of [39] (p. 359), where  $p_{11}p_{22} > 0$  and no fifth-order terms are needed in the amplitude equations (3.3.5). We observe that the system (3.3.5) has a trivial equilibrium  $E_0 = (0, 0)$  for all  $\mu_{1,2}$ . Moreover, there can be as many as three nontrivial equilibria. Equilibria on the coordinate axes

$$E_1 = (r_1, 0), \quad r_1 > 0; \quad E_2 = (0, r_2), \quad r_2 > 0,$$

where

$$r_1 = \sqrt{\frac{\mu_1}{-p_{11}}}; \quad r_2 = \sqrt{\frac{\mu_2}{-p_{22}}}$$

exist if  $\mu_1 > 0$ ,  $\mu_2 > 0$ , respectively. Another equilibrium

$$E_3 = (r_1, r_2), \quad r_1 > 0, \quad r_2 > 0,$$

where

$$r_1 = \sqrt{\frac{-\mu_1 + \theta\mu_2}{-p_{11}(\theta\delta - 1)}}, \quad r_2 = \sqrt{\frac{\delta\mu_1 - \mu_2}{-p_{22}(\theta\delta - 1)}}, \quad (3.3.6)$$

and

$$\theta = \frac{p_{12}}{p_{22}} = 2.03276, \quad \delta = \frac{p_{21}}{p_{11}} = 1.94940, \quad (3.3.7)$$

exists if both  $-\mu_1 + \theta\mu_2 > 0$  and  $\delta\mu_1 - \mu_2 > 0$ . The equilibria  $E_{1,2}$  bifurcate from the origin  $E_0$  at the bifurcation lines

$$H_1 = \{(\mu_1, \mu_2) \mid \mu_1 = 0\}, \quad H_2 = \{(\mu_1, \mu_2) \mid \mu_2 = 0\}, \quad (3.3.8)$$

and  $E_3$  bifurcates from  $E_2$  or  $E_1$  on the bifurcation lines

$$\begin{aligned} T_1 &= \{(\mu_1, \mu_2) \mid \mu_1 = \theta\mu_2, \mu_2 > 0\}, \\ T_2 &= \{(\mu_1, \mu_2) \mid \mu_2 = \delta\mu_1, \mu_1 > 0\}, \end{aligned} \quad (3.3.9)$$

### 3.3. Double Hopf Bifurcation

---

respectively. We plot the parametric portraits of (3.3.5) in Figure 3.1. In the left panel, the four lines  $H_1$ ,  $H_2$ ,  $T_1$  and  $T_2$  divide the  $(\mu_1, \mu_2)$  parameter plane into six open regions indicated by roman numerals. The corresponding phase portraits of the amplitude system (3.3.5) are also shown within each open region. The  $H_1$  (red dash-dot) line is the vertical  $\mu_2$ -axis, while  $H_2$  (black solid) is the horizontal  $\mu_1$ -axis. The  $T_1$  (magenta dashed) and  $T_2$  (blue dotted) lines separate regions III, IV and V. In region I, the amplitude system (3.3.5) has the unique equilibrium  $E_0$  and it is asymptotically stable. When entering region II (VI) from region I, crossing  $H_1$  ( $H_2$ ), the equilibrium  $E_1$  ( $E_2$ ) bifurcates from  $E_0$  and is asymptotically stable, while  $E_0$  is unstable. When entering region III (V) from region II (VI), crossing  $H_2$  ( $H_1$ ), another, unstable, equilibrium  $E_2$  ( $E_1$ ) bifurcates from  $E_0$  while  $E_1$  ( $E_2$ ) remains at large amplitude and asymptotically stable, and  $E_0$  is unstable. Finally, in region IV, there is bistability as the two equilibria  $E_1$  and  $E_2$  are both asymptotically stable. A fourth equilibrium  $E_3$  exists and is unstable, while  $E_0$  is unstable. Although  $E_3$  is unstable, it has an important effect on the overall dynamics. The unstable manifold of  $E_3$  forms the boundary between the basins of attraction of the two stable equilibria  $E_1$  and  $E_2$ . Thus the eventual limiting state of a generic trajectory depends on the location of its initial value relative to the unstable manifold of  $E_3$ . For more details, see [39]. If we fix other parameters at value (3.2.11) and only change  $\beta$  or  $D$  near the double Hopf point, the curves corresponding to  $H_j, T_j$  in the  $(\beta, D)$  plane are shown in the right panel of Figure 3.1. The red dash-dot curve corresponds to  $H_1$ , and the black solid red curve corresponds to  $H_2$ . The dashed magenta and dotted blue lines are tangent lines at the double Hopf point to the curves corresponding to  $T_1$  and  $T_2$ , respectively.

Restoring the angular variables to (3.3.5) to recover the truncated normal form (3.3.4), the equilibria of (3.3.5) get different interpretations. The origin  $E_0$  is still an equilibrium at the origin, but  $E_1$  and  $E_2$  are cycles, or periodic solutions of (3.3.4), while  $E_3$  for (3.3.4) is a two-dimensional invariant torus. Their stability properties remain the same. Thus the lines  $H_j$  correspond to Hopf bifurcations, and the lines  $T_j$  to torus (or Neimark-Sacker) bifurcations.

Because nondegeneracy conditions are satisfied in our case, restoring the higher-order terms to the truncated normal form (3.3.4) to return to (3.3.2) changes the bifurcation results only subtly. The torus bifurcation lines  $T_j$  become torus bifurcation curves  $T_1 : \mu_1 = \theta\mu_2 + O(\mu_2^2)$  and  $T_2 : \mu_2 = \delta\mu_1 + O(\mu_1^2)$  tangent at the origin to the lines (3.3.9), while solutions on the invariant two-torus are slightly changed, but the two-torus persists as an invariant manifold with the same stability type.

Finally, transferring the bifurcation and stability results to the original

### 3.3. Double Hopf Bifurcation

---

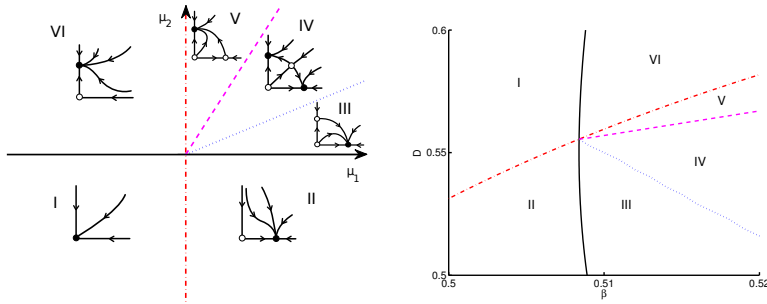


Figure 3.1: Parametric portrait of the amplitude equations (3.3.5) in the  $(\mu_1, \mu_2)$  plane near the origin with phase portraits of the amplitude equations (left panel), and the corresponding parametric portrait in the  $(\beta, D)$  plane near the double Hopf point (right panel). In the left panel, the red dash-dot vertical  $\mu_2$ -axis is  $H_1: \mu_1 = 0$ , the black solid horizontal  $\mu_1$ -axis is  $H_2: \mu_2 = 0$ , the magenta dashed line is  $T_1: \mu_2 = \delta\mu_1$  and the blue dotted line is  $T_2: \mu_1 = \theta\mu_2$ . In the right panel, the red dash-dot curve (Hopf bifurcation of anti-phase modes) corresponds to  $H_1$ , the black solid curve (Hopf bifurcation of in-phase modes) corresponds to  $H_2$ , the magenta dashed line (tangent at the double Hopf point to a curve of torus bifurcations from anti-phase modes) corresponds to  $T_1$  and the blue dotted line (tangent at the double Hopf point to a curve of torus bifurcations from in-phase modes) corresponds to  $T_2$ . Other parameter values are fixed at values (3.2.11). Note the right panel corresponds to the enlarged version of Fig. 2.2 in chapter §2 near the intersection of the blue solid curve and the red dashed curve.

### 3.3. Double Hopf Bifurcation

---

model system (3.3.1), or equivalently (3.1.1)–(3.1.5), is straightforward. The origin  $E_0$  corresponds to the steady state (3.2.1),  $E_1$  and  $E_2$  correspond to nonlinear oscillating anti-phase and in-phase modes, and  $E_3$  corresponds to an invariant two-torus or modulated oscillations, while the stability types remain the same. The lines  $H_1$  and  $H_2$  correspond to curves of Hopf bifurcations from the steady state, of anti-phase and in-phase modes, respectively. The line  $T_1$  corresponds to a curve of torus bifurcations from the anti-phase mode and  $T_2$  corresponds to torus bifurcations from the in-phase mode. Solutions on the invariant two-torus are characterized by two frequencies, one near  $\omega_1$  and the other near  $\omega_2$ .

To check our results we consider parameter paths near the double Hopf point in the  $(\beta, D)$  plane and plot corresponding bifurcation diagrams obtained by using AUTO on a spatially discretized finite-difference approximation of the model system (3.1.1)–(3.1.5). In Figure 3.2, we consider an elliptical parameter path around the double Hopf point, setting  $\beta = \beta_c + 0.005 \cos(\theta)$  and  $D = D_c + 0.025 \sin(\theta)$ , and increasing the path parameter  $\theta$  from  $-\pi$  to  $\pi$ . This parameter path, shown as a green curve in the inset panel, starts directly to the left of the double Hopf point, traces the ellipse in a counterclockwise direction as  $\theta$  increases, starting in region I and visiting the regions II, III, IV, etc. in sequence before returning to region I. The main panel of Figure 3.2 shows the bifurcation diagram obtained by AUTO for the finite-difference approximation of the model system, with the path parameter  $\theta$  plotted on the horizontal axis, and the  $V_-$  component of the vector solutions on the vertical axis. As the path parameter  $\theta$  increases from  $-\pi$ , the steady state is stable (solid curve), then first loses stability (beginning of dashed curve) as the stable anti-phase mode bifurcates (solid circles indicating maximum and minimum values of  $V_-(t)$  on the periodic solution) from the steady state. The anti-phase mode remains stable and with a large amplitude as the unstable (open circles) in-phase mode bifurcates from the unstable (dashed curve) steady state. As  $\theta$  increases further, the in-phase mode gains stability (transition from open circles to closed circles), and then there is an interval where both anti-phase and in-phase modes are stable (the solution branches appear to cross but this is only because only one component of each vector solution is plotted). Then the anti-phase mode loses stability (transition from closed circles to open circles), then as  $\theta$  increases there is a Hopf bifurcation back to the unstable (dashed curve) steady state. Finally there is a Hopf bifurcation of the stable in-phase mode (solid circles) back to the steady state as the steady state goes from unstable (dashed curve) to stable (solid curve). AUTO detects stability changes of the anti-phase and in-phase modes when a pair of com-

### 3.3. Double Hopf Bifurcation

plex conjugate Floquet multipliers for the oscillating modes crosses the unit circle in the complex plane, which is characteristic of a torus bifurcation. The sequence of stability changes and bifurcations found by AUTO is as predicted by the normal form analysis. Although the amplitude equations (due to truncation of higher-order terms) and the AUTO bifurcation computations (due to finite differences) are both approximations of the model system, the numerical values of the bifurcation points agree well, close to the double Hopf point.

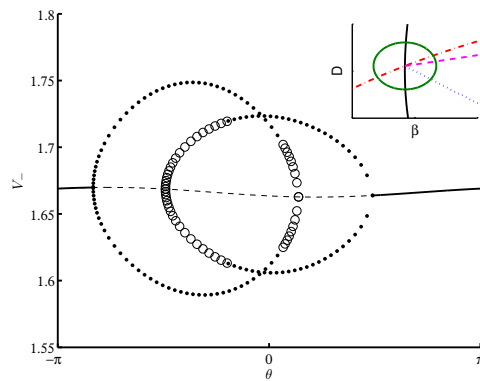


Figure 3.2: Bifurcation diagram for the model system, for a parameter path around the double Hopf point,  $\beta = \beta_c + 0.005 \cos(\theta)$ ,  $D = D_c + 0.025 \sin(\theta)$ , increasing  $\theta$  from  $-\pi$  to  $\pi$ , with other parameters fixed at the values (3.2.11). The inset panel shows the elliptical parameter path plotted in green in the  $(\beta, D)$  plane, together with the bifurcation curves obtained from the normal form. The parameter path starts directly to the left of the double Hopf point, in the region I where the steady state is stable. As  $\theta$  increases (moving counterclockwise from the leftmost point on the green ellipse), the parameter path crosses the red dash-dot Hopf bifurcation curve, the black solid Hopf bifurcation curve, the blue dotted torus bifurcation curve, the magenta dashed torus bifurcation curve, the red Hopf bifurcation curve, and finally the black Hopf bifurcation curve before returning to the starting point. The main panel shows the bifurcation diagram for the parameter path obtained using AUTO on the spatially discretized finite-difference approximation of the model system, with the path parameter  $\theta$  plotted on the horizontal axis, the  $V_-$  component of the vector solution on the vertical axis. See the main text for the coding of solution type and stability by line style.

AUTO is able to detect stability changes of periodic solutions that cor-

### 3.3. Double Hopf Bifurcation

---

respond to torus bifurcations, but is unable to continue along branches of invariant tori. To look for invariant tori where their existence is predicted by the normal form analysis, we simulated directly the model system (3.1.1)–(3.1.5) with finite differences in both space and time. Although the tori are unstable, if initial conditions are chosen close enough to an invariant torus, the solution will stay close to a solution on the unstable torus for some time before the exponentially growing drift apart becomes noticeable. We take  $\beta = 0.509$  and  $D = 0.55486$ , which, according to the normal form, is in the parameter region IV between the two torus bifurcation curves, where there is bistability due to both the anti-phase and in-phase modes being asymptotically stable, and an unstable invariant torus. We choose the initial condition corresponding to

$$X(0) = 2\text{Re}(r_1q_1 + r_2q_2), \quad (3.3.10)$$

recalling that the vector  $X(t)$  represents the deviation of variables from the steady state (3.2.1), and  $r_1, r_2$  are the amplitudes (3.3.6)–(3.3.7) given by the equilibrium  $E_3$  of the amplitude equations that corresponds to the invariant torus. Since the parameters are close to the double Hopf point, we reason that neglecting higher-order terms in the amplitude equations and in the local center manifold should not give seriously large errors, and therefore (3.3.10) represents an initial condition close to the unstable invariant torus. The simulated results appear to validate this choice of initial condition. A plot of the time evolution of  $V_-$  component of the solution is shown in the left panel of Figure 3.3. For a reasonably long time the numerical solution exhibits oscillations characterized by two periods which correspond to the two oscillating frequencies  $\omega_1$  and  $\omega_2$  at the double Hopf point. The signal displays a phenomenon similar to that of beats or amplitude modulation that occurs when two linear oscillations with nearly the same frequencies are added, with a fast “carrier” frequency  $|\omega_1 + \omega_2|/2$  and a slow modulated “envelope” frequency  $|\omega_1 - \omega_2|$ . The power spectrum from an FFT analysis of the time series of the numerical solution is shown in the right panel of Figure 3.3. The two peaks on the FFT plot indicate the two main frequency components from the time series in the left panel, and the peak locations on the horizontal axis agree with the values of  $\omega_1, \omega_2$ . This is consistent with the predictions of the normal form analysis.

### 3.3. Double Hopf Bifurcation

---

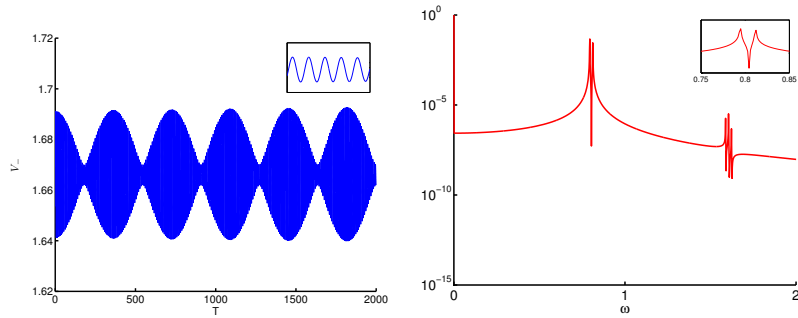


Figure 3.3: The time evolution of the  $V_-$  component of a simulated solution of the model system with initial condition (3.3.10) (left) and its corresponding power spectrum obtained from FFT analysis (right). In the left panel, we can observe two periods from the series. The shorter period corresponds to angular frequency  $|\omega_1 + \omega_2|/2$  and the longer period corresponds to angular frequency  $|\omega_1 - \omega_2|$ . The left inset panel shows the simulation results on a short time scale that more clearly resolves the rapid oscillations corresponding to the shorter period. In the right panel, the power spectrum of the solution is plotted, where the horizontal axis is angular frequency  $\omega$ . Two peaks in the power spectrum at  $\omega = 0.79$  and  $\omega = 0.81$  are clearly visible (other peaks correspond to integer linear combinations of  $\omega_1$  and  $\omega_2$ ). The right inset panel shows a more detailed graph near  $\omega = 0.8$ .

## Chapter 4

# Generalized Model in One Dimensional Space

The goal of this chapter is to formulate and analyze a general class of coupled membrane-bulk dynamics in a simplified 1-D spatial domain.

We first construct a general model system that describes the coupling of two dynamically active membranes, on which  $n$  species undergo chemical reactions, through the bulk diffusion in a one dimensional finite domain of length  $2L$  in §4.1.

In §4.2 we construct a steady-state solution for the general model system that is symmetric about the midline  $x = L$ . The analytical construction of this symmetric steady-state solution is reduced to the problem of determining roots to a nonlinear algebraic system involving both the local membrane kinetics and the nonlinear feedback and flux functions. We then formulate the linear stability problem associated with this steady-state solution. In our stability theory, we must allow for perturbations that are either symmetric or anti-symmetric about the midline, which leads to the possibility of either synchronous (in-phase) or asynchronous (out-of-phase) instabilities in the two membranes. By using a matrix determinant lemma for rank-one perturbations of a matrix, we show that the eigenvalue parameter associated with the linearization around the steady-state satisfies a rather simple transcendental equation for either the synchronous or asynchronous mode.

In §4.3 we analyze in detail the spectrum of the linearized problem associated with a one-component membrane dynamics. For the infinite-line problem, corresponding to the limit  $L \rightarrow +\infty$ , in §4.3.1 we use complex analysis together with a rigorous winding number criterion to derive sufficient conditions, in terms of properties of the reaction-kinetics and nonlinear feedback and flux, that delineate parameter ranges where Hopf bifurcations due to coupled membrane-bulk dynamics will occur. Explicit formulae for the Hopf bifurcation values, in terms of critical values of  $\tau$ , which characterize the time scale of bulk decay in the general model system, are also obtained. In §4.3.1 further rigorous results are derived that establish parameter ranges where no membrane oscillations are possible. For the finite-domain prob-

lem, and assuming a one-component membrane dynamics, we show in §4.3.2 that some of the rigorous results for the infinite-line problem, as derived in §4.3.1, are still valid. However, in general, for the finite-domain problem numerical computations of the winding number are needed to predict Hopf bifurcation points and to establish parameter ranges where the steady-state solution is linearly stable.

We remark that for the case of a one-component membrane dynamics, the eigenvalue problem derived in §4.3.1, characterizing the linear stability of the coupled membrane-bulk dynamics, is remarkably similar in form to the spectral problem that arises in the stability of localized spike solutions to reaction-diffusion (RD) systems of activator-inhibitor type (cf. [57] and [79] and the references therein). More specifically, on the infinite-line, the spectral problem for our coupled membrane-bulk dynamics is similar to that studied in §3.1 of [57] for a class of activator-inhibitor RD systems.

For a one-component membrane dynamics, in §4.4 we illustrate the theory of §4.3 for determining Hopf bifurcation points corresponding to the onset of either synchronous or asynchronous oscillatory instabilities. For the infinite-line problem, where these two instability thresholds have coalesced to a common value, we illustrate the theoretical results of §4.3.1 for the existence of a Hopf bifurcation point. For the finite-domain problem, where the two active membranes are separated by a finite distance  $2L$ , numerical computations of the winding-number are used to characterize the onset of either mode of instability. The theory is illustrated for a class of feedback models in §4.4.1, for an exactly solvable model problem in §4.4.2, for a kinase activity regulation model in §4.4.3, and for two specific biological systems in §4.4.4. The biological systems in §4.4.4 consist of a model of hormonal activity due to GnRH neurons in the hypothalamus (cf. [32], [47], and [17]), and a model of quorum sensing behavior of *Dictyostelium* (cf. [19]). For the problems in §4.4.1, 4.4.2, 4.4.4, we supplement our analytical theory with numerical bifurcation results, computed from the coupled membrane-bulk PDE-ODE system using the bifurcation software XPPAUT [16]. For the *Dictyostelium* model and the model in §4.4.2, our results shows that there is a rather large parameter range where stable synchronous membrane oscillations occur. Full numerical computations of the PDE-ODE system of coupled membrane-bulk dynamics, undertaken using a method-of-lines approach, are used to validate the theoretical predictions of stable synchronous oscillations.

In §4.5 we consider a specific coupled membrane-bulk model, having two active components on each membrane. For the case where the two membranes are identical, and have a common value of the coupling strength to

the bulk medium, we use a numerical winding number argument to predict the onset of either a synchronous or an asynchronous oscillatory solution branch that bifurcates from the steady-state solution. The numerical bifurcation package XPPAUT [16] shows that there is a parameter range where the synchronous solution branch exhibits bistable behavior. In contrast, when the coupling strengths to the two membranes are different, we show that the amplitude ratio of the oscillations in the two membranes can be rather large, with one membrane remaining, essentially, in a quiescent state.

For the case of a one-component membrane dynamics on a finite domain, in §4.6 we formulate and then implement a weakly nonlinear multiple time-scale theory to derive an amplitude equation that characterizes whether a synchronous oscillatory instability is subcritical or supercritical near the Hopf bifurcation point. For a specific choice of the nonlinearities, corresponding to the model considered in §4.4.2, theoretical predictions based on the amplitude equation are then confirmed with full bifurcation results computed using XPPAUT (cf. [16]). Similar analysis is applied to the *Dic-tyostelium* model. Moreover, for the model system considered in §4.4.2, time-dependent full numerical computations of the coupled membrane-bulk PDE-ODE system are performed to show a delayed triggered synchronous oscillation arising from the slow passage of a parameter through a Hopf bifurcation point. Similar delayed bifurcation problems in a purely ODE context have been studied in [1], [2], [36], and [49] (see the references therein).

We emphasize that the theoretical challenge and novelty of our weakly nonlinear analysis in §4.6 is that both the differential operator and the boundary condition on the membrane for the linearized problem involves the eigenvalue parameter. This underlying spectral problem, with an eigenvalue-dependent boundary condition, is not self-adjoint and is rather non-standard. Motivated by the theoretical approach developed in [18] to account for eigenvalue-dependent boundary conditions, we introduce an extended operator  $L$ , and an associated inner product, from which we determine the corresponding adjoint problem. In this way, we formulate an appropriate solvability condition in Lemma 4.6.1 that is one of the key ingredients, in our multiple time-scale analysis, for deriving the amplitude equation characterizing the branching behavior of synchronous oscillations near onset. We remark that a similar methodology of introducing an extended operator to treat a transcritical bifurcation problem involving an eigenvalue-dependent boundary condition, which arises in a mathematical model of thermoelastic contact of disc brakes, was undertaken in [60] and [61]. However, to our knowledge, there has been no previous work for the corresponding Hopf bifurcation problem of the type considered herein.

## 4.1 Model Formulation

In our simplified 1-D setting, we assume that there are two dynamically active membranes, located at  $x = 0$  and  $x = 2L$ , that can release a specific signaling molecule into the bulk region  $0 < x < 2L$ , and that this secretion is regulated by both the bulk concentration of that molecule together with its concentration on the membrane. In the bulk region, we assume that the signaling molecule undergoes passive diffusion with a specified bulk decay rate. If  $C(x, t)$  represents the concentration of the signaling molecule in the bulk, then its spatial-temporal evolution in this region is governed by the dimensionless model

$$\begin{aligned} \tau C_t &= DC_{xx} - C, & t > 0, & \quad 0 < x < 2L, \\ DC_x(0, t) &= G(C(0, t), u_1(t)), & -DC_x(2L, t) &= G(C(2L, t), v_1(t)), \end{aligned} \tag{4.1.1a}$$

where  $\tau > 0$  is a time-scale for the bulk decay and  $D/\tau > 0$  is the constant diffusivity. On the membranes  $x = 0$  and  $x = 2L$ , the fluxes  $G(C(0, t), u_1)$  and  $G(C(2L, t), v_1)$  model the influx of signaling molecule into the bulk, which depends on the bulk concentrations  $C(0, t)$  and  $C(2L, t)$  at the two membranes together with the local concentrations  $u_1(t)$  and  $v_1(t)$  of the signaling molecule on the membranes. We assume that on each membrane, there are  $n$  species that can interact, and that their dynamics are described by  $n$ -ODE's of the form

$$\frac{d\mathbf{u}}{dt} = \mathcal{F}(\mathbf{u}) + \beta\mathcal{P}(C(0, t), u_1)\mathbf{e}_1, \quad \frac{d\mathbf{v}}{dt} = \mathcal{F}(\mathbf{v}) + \beta\mathcal{P}(C(2L, t), v_1)\mathbf{e}_1, \tag{4.1.1b}$$

where  $\mathbf{e}_1 \equiv (1, 0, \dots, 0)^T$ . Here,  $\mathbf{u}(t) \equiv (u_1(t), \dots, u_n(t))^T$  and  $\mathbf{v}(t) \equiv (v_1(t), \dots, v_n(t))^T$  represents the concentration of the  $n$  species on the two membranes and  $\mathcal{F}(\mathbf{u})$  is the vector nonlinearity modeling the chemical kinetics for these membrane-bound species. In our formulation (4.1.1b), only one of these internal species, labeled by  $u_1$  and  $v_1$  at the two membranes, is capable of diffusing into the bulk. The coupling to the bulk is modeled by the two feedback terms  $\beta\mathcal{P}(C(0, t), u_1)$  and  $\beta\mathcal{P}(C(2L, t), v_1)$ , where the coupling parameter  $\beta$  models the strength of the membrane-bulk exchange.

## 4.2 The Steady-State Solution and the Formulation of the Linear Stability Problem

In this section we construct a steady-state solution for (4.1.1), and then formulate the associated linear stability problem. In (4.1.1), we have as-

## 4.2. The Steady-State Solution and the Formulation of the Linear Stability Problem

sumed for simplicity that the two membranes have the same kinetics and membrane-bulk coupling mechanisms. As such, this motivates the construction of a steady-state solution for (4.1.1) that is symmetric with respect to the midline  $x = L$  of the bulk region. The corresponding symmetric steady-state bulk solution  $C_e(x)$  and the membrane-bound steady-state concentration field  $\mathbf{u}_e$  satisfy

$$\begin{aligned} DC_{exx} - C_e &= 0, & 0 < x < L; \\ C_{ex}(L) &= 0, & DC_{ex}(0) = G(C_e(0), u_{1e}), \\ \mathcal{F}(\mathbf{u}_e) + \beta\mathcal{P}(C_e(0), u_{1e})\mathbf{e}_1 &= 0. \end{aligned} \quad (4.2.1)$$

We readily calculate that

$$C_e(x) = C_e^0 \frac{\cosh[\omega_0(L-x)]}{\cosh(\omega_0 L)}, \quad \omega_0 \equiv 1/\sqrt{D}, \quad (4.2.2a)$$

where  $C_e^0 \equiv C_e(0)$  and  $\mathbf{u}_e$  are the solutions to the  $n+1$  dimensional nonlinear algebraic system

$$-C_e^0 \tanh(\omega_0 L) = \omega_0 G(C_e^0, u_{1e}), \quad \mathcal{F}(\mathbf{u}_e) + \beta\mathcal{P}(C_e^0, u_{1e})\mathbf{e}_1 = 0. \quad (4.2.2b)$$

In general it is cumbersome to impose sufficient conditions on  $\mathcal{F}$ ,  $\mathcal{P}$ , and  $G$ , guaranteeing a solution to (4.2.2b). Instead, we will analyze (4.2.2b) for some specific models below in §4.4 and in §4.5.

To formulate the linear stability problem, we introduce the perturbation

$$C(x, t) = C_e(x) + e^{\lambda t} \eta(x), \quad \mathbf{u}(t) = \mathbf{u}_e + e^{\lambda t} \phi,$$

into (4.1.1) and linearize. In this way, we obtain the eigenvalue problem

$$\begin{aligned} \tau\lambda\eta &= D\eta_{xx} - \eta, & 0 < x < L; & \quad D\eta_x(0) = G_c^e \eta_0 + G_{u_1}^e \phi_1, \\ J_e \phi + \beta(\mathcal{P}_c^e \eta_0 + \mathcal{P}_{u_1}^e \phi_1)\mathbf{e}_1 &= \lambda\phi. \end{aligned} \quad (4.2.3)$$

Here we have defined  $\eta_0 \equiv \eta(0)$ ,  $G_c^e \equiv G_c(C_e^0, u_{1e})$ ,  $G_{u_1}^e \equiv G_{u_1}(C_e^0, u_{1e})$ ,  $\mathcal{P}_c^e \equiv \mathcal{P}_c(C_e^0, u_{1e})$ , and  $\mathcal{P}_{u_1}^e \equiv \mathcal{P}_{u_1}(C_e^0, u_{1e})$ . In addition,  $J_e$  is the Jacobian matrix of the nonlinear membrane kinetics  $\mathcal{F}$  evaluated at  $\mathbf{u}_e$ .

The formulation of the linear stability problem is complete once we impose a boundary condition for  $\eta$  at the midline  $x = L$ . There are two choices for this boundary condition. The choice  $\eta(L) = 0$  corresponds to an anti-phase asynchronization of the two membranes (asymmetric case), while the choice  $\eta_x(L) = 0$  corresponds to an in-phase synchronization of the two

## 4.2. The Steady-State Solution and the Formulation of the Linear Stability Problem

---

membranes. We will consider both anti-phase and in-phase instabilities in our analysis.

For the synchronous mode we solve (4.2.3) with  $\eta_x(L) = 0$  to obtain that

$$\eta(x) = \eta_0 \frac{\cosh[\Omega_\lambda(L-x)]}{\cosh(\Omega_\lambda L)}, \quad \Omega_\lambda \equiv \sqrt{\frac{1+\tau\lambda}{D}}, \quad (4.2.4)$$

where we have specified the principal branch of the square root if  $\lambda$  is complex. Upon substituting (4.2.4) into the boundary condition for  $\eta$  on  $x = 0$  in (4.2.3), we readily determine  $\eta_0$  in terms of  $\phi_1$  as

$$\eta_0 = -\frac{G_{u_1}^e \phi_1}{G_c^e + D\Omega_\lambda \tanh(\Omega_\lambda L)}. \quad (4.2.5)$$

We then substitute (4.2.5) into the last equation of (4.2.3), and rewrite the resulting expression in the form

$$(J_e - \lambda I) \phi = p_+(\lambda) \phi_1 e_1, \quad (4.2.6)$$

$$p_+(\lambda) \equiv \beta \left( \frac{G_{u_1}^e \mathcal{P}_c^e - \mathcal{P}_{u_1}^e G_c^e - \mathcal{P}_{u_1}^e D\Omega_\lambda \tanh(\Omega_\lambda L)}{G_c^e + D\Omega_\lambda \tanh(\Omega_\lambda L)} \right).$$

Similarly, for the asynchronous mode we solve (4.2.3) with  $\eta(L) = 0$  to get

$$\eta(x) = \eta_0 \frac{\sinh[\Omega_\lambda(L-x)]}{\sinh(\Omega_\lambda L)}.$$

Upon applying the boundary condition for  $\eta$  at  $x = 0$  from (4.2.3), we can write  $\eta_0$  in terms of  $\phi_1$  as

$$\eta_0 = -\frac{G_{u_1}^e \phi_1}{G_c^e + D\Omega_\lambda \coth(\Omega_\lambda L)}. \quad (4.2.7)$$

Upon substituting this expression into the last equation of (4.2.3), we can eliminate  $\eta_0$  to obtain

$$(J_e - \lambda I) \phi = p_-(\lambda) \phi_1 e_1, \quad (4.2.8)$$

$$p_-(\lambda) \equiv \beta \left( \frac{G_{u_1}^e \mathcal{P}_c^e - \mathcal{P}_{u_1}^e G_c^e - \mathcal{P}_{u_1}^e D\Omega_\lambda \coth(\Omega_\lambda L)}{G_c^e + D\Omega_\lambda \coth(\Omega_\lambda L)} \right).$$

In summary, we conclude that an eigenvalue  $\lambda$  and eigenvector  $\phi$  associated with the linear stability of the symmetric steady-state solution  $(C_e(x), \mathbf{u}_e)$  is determined from the matrix system

$$(J_e - \lambda I - p_\pm(\lambda)E) \phi = \mathbf{0}, \quad E \equiv \mathbf{e}_1 \mathbf{e}_1^T, \quad (4.2.9)$$

## 4.2. The Steady-State Solution and the Formulation of the Linear Stability Problem

where  $\mathbf{e}_1 \equiv (1, 0, \dots, 0)^T$ . Here  $p_+(\lambda)$  and  $p_-(\lambda)$  are defined for the synchronous and asynchronous modes by (4.2.6) and (4.2.8), respectively. We now seek values of  $\lambda$  for which (4.2.9) admits nontrivial solutions  $\phi \neq \mathbf{0}$ . These values of  $\lambda$  satisfy the transcendental equation

$$\det(J_e - \lambda I - p_{\pm}(\lambda)E) = 0. \quad (4.2.10)$$

Since  $E$  is an  $n \times n$  rank-one matrix, the transcendental equation (4.2.10) for the eigenvalue  $\lambda$  can be simplified considerably by using the following well-known Matrix Determinant Lemma:

**Lemma 4.2.1** *Let  $A$  be an invertible  $n \times n$  matrix and let  $\mathbf{a}$  and  $\mathbf{b}$  be two column vectors. Then,*

$$\det(A + \mathbf{a}\mathbf{b}^T) = (1 + \mathbf{b}^T A^{-1} \mathbf{a}) \det(A). \quad (4.2.11)$$

Therefore,  $(A + \mathbf{a}\mathbf{b}^T)\phi = \mathbf{0}$  has a nontrivial solution if and only if  $\mathbf{b}^T A^{-1} \mathbf{a} = -1$ .

**Proof:** We start the proof with a special choice  $A = I$  and consider the following equality

$$\begin{pmatrix} I & 0 \\ \mathbf{b}^T & 1 \end{pmatrix} \begin{pmatrix} I + \mathbf{a}\mathbf{b}^T & \mathbf{a} \\ 0 & 1 \end{pmatrix} \begin{pmatrix} I & 0 \\ -\mathbf{b}^T & 1 \end{pmatrix} = \begin{pmatrix} I & \mathbf{a} \\ 0 & 1 + \mathbf{b}^T \mathbf{a} \end{pmatrix}. \quad (4.2.12)$$

If we take determinants on both sides, the right hand side gives  $1 + \mathbf{b}^T \mathbf{a}$ . The determinant of the left hand side is the product of the determinants of three matrices. Note the first and third matrices are triangle matrices with unit diagonal, then their determinants are 1. Thus it follows that

$$\det(I + \mathbf{a}\mathbf{b}^T) = 1 + \mathbf{b}^T \mathbf{a}. \quad (4.2.13)$$

Then for a general invertible matrix  $A$ , we have

$$\det(A + \mathbf{a}\mathbf{b}^T) = \det(A) \det(I + A^{-1} \mathbf{a}\mathbf{b}^T) = \det(A)(1 + \mathbf{b}^T A^{-1} \mathbf{a}). \quad (4.2.14)$$

This completes the proof of the lemma. ■

Applying this lemma to (4.2.10) and (4.2.9), where we identify  $A \equiv J_e - \lambda I$ ,  $\mathbf{a} \equiv -p_{\pm} \mathbf{e}_1$ , and  $\mathbf{b} \equiv \mathbf{e}_1$ , we conclude that if  $\lambda$  is not an eigenvalue of  $J_e$ , then  $\lambda$  must satisfy

$$1 - p_{\pm}(\lambda) \mathbf{e}_1^T (J_e - \lambda I)^{-1} \mathbf{e}_1 = 0. \quad (4.2.15)$$

### 4.3. One-Component Membrane Dynamics

---

To simplify (4.2.15), we write  $(J_e - \lambda I)^{-1}$  in terms of the cofactor matrix  $M$  as

$$(J_e - \lambda I)^{-1} = \frac{1}{\det(J_e - \lambda I)} M^T,$$

where the entries  $M_{ij}$  of  $M$  are the cofactors of the element  $a_{i,j}$  of the matrix  $J_e - \lambda I$ . Since  $\mathbf{e}_1^T (J_e - \lambda I)^{-1} \mathbf{e}_1 = M_{11}/\det(J_e - \lambda I)$ , we obtain that (4.2.15) reduces to the following more explicit transcendental equation for  $\lambda$ :

$$1 - p_{\pm}(\lambda) \frac{M_{11}(\lambda)}{\det(J_e - \lambda I)} = 0, \quad (4.2.16a)$$

where

$$M_{11}(\lambda) \equiv \det \begin{pmatrix} \frac{\partial \mathcal{F}_2}{\partial u_2} \Big|_{\mathbf{u}=\mathbf{u}_e} - \lambda, & \cdots, & \frac{\partial \mathcal{F}_2}{\partial u_n} \Big|_{\mathbf{u}=\mathbf{u}_e} \\ \cdots, & \cdots, & \cdots \\ \frac{\partial \mathcal{F}_n}{\partial u_2} \Big|_{\mathbf{u}=\mathbf{u}_e}, & \cdots, & \frac{\partial \mathcal{F}_n}{\partial u_n} \Big|_{\mathbf{u}=\mathbf{u}_e} - \lambda \end{pmatrix}. \quad (4.2.16b)$$

Here  $\mathcal{F}_2, \dots, \mathcal{F}_n$  denote the components of the vector  $\mathcal{F} \equiv (\mathcal{F}_1, \dots, \mathcal{F}_n)^T$  characterizing the membrane kinetics.

For the special case of a two-component membrane dynamics of the form  $\mathcal{F} = (f, g)^T$ , with  $f = f(u_1, u_2)$  and  $g = g(u_1, u_2)$ , (4.2.16a) reduces to

$$1 - \frac{(g_{u_2} - \lambda)}{\det(J_e - \lambda I)} p_{\pm}(\lambda) = 0, \quad J_e \equiv \begin{pmatrix} \frac{\partial f}{\partial u_1} \Big|_{\mathbf{u}=\mathbf{u}_e}, & \frac{\partial f}{\partial u_2} \Big|_{\mathbf{u}=\mathbf{u}_e} \\ \frac{\partial g}{\partial u_1} \Big|_{\mathbf{u}=\mathbf{u}_e}, & \frac{\partial g}{\partial u_2} \Big|_{\mathbf{u}=\mathbf{u}_e} \end{pmatrix}, \quad (4.2.17)$$

where  $p_{\pm}(\lambda)$  are defined in (4.2.6) and (4.2.8). An example of this case is considered below in §4.5.

### 4.3 One-Component Membrane Dynamics

In this section we study the stability of steady-state solutions when the membrane dynamics consists of only a single component. For this case, it is convenient to label  $u_1 = u$  and to define  $F(C(0, t), u)$  by

$$F(C(0, t), u) \equiv \mathcal{F}(u) + \beta \mathcal{P}(C(0, t), u). \quad (4.3.1)$$

The symmetric steady-state solution  $C_e(x)$  is given by (4.2.2a), where  $C_e^0$  and  $u_e$  satisfy the nonlinear algebraic system

$$-C_e^0 \tanh(\omega_0 L) = \omega_0 G(C_e^0, u_{1e}), \quad F(C_e^0, u_e) = 0, \quad \text{where } \omega_0 \equiv 1/\sqrt{D}. \quad (4.3.2)$$

### 4.3. One-Component Membrane Dynamics

---

In terms of  $F$  defined in (4.3.1), the spectral problem characterizing the stability properties of this steady-state solution for either the synchronous or asynchronous mode is

$$\begin{aligned} D\Omega_\lambda \tanh(\Omega_\lambda L) &= -G_c^e + \frac{F_c^e G_u^e}{F_u^e - \lambda}, & (\text{sync}), \\ D\Omega_\lambda \coth(\Omega_\lambda L) &= -G_c^e + \frac{F_c^e G_u^e}{F_u^e - \lambda}, & (\text{async}), \end{aligned} \quad (4.3.3)$$

where  $\Omega_\lambda \equiv \sqrt{(1 + \tau\lambda)/D}$  is the principal branch of the square root. We will first derive theoretical results for the roots of (4.3.3) for the infinite-line problem where  $L \rightarrow \infty$ .

#### 4.3.1 Theoretical Results for a Hopf Bifurcation: The Infinite-Line Problem

For the infinite-line problem where  $L \rightarrow \infty$ , (4.3.3) reduces to the limiting spectral problem of finding the roots of  $\mathcal{G}(\lambda) = 0$  in  $\text{Re}(\lambda) \geq 0$ , where

$$\mathcal{G}(\lambda) \equiv \sqrt{1 + \tau\lambda} - g(\lambda), \quad \text{and} \quad g(\lambda) \equiv \frac{c + a\lambda}{b + \lambda}. \quad (4.3.4a)$$

Here the constants  $a$ ,  $b$ , and  $c$ , are defined by

$$a \equiv -\frac{G_c^e}{\sqrt{D}}, \quad b \equiv -F_u^e, \quad c \equiv \frac{1}{\sqrt{D}} [G_c^e F_u^e - G_u^e F_c^e]. \quad (4.3.4b)$$

Our goal is to characterize any roots of  $\mathcal{G}(\lambda) = 0$  in  $\text{Re}(\lambda) > 0$  as the coefficients  $a$ ,  $b$ , and  $c$ , are varied, and in particular to detect any Hopf bifurcation points. In (4.3.4),  $b$  represents the dependence of the local kinetics on the membrane-bound species. If  $b > 0$ , this term indicates a self-inhibiting effect, whereas if  $b < 0$  the membrane-bound species is self-activating. The sign of  $G_c^e$  represents the feedback from the environment to its own secretion. If  $G_c^e$  is positive (negative) it represents negative (positive) feedback. We remark that the spectral problem (4.3.4) has the same form, but with different possibilities regarding the signs of the coefficients, as the spectral problem studied in [57] characterizing the stability of a pulse solution for a singularly perturbed reaction-diffusion on the infinite line.

We first use a winding number argument to count the number  $N$  of roots of  $\mathcal{G}(\lambda) = 0$  in  $\text{Re}(\lambda) \geq 0$  in terms of the behavior of  $\mathcal{G}(\lambda)$  on the imaginary axis of the  $\lambda$ -plane. If  $N = 0$ , the symmetric steady-state solution is linearly stable, whereas if  $N > 0$  this solution is unstable.

### 4.3. One-Component Membrane Dynamics

---

**Lemma 4.3.1** *Let  $N$  be the number of zeroes of  $\mathcal{G}(\lambda) = 0$  in  $\text{Re}(\lambda) > 0$ , where  $\mathcal{G}(\lambda)$  is defined in (4.3.4). Assume that there are no such zeroes on the imaginary axis. Then,*

$$N = \frac{1}{4} + \frac{1}{\pi} [\arg \mathcal{G}]|_{\Gamma_{I_+}} + P, \quad (4.3.5)$$

where  $P = 0$  if  $b > 0$  and  $P = 1$  if  $b < 0$ . Here  $[\arg \mathcal{G}]|_{\Gamma_{I_+}}$  denotes the change in the argument of  $\mathcal{G}(\lambda)$  along the semi-infinite imaginary axis  $\lambda = i\omega$  with  $0 < \omega < \infty$ , traversed in the downwards direction.

**Proof:** We take the counterclockwise contour consisting of the imaginary axis  $-iR \leq \text{Im}\lambda \leq iR$ , decomposed as  $\Gamma_{I_+} \cup \Gamma_{I_-}$ , where  $\Gamma_{I_+} = i\omega$  and  $\Gamma_{I_-} = -i\omega$  with  $0 < \omega < R$ , together with the semi-circle  $\Gamma_R$ , given by  $|\lambda| = R > 0$  with  $|\arg \lambda| \leq \frac{\pi}{2}$ . We use the argument principle of complex analysis to obtain

$$\lim_{R \rightarrow \infty} [\arg \mathcal{G}]|_C = 2\pi(N - P), \quad C \equiv \Gamma_R \cup \Gamma_{I_+} \cup \Gamma_{I_-}, \quad (4.3.6)$$

where  $[\arg \mathcal{G}]|_C$  denotes the change in the argument of  $\mathcal{G}$  over the contour  $C$  traversed in the counter-clockwise direction, and  $P$  is the number of poles of  $\mathcal{G}$  inside  $C$ . Clearly  $P = 1$  if  $b < 0$  and  $P = 0$  if  $b > 0$ . We calculate  $\mathcal{G}(\lambda) \sim \sqrt{\tau R} e^{i\theta/2}$  on  $\Gamma_R$  as  $R \rightarrow \infty$ , where  $\theta = \arg \lambda$ , so that  $\lim_{R \rightarrow \infty} [\arg \mathcal{G}]_{\Gamma_R} = \pi/2$ . Moreover, since  $\mathcal{G}(\bar{\lambda}) = \overline{\mathcal{G}(\lambda)}$ , we get that  $[\arg \mathcal{G}]_{\Gamma_{I_+}} = [\arg \mathcal{G}]_{\Gamma_{I_-}}$ . In this way, we solve for  $N$  in (4.3.6) to obtain (4.3.5).  $\blacksquare$

Next, we set  $\lambda = i\omega$  in (4.3.4a) to calculate  $[\arg \mathcal{G}]|_{\Gamma_{I_+}}$  and detect any Hopf bifurcation points. Since we have specified the principal branch of the square root in (4.3.4a), we must have that  $\text{Re}(\sqrt{1 + \tau\lambda}) > 0$ . Therefore, if we square both sides of the expression for  $\mathcal{G} = 0$  in (4.3.4a) and solve for  $\tau$ , we may obtain spurious roots. We must then ensure that  $\text{Re}(g) > 0$  at any such root. Upon setting  $\lambda = i\omega$  in (4.3.4a) and squaring both sides, we obtain that  $\tau = i(1 - [g(i\omega)]^2) / \omega$ . Upon taking the real and imaginary parts of this expression we conclude that

$$\tau = \frac{1}{\omega} \text{Im} \left( [g(i\omega)]^2 \right) = \frac{2}{\omega} g_R(\omega) g_I(\omega) = \frac{2(cb + a\omega^2)}{(b^2 + \omega^2)^2} (ab - c). \quad (4.3.7a)$$

Here  $\omega > 0$  is a root of

$$\text{Re} \left( [g(i\omega)]^2 \right) = 1, \quad (4.3.7b)$$

### 4.3. One-Component Membrane Dynamics

---

for which  $g_R(\omega) > 0$  and  $g_I(\omega) > 0$  to ensure that  $\operatorname{Re}(\sqrt{1+i\tau\omega}) > 0$  and  $\tau > 0$ , respectively. In (4.3.7a),  $g(i\omega)$  has been decomposed into real and imaginary parts as  $g(i\omega) = g_R(\omega) + ig_I(\omega)$ , where

$$g_R(\omega) = \frac{bc + a\omega^2}{b^2 + \omega^2}, \quad g_I(\omega) = \frac{\omega(ab - c)}{b^2 + \omega^2}. \quad (4.3.7c)$$

In addition, if we separate  $\sqrt{1+i\tau\omega}$  into real and imaginary parts, we readily derive that

$$\begin{aligned} \operatorname{Re}(\sqrt{1+i\tau\omega}) &= \frac{1}{\sqrt{2}} \left[ \sqrt{1 + \tau^2\omega^2} + 1 \right]^{1/2}, \\ \operatorname{Im}(\sqrt{1+i\tau\omega}) &= \frac{1}{\sqrt{2}} \left[ \sqrt{1 + \tau^2\omega^2} - 1 \right]^{1/2}. \end{aligned} \quad (4.3.8)$$

We now apply the winding number criterion of Lemma 4.3.1 together with (4.3.7) to determine the location of the roots of  $\mathcal{G}(\lambda) = 0$  for various ranges of  $a$ ,  $b$ , and  $c$ , as the parameter  $\tau$  is varied.

**Proposition 4.3.1** *Suppose that  $cb < 0$  and that  $a \leq 0$ . Then, no Hopf bifurcations are possible as  $\tau > 0$  is varied. Moreover, if  $b > 0$  we have  $N = 0$ , so that the symmetric steady-state solution is linearly stable for all  $\tau > 0$ . Alternatively, when  $b < 0$  we have  $N = 1$ , and so the symmetric steady-state solution is unstable for all  $\tau > 0$ .*

**Proof:** We note that  $g(\lambda)$ , defined in (4.3.4a), is a bilinear form and is real-valued when  $\lambda$  is real. It does not have a pole at  $\lambda = 0$  since  $b \neq 0$ . Therefore, it follows that the imaginary axis  $\lambda = i\omega$  must map to a disk  $\mathcal{B}$  centered on the real axis in the  $(g_R, g_I)$  plane. When  $cb < 0$  and  $a \leq 0$ , it follows from (4.3.7c) that  $g_R < 0$ , and so this disk lies in the left half-plane  $\operatorname{Re}(g) < 0$ . When  $b > 0$ , we have that  $g(\lambda)$  is analytic in  $\operatorname{Re}(\lambda) > 0$ , and so the region  $\operatorname{Re}(\lambda) > 0$  must map to inside the disk  $\mathcal{B}$ . As such, since  $\operatorname{Re}(\sqrt{1+i\tau\lambda}) > 0$ , it follows that there are no roots to  $\mathcal{G}(\lambda) = 0$  in  $\operatorname{Re}(\lambda) > 0$ , and so  $N = 0$ .

For the case  $b < 0$ , we use the winding number criterion (4.3.5). Since  $cb < 0$  and  $a \leq 0$ , we have  $g_R(\omega) < 0$ , so that

$$\operatorname{Re}[\mathcal{G}(i\omega)] = \operatorname{Re}[\sqrt{1+i\tau\omega} - g(i\omega)] > 0.$$

We have  $\arg \mathcal{G}(i\omega) \rightarrow \pi/4$  as  $\omega \rightarrow +\infty$  and  $\mathcal{G}(0) > 0$ , so that  $\arg \mathcal{G}(0) = 0$ . This yields that  $[\arg \mathcal{G}]|_{\Gamma_{I+}} = -\pi/4$ . In addition, since  $P = 1$  in (4.3.5), we obtain that  $N = 1$  for all  $\tau > 0$ . ■

### 4.3. One-Component Membrane Dynamics

---

Next, we establish the following additional result that characterizes  $N$ , independent of the value of  $\tau > 0$ .

**Proposition 4.3.2** *When  $c > ab$ , there are no Hopf bifurcation points for any  $\tau > 0$ . If in addition, we have*

$$\begin{aligned}
 (I) \quad & b > 0, \text{ and } c/b < 1, \quad \text{then, } N = 0 \quad \forall \tau > 0, \\
 (II) \quad & b < 0, \text{ and } c/b < 1, \quad \text{then, } N = 1 \quad \forall \tau > 0, \\
 (III) \quad & b > 0, \text{ and } c/b > 1, \quad \text{then, } N = 1 \quad \forall \tau > 0, \\
 (IV) \quad & b < 0, \text{ and } c/b > 1, \quad \text{then, } N = 2 \quad \forall \tau > 0.
 \end{aligned} \tag{4.3.9}$$

**Proof:** We first observe from (4.3.8) and (4.3.7c) that  $\text{Im}(\mathcal{G}(i\omega)) > 0$  for all  $\tau > 0$  when  $c > ab$ . Therefore, there can be no Hopf bifurcations as  $\tau$  is increased. To establish (I) of (4.3.9) we use  $\mathcal{G}(0) > 0$ , since  $c/b < 1$ ,  $\arg \mathcal{G}(i\omega) \rightarrow \pi/4$  as  $\omega \rightarrow +\infty$ , and  $\text{Im}(\mathcal{G}(i\omega)) > 0$  to conclude that  $[\arg \mathcal{G}]|_{\Gamma_{I_+}} = -\pi/4$ . Then, since  $b > 0$  we have  $P = 0$ , and (4.3.5) yields  $N = 0$ . The proof of (II) of (4.3.9) is identical except that we have  $P = 1$  in (4.3.5) since  $b < 0$ , so that  $N = 1$ . This unstable eigenvalue is located on the positive real axis on the interval  $-b < \lambda < \infty$ . To prove (III) we note that  $\mathcal{G}(0) < 0$  since  $c/b > 1$ , and  $P = 0$  since  $b > 0$ . This yields  $[\arg \mathcal{G}]|_{\Gamma_{I_+}} = 3\pi/4$ , and  $N = 1$  from (4.3.5). This root is located on the positive real axis. Finally, to prove (IV) we use  $\mathcal{G}(0) < 0$  and  $b < 0$  to calculate  $[\arg \mathcal{G}]|_{\Gamma_{I_+}} = 3\pi/4$  and  $P = 1$ . This yields  $N = 2$  from (4.3.5). A simple plot of  $\sqrt{1 + \tau\lambda}$  and  $g(\lambda)$  on the positive real axis for this case shows that there is a real root in  $0 < \lambda < -b$  and in  $-b < \lambda < \infty$  for any  $\tau > 0$ . ■

Next, we consider the range  $ab > c$  and  $bc > 0$  for which Hopf bifurcations in  $\tau$  can be established for certain subranges of  $a$ ,  $b$ , and  $c$ . To analyze this possibility, we substitute  $g(i\omega)$  into (4.3.7b), to obtain that  $\omega$  must satisfy

$$\left(a\omega^2 + bc\right)^2 - \omega^2(ab - c)^2 = \left(b^2 + \omega^2\right)^2,$$

in the region  $bc + a\omega^2 > 0$ . Upon defining  $\xi = \omega^2$ , it follows for  $|a| \neq 1$  that we must find a root of the quadratic  $Q(\xi) = 0$  with  $\xi \in \mathcal{S}$ , where

$$Q(\xi) \equiv \xi^2 - a_0\xi + a_1 = (\xi - a_0/2)^2 + a_1 - a_0^2/4, \quad \mathcal{S} \equiv \{\xi \mid \xi > 0 \text{ and } a\xi > -cb\}. \tag{4.3.10a}$$

We refer to  $\mathcal{S}$  as the admissible set. Here  $a_0$  and  $a_1$  are defined by

$$a_0 = \frac{1}{a^2 - 1} \left[ (ab - c)^2 + 2b(b - ac) \right], \quad a_1 = \frac{b^2}{1 - a^2} (b^2 - c^2). \tag{4.3.10b}$$

For the special case where  $a = \pm 1$ , we have

$$\xi = b^2 \left( \frac{c/b - 1}{c/b + 3} \right), \quad \text{if } a = -1; \quad \xi = -b^2 \left( \frac{c/b + 1}{3 - c/b} \right), \quad \text{if } a = 1. \quad (4.3.10c)$$

Our first result shows that there are certain subranges of the regime  $ab > c$  and  $bc > 0$  for which we again have that no Hopf bifurcations can occur for any  $\tau > 0$ .

**Proposition 4.3.3** *Suppose that  $b < 0$ ,  $0 < c/b < 1$ , and  $c/b > a$ . Then,  $N = 1$  for all  $\tau > 0$ .*

**Proof:** We first establish, for any  $\tau > 0$ , that  $\text{Re}(\mathcal{G}(i\omega)) > 0$  when  $\omega > 0$ . We observe from (4.3.8) that  $\text{Re}(\sqrt{1 + i\tau\omega})$  is a monotone increasing function of  $\omega$ , while  $g_R(\omega)$ , defined in (4.3.7c), is a monotone decreasing function of  $\omega$  when  $c/b > a$ . This implies that  $\text{Re}(\mathcal{G}(i\omega))$  is monotone increasing in  $\omega$  when  $c/b > a$ . Since  $\text{Re}(\mathcal{G}(0)) = 1 - c/b > 0$  when  $c/b < 1$ , we conclude that  $\text{Re}(\mathcal{G}(i\omega)) > 0$  for  $\omega > 0$ . Then, since  $\text{Re}(\mathcal{G}(i\omega)) \rightarrow +\infty$  as  $\omega \rightarrow +\infty$ , we obtain  $[\arg \mathcal{G}]|_{\Gamma_{I_+}} = -\pi/4$ . Using this result in (4.3.5), together with  $P = 1$  since  $b < 0$ , we get that  $N = 1$  for all  $\tau > 0$ . ■

We now use Lemma 4.3.1 and (4.3.10) to identify a parameter regime in the range  $ab > c$  with  $bc > 0$  where there is a unique Hopf bifurcation value for  $\tau$ :

**Proposition 4.3.4** *Suppose that  $b < 0$ ,  $c/b > 1$  and  $a < 1$ . Then, we have either  $N = 0$  or  $N = 2$  for all  $\tau > 0$ . Moreover,  $N = 0$  for  $0 < \tau \ll 1$  and  $N = 2$  for  $\tau \gg 1$ . For  $a \neq -1$ , there is a unique Hopf bifurcation at  $\tau = \tau_H > 0$  given by*

$$\tau_H = \frac{2(cb + a\omega_H^2)}{(b^2 + \omega_H^2)^2}(ab - c), \quad \omega_H = \sqrt{\frac{a_0}{2} + \zeta \sqrt{\frac{a_0^2}{4} - a_1}}, \quad (4.3.11a)$$

where  $\zeta = +1$  if  $|a| < 1$  and  $\zeta = -1$  if  $a < -1$ . Here  $a_0$  and  $a_1$  are defined in (4.3.10b). When  $a = -1$ , we have

$$\tau_H = -\frac{2(cb - \omega_H^2)}{(b^2 + \omega_H^2)^2}(b + c), \quad \omega_H = |b| \sqrt{\frac{c/b - 1}{c/b + 3}}. \quad (4.3.11b)$$

**Proof:** We first establish that, for any  $\tau > 0$ , there is a unique root  $\omega^*$  to  $\text{Re}(\mathcal{G}(i\omega)) = 0$  in  $\omega > 0$ . To prove this we follow the proof of Proposition 4.3.3 to obtain that  $\text{Re}(\mathcal{G}(i\omega))$  is a monotone increasing function of  $\omega$  when  $c/b > a$ . Moreover, since  $\text{Re}(\mathcal{G}(0)) = 1 - c/b < 0$ , as a result of  $c/b > 1$ , and  $\text{Re}(\mathcal{G}(i\omega)) \rightarrow +\infty$  as  $\omega \rightarrow +\infty$ , we conclude that there is a unique root  $\omega^*$  to  $\text{Re}(\mathcal{G}(i\omega)) = 0$  in the region  $\omega > 0$ . The uniqueness of the root to  $\text{Re}(\mathcal{G}(i\omega)) = 0$ , together with the facts that  $\mathcal{G}(0) = 1 - c/b < 0$  and  $\arg \mathcal{G}(i\omega) \rightarrow \pi/4$  as  $\omega \rightarrow +\infty$ , establishes that either  $[\arg \mathcal{G}]|_{\Gamma_{I_+}} = 3\pi/4$  or  $[\arg \mathcal{G}]|_{\Gamma_{I_+}} = -5\pi/4$  depending on whether  $\text{Im}(\mathcal{G}(i\omega^*)) > 0$  or  $\text{Im}(\mathcal{G}(i\omega^*)) < 0$ , respectively. Therefore, since  $P = 1$ , owing to the fact that  $b < 0$ , we conclude from (4.3.5) that either  $N = 0$  or  $N = 2$  for any  $\tau > 0$ .

To determine  $N$  when either  $0 < \tau \ll 1$  or when  $\tau \gg 1$ , we examine the behavior of the unique root  $\omega^*$  to  $\text{Re}(\mathcal{G}(i\omega)) = 0$  for these limiting ranges of  $\tau$ . For  $\tau \gg 1$ , we readily obtain that  $\omega^* = \mathcal{O}(1/\tau)$ , so that  $\text{Im}(\mathcal{G}(i\omega^*)) > 0$  from estimating  $\text{Im}(\sqrt{1 + i\tau\omega})$  and  $g_I(\omega)$  in (4.3.8) and (4.3.7c). Thus,  $N = 2$  for  $\tau \gg 1$ . Alternatively, if  $0 < \tau \ll 1$ , we readily obtain that  $\omega^* = \mathcal{O}(1)$ , and that  $\text{Im}(\mathcal{G}(i\omega^*)) \sim -g_I(\omega^*) + \mathcal{O}(\tau^2) < 0$ . Therefore,  $N = 0$  when  $0 < \tau \ll 1$ . By continuity with respect to  $\tau$  it follows that there is a Hopf bifurcation at some  $\tau > 0$ .

To establish that the Hopf bifurcation value for  $\tau$  is unique and to derive a formula for it, we now analyze the roots of  $Q(\xi) = 0$  for  $\xi \in \mathcal{S}$ , where  $Q(\xi)$  and the admissible set  $\mathcal{S}$  are defined in (4.3.10). In our analysis, we must separately consider four ranges of  $a$ : (i)  $0 \leq a < 1$ , (ii)  $-1 < a < 0$ , (iii)  $a = -1$ , and (iv)  $a < -1$ .

For (i) where  $0 \leq a < 1$ , the admissible set  $\mathcal{S}$  reduces to  $\xi > 0$  since  $cb > 0$ . Moreover, we have  $Q(0) = a_1 < 0$  since  $c/b > 1$  and  $Q \rightarrow +\infty$  as  $\xi \rightarrow +\infty$ . Since  $Q(\xi)$  is a quadratic, it follows that there is a unique root to  $Q(\xi) = 0$  in  $\xi > 0$ , with the other (inadmissible) root to  $Q(\xi) = 0$  satisfying  $\xi < 0$ . By using (4.3.10a) to calculate the largest root of  $Q(\xi) = 0$ , and recalling (4.3.7a), we obtain (4.3.11a).

The proof of (ii) for the range  $-1 < a < 0$  is similar, but for this case the admissible set  $\mathcal{S}$  is the finite interval  $0 < \xi < -cb/a$ . Since  $Q(0) = a_1 < 0$  and  $Q$  is a quadratic, to prove that there is a unique root to  $Q(\xi) = 0$  on this interval it suffices to show that  $Q(-cb/a) > 0$ . A straightforward calculation using the expressions for  $a_0$  and  $a_1$  in (4.3.10b) yields, upon

re-arranging terms in the resulting expression, that

$$\begin{aligned} Q(-cb/a) &= \frac{c^2b^2}{a^2} - \frac{cb}{a(1-a^2)} \left[ (ab-c)^2 + 2b(b-ac) \right] + \frac{b^2(b^2-c^2)}{1-a^2}, \\ &= \frac{c^2b^2}{a^2} - \frac{cb}{a(1-a^2)}(ab-c)^2 + \frac{b^2}{1-a^2} \left[ (b-c)^2 + 2cb \left( 1 - \frac{1}{a} \right) \right]. \end{aligned}$$

Since  $cb > 0$  and  $-1 < a < 0$  all three terms in this last expression for  $Q(-cb/a)$  are positive. Thus, there is a unique root to  $Q(\xi) = 0$  in  $0 < \xi < -cb/a$ , which is given explicitly by (4.3.11a).

When  $a = -1$ , the admissible set  $\mathcal{S}$  is the interval  $0 < \xi < cb$ . It is then readily verified that the explicit formula for  $\xi$  given in (4.3.10c) when  $a = -1$  lies in this interval. In this way, we obtain (4.3.11b).

Finally, we consider the range (iv) where  $a < -1$ , where the admissible set is  $0 < \xi < -cb/a$ . Since  $c/b > 1$  and  $a < -1$  we have from (4.3.10b) that  $a_0 > 0$  and  $Q(0) = a_1 > 0$ . Thus the minimum value of  $Q(\xi)$  is at some point  $\xi = \xi_m > 0$ . To prove that there is a unique root to  $Q(\xi) = 0$  on  $0 < \xi < -cb/a$  we need only prove that  $Q(-cb/a) < 0$ . By re-arranging the terms in the expression for  $Q(-cb/a)$  we obtain, after some algebra, that

$$\begin{aligned} Q(-cb/a) &= -\frac{cb^3}{a^2(a^2-1)} \left[ \frac{c}{b}(1+a^2) - a \left( \frac{c^2}{b^2} + a^2 \right) \right] \\ &\quad - \frac{b^2}{a^2-1} \left[ (b-c)^2 + 2cb \frac{(a-1)}{a} \right]. \end{aligned}$$

Since  $cb > 0$  and  $a < -1$ , we have that the expressions inside each of the two square brackets are positive, while the terms multiplying the square brackets are negative. This establishes that  $Q(-cb/a) < 0$  and the existence of a unique root to  $Q(\xi) = 0$  in  $0 < \xi < -cb/a$ . By taking the smallest root of  $Q(\xi) = 0$  on  $\xi > 0$  we get (4.3.11a).  $\blacksquare$

Our next result is for the case  $b > 0$  on a subrange of where  $ab - c > 0$ .

**Proposition 4.3.5** *The following results hold for the case  $b > 0$ : (I) Suppose that  $c/b < a < 1$ . Then, we have  $N = 0$  for all  $\tau > 0$ . (II) Suppose that  $c/b < 1 < a$ . Then, there is a Hopf bifurcation at some  $\tau = \tau_H > 0$ . If  $0 < \tau < \tau_H$ , then  $N = 2$ , whereas if  $\tau > \tau_H$ , then  $N = 0$ . The Hopf bifurcation value  $\tau_H > 0$  is given by*

$$\tau_H = \frac{2(cb + a\omega_H^2)}{(b^2 + \omega_H^2)^2}(ab - c), \quad \omega_H = \sqrt{\frac{a_0}{2} + \sqrt{\frac{a_0^2}{4} - a_1}}, \quad (4.3.12)$$

### 4.3. One-Component Membrane Dynamics

---

where  $a_0$  and  $a_1$  are defined in (4.3.10b).

**Proof:** We first prove (I). When  $c/b < a < 1$ , we have from (4.3.7c) that  $g_R(\omega)$  is monotone increasing with  $c/b = g_R(0) < g_R(\omega) < g_R(\infty) = a < 1$ . Since  $\operatorname{Re}(\sqrt{1+i\omega\tau}) > 1$  for all  $\tau > 0$ , it follows that  $\operatorname{Re}(\mathcal{G}(i\omega)) > 0$  on  $0 \leq \omega < \infty$ , and consequently  $[\arg \mathcal{G}]|_{\Gamma_{I_+}} = -\pi/4$ . Then, since  $P = 0$ , owing to  $b > 0$ , (4.3.5) yields that  $N = 0$  for all  $\tau > 0$ .

To prove (II) we consider the range  $c \geq 0$  and  $c < 0$  separately, and we first examine the roots to  $Q(\xi) = 0$  for  $\xi \in S$ , as defined in (4.3.10). For the case  $c \geq 0$ , the admissible set is  $\xi > 0$ . Since the quadratic  $Q(\xi)$  satisfies  $Q(0) = a_1 < 0$  when  $0 < c/b < 1 < a$ , together with  $Q(\xi) \rightarrow +\infty$  as  $\xi \rightarrow \infty$ , it follows that there is a unique root to  $Q(\xi) = 0$  on  $\xi > 0$ . This yields the unique Hopf bifurcation value  $\tau_H$  given in (4.3.12). Alternatively, suppose that  $c < 0$ . Then the admissible set is  $\xi > -bc/a$ . We calculate  $Q(-bc/a)$  from (4.3.10), and after re-arranging the terms in the resulting expression, we obtain

$$\begin{aligned} Q(-bc/a) &= \frac{c^2b^2}{a^2} + \frac{cb}{a(a^2-1)} \left[ (ab-c)^2 + 2b(b-ac) \right] + \frac{b^2(b^2-c^2)}{1-a^2}, \\ &= \frac{bc}{a} \frac{(ab-c)^2}{a^2-1} + \frac{b^2(b^2-c^2)}{1-a^2} + \frac{c^2b^2}{a^2(a^2-1)} \left[ -a^2 - 1 + \frac{2ab}{c} \right]. \end{aligned}$$

Since each of the three terms in the last expression is negative when  $c/b < 1 < a$ , we have  $Q(-bc/a) < 0$ . It follows that there is a unique root to  $Q(\xi) = 0$  on  $-bc/a < \xi < \infty$ , and consequently a unique Hopf bifurcation point.

Combining the results for  $c \geq 0$  and  $c < 0$ , we conclude that there is a unique Hopf bifurcation point  $\tau_H > 0$  when  $c/b < 1 < a$  and  $b > 0$ . We now must prove the result that  $N = 0$  for  $\tau > \tau_H$  and  $N = 2$  for  $0 < \tau < \tau_H$ . To establish this result, we need only prove that  $N = 0$  for  $\tau \gg 1$  and  $N = 2$  for  $0 < \tau \ll 1$ . Then, by the uniqueness of  $\tau_H$ , the continuity of  $\lambda$  with respect to  $\tau$ , and the fact that  $\lambda = 0$  cannot be eigenvalue, the result follows. For  $\tau \gg 1$ , we obtain from the unboundedness of  $\operatorname{Re}(\sqrt{1+i\tau\omega})$  as  $\tau \rightarrow +\infty$  for  $\omega > 0$  fixed that  $\operatorname{Re}(\mathcal{G}(i\omega)) > 0$  on  $0 \leq \omega < \infty$  when  $\tau \gg 1$ . Therefore, since  $[\arg \mathcal{G}]|_{\Gamma_{I_+}} = -\pi/4$  and  $P = 0$ , owing to  $b > 0$ , (4.3.5) yields that  $N = 0$  for  $\tau \gg 1$ . Next, since  $a > 1$ , we readily observe that there are exactly two roots  $\omega_{\pm}$  with  $0 < \omega_- < \omega_+$  to  $\operatorname{Re}(\mathcal{G}(i\omega)) = 0$  on  $0 < \omega < \infty$ , with the property that  $\omega_- = \mathcal{O}(1)$  and  $\omega_+ = \mathcal{O}(\tau^{-1}) \gg 1$  when  $0 < \tau \ll 1$ . We readily estimate that  $\operatorname{Im}(\mathcal{G}(i\omega_+)) > 0$  and  $\operatorname{Im}(\mathcal{G}(i\omega_-)) < 0$  when  $\tau \ll 1$ . Therefore, since  $\arg \mathcal{G}(i\omega) \rightarrow \pi/4$  as  $\omega \rightarrow +\infty$  and  $\arg \mathcal{G}(0) = 0$  since

$c/b < 1$ , we conclude that  $[\arg \mathcal{G}]|_{\Gamma_{I_+}} = 7\pi/4$  when  $0 < \tau \ll 1$ . Finally, since  $P = 0$ , owing to  $b > 0$ , (4.3.5) yields  $N = 2$  when  $0 < \tau \ll 1$ . ■

Our final result is for the range  $1 < a < c/b$  with  $b < 0$  where there can be either two Hopf bifurcation values of  $\tau$  or none.

**Proposition 4.3.6** *Suppose that  $b < 0$  and  $1 < a < c/b$ . Then, if  $c/b \leq 3a + 2\sqrt{2}(a^2 - 1)^{1/2}$ , we have  $N = 2$  for all  $\tau > 0$ , and consequently no Hopf bifurcation points. Alternatively, if  $c/b > 3a + 2\sqrt{2}(a^2 - 1)^{1/2}$ , then there are two Hopf bifurcation values  $\tau_{H\pm}$ , with  $\tau_{H-} > \tau_{H+}$ , so that  $N = 0$  for  $\tau_{H+} < \tau < \tau_{H-}$  and  $N = 2$  when either  $0 < \tau < \tau_{H+}$  or  $\tau > \tau_{H-}$ .*

**Proof:** Since the proof of this result is similar to those of Propositions 4.3.4 and 4.3.5, we only briefly outline the derivation. First, since necessarily  $c < 0$ , the admissible set for  $Q(\xi)$  in (4.3.10a) is  $\xi \geq 0$ , and hence we focus on determining whether  $Q(\xi) = 0$  has any positive real roots. For the range  $1 < a < c/b$ , we calculate  $Q(0) = a_1 > 0$  from (4.3.10). As such it follows that there are either two real roots to  $Q(\xi) = 0$  in  $\xi > 0$ , a real positive root of multiplicity two, or no real roots. From (4.3.10), there are two real roots only when  $a_0 > 0$  and  $a_0^2/4 - a_1 > 0$ , where  $a_0$  and  $a_1$  are defined in (4.3.10b).

Upon using (4.3.10b) for  $a_0$  and  $a_1$ , we can show after some lengthy but straightforward algebra that  $a_0 > 0$  when  $c/b > 2a + \sqrt{3a^2 - 2}$ , and  $a_0^2/4 - a_1 > 0$  when

$$\left(\frac{c}{b} - 3a\right)^2 + 8(1 - a^2) > 0.$$

For any  $a > 1$ , the intersection of these two ranges of  $c/b$  is  $c/b > 3a + 2\sqrt{2}(a^2 - 1)^{1/2}$ . On this range,  $Q(\xi) = 0$  has two positive real roots, and hence there are two Hopf bifurcation values of  $\tau$ . For the range  $1 < a < c/b < 3a + 2\sqrt{2}(a^2 - 1)^{1/2}$ , then either  $a_0 < 0$  or  $a_0^2/4 - a_1 < 0$ , and so  $Q(\xi) = 0$  has no positive real roots.

The determination of  $N$  follows in a similar way as in the proof of Proposition 4.3.5. ■

### 4.3.2 A Finite Domain: Numerical Computations of the Winding Number

For finite domain length  $L$ , the synchronous and asynchronous modes will, in general, have different instability thresholds. For finite  $L$ , we use (4.3.3) to

#### 4.4. Examples of the Theory: One-Component Membrane Dynamics

---

conclude that we must find the roots of  $\mathcal{G}(\lambda) = 0$ , where we now re-define  $\mathcal{G}(\lambda)$  as

$$\mathcal{G}(\lambda) \equiv D\Omega_\lambda h(\Omega_\lambda) + G_c^e - \frac{F_c^e G_u^e}{F_u^e - \lambda}, \quad h(\Omega_\lambda) \equiv \begin{cases} \tanh(\Omega_\lambda L), & (\text{synchronous}) \\ \coth(\Omega_\lambda L), & (\text{asynchronous}) \end{cases}, \quad (4.3.13a)$$

where  $\Omega_\lambda = \sqrt{(1 + \tau\lambda)/D}$ . It is readily shown that (4.3.5) still holds, and so

$$N = \frac{1}{4} + \frac{1}{\pi} [\arg \mathcal{G}] \Big|_{\Gamma_{I_+}} + P, \quad (4.3.13b)$$

where  $P = 0$  if  $F_u^e < 0$  and  $P = 1$  if  $F_u^e > 0$ . To determine  $N$  for a specific membrane-bulk system, numerical computations of  $[\arg \mathcal{G}] \Big|_{\Gamma_{I_+}}$  must be performed separately for both the synchronous and asynchronous modes. This is illustrated below in §4.4 for some specific membrane-bulk systems.

We remark that some of the results in §4.3.1 are still valid when  $L$  is finite. To see this, we write (4.3.13a) in the form

$$\sqrt{1 + \tau\lambda} \frac{h(\Omega_\lambda)}{h(\omega_0)} = g(\lambda), \quad g(\lambda) \equiv \frac{c_L + a_L \lambda}{b + \lambda}, \quad (4.3.14a)$$

where  $\omega_0 = D^{-1/2}$ , and where we have defined  $a_L$ ,  $b$ , and  $c_L$ , by

$$a_L \equiv -\frac{G_c^e}{\sqrt{D}h(\omega_0)}, \quad b \equiv -F_u^e, \quad c_L \equiv \frac{1}{\sqrt{D}h(\omega_0)} [G_c^e F_u^e - G_u^e F_c^e]. \quad (4.3.14b)$$

We remark that as  $L \rightarrow \infty$ , (4.3.14) reduces to the eigenvalue problem (4.3.4a) for the infinite-line problem studied in §4.3.1.

With this reformulation, the left-hand side of (4.3.14a) has the same qualitative properties as  $\sqrt{1 + \tau\lambda}$  that were used in the proofs of some of the propositions in §4.3.1. In particular, Propositions 4.3.1–4.3.3 and part (I) of Proposition 4.3.5 still apply provided we replace  $a$  and  $c$  in these results by  $a_L$  and  $c_L$ . We do not pursue this extension any further here.

## 4.4 Examples of the Theory: One-Component Membrane Dynamics

In this section we consider some specific systems to both illustrate our stability theory and to show the existence of synchronous and asynchronous oscillatory instabilities induced by coupled membrane-bulk dynamics. Assuming a one-component membrane dynamics, we determine the stability

of the steady-state solution by numerically computing the number  $N$  of eigenvalues of the linearization in  $\text{Re}(\lambda) > 0$  from either (4.3.5) for the infinite-line problem, or from (4.3.13) for the finite-domain problem. For some subranges of the parameters in these systems, the theoretical results of §4.3.1 for the infinite-line problem determines  $N$  without the need for any numerical winding number computation.

To confirm our stability results for the case of a one-component membrane dynamics we also computed symmetric steady-state solutions of (4.1.1) and bifurcations of this solution to periodic solutions by first spatially discretizing (4.1.1) with finite differences. Then, from this method of lines approach, together with the path continuation program AUTO with the interface provided by XPPAUT (cf. [16]), branches of steady-state and periodic solution branches were computed numerically. To confirm predictions of oscillatory dynamics, full time-dependent numerical solutions of the coupled PDE-ODE system (4.1.1) were computed using the method of lines.

#### 4.4.1 A Class of Feedback Models

We first apply the theory of §4.3.1 to a class of membrane-bulk problems of the form

$$\begin{aligned} \tau C_t &= DC_{xx} - C, & t > 0, \quad x > 0; \\ DC_x|_{x=0} &= G(C(0, t), u); & C \rightarrow 0 \quad \text{as } x \rightarrow \infty, \\ \frac{du}{dt} &= F(C(0, t), u), & \text{where } F(C(0, t), u) \equiv \mathcal{F}(u) + \sigma G(C(0, t), u(t)), \end{aligned} \tag{4.4.1}$$

for some  $\sigma > 0$ . For this class, the flux on  $x = 0$  acts as a source term to the membrane dynamics. A special case of (4.4.1), which is considered below, is when the membrane-bulk coupling is linear and, for some  $\kappa > 0$ , has the form

$$G(C(0, t), u) \equiv \kappa [C(0, t) - u]. \tag{4.4.2}$$

To apply the theory in §4.3.1 to (4.4.1) we first must calculate  $a$ ,  $b$ , and  $c$ , from (4.3.4b). We readily obtain that

$$b = -\mathcal{F}'(u_e) - \sigma G_u^e, \quad a = -\frac{G_c^e}{\sqrt{D}}, \quad c = \frac{1}{\sqrt{D}} G_c^e \mathcal{F}'(u_e), \quad ab - c = \frac{\sigma}{\sqrt{D}} G_u^e G_c^e, \tag{4.4.3}$$

where  $u_e$  is a steady-state value for  $u$ . The first result for (4.4.1) shows that a Hopf bifurcation is impossible with a linear membrane-bulk coupling mechanism.

#### 4.4. Examples of the Theory: One-Component Membrane Dynamics

---

**Proposition 4.4.1** *Let  $C_e, u_e$  be a symmetric steady-state solution for (4.4.1) with the linear membrane-bulk coupling (4.4.2). Let  $N$  denote the number of unstable eigenvalues in  $\text{Re}(\lambda) > 0$  for the linearization of (4.4.1) around this steady-state solution. Then, for any  $\tau > 0$ , we have  $N = 0$  when  $\mathcal{F}'(u_e) < \mathcal{F}_{Lth}$ , and  $N = 1$  when  $\mathcal{F}'(u_e) > \mathcal{F}_{Lth}$ , where  $\mathcal{F}_{Lth} \equiv \sigma\kappa / \left[1 + \kappa/\sqrt{D}\right]$ .*

**Proof:** Since with the coupling (4.4.2) we have  $ab - c = -\kappa^2\sigma/\sqrt{D} < 0$ , it follows by Proposition 4.3.2 that there are no Hopf bifurcations for any  $\tau > 0$ . To determine the stability threshold, we calculate  $a = -\kappa/\sqrt{D} < 0$ ,  $b = -\mathcal{F}'(u_e) + \sigma\kappa$ , and  $c = \kappa\mathcal{F}'(u_e)/\sqrt{D}$ , and apply the results of Proposition 4.3.2. We separate our analysis into three ranges of  $\mathcal{F}'(u_e)$ . First suppose that  $\mathcal{F}'(u_e) < 0$ . Then, since  $b > 0$ ,  $c < 0$ , and  $a < 0$ , we have by (I) of Proposition 4.3.2 that  $N = 0$ . Next, suppose that  $0 < \mathcal{F}'(u_e) < \sigma\kappa$ , so that  $b > 0$  and  $c > 0$ . We calculate that  $c/b > 1$  if  $\mathcal{F}'(u_e) > \mathcal{F}_{Lth}$ , where  $\mathcal{F}_{Lth}$ , which satisfies  $0 < \mathcal{F}_{Lth} < \sigma\kappa$ , is defined above. Since  $c/b > 1$ , (III) of Proposition 4.3.2 proves that  $N = 1$  for all  $\tau > 0$ . Alternatively, if  $0 < \mathcal{F}'(u_e) < \mathcal{F}_{Lth}$ , then  $c/b < 1$ , and (I) of Proposition 4.3.2 proves that  $N = 0$  for all  $\tau > 0$ . Finally, suppose that  $\mathcal{F}'(u_e) > \sigma\kappa$ . Then,  $c > 0$ ,  $b < 0$ , so that  $bc < 0$  and  $a < 0$ . We conclude from Proposition 4.3.1 that  $N = 1$  for all  $\tau > 0$ . The proof is complete by combining these results on the three separate ranges of  $\mathcal{F}'(u_e)$ . ■

This result for the non-existence of oscillations for a linear membrane-bulk coupling mechanism holds only for the case of a single membrane-bound species. As shown in §4.5, when there are two species in the membrane, oscillatory dynamics can occur even with a linear membrane-bulk coupling mechanism. Our next result for (4.4.1) specifies a class of nonlinear coupling mechanisms  $G(C(0, t), u)$  for which no Hopf bifurcations of the steady-state solution are possible.

**Proposition 4.4.2** *When  $G_c^e G_u^e < 0$ , then the symmetric steady-state solution of (4.4.1) does not undergo a Hopf bifurcation for any  $\tau > 0$ . In particular, if  $G_u^e < 0$  and  $G_c^e > 0$ , then for any  $\tau > 0$  we have  $N = 1$  when  $\mathcal{F}'(u_e) > \mathcal{F}_{th}$ , and  $N = 0$  when  $\mathcal{F}'(u_e) < \mathcal{F}_{th}$ . Here  $\mathcal{F}_{th} > 0$  is the threshold value*

$$\mathcal{F}_{th} \equiv -\frac{\sigma G_u^e}{1 + G_c^e/\sqrt{D}}. \quad (4.4.4)$$

**Proof:** From (4.4.3) we have  $ab - c < 0$  when  $G_c^e G_u^e < 0$ . Proposition 4.3.2 proves that there are no Hopf bifurcations for any  $\tau > 0$ . The second part

#### 4.4. Examples of the Theory: One-Component Membrane Dynamics

---

of the proof parallels that done for Proposition 4.4.1.  $\blacksquare$

A similar analysis can be done for the case where  $G_u^e > 0$  and  $G_c^e < 0$ . For this case, the steady-state solution is unstable when  $G_c^e < -\sqrt{D}$  for all ranges of  $\mathcal{F}'(u_e)$ . When  $G_c^e > -\sqrt{D}$ , the steady-state is linearly stable only when  $\mathcal{F}'(u_e) < -\sigma G_u^e / \left[1 + G_c^e / \sqrt{D}\right]$ .

Our final result for (4.4.1) characterizes a class of nonlinear coupling mechanisms for which a Hopf bifurcation of the steady-state solution does occur for some value of  $\tau$ .

**Proposition 4.4.3** *Suppose that  $G_c^e > 0$  and  $G_u^e > 0$ . Then, for the symmetric steady-state solution of (4.4.1), we have:*

- (I) *If  $\mathcal{F}'(u_e) > \mathcal{F}_{th}$ , then  $N = 1 \forall \tau > 0$ ,*
  - (II) *If  $-\sigma G_u^e < \mathcal{F}'(u_e) < \mathcal{F}_{th}$ , then  $N = 2$  for  $\tau > \tau_H$ , and  $N = 0$  for  $0 < \tau < \tau_H$ ,*
  - (III) *If  $\mathcal{F}'(u_e) < -\sigma G_u^e$ , then  $N = 0 \forall \tau > 0$ .*
- (4.4.5)

Here  $\tau_H > 0$  is the unique Hopf bifurcation point, and  $\mathcal{F}_{th} < 0$  is defined in (4.4.4).

**Proof:** Since  $G_c^e > 0$ , we have  $a < 0$  from (4.4.3). To establish (III) we calculate from (4.4.3) that  $b > 0$  and  $c < 0$  when  $\mathcal{F}'(u_e) < -\sigma G_u^e$ . From the first statement of Proposition 4.3.1, we conclude that  $N = 0$ . To establish (II), we observe that  $b < 0$ ,  $c < 0$ , and  $c/b > 1$  when  $-\sigma G_u^e < \mathcal{F}'(u_e) < \mathcal{F}_{th} < 0$ . Proposition 4.3.4 then proves that there is a unique Hopf bifurcation value  $\tau = \tau_H > 0$  on this range of  $\mathcal{F}'(u_e)$ , as given in (4.3.11). Finally, to establish (I), we observe that  $b < 0$  and  $c/b < 1$  when  $\mathcal{F}'(u_e) > \mathcal{F}_{th}$ . For the range  $c < 0$ , where  $\mathcal{F}_{th} < \mathcal{F}'(u_e) < 0$ , we have from Proposition 4.3.3 that  $N = 1$ . Finally, for the range  $c > 0$ , where  $\mathcal{F}'(u_e) > 0$ , Proposition 4.3.1 also yields that  $N = 1$ .  $\blacksquare$

We now discuss the limiting behavior of  $\tau_H$  and the corresponding Hopf bifurcation frequency  $\omega_H$ , as given by (4.3.11), at the two edges of the interval for  $\mathcal{F}'(u_e)$  in (II) of Proposition 4.4.3. First, we observe that as  $\mathcal{F}'(u_e)$  approaches  $-\sigma G_u^e$  from above, we have that  $b \rightarrow 0^-$ . Therefore, from (4.3.11) we have  $a_1 \rightarrow 0$ , and so at this lower edge of the interval we have  $\omega_H \rightarrow 0^+$  and  $\tau_H \rightarrow +\infty$ . At the other end of the interval, where  $\mathcal{F}'(u_e)$  approaches  $\mathcal{F}_{th}$  from below, we have that  $c - b \rightarrow 0$ , so that again  $a_1 \rightarrow 0$  in (4.3.11). Therefore, from (4.3.11), we conclude at this upper

edge of the interval that  $\omega_H \rightarrow 0^+$ . However, since  $b = \mathcal{O}(1)$ , we have from (4.3.11a) that  $\tau_H \rightarrow 2(1-a)/|b| = \mathcal{O}(1)$  at the upper edge.

#### 4.4.2 A Phase Diagram for an Explicitly Solvable Model

Next, we consider a simple model where a phase diagram characterizing the possibility of Hopf bifurcations can be determined analytically for the infinite-line problem. For  $\beta > 0$ ,  $\gamma > 0$  and  $\kappa > 0$ , we consider

$$\begin{aligned} \tau C_t &= DC_{xx} - C, & t > 0, & \quad 0 < x < 2L, \\ DC_x|_{x=0} &= G(C(0,t), u) \equiv \kappa \frac{(C(0,t) - u)}{1 + \beta (C(0,t) - u)^2}, \\ \frac{du}{dt} &= F(C(0,t), u) \equiv \gamma C(0,t) - u, \end{aligned} \quad (4.4.6)$$

with identical membrane dynamics at  $x = 2L$ . We remark that in (4.4.6) the only nonlinearity arises from the flux term  $G(C(0,t), u)$ . The symmetric steady-state solution for (4.4.6) is  $C_e(x)$  given in (4.2.2a), where  $C_e^0 \equiv C_e(0)$  satisfies the cubic equation

$$(C_e^0)^3 \beta (\gamma - 1)^2 \tanh(\omega_0 L) - C_e^0 [\kappa \omega_0 (\gamma - 1) - \tanh(\omega_0 L)] = 0, \quad \omega_0 \equiv \sqrt{1/D_0}. \quad (4.4.7)$$

In our analysis, we will focus on periodic solutions that bifurcate from the steady-state solution branch where  $C_e^0$  is positive. From (4.4.7), the positive root is given explicitly by

$$\begin{aligned} C_e^0 &= \sqrt{\frac{\kappa \omega_0 (\gamma - 1) - \tanh(\omega_0 L)}{\beta (\gamma - 1)^2 \tanh(\omega_0 L)}}, \\ u_e &= \gamma C_e^0, \quad \text{when} \quad \kappa \omega_0 (\gamma - 1) - \tanh(\omega_0 L) > 0. \end{aligned} \quad (4.4.8)$$

We first consider the infinite-line problem where  $L \rightarrow \infty$  and we set  $D = 1$  for convenience. Then, (4.4.8) reduces to

$$C_e^0 = \sqrt{\frac{\kappa(\gamma - 1) - 1}{\beta(\gamma - 1)^2}}. \quad (4.4.9)$$

For this example, we calculate  $a$ ,  $b$ , and  $c$ , in (4.3.4b) as

$$\begin{aligned} a = -G_c^e &= -\frac{1}{\kappa(\gamma - 1)^2} [2 - \kappa(\gamma - 1)], & b &= 1, \\ c &= (\gamma - 1)G_c^e, & ab - c &= -\gamma G_c^e. \end{aligned} \quad (4.4.10)$$

#### 4.4. Examples of the Theory: One-Component Membrane Dynamics

We now apply the theory of §4.3.1 to obtain the phase-diagram Fig. 4.1 in the parameter space  $\kappa$  versus  $\gamma$ . Since  $C_e^0 > 0$  only when  $\gamma > 1$  and  $\kappa > 1/(\gamma - 1)$ , the boundary between region I and II in Fig. 4.1 is  $\kappa = 1/(\gamma - 1)$ . Next, we calculate that  $ab - c < 0$  and  $0 < c/b < 1$  when  $(\gamma - 1)^{-1} < \kappa < 2(\gamma - 1)^{-1}$ , which is labeled as region II in Fig. 4.1. Therefore, in this region, we conclude from condition (I) of Proposition 4.3.2 that the steady-state is stable for all  $\tau > 0$ . Next, we calculate from (4.4.10) that  $c/b < a < 1$  when  $2(\gamma - 1)^{-1} < \kappa < 2(\gamma - 1)^{-1}(2 - \gamma)^{-1}$  and  $\gamma > 1$ , which is region III of Fig. 4.1. For this range, Proposition 4.3.5 proves that the steady-state solution is stable for all  $\tau > 0$ . Finally, region IV of Fig. 4.1 given by  $\kappa > 2(\gamma - 1)^{-1}(2 - \gamma)^{-1}$  for  $1 < \gamma < 2$ , is where  $c/b < 1 < a$ . At each point in this region, Proposition 4.3.5 proves that there is a Hopf bifurcation value  $\tau = \tau_H > 0$ , and that the steady-state solution is unstable if  $0 < \tau < \tau_H$ .

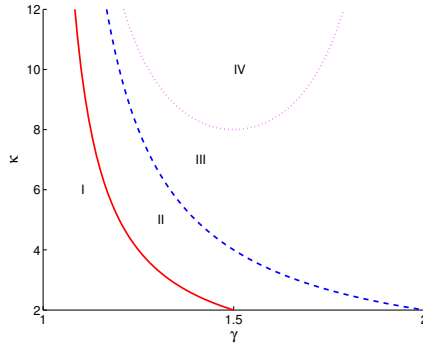


Figure 4.1: Phase diagram for (4.4.6) in the  $\kappa$  versus  $\gamma$  plane for the infinite-line problem when  $D = 1$ . In region I,  $\kappa < (\gamma - 1)^{-1}$  with  $\gamma > 1$ , and there is no steady-state solution. In region II, bounded by  $(\gamma - 1)^{-1} < \kappa < 2(\gamma - 1)^{-1}$  for  $\gamma > 1$ , we have  $ab - c < 0$  and  $b > 0$ , and the steady-state solution is linearly stable for all  $\tau > 0$ . In region III, bounded by  $2(\gamma - 1)^{-1} < \kappa < 2(\gamma - 1)^{-1}(2 - \gamma)^{-1}$  for  $\gamma > 1$ , we have  $b > 0$  and  $c/b < a < 1$ , and so by the first statement in Proposition 4.3.5 there is no Hopf bifurcation and the steady-state solution is linearly stable for all  $\tau > 0$ . In region IV, bounded by  $\kappa > 2(\gamma - 1)^{-1}(2 - \gamma)^{-1}$  for  $1 < \gamma < 2$ , we have  $b > 0$  and  $c/b < 1 < a$ , and so by the second statement in Proposition 4.3.5 there is a Hopf bifurcation and the steady-state solution is unstable if  $0 < \tau < \tau_H$  and is linearly stable if  $\tau > \tau_H$ , where  $\tau_H > 0$  is given by (4.3.12).

For the finite-domain problem with  $L = 2$ , and for two values of  $\kappa$ , in

#### 4.4. Examples of the Theory: One-Component Membrane Dynamics

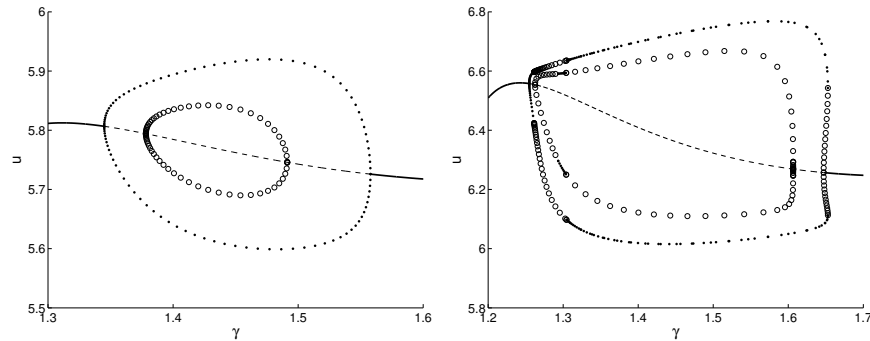


Figure 4.2: Two typical bifurcation diagrams for  $u$  versus  $\gamma$  for (4.4.6) on a finite domain with  $L = 2$ ,  $D = 1$ ,  $\tau = 0.1$ , and  $\beta = 1$ . Left panel:  $\kappa = 9$ . Right-panel:  $\kappa = 10.5$ . The solid and dashed lines denote linearly stable and unstable branches of steady-state solutions. The outer and inner closed loops correspond to branches of synchronous and asynchronous periodic solutions, respectively. The solid/open circles indicate linearly stable/unstable periodic solutions, respectively.

Fig. 4.2 we plot numerically computed bifurcation diagrams of  $u$  versus  $\gamma$  for both the steady-state and bifurcating periodic solution branches. For the corresponding infinite-line problem, this corresponds to taking a horizontal slice at fixed  $\kappa$  through the phase diagram of Fig. 4.1. The results in the left panel of Fig. 4.2 show that when  $\kappa = 9$  the bifurcating branch of synchronous oscillations is linearly stable, while the asynchronous branch is unstable. To confirm this prediction of a stable synchronous oscillation for  $\kappa = 9$  and  $\gamma = 1.45$ , in Fig. 4.3 we plot the full numerical solution computed from the PDE-ODE system (4.4.6). Starting from the initial condition  $C(x, 0) = 1$ , together with  $u_1(0) = 0.04$  and  $u_2(0) = 0.5$  in the left and right membranes, respectively, this plot shows the eventual synchrony of the oscillations in the two membranes. In the right panel of Fig. 4.2, where  $\kappa = 10.5$ , we show that the synchronous mode is stable for a wide range of  $\gamma$ , but that there is a narrow parameter range in  $\gamma$  where both the synchronous and asynchronous modes are unstable. For the value  $\gamma = 1.28$  within this dual-unstable zone, the full numerical solution of the PDE-ODE system (4.4.6), shown in Fig. 4.4 reveals a phase-locking phenomena in the oscillatory dynamics of the two membranes.

#### 4.4. Examples of the Theory: One-Component Membrane Dynamics

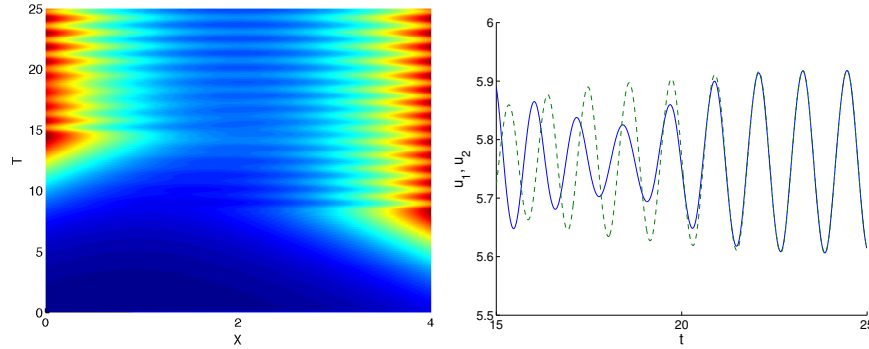


Figure 4.3: Full numerical solutions(left panel) of the PDE-ODE system for (4.4.6) for the finite-domain problem with  $L = 2$ ,  $D = 1$ ,  $\tau = 0.1$ ,  $\kappa = 9$ ,  $\gamma = 1.45$ , and  $\beta = 1$ . The initial condition is  $C(x, 0) = 1$  with  $u_1(0) = 0.04$  and  $u_2(0) = 0.5$  in the left and right membranes. On the infinite line the parameter values are in region IV of Fig. 4.1. For this value of  $\gamma$  and  $\kappa$  we observe from the left panel of the global bifurcation diagram Fig. 4.2 that only the synchronous mode is stable. The full numerical solutions for  $u_1$  and  $u_2$  (right panel) confirm this prediction.

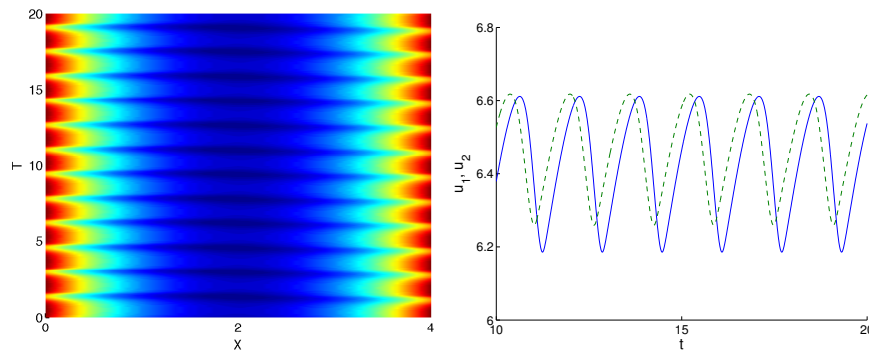


Figure 4.4: Full numerical solutions(left panel) of the PDE-ODE system for (4.4.6) for the finite-domain problem with  $L = 2$ ,  $D = 1$ ,  $\tau = 0.1$ ,  $\kappa = 10.5$ ,  $\gamma = 1.28$ , and  $\beta = 1$ . The initial condition is as given in Fig. 4.3. For this value of  $\gamma$  and  $\kappa$  we observe from the right panel of the global bifurcation diagram Fig. 4.2 that synchronous and asynchronous periodic solutions are both linearly unstable. The full numerical solutions for  $u_1$  and  $u_2$  (right panel) reveal a phase-locking phenomenon.

### 4.4.3 A Model of Kinase Activity Regulation

In the following, we study a model which describes the regulation of kinase activity by its diffusion in space and feedback through membrane-bound receptors from [30]. In [30],  $K(t, x)$  represent the concentration of active kinase,  $Q$  denotes the total concentration of the kinase,  $R(t)$  denotes the surface concentration of the active receptors and  $P$  represents the total surface concentration of the ligand bound receptors (including active and inactive). In the original paper [30], a 2D model in a ball domain with radius  $r_0$  is considered. Here we import the model in 1D and consider the domain  $[0, 2L]$ . The original system reads

$$\begin{aligned} K_t &= d_1 \Delta K - b_1 K, \\ -d_1 K_x \Big|_{x=0} &= a_1 R(Q - K(0, t)), \\ \frac{dR}{dt} &= a_2 K(0, t)(P - R) - b_2 R, \end{aligned} \quad (4.4.11)$$

where  $b_1 > 0$  denotes the dephosphorylation rate of kinase,  $d_1$  is the diffusion coefficient and  $a_1, a_2, b_2$  are positive reaction rates. To transform (4.4.11) into the same form of (4.1.1), we define

$$C(x, t) = K(x, t), \quad u(t) = R(t), \quad \tau = \frac{1}{b_1}, \quad D = \frac{d_1}{b_1}. \quad (4.4.12)$$

Then (4.4.11) can be rewritten to

$$\begin{aligned} \tau C_t &= D \Delta C - C, \\ DC_x(0, t) &= G(C(0, t), u), \\ \frac{du}{dt} &= F(C(0, t), u), \end{aligned} \quad (4.4.13)$$

with

$$G(C(0, t), u) = \frac{a_1}{b_1} u(Q - C(0, t)), \quad F(C(0, t), u) = a_2 C(0, t)(P - u) - b_2 u. \quad (4.4.14)$$

The steady state  $C_e(x)$  of the concentration of active kinase has same expression as (4.2.2) with

$$C_e^0 = \frac{\omega_0 a_2 P Q \frac{a_1}{b_1} - b_2 \tanh(\omega_0 L)}{a_2 \tanh(\omega_0 L) + \omega_0 a_2 P \frac{a_1}{b_1}}, \quad (4.4.15)$$

and

$$u_e = \frac{a_2 P C_e^0}{b_2 + a_2 C_e^0}. \quad (4.4.16)$$

#### 4.4. Examples of the Theory: One-Component Membrane Dynamics

---

For the linear stability analysis, we calculate that

$$b = -F_u^e = a_2 C_e^0 + b_2 > 0, \quad a = -\frac{G_c^e}{\sqrt{D}} = -\frac{a_1 u_e}{b_1 \sqrt{D}} < 0, \quad G_u^e < 0, \quad F_c^e > 0, \quad (4.4.17)$$

with

$$c = \frac{a_1}{b_1 \sqrt{D}} \frac{a_2 P(b_2 Q - a_2 (C_e^0)^2 - 2b_2 C_e^0)}{b_2 + a_2 C_e^0}, \quad (4.4.18)$$

$$ab - c = \frac{G_c^e F_u^e}{\sqrt{D}} - \frac{G_c^e F_u^e - G_u^e F_c^e}{\sqrt{D}} = \frac{G_u^e F_c^e}{\sqrt{D}} < 0.$$

From Proposition 4.3.2 case (I) or (III), depending on the parameter choices, we observe that no Hopf bifurcation is possible for this system for any value of  $\tau$  and  $N = 0$ (I) or  $N = 1$ (case (III)).

#### 4.4.4 Two Biologically-Inspired Models

Next, we consider two specific biologically-inspired models which undergo a Hopf bifurcation when parameters vary. The first example is a simplified version of the GnRH neuron model from [17, 32, 47]. In this context, the spatial variable  $C(x, t)$  represents the GnRH concentration in the bulk medium while  $u$  represents the membrane concentration of the activated  $\alpha$ -subunits of the G-protein  $G_i$  which is activated by the binding of GnRH to its receptor. As discussed in the Appendix, the functions describing the boundary flux and the membrane kinetics for this model are as follows:

$$G(C(0, t), u) = -\sigma \left[ 1 + \beta \left( \frac{\iota + 1 + \zeta q}{\mu + 1 + \delta q} \right)^3 \left( \eta + \frac{s}{\omega + u} \right)^3 \right], \quad (4.4.19a)$$

$$F(C(0, t), u) = \epsilon \left( \frac{[C(0, t)]^2}{k_i^2 + [C(0, t)]^2} - u \right),$$

where  $s$  and  $q$ , which depend on  $C(0, t)$ , are defined by

$$s \equiv \frac{[C(0, t)]^4}{k_s^4 + [C(0, t)]^4}, \quad q \equiv \frac{[C(0, t)]^2}{k_q^2 + [C(0, t)]^2}. \quad (4.4.19b)$$

The fixed parameters in this model, as discussed in [17, 32, 47], can be obtained from fitting experimental data.

For the bulk diffusion process we let  $D = 0.003$ ,  $\tau = 1$ , and  $L = 1$ . Since  $L/\sqrt{D} \approx 18.3 \gg 1$ , our analytical stability theory for the infinite-line problem will provide a good prediction for the stability properties associated

#### 4.4. Examples of the Theory: One-Component Membrane Dynamics

---

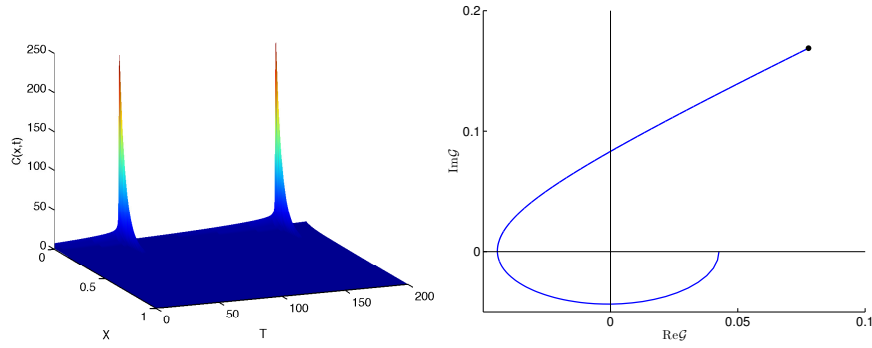


Figure 4.5: Left figure: Numerical results, showing oscillatory dynamics, for  $C(x,t)$  in the GnRH model (4.4.19). The bulk diffusion parameters are  $D = 0.003$ ,  $\tau = 1$ , and  $L = 1$ . The parameters in the membrane-bulk coupling and dynamics in (4.4.19) are  $\sigma = 0.047$ ,  $\beta = 5.256 \times 10^{-14}$ ,  $\iota = 764.7$ ,  $\zeta = 3747.1$ ,  $\mu = 0.012$ ,  $\delta = 0.588$ ,  $\eta = 0.410$ ,  $\omega = 0.011$ ,  $\epsilon = 0.0125$ ,  $k_i = 464$ ,  $k_s = 1$ , and  $k_q = 61$ . Right figure: Plot of the imaginary part versus the real part of  $\mathcal{G}(i\omega)$  when  $\lambda = i\omega$  and  $\omega$  decreases from 3 (black dot) to 0. This shows that the winding number  $[\arg \mathcal{G}]|_{\Gamma_{I_+}}$  is  $7\pi/4$ , and so  $N = 2$  from (4.3.13a).

#### 4.4. Examples of the Theory: One-Component Membrane Dynamics

---

with this finite-domain problem. By using the parameter values of [32], as written in the caption of Fig. 4.5, we calculate that

$$b = -F_u^e = \epsilon > 0, \quad a = -G_c^e/\sqrt{D} > 0, \quad F_c^e > 0, \quad G_u^e > 0. \quad (4.4.20)$$

In the right panel of Fig. 4.5 we show a numerical computation of the winding number, which establishes that  $[\arg \mathcal{G}]|_{\Gamma_{r_+}} = 7\pi/4$ . Since  $b > 0$ , we conclude from (4.3.5) that  $N = 2$ . Our full numerical simulations of the PDE-ODE system in the left panel of Fig. 4.5, showing an oscillatory dynamics, is consistent with this theoretical prediction. In fact, for the parameter values in the caption of Fig. 4.5 we have  $a = 1.8223$ ,  $b = 0.0125$ , and  $c = 0.0028$ . Since  $b > 0$  and  $c/b < 1 < a$ , the second statement in Proposition 4.3.5 proves that there is a Hopf bifurcation value of  $\tau$  for the corresponding infinite-line problem. We calculate  $\tau_H \approx 113.5$  with frequency  $\omega_H \approx 0.0169$ , which indicates a rather large period of oscillation at onset.

Another specific biological system is a model of cell signaling in *Dicystostelium* (cf. [19]). In this context, the spatial variable  $C(x, t)$  is the concentration of the cAMP in the bulk region, while  $u$  is the total fraction of cAMP receptor in the active state on the two membranes (binding of cAMP to this state of the receptor elicits cAMP synthesis). As discussed in the Appendix, the boundary flux and nonlinear membrane dynamics for this system are described

$$G(C(0, t), u) = -\sigma^* \frac{\alpha \left( \Lambda\theta + \frac{\epsilon u [C(0, t)]^2}{1 + [C(0, t)]^2} \right)}{(1 + \alpha\theta) + \left( \frac{\epsilon u [C(0, t)]^2}{1 + [C(0, t)]^2} \right) (1 + \alpha)}, \quad (4.4.21a)$$

$$F(C(0, t), u) = f_2(C(0, t)) - u[f_1(C(0, t)) + f_2(C(0, t))],$$

where

$$f_1(C(0, t)) \equiv \frac{k_1 + k_2 [C(0, t)]^2}{1 + [C(0, t)]^2}, \quad f_2(C(0, t)) \equiv \frac{k_1 L_1 + k_2 L_2 c_d^2 [C(0, t)]^2}{1 + c_d^2 [C(0, t)]^2}. \quad (4.4.21b)$$

The fixed parameters in this model, as discussed briefly in the Appendix, are given in (cf. [19]) after fitting the model to experimental data. They are written in the caption of Fig. 4.6,

For the bulk diffusion process we let  $D = 0.2$ ,  $\tau = 0.5$ , and  $L = 1$ . For this case where  $L/\sqrt{D} \approx 2.2$ , the analytical stability results for the infinite-domain problem do not accurately predict the stability thresholds for this finite-domain problem. For the parameter values in Fig. 4.6, we calculate that

$$b \equiv -F_u^e > 0, \quad F_c^e < 0, \quad G_u^e < 0, \quad G_c^e < 0.$$

#### 4.4. Examples of the Theory: One-Component Membrane Dynamics

In the right panel of Fig. 4.6 we show that  $[\arg \mathcal{G}]|_{\Gamma_{I_+}} = 7\pi/4$ . Since  $b > 0$ , we conclude from (4.3.13) that  $N = 2$ . Our full numerical simulations of the PDE-ODE system in the left panel of Fig. 4.6, showing an oscillatory dynamics, is consistent with this prediction. For the parameter values in the caption of Fig. 4.6 we have  $a = 1.4223$ ,  $b = 1.1525$ , and  $c = 0.2205$ . We remark that since  $b > 0$  and  $c/b < 1 < a$ , Proposition 4.3.5 proves that there is a Hopf bifurcation value of  $\tau$  for the corresponding infinite-line problem given by  $\tau_H \approx 0.5745$ .

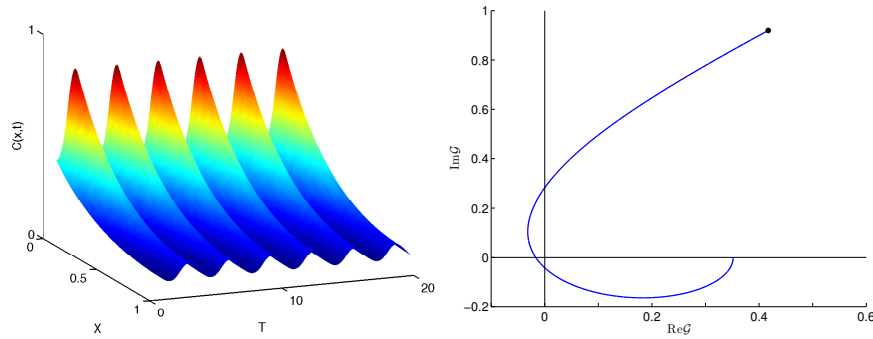


Figure 4.6: Left figure: Numerical results, showing oscillatory dynamics, for  $C(x,t)$  in the *Dictyostelium* model (4.4.21). The bulk diffusion parameters are  $D = 0.2$ ,  $\tau = 0.5$ , and  $L = 1$ . The parameters in the membrane-bulk coupling and dynamics in (4.4.21) are  $\sigma^* = 32$ ,  $\alpha = 1.3$ ,  $\Lambda = 0.005$ ,  $\theta = 0.1$ ,  $\epsilon = 0.2$ ,  $k_1 = 1.125$ ,  $L_1 = 316.228$ ,  $k_2 = 0.45$ ,  $L_2 = 0.03$ , and  $c_d = 100$ . Right figure: Plot of the imaginary part versus the real part of  $\mathcal{G}(i\omega)$  when  $\lambda = i\omega$  and  $\omega$  decreases from 100 (black dot) to 0. This shows that  $[\arg \mathcal{G}]|_{\Gamma_{I_+}} = 7\pi/4$ , and so  $N = 2$  from (4.3.13).

The parameters used in Fig. 4.6 are adopted from [19] (page 245) except for the values of  $\Lambda$ ,  $\theta$ ,  $\alpha$  and  $\sigma$ . In Fig. 4.7 we plot the numerically computed bifurcation diagram of steady-state solutions for (4.4.21) as  $D$  is varied, together with the branches of synchronous periodic solutions. In the left panel of Fig. 4.7 we took  $\Lambda = 0.005$ ,  $\theta = 0.1$  and  $\tau = 1.3$ , corresponding to Fig. 4.6, while in the right panel of Fig. 4.7 we took  $\Lambda = 0.01$ ,  $\theta = 0.01$  and  $\tau = 1.2$ . For the latter parameter set, the steady-state bifurcation diagram has an  $S$ -shaped bifurcation structure.

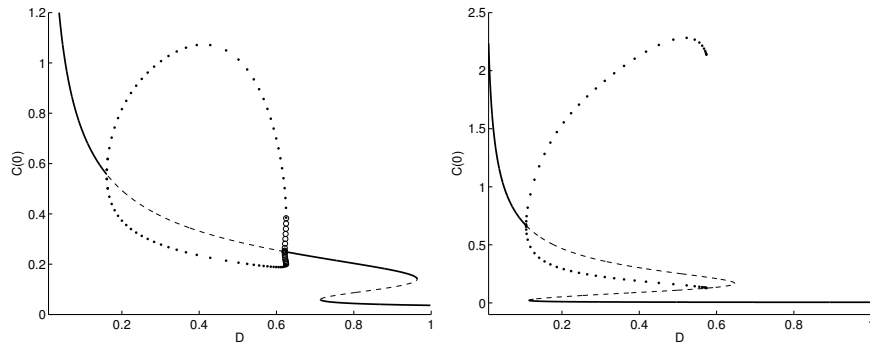


Figure 4.7: Bifurcation diagram of steady-state and synchronous periodic solution branches for the *Dictyostelium* model (4.4.21) with respect to the diffusivity  $D$ . The vertical axis is  $C(0)$ . Left panel:  $\Lambda = 0.005$ ,  $\theta = 0.1$  and  $\tau = 1.3$ . Right panel:  $\Lambda = 0.01$ ,  $\theta = 0.01$  and  $\tau = 1.2$ . In both panels the other parameter values used are the same as in Fig. 4.6. The solid/dashed lines denote stable/unstable branches of steady-state solutions. The solid/open circles indicates stable/unstable periodic solution branches of the synchronous mode. For the value  $D = 0.2$  used in in the left panel of Fig. 4.6, we observe from the left panel above that the steady-state solution is unstable (as expected).

## 4.5 Two-Component Membrane Dynamics: Extension of the Basic Model

In our analysis so far we have assumed that the two membranes are identical. We now extend our analysis to allow for the more general case where the two membranes have possibly different dynamics. From the laboratory experiments of Pik-Yin Lai [42], it was observed for a certain two-cell system that one cell can have oscillatory dynamics, while the other cell is essentially quiescent. To illustrate such a behavior theoretically, we now modify our previous analysis to remove the assumed symmetry of the bulk concentration about the midline at  $x = L$ , and instead consider the whole system on  $0 < x < 2L$ . Allowing for the possibility of heterogeneous membranes, we consider

$$\begin{aligned} \tau C_t &= DC_{xx} - C, & t > 0, & \quad 0 < x < 2L, \\ DC_x(0, t) &= G_1(C(0, t), u_1), & DC_x(2L, t) &= G_2(C(2L, t), v_1). \end{aligned} \quad (4.5.1a)$$

Here  $C(x, t)$  represents the bulk concentration of the signal, while  $u_1$  and  $v_1$  are their concentrations at the two membranes  $x = 0$  and  $x = 2L$ , respectively. Inside each membrane, we assume the two-component dynamics

$$\begin{aligned} \frac{du_1}{dt} &= f_1(u_1, u_2) + \beta_1 \mathcal{P}_1(C(0, t), u_1), & \frac{du_2}{dt} &= g_1(u_1, u_2), \\ \frac{dv_1}{dt} &= f_2(v_1, v_2) + \beta_2 \mathcal{P}_2(C(2L, t), v_1), & \frac{dv_2}{dt} &= g_2(v_1, v_2), \end{aligned} \quad (4.5.1b)$$

where the functions  $G_1, G_2, \mathcal{P}_1, \mathcal{P}_2, f_1, f_2, g_1$ , and  $g_2$  are given by

$$\begin{aligned} G_1(C(0, t), u_1) &= \kappa_1 [C(0, t) - u_1(t)], \\ G_2(C(2L, t), v_1) &= \kappa_2 [v_1(t) - C(2L, t)], \\ f_1(u_1, u_2) &= \sigma_1 u_2 - q_1 u_1 - q_2 \frac{u_1}{1 + q_3 u_1 + q_4 u_1^2}, & g_1(u_1, u_2) &= \frac{1}{1 + u_1^4} - u_2, \\ f_2(v_1, v_2) &= \sigma_2 v_2 - p_1 v_1 - p_2 \frac{v_1}{1 + p_3 v_1 + p_4 v_1^2}, & g_2(v_1, v_2) &= \frac{1}{1 + v_1^4} - v_2, \\ \mathcal{P}_1(C(0, t), u_1) &= [C(0, t) - u_1], & \mathcal{P}_2(C(2L, t), v_1) &= [C(2L, t) - v_1]. \end{aligned} \quad (4.5.1c)$$

This system, adopted from the key survey paper [74] for the design of realistic biological oscillators, models a gene expression process and protein production for a certain biological system. With our choices of  $G_i$  and  $\mathcal{P}_i$  for  $i = 1, 2$ , we have assumed a linear coupling between the bulk and the

#### 4.5. Two-Component Membrane Dynamics: Extension of the Basic Model

---

two membranes. The parameter values for  $\sigma$ ,  $q_i$  and  $p_i$ , for  $i = 1, 2, 3$ , used below in our simulations are computed using parameters given in Fig. 3 of [74].

A simple calculation shows that the steady-state concentrations  $u_{1e}$ ,  $u_{2e}$ ,  $v_{1e}$ , and  $v_{2e}$ , satisfy the nonlinear algebraic system

$$\begin{aligned} \frac{\sigma_1}{1 + u_{1e}^4} - q_1 u_{1e} - \frac{q_2 u_{1e}}{1 + q_3 u_{1e} + q_4 u_{1e}^2} + \beta_1 (a_e u_{1e} + b_e v_{1e} - u_{1e}) &= 0, \\ \frac{\sigma_2}{1 + v_{1e}^4} - p_1 v_{1e} - \frac{p_2 v_{1e}}{1 + p_3 v_{1e} + p_4 v_{1e}^2} + \beta_2 (c_e u_{1e} + d_e v_{1e} - v_{1e}) &= 0, \end{aligned} \quad (4.5.2)$$

where we have defined  $a_e$ ,  $b_e$ ,  $c_e$ ,  $d_e$ ,  $\Pi_1$ , and  $\Pi_2$ , by

$$\begin{aligned} a_e &\equiv \kappa_1 \delta^{-1} [D\omega_0 \coth(2L\omega_0) + \kappa_2], & b_e &\equiv \kappa_2 \delta^{-1} D\omega_0 \operatorname{csch}(2L\omega_0), \\ c_e &\equiv \kappa_1 \delta^{-1} D\omega_0 \operatorname{csch}(2L\omega_0), & d_e &\equiv \kappa_2 \delta^{-1} [D\omega_0 \coth(2L\omega_0) + \kappa_1], \\ \delta &\equiv D^2 \omega_0^2 + D\omega_0 (\kappa_1 + \kappa_2) \coth(2L\omega_0) + \kappa_1 \kappa_2, \end{aligned} \quad (4.5.3)$$

where  $\omega_0 \equiv D^{-1/2}$ . In terms of  $u_{1e}$ ,  $v_{1e}$ ,  $u_{2e}$ , and  $v_{2e}$ , we have

$$\begin{aligned} C_e(0) = a_e u_{1e} + b_e v_{1e}, & \quad u_{2e} = \frac{1}{1 + u_{1e}^4}, \\ C_e(2L) = c_e u_{1e} + d_e v_{1e}, & \quad v_{2e} = \frac{1}{1 + v_{1e}^4}. \end{aligned} \quad (4.5.4)$$

To examine the stability of this steady-state solution, we introduce  $C(x, t) = C_e(x) + e^{\lambda t} \eta(x)$ , together with

$$\begin{aligned} u_1(t) &= u_{1e} + e^{\lambda t} \phi_1, & u_2(t) &= u_{2e} + e^{\lambda t} \phi_2, \\ v_1(t) &= v_{1e} + e^{\lambda t} \psi_1, & v_2(t) &= v_{2e} + e^{\lambda t} \psi_2. \end{aligned}$$

Upon linearizing (4.5.1), we obtain the eigenfunction  $\eta(x)$  satisfies

$$\eta(x) = \eta(0) \frac{\sinh((2L - x)\Omega_\lambda)}{\sinh(2L\Omega_\lambda)} + \eta(2L) \frac{\sinh(x\Omega_\lambda)}{\sinh(2L\Omega_\lambda)},$$

We readily calculate the derivative of  $\eta(x)$

$$\eta_x(x) = -\Omega_\lambda \eta(0) \frac{\cosh((2L - x)\Omega_\lambda)}{\sinh(2L\Omega_\lambda)} + \Omega_\lambda \eta(2L) \frac{\cosh(x\Omega_\lambda)}{\sinh(2L\Omega_\lambda)},$$

In addition, the boundary condition at  $x = 0$  and  $2L$  gives

$$D\eta_x(0) = \eta(0)G_{1c}^e + \phi_1 G_{1u_1}^e, \quad D\eta_x(2L) = \eta(2L)G_{2c}^e + \psi_1 G_{2v_1}^e.$$

#### 4.5. Two-Component Membrane Dynamics: Extension of the Basic Model

---

Substitute the expression of  $\eta(x)$  into above expressions, we obtain

$$\begin{aligned} D(-\Omega_\lambda \eta(0) \coth(2L\Omega_\lambda) + \Omega_\lambda \eta(2L) \operatorname{csch}(2L\Omega_\lambda)) &= \eta(0)G_{1c}^e + \phi_1 G_{1u_1}^e, \\ D(-\Omega_\lambda \eta(0) \operatorname{csch}(2L\Omega_\lambda) + \Omega_\lambda \eta(2L) \coth(2L\Omega_\lambda)) &= \eta(2L)G_{2c}^e + \psi_1 G_{2v_1}^e, \end{aligned}$$

Then we can solve

$$\eta(0) = A\phi_1 + B\psi_1, \quad \eta(2L) = C\phi_1 + D\psi_1.$$

For the local kinetics, we have

$$\begin{aligned} \lambda\phi_1 &= f_{1u1}\phi_1 + f_{1u2}\phi_2 + \beta_1(P_{1c}\eta(0) + P_{1u1}\phi_1), \\ \lambda\phi_2 &= g_{1u1}\phi_1 + g_{1u2}\phi_2, \\ \lambda\psi_1 &= f_{2v1}\psi_1 + f_{2v2}\psi_2 + \beta_2(P_{2c}\eta(2L) + P_{2v1}\psi_1), \\ \lambda\psi_2 &= g_{2v1}\psi_1 + g_{2v2}\psi_2, \end{aligned}$$

where we use  $f_{ijk}$ ,  $g_{ijk}$  to represent the partial derivatives of  $f_i$  and  $g_i$  with respect to  $j_k$ ,  $i, k = 1, 2$ ,  $j = u, v$ . So it gives

$$\phi_2 = \frac{g_{1u1}\phi_1}{\lambda - g_{1u2}}, \quad \psi_2 = \frac{g_{2v1}\psi_1}{\lambda - g_{2v2}},$$

and

$$\begin{aligned} \left[ \lambda - f_{1u1} - \frac{f_{1u2}g_{1u1}}{\lambda - g_{1u2}} - \beta_1 P_{1u1} - \beta_1 P_{1c} A \right] \phi_1 - \beta_1 P_{1c} B \psi_1 &= 0, \\ -\beta_2 P_{2c} C \phi_1 + \left[ \lambda - f_{2v1} - \frac{f_{2v2}g_{2v1}}{\lambda - g_{2v2}} - \beta_2 P_{2v1} - \beta_2 P_{2c} D \right] \psi_1 &= 0, \end{aligned}$$

So the eigenvalue  $\lambda$  satisfies the transcendental equation

$$\det \begin{pmatrix} \lambda - f_{1u1} - \frac{f_{1u2}g_{1u1}}{\lambda - g_{1u2}} + \beta_1 - \beta_1 \mathcal{A}, & -\beta_1 \mathcal{B} \\ -\beta_2 \mathcal{C}, & \lambda - f_{2v1} - \frac{f_{2v2}g_{2v1}}{\lambda - g_{2v2}} + \beta_2 - \beta_2 \mathcal{D} \end{pmatrix} = 0, \quad (4.5.5)$$

where we have defined  $\mathcal{A}$ ,  $\mathcal{B}$ ,  $\mathcal{C}$ , and  $\mathcal{D}$ , by

$$\begin{aligned} \mathcal{A} &\equiv \kappa_1 \Delta^{-1} [\kappa_2 + D\Omega_\lambda \coth(2L\Omega_\lambda)], & \mathcal{B} &\equiv \kappa_2 \Delta^{-1} D\Omega_\lambda \operatorname{csch}(2L\Omega_\lambda), \\ \mathcal{C} &\equiv \kappa_1 \Delta^{-1} D\Omega_\lambda \operatorname{csch}(2L\Omega_\lambda), & \mathcal{D} &\equiv \kappa_2 \Delta^{-1} [\kappa_1 + D\Omega_\lambda \coth(2L\Omega_\lambda)], \\ \Delta &\equiv D^2 \Omega_\lambda^2 + \kappa_1 \kappa_2 + (\kappa_1 + \kappa_2) D\Omega_\lambda \coth(2L\Omega_\lambda). \end{aligned}$$

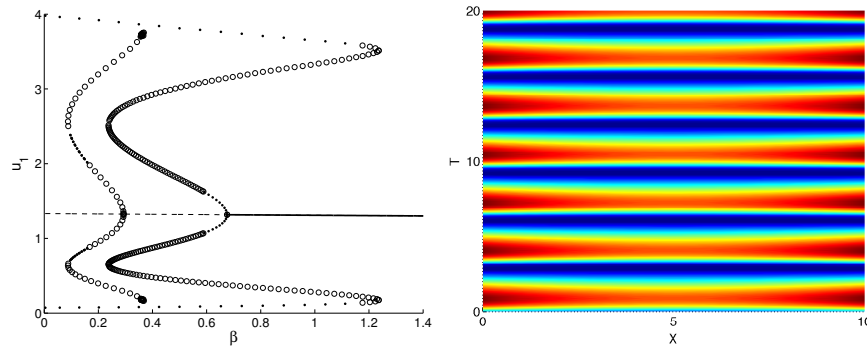


Figure 4.8: Left panel: Bifurcation diagram with respect to  $\beta$  in the two identical membrane case. The larger and smaller values of  $\beta$  at the two Hopf bifurcation points correspond to the synchronous and asynchronous modes respectively. The branches of periodic solutions corresponding to synchronous and asynchronous oscillations are shown. There are secondary instabilities bifurcating from these branches that are not shown. The solid/open circles indicates stable/unstable portions of the periodic solution branches. The parameter values for bulk diffusion are  $D = 50$ ,  $\tau = 0.1$ , and  $L = 5$ , while the parameter values for the membrane dynamics are identical for both membranes and are fixed at  $p_1 = q_1 = 1$ ,  $p_2 = q_2 = 200$ ,  $p_3 = q_3 = 10$ ,  $p_4 = q_4 = 35$ ,  $\sigma_1 = \sigma_2 = 20$ , and  $\kappa_1 = \kappa_2 = 20.0$ . Right panel: Full numerical solution of the PDE-ODE system (4.5.1) when  $\beta = 0.4$ , revealing a synchronous oscillatory instability.

#### 4.5. Two-Component Membrane Dynamics: Extension of the Basic Model

---

Here  $\Omega_\lambda \equiv \sqrt{\frac{1+\tau\lambda}{D}}$  and  $f_{is_j}$  denote partial derivatives of  $f_i$  where  $i = 1, 2$  with respect to  $s_j$ ,  $s = u, v$  and  $j = 1, 2$ .

When there are two identical membranes, the eigenvector of the matrix in (4.5.5) corresponding to the eigenvalue at the stability threshold is either  $(1, 1)^T$  (in-phase synchronization) or  $(1, -1)^T$  (anti-phase synchronization). For this identical membrane case where  $\beta \equiv \beta_1 = \beta_2$ , in the left panel of Fig. 4.8 we plot the numerically computed bifurcation diagram in terms of  $\beta$ , showing the possibility of either synchronous or asynchronous oscillatory dynamics in the two membranes. In the right panel of Fig. 4.8 we plot the full numerical solution computed from the PDE-ODE system (4.5.1) when  $\beta = 0.4$ , which reveals a synchronous oscillatory instability. The parameter values used in the simulation are given in the caption of Fig. 4.8. To determine the number  $N$  of eigenvalues of the linearization in  $\text{Re}(\lambda) > 0$  for the identical membrane case, where  $f_1 = f_2 \equiv f$  and  $g_1 = g_2 \equiv g$ , we recall that  $\lambda$  must be a root of (4.2.17). As such, we seek roots of  $\mathcal{G}(\lambda) = 0$  in  $\text{Re}(\lambda) > 0$ , where

$$\mathcal{G}(\lambda) \equiv \frac{1}{p_\pm(\lambda)} - \frac{(g_{u_2} - \lambda)}{\det(J_e - \lambda I)}, \quad J_e \equiv \begin{pmatrix} \left. \frac{\partial f}{\partial u_1} \right|_{\mathbf{u}=\mathbf{u}_e} & \left. \frac{\partial f}{\partial u_2} \right|_{\mathbf{u}=\mathbf{u}_e} \\ \left. \frac{\partial g}{\partial u_1} \right|_{\mathbf{u}=\mathbf{u}_e} & \left. \frac{\partial g}{\partial u_2} \right|_{\mathbf{u}=\mathbf{u}_e} \end{pmatrix}. \quad (4.5.6)$$

Here  $p_+(\lambda)$  and  $p_-(\lambda)$  are defined in (4.2.6) and (4.2.8), respectively. For our example we find that  $p_\pm(\lambda)$  is non-vanishing in  $\text{Re}(\lambda) > 0$ . Then, by using the argument principle as in the proof of Lemma 4.3.1, and noting that  $\mathcal{G}(\lambda)$  is bounded as  $|\lambda| \rightarrow +\infty$  in  $\text{Re}(\lambda) > 0$ , we obtain that

$$N = P + \frac{1}{\pi} [\arg \mathcal{G}] \Big|_{\Gamma_{I_+}}. \quad (4.5.7)$$

Here  $P$  is the number of roots of  $\det(J_e - \lambda I) = 0$  (counting multiplicity) in  $\text{Re}(\lambda) > 0$ , and  $[\arg \mathcal{G}] \Big|_{\Gamma_{I_+}}$  denotes the change in the argument of  $\mathcal{G}(\lambda)$  along the semi-infinite imaginary axis  $\lambda = i\omega$  with  $0 < \omega < \infty$ , traversed in the downwards direction. In Fig. 4.9 we show a numerical computation of the winding number (4.5.7) near the values of  $\beta$  at the bifurcation points of the synchronous and asynchronous solution branches shown in the left panel of Fig. 4.8.

However, when the two membranes are not identical, the matrix in (4.5.5) can have eigenvectors that are close to  $(1, 0)^T$  or  $(0, 1)^T$ , which corresponds to a large difference in the amplitude of the oscillations in the two membranes. In such a case, we will observe a prominent oscillation in

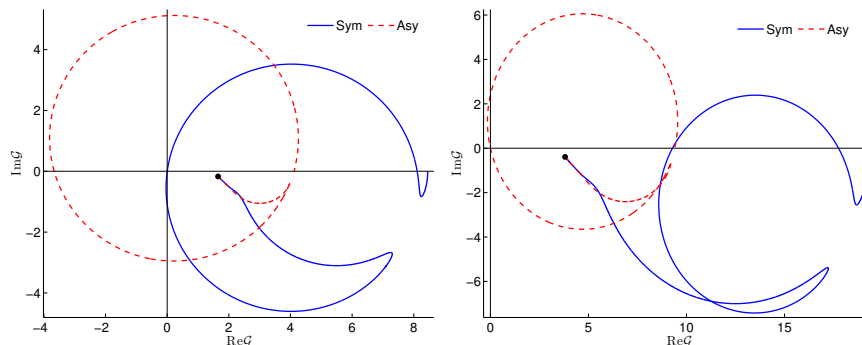


Figure 4.9: Winding number computation verifying the location of the Hopf bifurcation point of the synchronous mode (left panel  $\beta = 0.6757$ ) and the asynchronous mode (right panel  $\beta = 0.2931$ ) corresponding to the bifurcation diagram shown in the left panel of Fig. 4.8. The other parameter values are as given in the caption of Fig. 4.8. The formula (4.5.7) determines the number  $N$  of unstable eigenvalues in  $\text{Re}(\lambda) > 0$ . For both plots  $P = 2$  in (4.5.7). When the change in the argument of  $\mathcal{G}(i\omega)$  is  $-2\pi$ , then  $N = 0$ . Otherwise if the change in the argument is 0, then  $N = 2$ .

only one of the two membranes. We choose the coupling strengths  $\beta_1$  and  $\beta_2$  to be the bifurcation parameters, and denote  $\mu$  by  $\mu \equiv \beta_2 - \beta_1$ . The other parameter values in the model are taken to be the identical for the two membranes. To illustrate that a large oscillation amplitude ratio between the two membranes can occur, in Fig. 4.10 we show full numerical results from the PDE-ODE system (4.5.1) with  $D = 1$  when  $\beta_1 = 0.2$  and  $\beta_2 = 0.7$ . From this figure we observe that the concentration of the signaling molecule undergoes a large amplitude oscillation near one boundary and a significantly smaller amplitude oscillation near the other boundary.

## 4.6 Weakly Nonlinear Theory for Synchronous Oscillations

In §4.3 we showed that, depending on the nature of the membrane-bulk coupling mechanism, spatial-temporal oscillations are possible for a membrane-bulk model consisting of a single species on each membrane that is coupled through linear bulk diffusion. These oscillations originate from a Hopf bifurcation associated with the symmetric steady-state solution branch. In

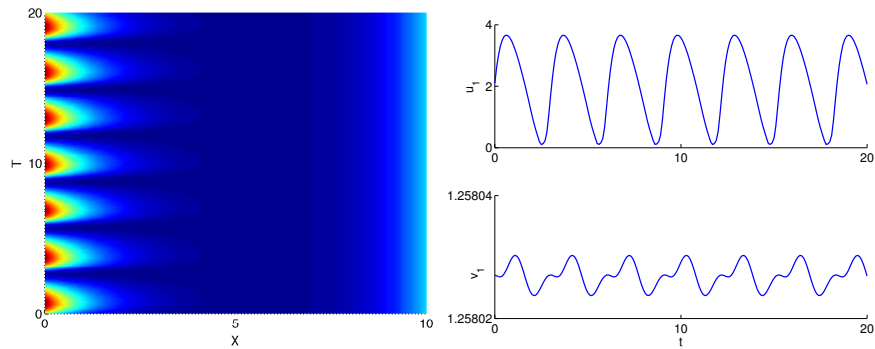


Figure 4.10: Left panel: Contour plot of the oscillatory instability for the case of heterogeneous membranes as computed from the PDE-ODE system (4.5.1) with  $D = 1$ ,  $\kappa_1 = \kappa_2 = 0.1$ , and with the same parameters as in the caption of Fig. 4.8. The two membranes differ only in their coupling strengths with  $\beta_1 = 0.2$  and  $\beta_2 = 0.7$ . The oscillation is pronounced only in the membrane at  $x = 0$ , with only a small-scale oscillation in the second membrane at  $x = 2L$  with  $L = 5$ . Right panel: similar plot showing  $u_1$  (left boundary) and  $v_1$  (right boundary) versus  $t$ , showing the amplitude difference.

this section we develop a weakly nonlinear analysis in the vicinity of this Hopf bifurcation, which leads to an amplitude equation characterizing small amplitude oscillations. By evaluating the coefficients in this amplitude equation, we determine whether the Hopf bifurcation is supercritical or subcritical. This asymptotic prediction for the stationary periodic solution near the bifurcation point is then compared favorably with full numerical results for two specific systems.

We illustrate our weakly nonlinear theory only for the case of synchronous oscillations. The resulting model, assuming only one species on the membrane, is formulated as

$$\begin{aligned} C_{xx} - \frac{1}{D}C &= \frac{\tau}{D}C_t, & t > 0, \quad 0 < x < L; \\ C_x(L, t) &= 0; \quad DC_x|_{x=0} &= G(C(0, t), u), \end{aligned} \quad (4.6.1a)$$

with the local membrane dynamics

$$\frac{du}{dt} = F(C(0, t), u(t)). \quad (4.6.1b)$$

The steady-state solution  $(C_e(x), u_e)$  of (4.6.1) satisfies

$$\begin{aligned} C_{e,xx} - \frac{1}{D}C_e &= 0, & 0 < x < L; \quad C_{e,x}(L) &= 0, \\ DC_{e,x}(0) &= G(C_e(0), u_e), & F(C_e(0), u_e) &= 0. \end{aligned} \quad (4.6.2)$$

We choose the diffusivity  $D$  as the bifurcation parameter. We assume that when  $D = D_0$  the linearization of (4.6.1) around the steady-state solution has a complex conjugate pair of imaginary eigenvalues, and that all the other eigenvalues of the linearization satisfy  $\text{Re}(\lambda) < 0$ .

We will analyze the weakly nonlinear dynamics of (4.6.1) when  $D$  is close to  $D_0$ . As such, we introduce  $\epsilon \ll 1$  and a detuning-parameter  $D_1$  by  $D = D_0 + \epsilon^2 D_1$ , with  $D_1 = \pm 1$  indicating the direction of the bifurcation, so that

$$D = D_0 + \epsilon^2 D_1, \quad \frac{1}{D} = \frac{1}{D_0 + \epsilon^2 D_1 + \mathcal{O}(\epsilon^4)} = \frac{1}{D_0} - \epsilon^2 \frac{D_1}{D_0^2} + \mathcal{O}(\epsilon^4). \quad (4.6.3)$$

To derive the amplitude equation, we will employ a formal two time-scale asymptotic method where we introduce the slow time  $T = \epsilon^2 t$ , so that  $d/dt = \partial/\partial t + \epsilon^2 \partial/\partial T$ . For  $D - D_0 = \mathcal{O}(\epsilon^2)$ , we then expand the solution

to (4.6.1) as

$$\begin{aligned} C(x, t, T) &= C_e(x) + \epsilon C_1(x, t, T) + \epsilon^2 C_2(x, t, T) + \epsilon^3 C_3(x, t, T) + \dots, \\ u(t, T) &= u_e + \epsilon u_1(t, T) + \epsilon^2 u_2(t, T) + \epsilon^3 u_3(t, T) + \dots. \end{aligned} \quad (4.6.4)$$

We then substitute (4.6.4) into (4.6.1) and equate powers of  $\epsilon$ .

To leading-order in  $\epsilon$ , we obtain the steady-state problem (4.6.2) when  $D = D_0$ . This has the solution

$$C_e(x) = C_e^0 \frac{\cosh[\omega_0(L-x)]}{\cosh(\omega_0 L)}, \quad \omega_0 \equiv 1/\sqrt{D_0}, \quad (4.6.5a)$$

with  $C_e^0 \equiv C_e(0)$ , where the constants  $C_e^0$  and  $u_e$  are determined from the nonlinear algebraic system

$$-C_e^0 \tanh(\omega_0 L) = \omega_0 G(C_e^0, u_e), \quad F(C_e^0, u_e) = 0. \quad (4.6.5b)$$

The  $\mathcal{O}(\epsilon)$  system is the linearization of (4.6.1) around the steady-state solution, which is written as

$$\begin{aligned} C_{1xx} - \frac{1}{D_0} C_1 &= \frac{\tau}{D_0} C_{1t}, \quad t > 0, \quad 0 < x < L; \quad C_{1x}(L, t, T) = 0, \\ D_0 C_{1x}|_{x=0} &= C_1 G_c^e + u_1 G_u^e, \quad \text{on } x = 0, \\ u_{1t} &= C_1 F_c^e + u_1 F_u^e, \quad \text{on } x = 0. \end{aligned} \quad (4.6.6)$$

Here  $F_j^e$ ,  $G_j^e$  denote partial derivatives of  $F$  or  $G$  with respect to  $i$  evaluated at the steady-state solution  $(C_e(0), u_e)$  at  $x = 0$ , where  $j = \{C, u\}$ . At  $\mathcal{O}(\epsilon^2)$ , we have that  $C_2(x, t, T)$  and  $u_2(t, T)$  satisfy

$$\begin{aligned} C_{2xx} - \frac{1}{D_0} C_2 &= \frac{\tau}{D_0} C_{2t} - \frac{D_1}{D_0^2} C_e, \quad t > 0, \quad 0 < x < L; \quad C_{2x}(L, t, T) = 0, \\ D_0 C_{2x}|_{x=0} &= C_2 G_c^e + u_2 G_u^e + \frac{1}{2} \left( C_1^2 G_{cc}^e + u_1^2 G_{uu}^e + 2C_1 u_1 G_{cu}^e \right) - \frac{D_1}{D_0} G^e, \\ &\quad \text{on } x = 0, \\ u_{2t} &= C_2 F_c^e + u_2 F_u^e + \frac{1}{2} \left( C_1^2 F_{cc}^e + u_1^2 F_{uu}^e + 2C_1 u_1 F_{cu}^e \right), \quad \text{on } x = 0. \end{aligned} \quad (4.6.7)$$

In a similar notation,  $F_{cc}^e$  denotes the second partial derivative of  $F$  with respect to  $C$  evaluated at the steady-state pair  $(C_e(0), u_e)$ . Lastly, the  $\mathcal{O}(\epsilon^3)$

system for  $C_3(x, t, T)$  and  $u_3(t, T)$ , where resonances will first appear, is

$$\begin{aligned}
 C_{3xx} - \frac{1}{D_0}C_3 &= \frac{\tau}{D_0}C_{3t} - \frac{D_1}{D_0^2}C_1 - \frac{D_1\tau}{D_0^2}C_{1t} + \frac{\tau}{D_0}C_{1T}, \quad t > 0, \quad 0 < x < L; \\
 C_{3x}(L, t, T) &= 0, \\
 D_0C_{3x}|_{x=0} &= C_3G_c^e + u_3G_u^e + C_1C_2G_{cc}^e + u_1u_2G_{uu}^e + (C_1u_2 + C_2u_1)G_{cu}^e \\
 &\quad + \frac{1}{6}\left(C_1^3G_{ccc}^e + 3C_1^2u_1G_{ccu}^e + 3C_1u_1^2G_{cuu}^e + u_1^3G_{uuu}^e\right) \\
 &\quad - \frac{D_1}{D_0}(C_1G_c^e + u_1G_u^e), \quad \text{on } x = 0, \\
 u_{3t} &= -u_{1T} + C_3F_c^e + u_3F_u^e + C_1C_2F_{cc}^e + u_1u_2F_{uu}^e + (C_1u_2 + C_2u_1)F_{cu}^e \\
 &\quad + \frac{1}{6}\left(C_1^3F_{ccc}^e + 3C_1^2u_1F_{ccu}^e + 3C_1u_1^2F_{cuu}^e + u_1^3F_{uuu}^e\right), \quad \text{on } x = 0.
 \end{aligned} \tag{4.6.8}$$

When  $D = D_0$ , (4.6.6) is assumed to have a complex conjugate pair of pure imaginary eigenvalues, and so we write

$$C_1(x, t, T) = A(T)e^{i\lambda_I t}\eta_0(x) + \text{c.c.}, \quad u_1(t, T) = A(T)e^{i\lambda_I t}\phi_0 + \text{c.c.}, \tag{4.6.9}$$

for some  $\lambda_I > 0$ . Here  $\eta_0(x)$  and  $\phi_0$  is the eigenpair associated with the linearized problem, and c.c. denotes the complex conjugate. An ODE for the unknown complex amplitude  $A(T)$  will be derived by imposing a non-resonance condition on the  $\mathcal{O}(\epsilon^3)$  system (4.6.8). To normalize the eigenpair, we impose for convenience that  $\eta_0(0) = 1$ .

Upon substituting (4.6.9) into (4.6.6), we obtain that  $\eta_0(x)$  and  $\phi_0$  satisfy

$$\begin{aligned}
 \eta_0'' - \frac{(1 + i\lambda_I\tau)}{D_0}\eta_0 &= 0, \quad 0 < x < L; \\
 D_0\eta_{0x}(0) &= G_c^e\eta_0(0) + G_u^e\phi_0, \quad \eta_{0x}(L) = 0, \\
 F_c^e\eta_0(0) + F_u^e\phi_0 &= i\lambda_I\phi_0, \quad \text{on } x = 0.
 \end{aligned} \tag{4.6.10}$$

We solve this system, and impose the normalization  $\eta_0(0) = 1$ , to obtain

$$\eta_0(x) = \frac{\cosh[\Omega_\lambda(L-x)]}{\cosh(\Omega_\lambda L)}, \quad \phi_0 = \frac{F_c^e}{i\lambda_I - F_u^e}, \quad \Omega_\lambda \equiv \sqrt{\frac{1 + i\tau\lambda_I}{D_0}}, \tag{4.6.11}$$

where we must take the principal value of the square root. From the condition for  $\eta_{0x}$  on  $x = 0$  in (4.6.10), we obtain that  $i\lambda_I$  is a root of the following transcendental equation, which occurs at the critical value  $D_0$  of  $D$ :

$$(D_0\Omega_\lambda \tanh(\Omega_\lambda L) + G_c^e)(i\lambda_I - F_u^e) + F_c^e G_u^e = 0. \tag{4.6.12}$$

The spectral problem (4.6.10) is a nonstandard eigenvalue problem since the eigenvalue parameter appears in both the differential operator as well as in the boundary condition on  $x = 0$ . Therefore, we cannot simply define the operator  $L = \frac{D_0}{\tau} \frac{d}{dx^2} - \frac{1}{\tau}$  and consider the problem as a special case of  $Lu = \lambda u$ , owing to the fact that the domain of  $L$  depends on  $\lambda$ . Instead, we must extend our definition of  $L$ , construct its adjoint and find an expansion theorem following the approach in [18] for treating non self-adjoint spectral problems with an eigenvalue-dependent boundary condition. This formalism will then allow for a systematic imposition of a solvability condition on the  $\mathcal{O}(\epsilon^3)$  problem (4.6.8), which leads to the amplitude equation for  $A(T)$ .

Motivated by the form of (4.6.10), we define an operator  $L$  acting on a two-component vector  $U \equiv (u(x), u_1)^T$  by

$$L \begin{pmatrix} u(x) \\ u_1 \end{pmatrix} \equiv \begin{pmatrix} \frac{D_0}{\tau} u''(x) - \frac{1}{\tau} u(x) \\ F_c^e u(0) + F_u^e u_1 \end{pmatrix}, \quad (4.6.13a)$$

where  $u(x)$  satisfies the boundary conditions

$$u_x(L) = 0, \quad D_0 u_x(0) = G_c^e u(0) + G_u^e u_1. \quad (4.6.13b)$$

The calculation in (4.6.11) shows that  $LU = i\lambda_I U$ , with normalization  $u(0) = 1$ , where  $U$  is given by

$$U = \begin{pmatrix} \frac{\cosh[\Omega_\lambda(L-x)]}{\cosh(\Omega_\lambda L)} \\ \frac{F_c^e}{i\lambda_I - F_u^e} \end{pmatrix}. \quad (4.6.14)$$

Next, we define an inner product of two vectors  $U \equiv (u(x), u_1)^T$  and  $V \equiv (v(x), v_1)^T$  by

$$\langle U, V \rangle \equiv \int_0^L u(x) \bar{v}(x) dx + u_1 \bar{v}_1, \quad (4.6.15)$$

where the overbar denotes complex conjugate, and where we restrict our attention to the subspace where

$$u_x(L) = 0, \quad D_0 u_x(0) = G_c^e u(0) + G_u^e u_1. \quad (4.6.16)$$

With this definition of the inner product, we integrate by parts to establish that  $\langle LU, V \rangle = \langle U, L^*V \rangle$ , in terms of an adjoint operator  $L^*$  defined by

$$L^*V \equiv \begin{pmatrix} \frac{D_0}{\tau} v''(x) - \frac{1}{\tau} v(x) \\ F_u^e v_1 - G_u^e v(0)/\tau \end{pmatrix}. \quad (4.6.17)$$

#### 4.6. Weakly Nonlinear Theory for Synchronous Oscillations

---

Here  $V$  is a two-component vector satisfying the adjoint boundary conditions

$$v_x(L) = 0, \quad D_0 v_x(0) = G_c^e v(0) - \tau F_c^e v_1. \quad (4.6.18)$$

A simple calculation shows that  $-i\lambda_I$  is also an eigenvalue of  $L^*$  (as expected), and that the eigenvector satisfying the adjoint problem  $L^*V = -i\lambda_I V$ , normalized by  $v(0) = 1$ , and where  $\Omega_\lambda$  is defined in (4.6.11), is

$$V = \begin{pmatrix} \frac{\cosh[\overline{\Omega}_\lambda(L-x)]}{\cosh(\overline{\Omega}_\lambda L)} \\ \frac{G_u^e}{\tau(F_u^e + i\lambda_I)} \end{pmatrix}. \quad (4.6.19)$$

With the determination of the solution to (4.6.6) now complete, we then proceed to the  $\mathcal{O}(\epsilon^2)$  system (4.6.7). We substitute (4.6.9) into (4.6.7) and separate variables to conclude that  $C_2(x, t, T)$  and  $u_2(t, T)$  must have the form

$$\begin{aligned} C_2(x, t, T) &= g_0(x, T) + g_1(x, T)e^{i\lambda_I t} + g_2(x, T)e^{2i\lambda_I t} + \text{c.c.}, \\ u_2(t, T) &= h_0(T) + h_1(T)e^{i\lambda_I t} + h_2(T)e^{2i\lambda_I t} + \text{c.c.}, \end{aligned} \quad (4.6.20)$$

where  $g_j(x, T)$  and  $h_j(T)$  for  $j = 0, 1, 2$  are to be determined. Since the problem for  $g_1$  and  $h_1$  is simply the linearized problem (4.6.6), without loss of generality we can take  $g_1 \equiv 0$  and  $h_1 \equiv 0$ . By comparing terms independent of powers of  $e^{i\lambda_I t}$ , we conclude, upon using  $\eta_0(0) = 1$ , that  $g_0$  and  $h_0$  are real-valued and satisfy

$$\begin{aligned} g_{0xx} - \frac{1}{D_0}g_0 &= -\frac{D_1}{D_0^2}C_e, \quad 0 < x < L; \quad g_{0x}(L) = 0, \\ Dg_{0x}(0) - (g_0(0)G_c^e + h_0G_u^e) &= |A|^2 \frac{\Pi_2}{2} - \frac{D_1}{D_0}G^e, \quad \text{on } x = 0, \\ g_0(0)F_c^e + h_0F_u^e &= -|A|^2 \frac{\Delta_2}{2} \quad \text{on } x = 0. \end{aligned} \quad (4.6.21a)$$

In the notation in (4.6.21a) we have suppressed the dependence of  $g_0$  on  $T$ . Here we have defined  $\Pi_2$  and  $\Delta_2$  by

$$\Pi_2 \equiv 2G_{cc}^e + 2|\phi_0|^2 G_{uu}^e + 4\text{Re}(\phi_0)G_{cu}^e, \quad \Delta_2 \equiv 2F_{cc}^e + 2|\phi_0|^2 F_{uu}^e + 4\text{Re}(\phi_0)F_{cu}^e, \quad (4.6.21b)$$

where  $|z|$  denotes the modulus of  $z$ . In a similar way, upon comparing  $e^{2i\lambda_I t}$

terms, we obtain that  $g_2$  and  $h_2$  satisfy

$$\begin{aligned} g_{2xx} - \frac{(1 + 2i\tau\lambda_I)}{D_0}g_2 &= 0, & 0 < x < L; & \quad g_{2x}(L) = 0, \\ Dg_{2x}(0) - (g_2(0)G_c^e + h_2G_u^e) &= |A|^2\frac{\Pi_1}{2}, & \text{on } x = 0, \\ g_2(0)F_c^e + h_2F_u^e - 2i\lambda_I h_2 &= -|A|^2\frac{\Delta_1}{2} & \text{on } x = 0, \end{aligned} \quad (4.6.22a)$$

and are complex-valued. Here, we have defined  $\Pi_1$  and  $\Delta_1$  by

$$\Pi_1 \equiv G_{cc}^e + \phi_0^2 G_{uu}^e + 2\phi_0 G_{cu}^e, \quad \Delta_1 \equiv F_{cc}^e + \phi_0^2 F_{uu}^e + 2\phi_0 F_{cu}^e. \quad (4.6.22b)$$

Next, we solve the problem (4.6.21) for  $g_0(x)$  and  $h_0$  explicitly. Since the inhomogeneous term proportional to  $C_e$  in the differential operator for  $g_0$  satisfies the homogeneous problem, we can readily determine the particular solution for (4.6.21a). With this observation, and after some algebra, we obtain that

$$g_0 = g_0^1 \cosh[\omega_0(L-x)] + \frac{P_0 D_1 L}{2\omega_0} \sinh[\omega_0(L-x)] - \frac{P_0 D_1}{2\omega_0} x \sinh[\omega_0(L-x)], \quad (4.6.23a)$$

where  $\omega_0 \equiv \sqrt{1/D_0}$  and  $P_0$  is defined by

$$P_0 \equiv -\frac{C_e^0}{D_0^2 \cosh(\omega_0 L)}. \quad (4.6.23b)$$

In (4.6.23a), the constant  $g_0^1$  is given by

$$g_0^1 = D_1 \chi_1 + |A|^2 \chi_2, \quad (4.6.23c)$$

where  $\chi_1$  and  $\chi_2$  are defined in terms of  $\Delta_2$  and  $\Pi_2$ , given in (4.6.21b), by

$$\chi_1 \equiv \frac{P_{03} G_u^e - P_{02} F_u^e}{P_{01} F_u^e - F_c^e G_u^e \cosh(\omega_0 L)}, \quad \chi_2 \equiv \frac{1}{2} \left( \frac{\Delta_2 G_u^e - \Pi_2 F_u^e}{P_{01} F_u^e - F_c^e G_u^e \cosh(\omega_0 L)} \right). \quad (4.6.23d)$$

Here the three new quantities  $P_{01}$ ,  $P_{02}$ , and  $P_{03}$ , are defined in terms of  $P_0$  of (4.6.23b), by

$$\begin{aligned} P_{01} &\equiv D_0 \omega_0 \sinh(\omega_0 L) + G_c^e \cosh(\omega_0 L), & P_{03} &\equiv F_c^e \left( \frac{P_0 L}{2\omega_0} \right) \sinh(\omega_0 L), \\ P_{02} &\equiv \frac{P_0 L}{2\omega_0} [D_0 \omega_0 \cosh(\omega_0 L) + G_c^e \sinh(\omega_0 L)] + \frac{P_0 D_0}{2\omega_0} \sinh(\omega_0 L) - \frac{G^e}{D_0}. \end{aligned} \quad (4.6.23e)$$

#### 4.6. Weakly Nonlinear Theory for Synchronous Oscillations

---

In addition, the real-valued constant  $h_0$  is given by in terms of  $P_0$ ,  $P_{01}$ ,  $P_{02}$ ,  $P_{03}$ ,  $\Pi_2$ , and  $\Delta_2$ , by

$$h_0 = D_1\chi_3 + |A|^2\chi_4, \quad (4.6.24a)$$

where  $\chi_3$  and  $\chi_4$  are defined by

$$\chi_3 \equiv \frac{P_{02}F_c^e \cosh(\omega_0 L) - P_{01}P_{03}}{P_{01}F_u^e - G_u^e F_c^e \cosh(\omega_0 L)}, \quad \chi_4 \equiv \frac{1}{2} \left( \frac{\Pi_2 F_c^e \cosh(\omega_0 L) - \Delta_2 P_{01}}{P_{01}F_u^e - G_u^e F_c^e \cosh(\omega_0 L)} \right). \quad (4.6.24b)$$

Finally, in our solvability condition for the amplitude equation to be derived below, we will need to evaluate  $g_0$  at  $x = 0$ . Upon using (4.6.23a) and (4.6.23c), we can write  $g_0(0)$  as

$$g_0(0) = D_1 g_{0c} + g_{0A} |A|^2; \quad (4.6.25)$$

$$g_{0c} \equiv \chi_1 \cosh(\omega_0 L) + \frac{P_0 L}{2\omega_0} \sinh(\omega_0 L), \quad g_{0A} \equiv \chi_2 \cosh(\omega_0 L).$$

Next, we solve the problem (4.6.22) for  $g_2$  and  $h_2$ . We readily calculate that

$$g_2(x) = g_2^0 \frac{\cosh[\Omega_{2\lambda}(L-x)]}{\cosh(\Omega_{2\lambda}L)}, \quad \Omega_{2\lambda} \equiv \sqrt{\frac{1+2i\tau\lambda_I}{D_0}},$$

where  $g_2^0$  and  $h_2$  satisfy the  $2 \times 2$  linear system

$$\begin{aligned} [D_0\Omega_{2\lambda} \tanh(\Omega_{2\lambda}L) + G_c^e] g_2^0 + G_u^e h_2 &= -\frac{\Pi_1}{2} A^2, \\ F_c^e g_2^0 + (F_u^e - 2i\lambda_I) h_2 &= -\frac{\Delta_1}{2} A^2. \end{aligned}$$

Here  $\Pi_1$  and  $\Delta_1$  are defined in (4.6.22b). By solving this linear system, we obtain that

$$g_2(0) \equiv g_2^0 = \chi_6 A^2, \quad h_2 = \chi_5 A^2, \quad (4.6.26a)$$

where  $\chi_5$  and  $\chi_6$  are defined by

$$\begin{aligned} \chi_5 &\equiv \frac{1}{2} \left( \frac{\Pi_1 F_c^e - \Delta_1 (D_0\Omega_{2\lambda} \tanh(\Omega_{2\lambda}L) + G_c^e)}{(D_0\Omega_{2\lambda} \tanh(\Omega_{2\lambda}L) + G_c^e) (F_u^e - 2i\lambda_I) - G_u^e F_c^e} \right), \\ \chi_6 &\equiv \frac{1}{2} \left( \frac{\Pi_1 (2i\lambda_I - F_u^e) + \Delta_1 G_u^e}{(D_0\Omega_{2\lambda} \tanh(\Omega_{2\lambda}L) + G_c^e) (F_u^e - 2i\lambda_I) - G_u^e F_c^e} \right). \end{aligned} \quad (4.6.26b)$$

With the solution of the  $\mathcal{O}(\epsilon^2)$  system (4.6.7) complete, we now proceed to the  $\mathcal{O}(\epsilon^3)$  problem (4.6.8), where the resonance term comes into play.

#### 4.6. Weakly Nonlinear Theory for Synchronous Oscillations

---

We substitute the expression of  $C_1, u_1$  and  $C_2, u_2$  from (4.6.9) and (4.6.20), respectively, into (4.6.8), and identify all terms that are proportional to  $e^{i\lambda_I t}$ . In order to eliminate resonance in (4.6.8), thereby ensuring that  $C_3(x, t, T)$  and  $u_3(t, T)$  remain bounded on asymptotically long time intervals of order  $t = \mathcal{O}(\epsilon^{-1})$ , we require that the coefficients of the  $e^{i\lambda_I t}$  terms satisfy a certain compatibility condition. This leads to an amplitude equation for  $A(T)$ .

To derive this amplitude equation, we substitute

$$\begin{aligned} C_3(x, t, T) &= C_4(x, T) + C_3(x, T)e^{i\lambda_I t} + C_2(x, T)e^{2i\lambda_I t} + C_1(x, T)e^{3i\lambda_I t} + \text{c.c.}, \\ u_3(t, T) &= U_4(T) + U_3(T)e^{i\lambda_I t} + U_2(T)e^{2i\lambda_I t} + U_1(T)e^{3i\lambda_I t} + \text{c.c.}, \end{aligned} \quad (4.6.27)$$

together with (4.6.9) and (4.6.20) into (4.6.8), to obtain, after a lengthy but straightforward calculation, that  $C_3, U_3$  satisfy

$$L \begin{pmatrix} C_3 \\ U_3 \end{pmatrix} \equiv \begin{pmatrix} \frac{D_0}{\tau} C_{3xx} - \frac{1}{\tau} C_3 \\ F_c^e C_3(0) + F_u^e U_3 \end{pmatrix} = i\lambda_I \begin{pmatrix} C_3 \\ U_3 \end{pmatrix} + \begin{pmatrix} \mathcal{R}_1 \\ A'\phi_0 - \mathcal{R}_3 \end{pmatrix}, \quad 0 < x < L, \quad (4.6.28a)$$

where  $C_3(x)$  satisfies the boundary conditions

$$C_{3x}(L) = 0, \quad D_0 C_{3x}|_{x=0} - [G_c^e C_3(0) + G_u^e U_3] = \mathcal{R}_2. \quad (4.6.28b)$$

In the notation of (4.6.28) we have suppressed the dependence of  $C_3$  on  $T$ . In (4.6.28),  $\mathcal{R}_1$  is defined by

$$\mathcal{R}_1 \equiv A'\eta_0 - \frac{D_1}{D_0\tau} (1 + i\tau\lambda_I) A\eta_0, \quad (4.6.29a)$$

and the residuals  $\mathcal{R}_2$  and  $\mathcal{R}_3$  have the form

$$\mathcal{R}_2 = D_1 A \mathcal{R}_{20} + A|A|^2 \mathcal{R}_{21}, \quad \mathcal{R}_3 = D_1 A \mathcal{R}_{30} + A|A|^2 \mathcal{R}_{31}. \quad (4.6.29b)$$

The coefficients  $\mathcal{R}_{20}$  and  $\mathcal{R}_{30}$  of the linear term in  $A$  are

$$\begin{aligned} \mathcal{R}_{20} &\equiv g_{0c} G_{cc}^e + \phi_0 \chi_3 G_{uu}^e + \phi_0 g_{0c} G_{cu}^e + \chi_3 G_{cu}^e - \frac{1}{D_0} (G_c^e + \phi_0 G_u^e), \\ \mathcal{R}_{30} &\equiv g_{0c} F_{cc}^e + \phi_0 \chi_3 F_{uu}^e + \phi_0 g_{0c} F_{cu}^e + \chi_3 F_{cu}^e, \end{aligned} \quad (4.6.29c)$$

where  $g_{0c}$ ,  $\chi_3$ , and  $\phi_0$ , are defined in (4.6.25), (4.6.24b), and (4.6.11), respectively. In addition, the coefficients  $\mathcal{R}_{21}$  and  $\mathcal{R}_{31}$  of the cubic term in

(4.6.29b) are given by

$$\begin{aligned} \mathcal{R}_{21} \equiv & \frac{1}{2} \left[ G_{ccc}^e + G_{uuu}^e \phi_0^2 \bar{\phi}_0 + G_{ccu}^e (\bar{\phi}_0 + 2\phi_0) + G_{cuu}^e (\phi_0^2 + 2\phi_0 \bar{\phi}_0) \right] \\ & + g_{0A} G_{cc}^e + \chi_6 G_{cc}^e + \phi_0 \chi_4 G_{uu}^e + \bar{\phi}_0 \chi_5 G_{uu}^e \\ & + G_{cu}^e (\phi_0 g_{0A} + \bar{\phi}_0 \chi_6 + \chi_4 + \chi_5), \end{aligned} \quad (4.6.29d)$$

and

$$\begin{aligned} \mathcal{R}_{31} \equiv & \frac{1}{2} \left[ F_{ccc}^e + F_{uuu}^e \phi_0^2 \bar{\phi}_0 + F_{ccu}^e (\bar{\phi}_0 + 2\phi_0) + F_{cuu}^e (\phi_0^2 + 2\phi_0 \bar{\phi}_0) \right] \\ & + g_{0A} F_{cc}^e + \chi_6 F_{cc}^e + \phi_0 \chi_4 F_{uu}^e + \bar{\phi}_0 \chi_5 F_{uu}^e + F_{cu}^e (\phi_0 g_{0A} + \bar{\phi}_0 \chi_6 + \chi_4 + \chi_5). \end{aligned} \quad (4.6.29e)$$

In (4.6.29d) and (4.6.29e), the quantities  $g_{0A}$ ,  $\chi_3$ ,  $\chi_4$ ,  $\chi_5$ , and  $\chi_6$  are defined in (4.6.25), (4.6.24b), and (4.6.26b).

The following lemma, consisting of a compatibility relation between  $\mathcal{R}_1$ ,  $\mathcal{R}_2$ , and  $\mathcal{R}_3$ , provides a necessary condition for the existence of a solution to (4.6.28).

**Lemma 4.6.1** *A necessary condition for (4.6.28) to have a solution is that  $A(T)$  satisfies*

$$A' \left[ \int_0^L \eta_0 \bar{v} dx + \phi_0 \bar{v}_1 \right] = \frac{D_1}{D_0 \tau} (1 + i\tau \lambda_I) A \int_0^L \eta_0 \bar{v} dx + \bar{v}_1 \mathcal{R}_3 - \mathcal{R}_2 / \tau, \quad (4.6.30)$$

where  $V \equiv (v, v_1)^T$  is the nontrivial solution, given in (4.6.19), to the homogeneous adjoint problem  $L^*V = -i\lambda_I V$ .

**Proof:** We define  $U \equiv (\mathcal{C}_3, U_3)^T$ , and we calculate from (4.6.28), and the definition of the inner product in (4.6.15), that

$$\langle LU - i\lambda_I U, V \rangle = \int_0^L \mathcal{R}_1 \bar{v} dx + (A' \phi_0 - \mathcal{R}_3) \bar{v}_1. \quad (4.6.31)$$

We then integrate by parts on the left-hand side of (4.6.31), and use the boundary conditions for  $v$  and  $\mathcal{C}_3$  from (4.6.18) and (4.6.28b), respectively.

In this way, we obtain

$$\begin{aligned}
 \langle LU - i\lambda_I U, V \rangle &= \int_0^L \left( \frac{D_0}{\tau} \bar{v}_{xx} - \frac{\bar{v}}{\tau} \right) \mathcal{C}_3 dx + [F_c^e \mathcal{C}_3(0) + F_u^e U_3] \bar{v}_1 \\
 &\quad + \frac{D_0}{\tau} [\mathcal{C}_3(0) \bar{v}_x(0) - \mathcal{C}_{3x}(0) \bar{v}(0)] - i\lambda_I \langle U, V \rangle \\
 &= \int_0^L \left( \frac{D_0}{\tau} \bar{v}_{xx} - \frac{\bar{v}}{\tau} \right) \mathcal{C}_3 dx + \left( \bar{v}_1 F_u^e - \frac{1}{\tau} \bar{v}(0) G_u^e \right) U_3 \\
 &\quad - \frac{\bar{v}(0)}{\tau} \mathcal{R}_2 - i\lambda_I \langle U, V \rangle, \\
 &= \langle U, L^* V + i\lambda_I V \rangle - \frac{\bar{v}(0)}{\tau} \mathcal{R}_2.
 \end{aligned} \tag{4.6.32}$$

To obtain the compatibility condition, we compare (4.6.31) with (4.6.32) and use  $L^*V + i\lambda_I V = 0$ . By substituting (4.6.29a) for  $\mathcal{R}_1$  into this condition, and recalling that  $v(0) = 1$ , we readily obtain (4.6.30). ■

Finally, upon substituting (4.6.29) into (4.6.30), we obtain the following amplitude equation for  $A(T)$ :

$$A' = D_1 b_1 A + b_2 A^2 \bar{A}, \tag{4.6.33a}$$

where the complex-valued coefficients  $b_1$  and  $b_2$ , which are independent of  $D_1$ , are given by

$$b_1 \equiv \frac{1}{\mathcal{N}} \left[ \frac{(1 + i\tau\lambda_I)}{D_0\tau} \int_0^L \eta_0 \bar{v} dx + \bar{v}_1 \mathcal{R}_{30} - \mathcal{R}_{20}/\tau \right], \quad b_2 \equiv \frac{1}{\mathcal{N}} [\bar{v}_1 \mathcal{R}_{31} - \mathcal{R}_{21}/\tau], \tag{4.6.33b}$$

where we have defined  $\mathcal{N}$  by

$$\mathcal{N} \equiv \left[ \int_0^L \eta_0 \bar{v} dx + \phi_0 \bar{v}_1 \right]. \tag{4.6.33c}$$

In (4.6.33b), the coefficients  $\mathcal{R}_{20}$ ,  $\mathcal{R}_{30}$ ,  $\mathcal{R}_{21}$ , and  $\mathcal{R}_{31}$ , are defined in (4.6.29c), (4.6.29d), and (4.6.29e). Moreover,  $v(x)$  and  $v_1$  are the components of the adjoint eigenfunction  $V$ , satisfying  $L^*V = -i\lambda_I V$ , given in (4.6.19).

The ODE (4.6.33a), commonly referred to as the Stuart-Landau equation, characterizes the weakly nonlinear behavior of the oscillation near the critical stability threshold. We write  $A$  as  $A = r e^{i\theta}$  and decompose  $b_1$  and  $b_2$  into real and imaginary parts as  $b_1 = b_{1R} + i b_{1I}$  and  $b_2 = b_{2R} + i b_{2I}$ . From (4.6.33a), we obtain that  $r$  and  $\theta$  satisfy

$$r' = r \left( D_1 b_{1R} + b_{2R} r^2 \right), \quad \theta' = D_1 b_{1I} + b_{2I} r^2. \tag{4.6.34}$$

The fixed points in  $r$ , when they exist, correspond to periodic solutions for A. These special solutions are

$$r_e = \sqrt{-\frac{b_{1R}D_1}{b_{2R}}}; \quad \theta = \tilde{\theta}T, \quad \tilde{\theta} \equiv D_1b_{1I} + b_{2I}r_e^2. \quad (4.6.35)$$

For  $\epsilon \rightarrow 0$ , and with  $D - D_0 = \epsilon^2 D_1$ , we conclude from (4.6.4), (4.6.9), and (4.6.35), that there is a periodic solution near the Hopf bifurcation point of the form

$$\begin{pmatrix} C(x, t, T) \\ u(t, T) \end{pmatrix} \sim \begin{pmatrix} C_e(x) \\ u_e \end{pmatrix} + \epsilon \left[ r_e e^{i(\lambda_I + \epsilon^2 \tilde{\theta})t} \begin{pmatrix} \eta_0(x) \\ \phi_0 \end{pmatrix} + \text{c.c.} \right]. \quad (4.6.36)$$

The analysis of the amplitude equation (4.6.34) is routine, and depends on the signs of  $b_{1R}$  and  $b_{2R}$ . The Hopf bifurcation is supercritical when  $b_{2R} < 0$  and is subcritical if  $b_{2R} > 0$ . More precisely, if  $b_{1R} > 0$ , the symmetric steady-state solution  $(C_e(x), u_e)$  is linearly stable if  $D_1 < 0$  and is unstable if  $D_1 > 0$ . An unstable branch of periodic solutions exists in the region  $D_1 < 0$  if  $b_{2R} > 0$  (subcritical Hopf). If  $b_{2R} < 0$ , then there is a stable periodic solution branch in the region  $D_1 > 0$  (supercritical Hopf). In contrast, if  $b_{1R} < 0$ , the symmetric steady-state solution  $(C_e(x), u_e)$  is linearly stable if  $D_1 > 0$  and is unstable if  $D_1 < 0$ . An unstable branch of periodic solutions exists in the region  $D_1 > 0$  if  $b_{2R} > 0$  (subcritical Hopf). If  $b_{2R} < 0$ , there is a stable periodic solution branch for  $D_1 < 0$  (supercritical Hopf).

**Remark 4.6.1** *A similar weakly nonlinear analysis can be done to determine whether an asynchronous periodic solution branch is subcritical or supercritical at the Hopf bifurcation point. To consider this case, we simply replace the no-flux condition at  $x = L$  for  $\eta(x)$ ,  $v(x)$ , and  $C_j(x)$  for  $j = 1, \dots, 3$  with a homogeneous Dirichlet condition. We do not carry out the details of this calculation here.*

#### 4.6.1 Numerical Validation of the Weakly Nonlinear Theory With the Explicitly Solvable Model

We now apply our weakly nonlinear theory to the explicitly solvable model system of §4.4.2, where  $G(C(0, t), u)$  and  $F(C(0, t), u)$  are given in (4.4.6). Since, for this example,  $F(C(0, t), u)$  is linear in its variables, the only nonlinearity in (4.6.1) arises from  $G(C(0, t), u)$ . In our analysis, we will focus

on periodic solutions that bifurcate from the steady-state solution branch where  $C_e^0 \equiv C_e(0)$  is positive, and given explicitly in (4.4.8). For this system we compare predictions from the amplitude equation (4.6.33) with full numerical results computed from the numerical bifurcation software XPPAUT (cf. [16]). The numerical procedure used to compute these bifurcation diagrams is described in §4.4.

Treating  $D$  as the main bifurcation parameter we numerically computed steady-state and periodic solution branches of (4.6.1) for two values of  $\gamma$ . In our numerical experiments, we found that a periodic solution bifurcates via a Hopf bifurcation from the positive steady-state solution branch. As shown in Fig. 4.11, by tuning the parameter  $\gamma$ , while holding the other parameters fixed, the Hopf bifurcation was found to change from supercritical to subcritical.

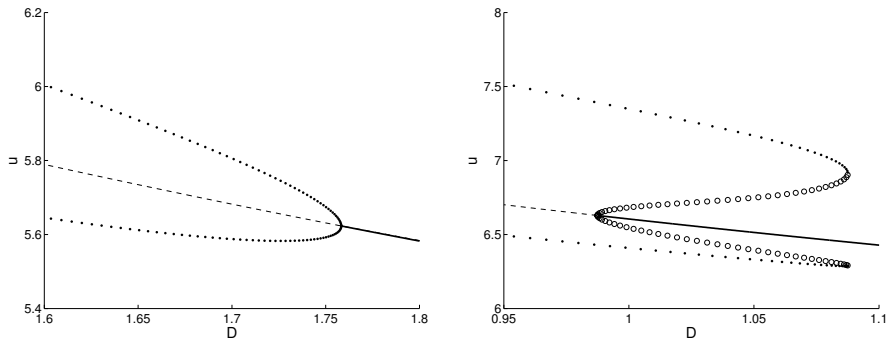


Figure 4.11: Bifurcation diagrams with diffusivity  $D$  as bifurcation parameter showing either a supercritical or subcritical Hopf bifurcation structure for (4.6.1), with coupling functions given in (4.4.6), for two values of  $\gamma$ . Left panel:  $\gamma = 1.55$  (supercritical). Right panel:  $\gamma = 1.7$  (subcritical). The solid and dashed lines represent stable and unstable steady-state solutions, respectively. Open circles indicate the max/min amplitude of unstable periodic solutions, while the solid dots correspond to linearly stable periodic solution branches. The bulk diffusion parameters are  $\tau = 0.1$  and  $L = 5$ . The membrane kinetic and coupling parameters are  $\beta = 1$  and  $\kappa = 12$ .

By using the amplitude equation (4.6.33), our weakly nonlinear asymptotic theory predicts that the switching point from a supercritical to a subcritical Hopf bifurcation occurs at  $\gamma = 1.628$  (accurate to three decimal places), which agrees with the corresponding numerical result. Furthermore, the amplitude equation also allow us to approximate the solution near the

Hopf bifurcation point as shown in (4.6.36). For the local variable  $u(t)$ , we obtain from (4.6.36) that the amplitude of the periodic solution can be written as

$$|u(t, T) - u_e| = \epsilon r_e |e^{i(\lambda_I + \epsilon^2 \tilde{\theta})t} \phi_0 + \text{c.c.}| = 2\epsilon r_e |\phi_0|, \quad (4.6.37)$$

where  $r_e$  is the fixed point of the amplitude equation given in (4.6.35). Here  $\epsilon \ll 1$  and  $\phi_0$  is the eigenfunction of  $u(t)$ , given explicitly in (4.6.11). If we define  $u_{\text{amp}} \equiv |u(t, T) - u_e|$  and plot  $u_{\text{amp}}$  versus the diffusivity  $D$ , then  $u_{\text{amp}}$  should be proportional to  $\epsilon \equiv \sqrt{D - D_0}$  in the vicinity of the Hopf bifurcation point  $D_0$ . The quantity  $u_{\text{amp}}$  is plotted in Fig. 4.12.

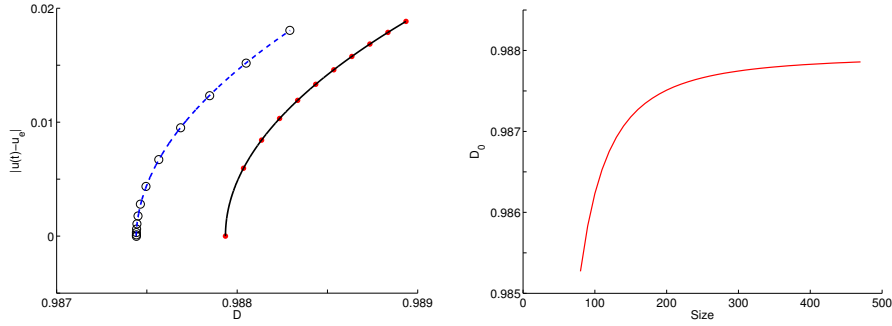


Figure 4.12: Left panel: Comparison of bifurcation diagrams near a subcritical Hopf bifurcation obtained from full numerics and from the weakly nonlinear analysis. Red dots represent the amplitude of the unstable periodic solution  $u_{\text{amp}}$  (see the text) obtained from the amplitude equation (4.6.33) and the black circles are from the full numerical simulations. The black and blue curves are the corresponding fitted parabola and the curvature of the two curves are 5.6 (black) and 5.0 (blue), respectively, at the Hopf bifurcation point  $D_0 = 0.9879$  (red dots) and  $D_0 = 0.9874$  (black circles). The computations are done with 80 interior spatial meshpoints. Right panel: Plot of the Hopf bifurcation point  $D_0$  versus the number of spatial meshpoints of the discretized system. The parameter values are the same as those used in Fig. 4.11 with  $\gamma = 1.7$ .

The left panel of Fig. 4.12 shows a comparison between the analytical and numerical bifurcation diagrams near a subcritical Hopf bifurcation point  $D_0$ . In our numerical experiments, since we discretized the PDE-ODE system (4.6.1), with coupling functions (4.4.6), with finite differences into a system of ODE's, some error is incurred in predicting the location of the

Hopf bifurcation value  $D_0$ . In contrast, in the implementation of the weakly nonlinear theory we solved the transcendental equation (4.6.12) for a complex conjugate pair of imaginary eigenvalues and  $D_0$  directly. Therefore, the  $D_0$  calculated from (4.6.12) is more accurate than the one computed from the numerics and it results in the shifting of the bifurcation point  $D_0$ , as shown in the left panel of Fig. 4.12. The right panel of Fig. 4.12 shows how the numerically calculated value  $D_0$  shifts towards the more accurate value, computed from (4.6.12), when we increase the number of spatial meshpoints in the discretized system. Although, there is a small difference in predicting the value of  $D_0$ , the amplitude calculated by the weakly nonlinear theory shows good agreement with the corresponding amplitude computed from the numerical bifurcation software, as evidenced by the close comparison of the curvature of the two curves in Fig. 4.12 at  $D = D_0$ .

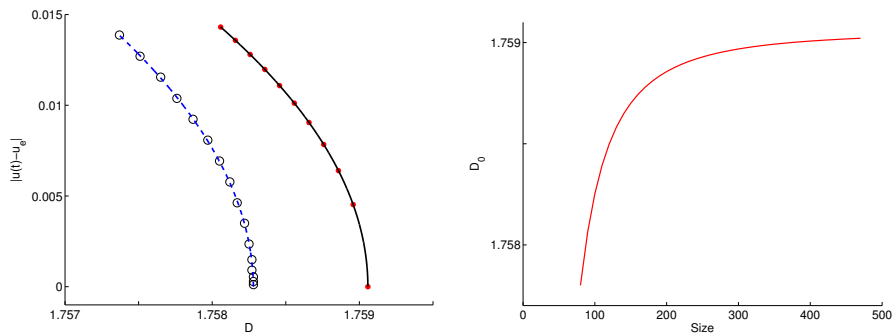


Figure 4.13: Left panel: Comparison of bifurcation diagrams near a supercritical Hopf bifurcation obtained from full numerics and from the weakly nonlinear analysis. The notations are the same as those in Fig. 4.12 except now the red dots and black circles represent the stable periodic solution branch. The curvature of the two curves are 9.8 (black) and 9.3 (blue), respectively, at the Hopf bifurcation point  $D_0 = 1.7591$  (red dots) and  $D_0 = 1.7583$  (black circles). The computations are done with 80 interior spatial meshpoints. Right panel: Plot of the Hopf bifurcation point  $D_0$  versus the number of spatial meshpoints of the discretized system. The parameter values are the same as those used in Fig. 4.11 with  $\gamma = 1.55$ .

Fig. 4.13 compares the numerical bifurcation diagram with the asymptotic prediction near a supercritical Hopf bifurcation point  $D_0$ . The amplitude of the stable periodic orbits calculated by the weakly nonlinear theory and the numerical simulations are seen to compare favorably. The right

panel of Fig. 4.13 shows that the numerically calculated Hopf bifurcation point shifts toward the more accurate value as the number of interior mesh-points increase.

In Fig. 4.11, we observe that when  $\gamma = 1.7$  the system (4.6.1), with coupling functions (4.4.6), undergoes a subcritical Hopf bifurcation at  $D_0 = 0.9879$ . In Fig. 4.14 we show that as  $D$  is decreased slowly below  $D_0$  on the range from 1 to 0.95, that there is a delayed bifurcation effect whereby the transition from stable steady-state to stable periodic orbits occurs when  $D$  is somewhat below the critical value  $D_0$  predicted from the bifurcation analysis. For our choice  $D = 1 - \sigma t$ , where  $\sigma = 0.0001$ , we plot  $D$  versus  $t$  in the left panel of Fig. 4.14. The method of lines and the forward Euler method is then used to solve (4.6.1), with coupling functions as given in (4.4.6). In the right panel of Fig. 4.14 we plot the numerically computed  $u(t)$  versus  $D(t)$ , which clearly illustrates the delayed transition to the periodic state.

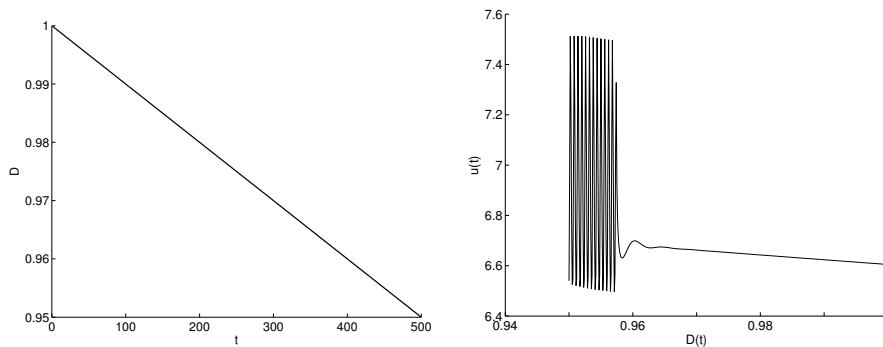


Figure 4.14: Left panel: Plot the diffusivity  $D$  as a function of time for  $D = 1 - \sigma t$ , where  $\sigma = 0.0001$ . Right panel: Plot of the local variable  $u(t)$  versus  $D(t)$ . As  $D$  passes slowly below the critical value  $D_0$ , the periodic solution appears when  $D$  is around 0.965, which due to the delayed bifurcation effect is less than the theoretically predicted value. The parameter values used are the same as in the right panel of Fig. 4.11.

#### 4.6.2 Numerical Validation of the Weakly Nonlinear Theory With the *Dictyostelium* Model

In the following, we apply our weakly nonlinear theory to the model of cell signaling in *Dictyostelium* studied in §4.4.4, where  $G(C(0, t), u)$  and  $F(C(0, t), u)$  are given in (4.4.21).

Similar to the analysis done in §4.6.1, we will compare predictions from the amplitude equation (4.6.33) with full numerical results computed from the numerical bifurcation software XPPAUT (cf. [16]). We use the diffusion coefficient  $D$  as the bifurcation parameters, numerically compute steady state and the synchronous periodic solution branches. One typical bifurcation diagram of this system is given in the left panel of Fig. 4.7. We observe that when  $D$  is gradually decreasing from 0.65, the steady state solution becomes unstable at the Hopf bifurcation point  $D_0 \approx 0.62$  and an unstable synchronous periodic solution appears, which indicates a subcritical Hopf bifurcation.

In Fig. 4.7, the vertical axis represents the value of the global variable  $C(x, t)$  near the membrane  $x = 0$ . Then from (4.6.36), we readily calculate the amplitude of the periodic solution can be written as

$$|C(0, t, T) - C_e(0)| = \epsilon r_e |e^{i(\lambda_I + \epsilon^2 \tilde{\theta})t} \eta_0(0) + \text{c.c.}| = 2\epsilon r_e |\eta_0(0)|, \quad (4.6.38)$$

where  $r_e$  is the fixed point of the amplitude equation given in (4.6.35).  $\epsilon \ll 1$  and  $\eta_0(0)$  is the eigenfunction of  $C(x, t)$  evaluated at  $x = 0$ . Similarly, we define  $c_{\text{amp}} \equiv |C(0, t, T) - C_e(0)|$  and plot  $c_{\text{amp}}$  versus the diffusivity  $D$ , then  $c_{\text{amp}}$  should be proportional to  $\epsilon \equiv \sqrt{D - D_0}$  in the vicinity of the Hopf bifurcation point  $D_0$ . The left panel of Fig. 4.15 shows the plot of  $c_{\text{amp}}$  versus  $D$  in the neighborhood of  $D_0$ . The amplitude of the unstable periodic orbits calculated by the weakly nonlinear theory and the numerical simulations are seen to compare favorably. In the right panel of Fig. 4.15 we observe the value of the Hopf bifurcation  $D_0$  is gradually approaching a horizontal asymptote when the number of spatial meshpoints of the discretized system increases.

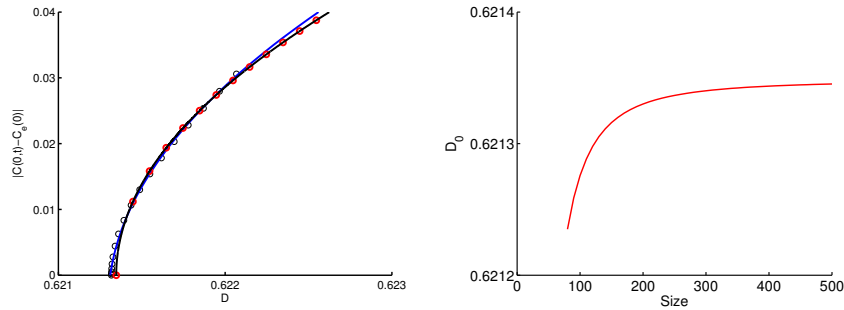


Figure 4.15: Left panel: Comparison of bifurcation diagrams near a sub-critical Hopf bifurcation obtained from full numerics and from the weakly nonlinear analysis. The notation are the same as those in Fig. 4.12. The curvature of the two curves are 0.63(black) and 0.77(blue), respectively at the Hopf bifurcation point  $D_0 = 0.62134$ (red dots) and  $D_0 = 0.62132$ (black dots). The computations are done with 100 interior spatial meshpoints. Right panel: Plot of the Hopf bifurcation point  $D_0$  versus the number of spatial meshpoints of the discretized system. The parameter values are the same as those used in the left panel of Fig. 4.7.

## Chapter 5

# A Model of Bulk-Diffusion Coupled to Active Membranes With Slow-Fast Kinetics

In a previous work [23] by Gomez et. al, a model of coupled active membranes with activator-inhibitor dynamics is proposed. They use numerical simulations together with nullcline analysis to explore different oscillatory patterns that the system possessed and predict the stability boundary of the steady state of the system.

The goal of this chapter is to give a detailed analysis of the triggering of synchronous oscillations for the coupled 1-D coupled membrane-bulk model of [23]. This chapter proceeds as follows.

In §5.1, we restate the model system constructed in [23] and give a review of the nullcline analysis in the slow-fast limit where the time scale of the activator and inhibitor dynamics are largely distinct. In §5.2 we construct a symmetric steady-state solution, and we formulate the linear stability problem for this solution. In §5.3 we consider a one-bulk species model where only the inhibitor  $V$  can diffuse in the bulk. For this case, in §5.3.1 an asymptotic analysis for  $\epsilon \rightarrow 0$  of the stability problem is provided to analyze Hopf bifurcations of the symmetric steady-state and the emergence of asymmetric steady-states. The  $\epsilon = \mathcal{O}(1)$  problem for one diffusing bulk species is studied numerically in §5.3.2. In §5.4 we extend our analysis to the full model which consists of two diffusing bulk species.

### 5.1 Coupled Membrane-bulk Model With Activator-Inhibitor Dynamics

The coupled membrane-bulk model of [23] on a one-dimensional spatial domain consists of two active membranes with activator-inhibitor dynamics

### 5.1. Coupled Membrane-bulk Model With Activator-Inhibitor Dynamics

---

at  $x = 0$  and  $x = L$  that are coupled through passive diffusion in the bulk region  $0 < x < L$ . In the bulk we assume that there are two diffusing species with concentrations  $U(x, t)$  and  $V(x, t)$  satisfying

$$U_t = D_u U_{xx} - \sigma_u U, \quad V_t = D_v V_{xx} - \sigma_v V, \quad 0 < x < L, \quad t > 0. \quad (5.1.1a)$$

Here  $D_u$  and  $D_v$  are the two diffusion coefficients, while  $\sigma_u$  and  $\sigma_v$  are the constant bulk decay rates. The kinetics on the two active membranes at  $x = 0$  and  $x = L$  are assumed to be identical, and given by

$$\begin{aligned} u'_1 &= f(u_1, v_1) + k_u U_x(0, t), & v'_1 &= \epsilon g(u_1, v_1) + k_v V_x(0, t), \\ u'_2 &= f(u_2, v_2) - k_u U_x(L, t), & v'_2 &= \epsilon g(u_2, v_2) - k_v V_x(L, t), \end{aligned} \quad (5.1.1b)$$

where  $u_i$  and  $v_i$ ,  $i = 1, 2$  denote the two concentrations on the membrane, so that  $u_1(t) = U(0, t)$ ,  $u_2(t) = U(L, t)$ ,  $v_1(t) = V(0, t)$  and  $v_2 = V(L, t)$ . The parameter  $\epsilon$  that accompanies  $g(u_i, v_i)$  determines the relative difference in the time-scale for the boundary kinetics, so that the time evolution of  $u$  is much faster than  $v$  if  $0 < \epsilon \ll 1$ . The terms  $k_u U_x(0, t)$  and  $k_v V_x(0, t)$  account for the exchange of species between the membrane and the bulk, where the constants  $k_u$  and  $k_v$  are the coupling strengths. The kinetics  $f(u, v)$  and  $g(u, v)$  are chosen to account for a local activator-inhibitor dynamics, and we use the Fitzhugh-Nagumo type kinetics considered in [23], given for  $q > 0$  and  $z > 0$  by

$$f(u, v) = u - q(u - 2)^3 + 4 - v, \quad g(u, v) = uz - v. \quad (5.1.1c)$$

The qualitative mechanism, as discussed in [23], for the triggering of time-periodic solutions for the coupled system (5.1.1) in the slow-fast limit  $\epsilon \rightarrow 0$  is based on a simple nullcline analysis, and is described in the caption of Fig. 5.1. We assume that the parameters  $q$  and  $z$  are chosen so that the membrane kinetics in the absence of any coupling to the bulk has a single stable equilibrium point. For  $q = 5$  and  $z = 3.5$ , this stable fixed point  $(u_e, v_e)$  occurs at the intersection of the two nullclines  $v = \mathcal{V}(u) = u - q(u - 2)^3 + 4$  and  $v = zu$  where  $f(u, \mathcal{V}(u)) = 0$  and  $g(u, zu) = 0$ . In the limit  $\epsilon \rightarrow 0$ , it is readily shown from the Jacobian of the membrane kinetics that the equilibrium state  $(u_e, v_e)$  is linearly stable only when  $\mathcal{V}'(u_e) < 0$ , and undergoes a Hopf bifurcation when  $\mathcal{V}'(u_e)$  crosses through zero. For a coupling strength in (5.1.1b) for which  $k_u = O(\epsilon)$  and  $k_v = O(\epsilon)$ , it readily follows, to leading order in  $\epsilon$ , that the steady-state of (5.1.1b) remains on the nullcline  $f(u, v) = 0$ . However, the effect of the coupling to the bulk for  $V$  is to shift the nullcline for the  $v$ -component in (5.1.1b) to  $v = \beta u$ , for some  $\beta$

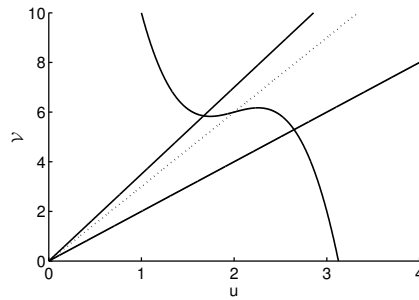


Figure 5.1: Plot of the nullcline  $\mathcal{V}(u) = u - q(u-2)^3 + 4$  with  $q = 5$  for which  $f(u, \mathcal{V}(u)) = 0$ . The straight lines are  $v = \beta u$  with  $\beta = 3.5$ ,  $\beta = 3$ , and  $\beta = 2$ . The straight line  $v = 3.5u$  is the nullcline of  $g(u, v) = 0$  when  $z = 3.5$  for the uncoupled membrane-bulk problem. As the bulk-coupling strength  $k_v = O(\epsilon)$  increases, the effective parameter  $\beta$  decreases. The dotted line with  $\beta = 3$  intersects  $\mathcal{V}(u)$  in the unstable region where  $\mathcal{V}'(u) > 0$ . For  $\beta = 2.0$ , the intersection again occurs in the stable region for the membrane kinetics. For a coupling strength where  $k_u = O(\epsilon)$  in (5.1.1b) the nullcline for  $f(u, v) = 0$  is, to leading order in  $\epsilon$ , unchanged by the coupling of the membrane to the bulk.

## 5.2. *The Steady-State Solution and the Formulation of the Linear Stability Problem*

---

that is a monotonically decreasing function of  $k_v$ . This shows that there is an intermediate range of  $\beta$  where the equilibrium point is unstable, such as given by the dotted line in Fig. 5.1. Although this mechanism of [23] does provide a clear qualitative reason underlying the triggering of oscillations induced by membrane-bulk coupling in the limit  $\epsilon \rightarrow 0$ , it does not provide a detailed quantitative characterization of these oscillations.

As an extension of this qualitative and numerical analysis of [23], we use asymptotic analysis together with bifurcation and stability theory to give a detailed theoretical analysis of the onset of oscillatory dynamics for (5.1.1). In the singular limit  $\epsilon \rightarrow 0$  of slow-fast membrane dynamics, and assuming only one diffusing species in the bulk, our stability analysis of the unique symmetric steady-state solution will provide a detailed phase diagram in parameter space where various types of oscillatory dynamics can occur. In the limit  $\epsilon \rightarrow 0$ , our asymptotic analysis of the spectral problem, and in particular the winding number, will yield asymptotic approximations for the Hopf bifurcation thresholds in parameter space for both the synchronous and asynchronous periodic solution branches, as well as the Hopf bifurcation frequencies near onset. In addition, zero-eigenvalue crossings corresponding to the emergence of asymmetric steady-state solutions will be studied. In the non-singular case, where  $\epsilon = \mathcal{O}(1)$ , a numerical study of the winding number together with the numerical bifurcation software XPPAUT [16] will be used to construct global bifurcation diagrams of steady-states and periodic solution branches for the case of either one or two diffusing species in the bulk. Overall, we show that stable synchronous oscillations between the two membranes is a robust feature of the dynamics that occurs in a wide parameter regime. A glimpse at some more exotic dynamics such as a torus bifurcation, arising from secondary bifurcations, is given.

## **5.2 The Steady-State Solution and the Formulation of the Linear Stability Problem**

In this section we determine a symmetric steady-state solution for (5.1.1) and analyze the linear stability properties of this solution. Since the two membranes are identical, it is natural to seek a steady-state solution that is symmetric about the midline  $x = L/2$ , so that for the steady-state problem of (5.1.1) we consider  $0 < x < L/2$  and impose zero flux conditions at  $x = L/2$ . In the steady-state analysis, for convenience we drop the subscripts for  $u$  and  $v$  at the left membrane. As such, the symmetric steady-state

## 5.2. The Steady-State Solution and the Formulation of the Linear Stability Problem

solution  $U_e$  and  $V_e$  for (5.1.1) satisfies

$$D_u U_{exx} - \sigma_u U_e = 0, \quad D_v V_{exx} - \sigma_v V_e = 0, \quad 0 < x < L/2, \quad (5.2.1)$$

with boundary conditions  $U_e(0) = u_e$ ,  $V_e(0) = v_e$ ,  $U_{ex}(L/2) = 0$ , and  $V_{ex}(L/2) = 0$ . The solution to this problem is

$$\begin{aligned} U_e(x) &= u_e \frac{\cosh\left[\omega_u\left(\frac{L}{2} - x\right)\right]}{\cosh(\omega_u L/2)}, & \omega_u &\equiv \sqrt{\frac{\sigma_u}{D_u}}, \\ V_e(x) &= v_e \frac{\cosh\left[\omega_v\left(\frac{L}{2} - x\right)\right]}{\cosh(\omega_v L/2)}, & \omega_v &\equiv \sqrt{\frac{\sigma_v}{D_v}}. \end{aligned} \quad (5.2.2)$$

Then, by using (5.1.1b) with kinetics (5.1.1c), we readily derive that  $u = u_e$  is a root of the cubic  $\mathcal{H}(u) = 0$ , given by

$$\mathcal{H}(u) \equiv qu^3 - 6qu^2 + (12q - 1 + a_u + \beta)u - (8q + 4), \quad (5.2.3a)$$

where we have defined  $a_u$  and  $\beta$ , by

$$a_u \equiv k_u \omega_u \tanh(\omega_u L/2), \quad \beta \equiv \epsilon z / (\epsilon + a_v), \quad \text{where } a_v \equiv k_v \omega_v \tanh(\omega_v L/2). \quad (5.2.3b)$$

In terms of any solution  $u = u_e$  to the cubic,  $v_e$  is given by  $v_e = \beta u_e$ .

We now claim that (5.1.1) has a unique positive symmetric steady-state solution. To show this, we must verify that there is a unique root  $u_e > 0$  to  $\mathcal{H}(u) = 0$  when  $u > 0$ . In our proof below we will consider two cases: Case I:  $a_u + \beta > 1$ . Case II:  $0 < a_u + \beta \leq 1$ . We first consider Case I. We calculate that  $\mathcal{H}(0) = -(8q + 4) < 0$  and  $\mathcal{H}(u) \rightarrow +\infty$  as  $u \rightarrow +\infty$ . Moreover, we derive that  $\mathcal{H}'(u) = 3q(u - 2)^2 + (a_u + \beta - 1)$ , so that  $\mathcal{H}'(u) > 0$  for  $u > 0$  in Case I. Since  $\mathcal{H}(0) < 0$ ,  $\mathcal{H}(u) \rightarrow +\infty$  as  $u \rightarrow \infty$ , and  $\mathcal{H}(u)$  is monotone increasing on  $u > 0$ , there is a unique root to  $\mathcal{H}(u) = 0$  in  $u > 0$  in Case I.

Next, we consider Case II. We conclude that  $\mathcal{H}'(u) = 0$  at exactly two points  $u = u_{\pm}$ , given by

$$u_{\pm} \equiv 2 \pm \frac{1}{\sqrt{3q}} \sqrt{1 - a_u - \beta}. \quad (5.2.4)$$

Here  $u_- < 2 < u_+$ , with  $u_-$  and  $u_+$  a local maximum and local minimum of  $\mathcal{H}(u)$ , respectively. Therefore, since  $2 < u_+$ ,  $\mathcal{H}(2) = -6 + 2(a_u + \beta) < 0$ ,  $\mathcal{H}(u) \rightarrow +\infty$  as  $u \rightarrow \infty$ , and  $u_+$  is a local minimum point of  $\mathcal{H}(u)$ , we conclude that there is a unique root to  $\mathcal{H}(u) = 0$  in  $u > 2$ . To conclude the proof for Case II, we need only show that  $\mathcal{H}(u_-) < 0$  whenever  $u_-$  is on

## 5.2. The Steady-State Solution and the Formulation of the Linear Stability Problem

---

the range  $0 < u_- < 2$ . To show this we use  $3q(u_- - 2)^2 = 1 - (a_u + \beta)$  to calculate

$$\begin{aligned}\mathcal{H}(u_-) &= q(u_- - 2)^3 - u_- - 4 + (a_u + \beta)u_- \\ &= \frac{[1 - (\beta + a_u)]}{3}(u_- - 2) - u_- - 4 + (a_u + \beta)u_-, \\ &= \frac{1}{3} \left( -2u_- [1 - (a_u + \beta)] - 14 + 2(a_u + \beta) \right).\end{aligned}$$

Since the last expression shows that  $\mathcal{H}(u_-) < 0$  for  $0 < u_- < 2$  when  $0 < a_u + \beta \leq 1$ , we conclude that there are no additional roots to  $\mathcal{H}(u) = 0$  located on  $0 < u < 2$  whenever  $0 < a_u + \beta \leq 1$ . Combining the results of Case I and Case II, we conclude that, for any  $a_u + \beta > 0$ , there is a unique positive symmetric steady-state solution to (5.1.1).

We will assume that  $z$  and  $q$  are such that the steady-state of the membrane kinetics, when uncoupled to the bulk, is a linearly stable fixed point. As a result, any instability that arises in our analysis is due specifically to the coupling of the two membranes by the bulk. For the uncoupled problem, where  $a_u = 0$  and  $a_v = 0$  in (5.2.3), we obtain that  $u_e$  is a root of (5.2.3a) in which we set  $a_u = 0$  and  $\beta = z$  in (5.2.3a). In terms of  $u_e$ , the Jacobian of the membrane kinetics is

$$J_e^0 \equiv \begin{pmatrix} f_u^e & f_v^e \\ \epsilon g_u^e & \epsilon g_v^e \end{pmatrix} = \begin{pmatrix} 1 - 3q(u_e - 2)^2 & -1 \\ \epsilon z & -\epsilon \end{pmatrix}, \quad (5.2.5)$$

when uncoupled from the bulk. We calculate the determinant and trace of this matrix as

$$\det J_e^0 = \epsilon [z - 1 + 3q(u_e - 2)^2], \quad \text{tr} J_e^0 = 1 - \epsilon - 3q(u_e - 2)^2. \quad (5.2.6)$$

To ensure that the uncoupled membrane kinetics has a stable fixed point, we will assume that  $z > 1$ , so that  $\det J_e^0 > 0$  for any parameter set. Therefore, the stability of the fixed point is determined by the sign of  $\text{tr} J_e^0$ . To determine the region of the  $(q, z)$  plane, with  $z > 1$ , for which  $\text{tr} J_e^0 < 0$ , we simply locate the stability boundary where  $\text{tr} J_e^0 = 0$ . We solve (5.2.6) for  $q$  and then (5.2.3a), with  $a_u = 0$  and  $\beta = z$ , for  $z$ , to readily obtain a parametric description of this stability boundary in the form  $q = Q(u)$  and  $z = Z(u)$ , for  $u \geq 0$ , where

$$q = Q(u) \equiv \frac{(1 - \epsilon)}{3(u - 2)^2}, \quad z = Z(u) \equiv 1 + \frac{4}{u} - \frac{(1 - \epsilon)}{3u}(u - 2). \quad (5.2.7)$$

## 5.2. The Steady-State Solution and the Formulation of the Linear Stability Problem

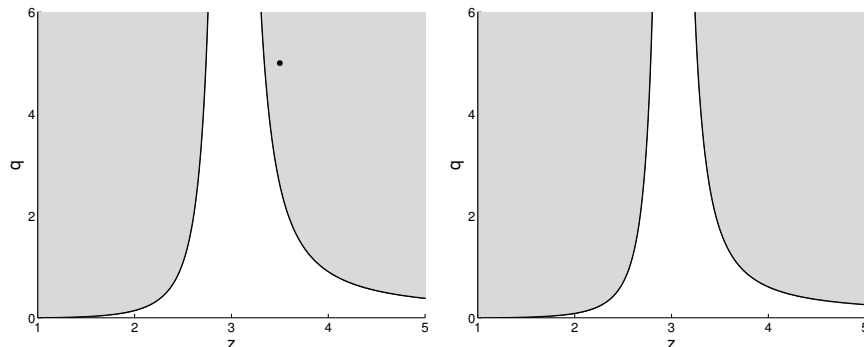


Figure 5.2: The stability boundary when  $\epsilon = 0.015$  (left panel) and when  $\epsilon = 0.3$  (right panel) for the membrane dynamics when uncoupled to the bulk diffusion. The heavy solid curve is the stability boundary (5.2.7) where  $\text{tr}J_e^0 = 0$ . Above this curve in the shaded region,  $\text{tr}J_e^0 < 0$  so that the uncoupled membrane kinetics has a stable fixed point in this region. For  $\epsilon = 0.015$ , the parameter values  $z = 3.5$  and  $q = 5$ , used in [23], correspond to the marked point.

For  $\epsilon = 0.015$  and  $\epsilon = 0.3$  in the left and right panels of Fig. 5.2, respectively, we plot the stability boundary (5.2.7) for the uncoupled problem in the  $(q, z)$  plane for  $z > 1$ . In the shaded regions of this figure we have  $\text{tr}J_e^0 < 0$ . In our analysis below, we will assume that the pair  $(q, z)$  belongs to this region, which ensures that the fixed point associated with the uncoupled membrane kinetics is linearly stable. As a remark, for the parameter values  $z = 3.5$ ,  $q = 5.0$ , and  $\epsilon = 0.015$ , as used in [23], we calculate from (5.2.3a) and (5.2.6) that  $u_e \approx 1.67$  and  $\text{tr}J_e^0 \approx -0.649 < 0$ , so that the fixed point for the uncoupled dynamics is stable. This point is marked in the left panel of Fig. 5.2.

### 5.2.1 Formulation of the Linear Stability Problem

Next, we derive the linear stability problem associated with the symmetric steady-state solution. We introduce

$$\begin{aligned} U(x, t) &= U_e(x) + \varphi(x)e^{\lambda t}, & u(t) &= u_e + \xi e^{\lambda t}, \\ V(x, t) &= V_e(x) + \psi(x)e^{\lambda t}, & v(t) &= v_e + \eta e^{\lambda t}, \end{aligned}$$

## 5.2. The Steady-State Solution and the Formulation of the Linear Stability Problem

---

into (5.1.1). Upon linearizing the resulting system we obtain that

$$D_u \varphi_{xx} - (\sigma_u + \lambda) \varphi = 0, \quad D_v \psi_{xx} - (\sigma_v + \lambda) \psi = 0, \quad 0 < x < L/2, \quad (5.2.8a)$$

with  $\varphi(0) = \xi$  and  $\psi(0) = \eta$ , together with the linearized membrane kinetics on  $x = 0$  given by

$$\xi \lambda = \xi f_u^e + \eta f_v^e + k_u \varphi'(0), \quad \eta \lambda = \epsilon \xi g_u^e + \epsilon \eta g_v^e + k_v \psi'(0). \quad (5.2.8b)$$

Since the two membranes, one at  $x = 0$  and the other at  $x = L$ , are identical, then due to reflection symmetry there are two types of eigenfunctions for (5.2.8). One type is the synchronous, or in-phase, mode with

$$\varphi'(L/2) = 0, \quad \psi'(L/2) = 0, \quad (5.2.9)$$

while the other is the asynchronous, or anti-phase, mode for which

$$\varphi(L/2) = 0, \quad \psi(L/2) = 0. \quad (5.2.10)$$

Upon solving (5.2.8) for the in-phase, or synchronous ('+') mode, we get

$$\varphi_+(x) = \xi \frac{\cosh \left[ \Omega_u \left( \frac{L}{2} - x \right) \right]}{\cosh \left( \Omega_u L/2 \right)}, \quad \psi_+(x) = \eta \frac{\cosh \left[ \Omega_v \left( \frac{L}{2} - x \right) \right]}{\cosh \left( \Omega_v L/2 \right)}, \quad (5.2.11)$$

where we have defined  $\Omega_u = \Omega_u(\lambda)$  and  $\Omega_v = \Omega_v(\lambda)$  by

$$\Omega_u \equiv \sqrt{\frac{\sigma_u + \lambda}{D_u}}, \quad \Omega_v \equiv \sqrt{\frac{\sigma_v + \lambda}{D_v}}. \quad (5.2.12)$$

In (5.2.12) we have chosen the principal value of the square root, which ensures that  $\varphi_+$  and  $\psi_+$  are analytic in  $\text{Re}(\lambda) > 0$  and decay at  $x = L/2$  when  $L \gg 1$ . By substituting (5.2.11) into the boundary condition (5.2.8b) at  $x = 0$ , we get that  $\xi$  and  $\eta$  satisfy the homogeneous linear system

$$(f_u^e - \lambda - k_u p_+ \Omega_u) \xi + f_v^e \eta = 0, \quad \epsilon g_u^e \xi + (\epsilon g_v^e - \lambda - k_v q_+ \Omega_v) \eta = 0, \quad (5.2.13)$$

where we have defined  $p_+ = p_+(\lambda)$  and  $q_+ = q_+(\lambda)$  by

$$p_+ \equiv \tanh \left( \Omega_u L/2 \right), \quad q_+ \equiv \tanh \left( \Omega_v L/2 \right). \quad (5.2.14)$$

## 5.2. The Steady-State Solution and the Formulation of the Linear Stability Problem

By setting the determinant of the coefficient matrix of this linear system to zero, this linear system has a nontrivial solution if and only if  $\lambda$  is a root of the transcendental equation

$$(f_u^e - \lambda - k_u p_+ \Omega_u)(\epsilon g_v^e - \lambda - k_v q_+ \Omega_v) - \epsilon f_v^e g_u^e = 0. \quad (5.2.15)$$

Similarly, for the anti-phase, or asynchronous ('-'), mode we obtain from (5.2.8a) and (5.2.10) that

$$\varphi_-(x) = \xi \frac{\sinh \left[ \Omega_u \left( \frac{L}{2} - x \right) \right]}{\sinh (\Omega_u L / 2)}, \quad \psi_-(x) = \eta \frac{\sinh \left[ \Omega_v \left( \frac{L}{2} - x \right) \right]}{\sinh (\Omega_v L / 2)},$$

where  $\lambda$  satisfies

$$(f_u^e - \lambda - k_u p_- \Omega_u)(\epsilon g_v^e - \lambda - k_v q_- \Omega_v) - \epsilon f_v^e g_u^e = 0. \quad (5.2.16)$$

Here we have defined  $p_- = p_-(\lambda)$  and  $q_- = q_-(\lambda)$  by

$$p_- \equiv \coth (\Omega_u L / 2), \quad q_- \equiv \coth (\Omega_v L / 2). \quad (5.2.17)$$

The eigenvalue problems (5.2.15) and (5.2.16) for the synchronous and asynchronous modes can be written in terms of locating the roots  $\lambda$  of  $\mathcal{F}_\pm(\lambda) = 0$ , where

$$\mathcal{F}_\pm(\lambda) \equiv \frac{1}{k_u k_v p_\pm q_\pm} + \frac{\Omega_u \Omega_v}{\det(J_e - \lambda I)} - \frac{\Omega_u (\epsilon g_v^e - \lambda)}{k_v q_\pm \det(J_e - \lambda I)} - \frac{\Omega_v (f_u^e - \lambda)}{k_u p_\pm \det(J_e - \lambda I)}. \quad (5.2.18)$$

Here  $J_e$  is the Jacobian matrix of the membrane dynamics (5.1.1b), evaluated at the steady-state solution associated with the coupled membrane-bulk model. Therefore, from (5.2.6), we have

$$\begin{aligned} \det(J_e - \lambda I) &= \lambda^2 - (\text{tr} J_e) \lambda + \det J_e, \\ \text{tr} J_e &= 1 - \epsilon - 3q(u_e - 2)^2, \quad \det J_e = \epsilon \left[ z - 1 + 3q(u_e - 2)^2 \right], \end{aligned} \quad (5.2.19)$$

where  $u_e$  is the unique root of  $\mathcal{H}(u) = 0$ , with  $\mathcal{H}(u)$  as defined in (5.2.3a). In (5.2.18) we have  $\epsilon g_v^e = -\epsilon$  and  $f_u^e = \text{tr} J_e + \epsilon$ .

To analyze the stability of the steady-state solution, we use the argument principle of complex analysis to count the number  $N$  of roots of  $\mathcal{F}_\pm(\lambda) = 0$  in the right half-plane  $\text{Re}(\lambda) > 0$ . We take the counterclockwise contour consisting of the imaginary axis  $-iR \leq \text{Im} \lambda \leq iR$ , denoted by  $\Gamma_- \cup \Gamma_+$ , and the semicircle  $\Gamma_R$ , given by  $|\lambda| = R > 0$ , for  $|\arg \lambda| \leq \pi/2$ . Since  $1/p_\pm, 1/q_\pm$ ,

### 5.3. One Diffusive Species in the Bulk

---

$\Omega_u$ , and  $\Omega_v$  are analytic functions of  $\lambda$  in the right half-plane  $\text{Re}\lambda > 0$ , and  $\det J_e > 0$  since  $z > 1$ , it follows that the number  $P$  of poles of  $\mathcal{F}_\pm(\lambda)$  in the right half-plane depends only on the sign of  $\text{tr}J_e$ .

Since  $p_\pm \rightarrow 1$  and  $q_\pm \rightarrow 1$  as  $R \rightarrow \infty$  on  $\Gamma_R$ , with  $\lambda = Re^{i\omega}$  and  $|\omega| \leq \pi/2$ , we have that the decay of  $\mathcal{F}_\pm(\lambda)$  as  $R \rightarrow \infty$  is dominated by the first term in (5.2.18), so that

$$\mathcal{F}_\pm(\lambda) = \frac{1}{k_u k_v} + \mathcal{O}\left(R^{-1/2}\right), \quad \text{as } R \rightarrow \infty,$$

on  $\Gamma_R$ . Therefore, there is no change in the argument of  $\mathcal{F}_\pm(\lambda)$  over  $\Gamma_R$  as  $R \rightarrow \infty$ . By using the argument principle, together with  $\mathcal{F}_\pm(\bar{\lambda}) = \overline{\mathcal{F}_\pm(\lambda)}$ , we conclude that

$$N = P + \frac{1}{\pi} [\arg \mathcal{F}_\pm]_{\Gamma_+}, \quad \text{where} \quad P = \begin{cases} 2 & \text{if } \text{tr}J_e > 0 \\ 0 & \text{if } \text{tr}J_e < 0 \end{cases}. \quad (5.2.20)$$

Here  $[\arg \mathcal{F}_\pm]_{\Gamma_+}$  denotes the change in the argument of  $\mathcal{F}_\pm$  along the semi-infinite imaginary axis  $\Gamma_+ = i\lambda_I$ , with  $0 \leq \lambda_I < \infty$ , traversed downwards. When the membrane dynamics are uncoupled with the bulk we have assumed  $\text{tr}J_e < 0$ , so that  $P = 0$ . For the coupled problem, we show below that  $P$  depends on the strength of the coupling between the membrane and the bulk. We remark that, although, it is analytically intractable to calculate  $[\arg \mathcal{F}_\pm]_{\Gamma_+}$ , this quantity is easily evaluated numerically after separating  $\mathcal{F}_\pm(i\lambda_I)$  into real and imaginary parts. In terms of this readily-computed quantity, the global criterion (5.2.20) yields the number of unstable eigenvalues of the linearization (5.2.8) in  $\text{Re}(\lambda) > 0$ .

In §5.3 we determine  $P$  and  $[\arg \mathcal{F}_\pm]_{\Gamma_+}$  for the synchronous and asynchronous modes in the limiting case where there is only one bulk diffusing species. The general case of two diffusing bulk species is considered in §5.4.

### 5.3 One Diffusive Species in the Bulk

In this section we analyze the special case, considered in [23], where there is only one diffusing species in the bulk. As in [23], we assume that only the inhibitor  $V$  can detach from the membrane and diffuse and be degraded in the bulk. As such, in this section we consider the limiting problem where  $k_u = 0$  in (5.1.1) so that  $U(x, t)$  has no effect on the membrane kinetics, and can be neglected. The one-bulk species model is formulated as

$$V_t = D_v V_{xx} - \sigma_v V, \quad 0 < x < L, \quad t > 0, \quad (5.3.1a)$$

### 5.3. One Diffusive Species in the Bulk

---

coupled to the membrane dynamics  $v_1(t) = V(0, t)$  and  $v_2(t) = V(L, t)$ , where

$$\begin{aligned} u'_1 &= f(u_1, v_1), & v'_1 &= \epsilon g(u_1, v_1) + k_v V_x(0, t); \\ u'_2 &= f(u_2, v_2), & v'_2 &= \epsilon g(u_2, v_2) - k_v V_x(L, t). \end{aligned} \quad (5.3.1b)$$

Here  $f(u, v)$  and  $g(u, v)$  are given in (5.1.1c). For this limiting problem, the symmetric steady-state solution satisfies

$$D_v V_{exx} - \sigma_v V_e = 0, \quad 0 < x < L/2; \quad V_e(0) = v_e, \quad V_{ex}(L/2) = 0, \quad (5.3.2a)$$

$$f(u_e, v_e) = 0, \quad \epsilon g(u_e, v_e) + k_v V_{ex}(0) = 0. \quad (5.3.2b)$$

Defining  $\omega_v \equiv \sqrt{\sigma_v/D_v}$ , we obtain that  $u_e$  is the unique root of  $\mathcal{H}(u) = 0$ , where

$$\begin{aligned} \mathcal{H}(u) &\equiv qu^3 - 6qu^2 + (12q - 1 + \beta)u - (8q + 4); \\ \beta &\equiv z/(1 + \epsilon^{-1}a_v), \quad a_v \equiv k_v \omega_v \tanh(\omega_v L/2). \end{aligned} \quad (5.3.3)$$

By setting  $k_u = 0$  in the stability analysis of §5.2.1, we obtain that the linear stability properties of this symmetric steady-state is determined by the roots of  $\mathcal{G}_{\pm}(\lambda) = 0$ , defined by

$$\mathcal{G}_{\pm}(\lambda) = \frac{1}{k_v q_{\pm}} - \frac{\Omega_v(f_u^e - \lambda)}{\det(J_e - \lambda I)}, \quad (5.3.4)$$

where  $\Omega_v$ ,  $q_+$ , and  $q_-$ , are defined in (5.2.12), (5.2.14), and (5.2.17), respectively.

To analyze the roots of (5.3.4), it is convenient to write (5.3.3) and (5.3.4) in terms of dimensionless bifurcation parameters. To this end, we introduce two parameter  $l_1$  and  $l_0$ , and define  $\beta$  in (5.3.3) in terms of them as

$$l_1 = k_v/\epsilon, \quad l_0 = \sqrt{D_v/\sigma_v} = 1/\omega_v, \quad \beta = z \left[ 1 + \frac{l_1}{l_0} \tanh\left(\frac{L}{2l_0}\right) \right]^{-1}. \quad (5.3.5)$$

The ratio  $L/l_0$  is a nondimensional measure of the distance between the compartments to the diffusion length  $l_0$ , while  $l_1/l_0$  is a nondimensional measure of the strength of the membrane-bulk coupling relative to the diffusion length.

Next, we define  $b \equiv \text{tr}J_e$ , and use (5.2.19) to write

$$f_u^e = b + \epsilon, \quad \det J_e = ca, \quad a \equiv z - \epsilon - b > 0, \quad \text{where } b = 1 - \epsilon - 3q(u_e - 2)^2. \quad (5.3.6)$$

### 5.3. One Diffusive Species in the Bulk

---

We recall that  $a > 0$  since we assume from §5.2 that  $z > 1$ . In this way, and upon writing  $q_{\pm}$  and  $\Omega_v$  in terms of  $l_0$  and  $l_1$ , we obtain that (5.3.4) can be written as  $\mathcal{G}_{\pm}(\lambda) = [1/(\epsilon l_0)] \mathcal{G}_{\pm}^0(\lambda)$ , where  $\mathcal{G}_{\pm}^0(\lambda)$  is defined by

$$\mathcal{G}_{\pm}^0(\lambda) \equiv \frac{l_0}{l_1 q_{\pm}(\tau_v \lambda)} - \epsilon \sqrt{1 + \tau_v \lambda} \left( \frac{b + \epsilon - \lambda}{\lambda^2 - b\lambda + \epsilon a} \right), \quad (5.3.7)$$

where  $q_{\pm}(\tau_v \lambda)$ , with  $\tau_v \equiv 1/\sigma_v$ , is defined by

$$q_{\pm}(\tau_v \lambda) = \begin{cases} \tanh \left[ \frac{L}{2l_0} \sqrt{1 + \tau_v \lambda} \right], & \text{synchronous (+) mode} \\ \coth \left[ \frac{L}{2l_0} \sqrt{1 + \tau_v \lambda} \right], & \text{asynchronous (-) mode} \end{cases}. \quad (5.3.8)$$

By using a winding number argument, similar to that in §5.2.1, the number  $N$  of unstable roots of (5.3.7) in  $\text{Re}(\lambda) > 0$  is

$$N = P + \frac{1}{\pi} [\arg \mathcal{G}_{\pm}^0]_{\Gamma_+}, \quad \text{where} \quad P = \begin{cases} 2 & \text{if } b = \text{tr} J_e > 0 \\ 0 & \text{if } b = \text{tr} J_e < 0 \end{cases}. \quad (5.3.9)$$

In terms of our dimensionless parameters, we remark that the symmetric steady-state solution, and consequently  $b = \text{tr} J_e$ , depends on  $l_1/l_0$  and  $L/l_0$ . In contrast, the stability properties of this solution, as to be analyzed from (5.3.7) below in §5.3.1, depends on  $l_1/l_0$ ,  $L/l_0$ , and  $\tau_v \equiv 1/\sigma_v$ .

In our stability analysis we will consider two distinct cases. In §5.3.1 we analyze (5.3.7) in the limit  $\epsilon \rightarrow 0$  where the membrane-bulk coupling parameter satisfies  $k_v = \mathcal{O}(\epsilon)$ , so that  $\beta = \mathcal{O}(1)$  in (5.3.5). For the parameter values given in [23]

$$D_v = 0.5, \quad \epsilon = 0.015, \quad \sigma_v = D_v/100, \quad z = 3.5, \quad q = 5, \quad L = 10, \quad k_v = 0.0225, \quad (5.3.10a)$$

we calculate that

$$l_1 = 1.5, \quad l_0 = 10, \quad \tau_v = 200, \quad \frac{l_1}{l_0} = 0.15, \quad \frac{L}{l_0} = 1. \quad (5.3.10b)$$

For this parameter set, our small  $\epsilon$  stability analysis below will provide a theoretical understanding of the numerical results in [23]. In §5.3.2, we use a numerical winding number approach together with numerically computed global bifurcation diagrams, obtained using the bifurcation software XPPAUT [16], to study the  $\epsilon = \mathcal{O}(1)$  problem.

### 5.3.1 Stability Analysis for the $\epsilon \rightarrow 0$ Limiting Problem

In this subsection we study the roots of (5.3.7) for various ranges of  $b$ . To determine the winding number  $[\arg \mathcal{G}_{\pm}^0]_{\Gamma_{\pm}}$  in (5.3.9) we must consider several distinct ranges of  $\lambda_I$ . For  $\epsilon \ll 1$ , we will calculate this winding number analytically.

We first observe that  $\text{Re}(\mathcal{G}_{\pm}^0(i\lambda_I)) \rightarrow l_0/l_1 > 0$  as  $\lambda_I \rightarrow +\infty$ , so that in the  $(\mathcal{G}_{R\pm}^0, \mathcal{G}_{I\pm}^0)$  plane, where  $\mathcal{G}_{R\pm}^0(\lambda_I) \equiv \text{Re}(\mathcal{G}_{\pm}^0(i\lambda_I))$  and  $\mathcal{G}_{I\pm}^0(\lambda_I) \equiv \text{Im}(\mathcal{G}_{\pm}^0(i\lambda_I))$ , we begin at a point on the positive real axis. Then, since  $\text{Re}(\sqrt{1 + \tau_v \lambda}) > 0$ , and both  $\text{Re}(\tanh z) > 0$  and  $\text{Re}(\coth z) > 0$  when  $\text{Re}(z) > 0$ , we conclude for  $\epsilon \rightarrow 0$  from (5.3.7) that  $\mathcal{G}_{R\pm}^0(\lambda_I) > 0$  for  $\lambda_I > 0$  with  $\lambda_I = \mathcal{O}(1)$ . We then use (5.3.7) to calculate  $\mathcal{G}_{\pm}^0(0)$ , for any  $\epsilon > 0$ , as

$$\mathcal{G}_{\pm}^0(0) = \frac{l_0}{l_1 q_{\pm}(0)} - \frac{(b + \epsilon)}{a}, \quad \text{where} \quad a = z - \epsilon - b > 0. \quad (5.3.11)$$

We conclude that  $\mathcal{G}_{\pm}^0(0) > 0$  when  $b + \epsilon < a l_0 / [l_1 q_{\pm}(0)]$ . Since  $a = z - \epsilon - b > 0$ , we solve this inequality for  $b$  to obtain that  $\mathcal{G}_{\pm}^0(0) > 0$  when  $b < b_{\pm}$  and  $\mathcal{G}_{\pm}^0(0) < 0$  when  $b > b_{\pm}$ , where  $b_{\pm}$  is defined by

$$b < b_{\pm} \equiv z \left[ 1 + \frac{l_1 q_{\pm}(0)}{l_0} \right]^{-1} - \epsilon. \quad (5.3.12)$$

For the synchronous (+) mode, we now show that  $b < b_+$  always holds for any root to the cubic  $\mathcal{H}(u) = 0$ , defined in (5.3.3). In particular, we will prove that  $b > b_+$  is incompatible with a root of (5.3.3). To show this, we first observe that since  $q_+(0) = \tanh(L/2l_0)$ , the condition  $b > b_+$  is equivalent to  $b > \beta - \epsilon$ , where  $\beta$  is defined in (5.3.5). We have from (5.3.6) that  $b > \beta - \epsilon$  and  $\beta > 0$ , when  $0 < \beta < 1 - 3q(u-2)^2$ , where  $u > 0$  is the unique root of  $\mathcal{H}(u) \equiv q(u-2)^3 + \beta u - (4+u) = 0$ . From this inequality on  $\beta$ , we calculate

$$\begin{aligned} \mathcal{H}(u) &< q(u-2)^3 + u \left[ 1 - 3q(u-2)^2 \right] - (4+u) \\ &= q(u-2)^3 - 4 - 3qu(u-2)^2 = -2q(u-2)^2(u+1) - 4 < 0, \end{aligned}$$

for all  $u > 0$ . Therefore, there is no root to  $\mathcal{H}(u) = 0$  when  $b > b_+$ . As a consequence, we must have  $b < b_+$ , so that for the synchronous mode we have  $\mathcal{G}_+^0(0) > 0$  unconditionally.

To determine the curve in the  $l_1/l_0$  versus  $L/l_0$  plane where the asynchronous (-) mode has a zero-eigenvalue crossing, we set  $b = b_-$ , and use

### 5.3. One Diffusive Species in the Bulk

---

(5.3.12) together with (5.3.3) to obtain that a zero eigenvalue crossing occurs when

$$\begin{aligned} z \left[ 1 + \frac{l_1}{l_0} \tanh \left( \frac{L}{2l_0} \right) \right]^{-1} &= -\frac{q(u-2)^3}{u} + \frac{4}{u} + 1, \\ z \left[ 1 + \frac{l_1}{l_0} \coth \left( \frac{L}{2l_0} \right) \right]^{-1} &= 1 - 3q(u-2)^2. \end{aligned}$$

We rearrange these expressions to get

$$\begin{aligned} \frac{l_1}{l_0} \tanh \left( \frac{L}{2l_0} \right) &= \chi_1(u), & \chi_1(u) &\equiv \frac{zu}{-q(u-2)^3 + 4 + u} - 1, \\ \frac{l_1}{l_0} \coth \left( \frac{L}{2l_0} \right) &= \chi_2(u), & \chi_2(u) &\equiv \frac{zu}{1 - 3q(u-2)^2} - 1. \end{aligned} \quad (5.3.13)$$

For the range of  $u > 0$  for which  $\chi_1 > 0$ ,  $\chi_2 > 0$ , and  $\chi_1/\chi_2 < 1$ , we readily derive from (5.3.13) that the curve in the  $l_1/l_0$  versus  $L/l_0$  plane where the asynchronous (-) mode has a zero-eigenvalue crossing is given parametrically in terms of  $u$  by

$$\frac{l_1}{l_0} = \sqrt{\chi_1(u)\chi_2(u)}, \quad \frac{L}{l_0} = \ln \left( \frac{\sqrt{\chi_2(u)} + \sqrt{\chi_1(u)}}{\sqrt{\chi_2(u)} - \sqrt{\chi_1(u)}} \right). \quad (5.3.14)$$

For  $q = 5$ ,  $z = 3.5$ , (5.3.14) yields the upward facing horseshoe-shaped curve shown in the left panel of Fig. 5.4. Below in (5.3.30), we show that this zero-eigenvalue crossing for the asynchronous mode is a bifurcation point where asymmetric equilibria of (5.3.1) bifurcate from the symmetric steady-state solution branch.

Now that the possibility of zero-eigenvalue crossings has been analyzed, we proceed to determine  $[\arg \mathcal{G}_{\pm}^0]_{\Gamma_+}$ . Since  $\mathcal{G}_{R\pm}^0(\lambda_I) > 0$  for  $\lambda_I > 0$  with  $\lambda_I = \mathcal{O}(1)$ , we need only analyze (5.3.7) with  $\lambda = i\lambda_I$  and  $\lambda_I$  near the origin. For  $|b| \gg \mathcal{O}(\epsilon)$ , we set  $\lambda_I = \epsilon\lambda_I^0$  with  $\lambda_I^0 = \mathcal{O}(1)$  in (5.3.7) to obtain

$$\mathcal{G}_{R\pm}^0 = \text{Re} \left( \mathcal{G}_{\pm}^0(i\epsilon\lambda_I^0) \right) \sim \frac{l_0}{l_1 q_{\pm}(0)} - \frac{ba}{a^2 + b^2(\lambda_I^0)^2}. \quad (5.3.15)$$

For the synchronous mode, we conclude from (5.3.15) that  $\mathcal{G}_{R\pm}^0 > 0$  when  $\lambda_I = \mathcal{O}(\epsilon)$ , and consequently  $[\arg \mathcal{G}_{\pm}^0]_{\Gamma_+} = 0$ , for any  $b$  with  $|b| \gg \mathcal{O}(\epsilon)$ . As a result, for the synchronous mode, we obtain from (5.3.9) that

$$N = P, \quad \text{where} \quad P = \begin{cases} 2 & \text{if } b = \text{tr} J_e > 0 \\ 0 & \text{if } b = \text{tr} J_e < 0 \end{cases}, \quad (\text{synchronous mode}). \quad (5.3.16)$$

### 5.3. One Diffusive Species in the Bulk

In contrast, for the asynchronous mode, we conclude from (5.3.15) that for  $\lambda_I = \mathcal{O}(\epsilon)$  and  $|b| \gg \mathcal{O}(\epsilon)$ , we have  $\mathcal{G}_{R-}^0(\lambda_I) > 0$  when  $b < b_-$ , and  $\mathcal{G}_{R-}^0(\lambda_I) < 0$  when  $b > b_-$ , where  $b_-$  is defined in (5.3.12). Therefore, for the asynchronous mode, we have  $[\arg \mathcal{G}_{-}^0]_{\Gamma_+} = 0$  when  $b < b_-$ , so that (5.3.16) still holds when  $b < b_-$  and  $|b| \gg \mathcal{O}(\epsilon)$ . However, it remains to calculate  $[\arg \mathcal{G}_{-}^0]_{\Gamma_+} = 0$  when  $b > b_-$ , for which  $\mathcal{G}_{R-}^0(\lambda_I) < 0$ . This computation is done numerically below.

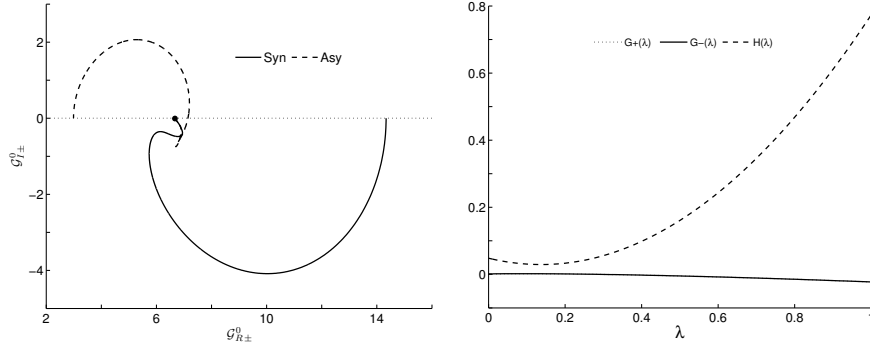


Figure 5.3: Left panel: The path  $\mathcal{G}_{\pm}^0(i\lambda_I) = \mathcal{G}_{R\pm}^0(\lambda_I) + i\mathcal{G}_{I\pm}^0(\lambda_I)$ , for the parameter set (5.3.10a) of [23]. For both  $\pm$  modes, we start at  $\lambda_I = 100$  (solid dot), which corresponds to the common value  $\mathcal{G}_{R\pm}^0 \sim l_0/l_1 > 0$  and  $\mathcal{G}_{I\pm}^0 = 0$ . As  $\lambda_I$  increases,  $\mathcal{G}_{R\pm}^0$  remains positive, and the path for each mode terminates when  $\lambda_I = 0$  at different points on the positive real axis, without wrapping around the origin. This establishes that  $[\arg \mathcal{G}_{\pm}^0]_{\Gamma_+} = 0$ . Right panel: The functions  $G_{\pm}(\lambda)$  and  $H(\lambda)$ , as defined in (5.3.17), when  $\lambda > 0$  is real, for the parameter set (5.3.10a). The curves for  $G_{+}$  and  $G_{-}$  essentially coincide. Since there are no intersections between  $G_{\pm}$  and  $H(\lambda)$ , then there are no real positive roots to  $\mathcal{G}_{\pm}^0(\lambda) = 0$  in (5.3.7) for either the synchronous or asynchronous modes.

For any  $b$  independent of  $\epsilon$ , this analysis shows for the synchronous mode that  $N = 0$  for  $b < 0$  and  $N = 2$  for any  $b > 0$ . For the asynchronous mode we have  $N = 0$  for  $b < 0$  and  $N = 2$  for any  $0 < b < b_-$ . As a result, to leading order in  $\epsilon$ , we conclude that both the synchronous and asynchronous modes undergo a Hopf bifurcation as  $b$  crosses through zero. For the parameter set (5.3.10a), as used in [23], in the left panel of Fig. 5.3 we plot the numerically computed path of  $\mathcal{G}_{\pm}^0(i\lambda_I)$  in the plane  $(\mathcal{G}_{R\pm}^0, \mathcal{G}_{I\pm}^0)$ . For this parameter set we calculate numerically that  $b_- \approx 2.627$  and  $b_+ \approx 3.258$  from (5.3.12), and  $b = \text{tr}J_e = 1 - \epsilon - 3q(u_e - 2)^2 \approx 0.2746$ , from (5.2.19),

### 5.3. One Diffusive Species in the Bulk

where  $u_e$  is the unique root of  $\mathcal{H}(u) = 0$  defined in (5.3.3). Since  $b < b_-$ , our theoretical prediction that  $[\arg \mathcal{G}_{\pm}^0]_{\Gamma_+} = 0$  is confirmed from the plot in the left panel of Fig. 5.3.

To determine the location of the two unstable eigenvalues of the linearization for the parameter set of (5.3.10a), we look for zeroes of (5.3.7) on the positive real axis  $\lambda > 0$ . To this end, we rewrite (5.3.7) as

$$\mathcal{G}_{\pm}^0(\lambda) = \frac{H(\lambda) - G_{\pm}(\lambda)}{\left[ \frac{l_1}{l_0} H(\lambda) q_{\pm}(\tau_v \lambda) \right]},$$

$$H(\lambda) \equiv \lambda^2 - b\lambda + \epsilon a, \quad G_{\pm}(\lambda) \equiv \frac{\epsilon l_1}{l_0} (b + \epsilon - \lambda) q_{\pm}(\tau_v \lambda) \sqrt{1 + \tau_v \lambda}.$$
(5.3.17)

For the parameter set of (5.3.10a), in the right panel of Fig. 5.3 we plot  $G_{\pm}(\lambda)$  and  $H(\lambda)$  for  $\lambda > 0$  real, which shows that there are no real positive roots to  $\mathcal{G}_{\pm}^0(\lambda) = 0$ . As a result, the two unstable eigenvalues for the parameter set (5.3.10a) are not real-valued, and do indeed generate an oscillatory instability of the symmetric steady-state solution.

Next, we examine the region near  $b = 0$  where a Hopf bifurcation for either of the two modes must occur. To determine the precise location of the Hopf bifurcation point we look for a root  $\lambda_I$  of (5.3.7), with  $\lambda_I \ll 1$ , when  $b = \mathcal{O}(\epsilon)$ . We Taylor-expand the right-hand side of (5.3.7) as  $\lambda_I \rightarrow 0$ , and set  $\mathcal{G}_{\pm}^0(i\lambda_I) = 0$  to obtain that

$$-\lambda_I^2 - ib\lambda_I + \epsilon(z - \epsilon - b)$$

$$\sim \epsilon \left( c_{\pm} + i\lambda_I s_{\pm} + \mathcal{O}(\lambda_I^2) \right) \left( 1 + \frac{i}{2} \tau_v \lambda_I + \mathcal{O}(\lambda_I^2) \right) (b + \epsilon - i\lambda_I),$$
(5.3.18)

where  $c_{\pm}$  and  $s_{\pm}$  are determined from the Taylor series of  $l_1 q_{\pm}(i\tau_v \lambda_I)/l_0$  as

$$\frac{l_1}{l_0} q_{\pm}(i\tau_v \lambda_I) = c_{\pm} + i\lambda_I s_{\pm} + \mathcal{O}(\lambda_I^2); \quad c_{\pm} \equiv \frac{l_1}{l_0} q_{\pm}(0), \quad s_{\pm} \equiv \frac{l_1}{l_0} \tau_v q'_{\pm}(0).$$
(5.3.19)

Upon expanding the right-hand side of (5.3.18), we obtain that

$$-\lambda_I^2 - ib\lambda_I + \epsilon(z - \epsilon - b) \sim \epsilon \left[ c_{\pm} + i \left( s_{\pm} + \frac{c_{\pm}}{2} \tau_v \right) \lambda_I + \mathcal{O}(\lambda_I^2) \right] (b + \epsilon - i\lambda_I).$$
(5.3.20)

To determine  $\lambda_I$  and the critical value of  $b$  for a Hopf bifurcation we take the real and imaginary parts of both sides of (5.3.20). From the imaginary

### 5.3. One Diffusive Species in the Bulk

---

parts, we get

$$b \sim \epsilon c_{\pm} - \epsilon(b + \epsilon) \left( s_{\pm} + \frac{c_{\pm}}{2} \tau_v \right).$$

Upon solving this equation asymptotically for  $b$ , we obtain that

$$b \sim \epsilon c_{\pm} - \epsilon^2(c_{\pm} + 1) \left( s_{\pm} + \frac{c_{\pm}}{2} \tau_v \right). \quad (5.3.21)$$

Next, by taking the real parts of both sides of (5.3.18), we get

$$-\lambda_I^2 + \epsilon(z - \epsilon - b) \sim \epsilon(b + \epsilon)c_{\pm} + \epsilon\lambda_I^2 \left( s_{\pm} + \frac{c_{\pm}}{2} \tau_v \right).$$

We substitute  $b \sim \epsilon c_{\pm}$  into this equation, and simplify the resulting expression to get

$$\lambda_I^2 \sim \epsilon z - \epsilon^2(c_{\pm} + 1)^2 - \epsilon\lambda_I^2 \left( s_{\pm} + \frac{c_{\pm}}{2} \tau_v \right).$$

For  $\epsilon \ll 1$ , we readily derive from this last expression that

$$\lambda_I \sim \epsilon^{1/2} z^{1/2} \left( 1 - \frac{\epsilon}{2z} \left[ (c_{\pm} + 1)^2 + z \left( s_{\pm} + \frac{c_{\pm}}{2} \tau_v \right) \right] \right) + \mathcal{O}(\epsilon^2). \quad (5.3.22a)$$

Upon recalling (5.3.19) and (5.3.8), we determine  $c_{\pm}$  and  $s_{\pm}$  as

$$\begin{aligned} c_{\pm} &= \begin{cases} \frac{l_1}{l_0} \tanh\left(\frac{L}{2l_0}\right), & \text{synchronous (+)} \\ \frac{l_1}{l_0} \coth\left(\frac{L}{2l_0}\right), & \text{asynchronous (-)} \end{cases}, \\ s_{\pm} &= \begin{cases} \frac{\tau_v}{4} \left(\frac{l_1}{l_0}\right) \left(\frac{L}{l_0}\right) \operatorname{sech}^2\left(\frac{L}{2l_0}\right), & \text{synchronous (+)} \\ -\frac{\tau_v}{4} \left(\frac{l_1}{l_0}\right) \left(\frac{L}{l_0}\right) \operatorname{csch}^2\left(\frac{L}{2l_0}\right), & \text{asynchronous (-)} \end{cases}. \end{aligned} \quad (5.3.22b)$$

In summary, we conclude to leading-order in the limit  $\epsilon \rightarrow 0$  that there is a Hopf bifurcation when  $b \equiv \operatorname{tr} J_e \sim \epsilon c_{\pm}$  with leading-order frequency  $\lambda_I \sim \epsilon^{1/2} z^{1/2}$ . Therefore, the period  $T$  of small-amplitude oscillations at the onset of the Hopf bifurcation is long as  $\epsilon \rightarrow 0$ , with scaling  $T \sim 2\pi/\sqrt{\epsilon z}$ . A higher-order asymptotic formulae for the Hopf bifurcation point is given in (5.3.21) and (5.3.22). We observe that the critical threshold for  $b$ , given by  $b \sim \epsilon c_{\pm}$ , shows that the Hopf bifurcation threshold for the synchronous and asynchronous modes are only slightly different when  $\epsilon \ll 1$ .

### 5.3. One Diffusive Species in the Bulk

---

To determine the curves in the  $l_1/l_0$  versus  $L/l_0$  parameter plane where Hopf Bifurcations occur, we set  $b = \text{tr}J_e = 1 - \epsilon - 3q(u_e - 2)^2 = \epsilon c_{\pm}$ , and solve for  $u_e$ . This yields the two roots  $u_{1\pm}$  and  $u_{2\pm}$ , defined by

$$u_{1\pm} = 2 - \frac{1}{\sqrt{3q}} \sqrt{1 - \epsilon(1 + c_{\pm})}, \quad u_{2\pm} = 2 + \frac{1}{\sqrt{3q}} \sqrt{1 - \epsilon(1 + c_{\pm})}. \quad (5.3.23)$$

By using (5.3.3), we then solve  $\mathcal{H}(u_{1\pm}) = 0$  and  $\mathcal{H}(u_{2\pm}) = 0$  for  $\beta$  to obtain that  $\beta = Z(u_{1\pm})$  and  $\beta = Z(u_{2\pm})$ , where

$$Z(u) \equiv 1 + \frac{4}{u} - \frac{(1 - \epsilon)}{3u}(u - 2). \quad (5.3.24)$$

Finally, we use (5.3.5) to relate  $\beta$  to  $l_1/l_0$  and  $L/l_0$ . Upon solving the resulting expression for  $l_1/l_0$  we obtain that the Hopf bifurcation curves for the synchronous and asynchronous modes are given by

$$\frac{l_1}{l_0} = \left[ \frac{z}{Z(u_{j+})} - 1 \right] \coth \left( \frac{L}{2l_0} \right), \quad \text{for } j = 1, 2; \quad \text{synchronous (+) mode,} \quad (5.3.25a)$$

$$\frac{l_1}{l_0} = \left[ \frac{z}{Z(u_{j-})} - 1 \right] \coth \left( \frac{L}{2l_0} \right), \quad \text{for } j = 1, 2; \quad \text{asynchronous (-) mode,} \quad (5.3.25b)$$

where  $Z(u)$  is defined in (5.3.24) and  $c_{\pm}$  is defined in (5.3.22b). We remark that since  $c_{\pm}$  depends on  $l_1/l_0$ , (5.3.25) is a weakly implicit equation for  $l_1/l_0$  when  $\epsilon \ll 1$ . We solve (5.3.25) when  $\epsilon \ll 1$  for  $l_1/l_0$  using one step of a fixed point iteration.

In the left panel of Fig. 5.4 we plot the Hopf bifurcation curves from (5.3.25) in the  $l_1/l_0$  versus  $L/l_0$  plane when  $\epsilon = 0.015$ ,  $q = 5$ , and  $z = 3.5$ . For this parameter set, we observe from this figure that the Hopf bifurcation thresholds for the synchronous and asynchronous modes almost coincide. Inside the region bounded by the curves, the symmetric steady-state solution is unstable and there may either be stable or unstable periodic solutions. The parameter set (5.3.10a), as used in [23], corresponds to the marked point  $l_1/l_0 = 0.15$  and  $L/l_0 = 1$  in this figure that is near the stability boundary. This phase diagram is comparable to the one obtained in [23]. However, as discussed in §5.1, in [23] the Hopf bifurcation boundary for the leading order theory, where the synchronous and asynchronous modes have a common threshold, was obtained qualitatively through an analysis based on the crossing of nullclines. No zero-eigenvalue crossing was noted

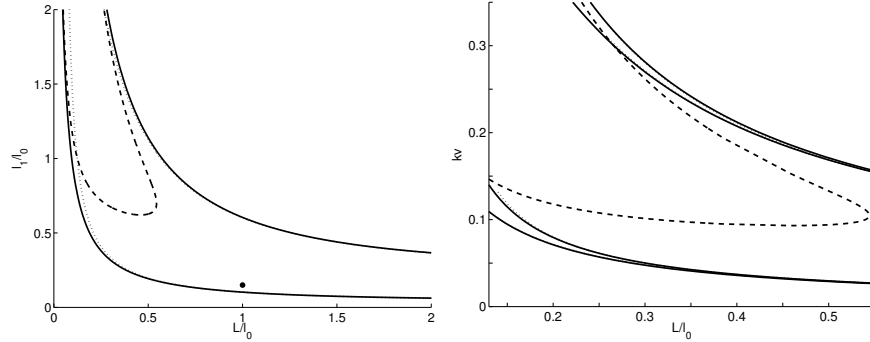


Figure 5.4: Left panel: The Hopf bifurcation boundaries for the synchronous mode (solid curves) and asynchronous mode (dotted curves), as computed from (5.3.25), for the one-bulk species model (5.3.1) when  $q = 5$ ,  $z = 3.5$ ,  $\tau_v = 200$ , and  $\epsilon = 0.015$ . These Hopf bifurcation thresholds essentially coincide except when  $L/l_0$  is small. The upward horseshoe-shaped curve corresponds to a zero-eigenvalue crossing for the asynchronous mode, as given parametrically by (5.3.14). The marked point corresponds to the parameter set  $l_1/l_0 = 0.15$  and  $L/l_0 = 1$  used in [23]. Right panel: Phase diagram in the  $k_v$  versus  $L/l_0$  plane when  $l_0 = 10$  showing a clear difference between the Hopf bifurcation boundaries for the synchronous (outer solid) and asynchronous (inner solid) curves. Between the two outer solid curves, the synchronous mode is unstable while between the inner solid curves the asynchronous mode is unstable. The dashed horseshoe shaped-curve corresponds to the zero eigenvalue crossing (5.3.14). Inside the region bounded by horseshoe-shaped curve there are asymmetric steady-state solutions. The Hopf curves coincide almost exactly with full numerical results computed by solving (5.3.4) for a pure imaginary eigenvalue  $\lambda = i\omega$  using Maple [50] (dotted curve).

### 5.3. One Diffusive Species in the Bulk

in [23]. Our stability analysis for the limiting problem  $\epsilon \rightarrow 0$  has been able to determine two-term approximations to the Hopf boundaries for both the synchronous and asynchronous modes, to determine the Hopf bifurcation frequencies near onset, and to detect zero-eigenvalue crossings corresponding to the emergence of asymmetric steady-state solutions of (5.3.1).

In the right panel of Fig. 5.4 we plot the corresponding Hopf bifurcation curves in the  $k_v$  versus  $L/l_0$  when  $l_0 = 10$ , which shows a clearer distinction between the synchronous and asynchronous modes of instability. Between the two outer solid curves, representing the Hopf threshold for the synchronous mode, the synchronous mode is unstable. Similarly, between the two inner solid curves, representing the Hopf threshold for the asynchronous mode, the asynchronous mode is unstable. The dashed horseshoe-shaped curve corresponds to a zero eigenvalue crossing. Inside this horseshoe-shaped region, there are asymmetric steady-state solutions to (5.3.1). This plot shows that for a given value of  $L/l_0$  the symmetric steady-state solution is unstable to an oscillatory instability only for some intermediate range  $k_{v-} < k_v < k_{v+}$  of the coupling strength between the membrane and the bulk. We remark that the analytical stability boundaries in Fig. 5.4 were all verified numerically by determining the complex roots of  $\mathcal{G}_{\pm} = 0$ , as defined in (5.3.4), using Maple [50].

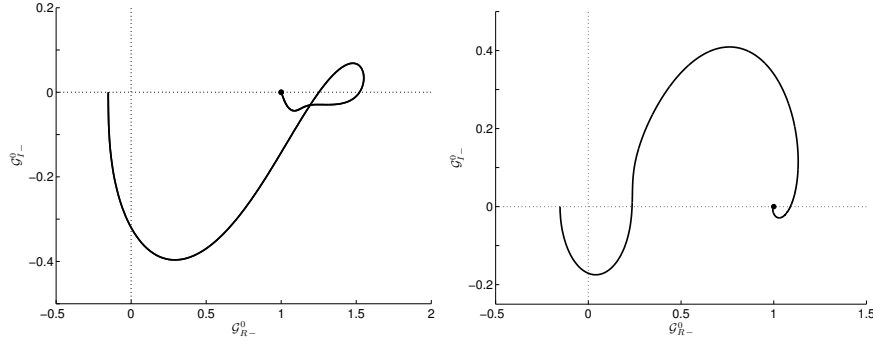


Figure 5.5: Plot of  $\mathcal{G}_{-}^0(i\lambda_I) = \mathcal{G}_{R-}^0(\lambda_I) + i\mathcal{G}_{I-}^0(\lambda_I)$  for the parameter set  $l_1/l_0 = 1.0$ ,  $L/l_0 = 0.4$ ,  $q = 5.0$ ,  $z = 3.5$ , that lies within the horseshoe-shaped region of the left panel of Fig. 5.4 where  $b > b_-$ . Left panel:  $\tau_v = 200$ . Right panel:  $\tau_v = 1$ . For  $\lambda_I \rightarrow \infty$ , both paths begin on the positive real axis, and end on the negative real axis when  $\lambda_I = 0$ . For both values of  $\tau_v$  we have  $[\arg\mathcal{G}_{-}^0]_{\Gamma_+} = -\pi$ , so that  $N = 1$  from (5.3.9).

Next, we numerically compute the winding number  $[\arg\mathcal{G}_{-}^0]_{\Gamma_+}$  to count

the number of unstable eigenvalues for the asynchronous mode for parameter values inside the horseshoe-shaped zero-eigenvalue crossing curve in the left panel of Fig. 5.4. Recall that within this region, we have  $b > b_-$  and so  $\mathcal{G}_-^0(0) < 0$ . For the particular point  $l_1/l_0 = 1.0$  and  $L/l_0 = 0.4$  in this region, and for  $q = 5$  and  $z = 3.5$ , in Fig. 5.5 we show that  $[\arg \mathcal{G}_-^0]_{\Gamma_+} = -\pi$  for two different values of  $\tau_v$ . From (5.3.9) this implies that  $N = 1$ , and so for the asynchronous mode the linearization around the symmetric steady-state has a unique unstable real eigenvalue. By further similar numerical computations of the winding number (not shown), we conjecture that  $[\arg \mathcal{G}_-^0]_{\Gamma_+} = -\pi$ , and consequently  $N = 1$  for the asynchronous mode, whenever  $b > b_-$ .

In the left panel of Fig. 5.6 we show the numerically computed spectrum of the linearization, obtained using Maple [50] on (5.3.7), when we take a vertical slice at fixed  $L/l_0 = 0.3$  in the right panel of Fig. 5.4 that begins within the horseshoe-shaped region, first traversing above the zero-eigenvalue curve, then past the asynchronous Hopf threshold, and finally beyond the synchronous Hopf threshold. A zoom of the region in Fig. 5.4 where these crossings are undertaken is shown in the right panel of Fig. 5.6. The expected transition in the spectrum as predicted by our theory, and discussed in the caption of Fig. 5.6, is confirmed.

Next, we show analytically that the zero-eigenvalue crossing for the asynchronous mode at  $b = b_-$  corresponds to a bifurcation point where asymmetric equilibria of (5.3.1) bifurcate from the symmetric steady-state solution branch. To show this, we first construct a more general steady-state solution (5.3.1), where we remove the symmetry assumption about the midline  $x = L/2$ . For this more general steady-state, we calculate from the steady-state system for (5.3.1) that

$$V_e(x) = v_1 \frac{\sinh[\omega_v(L-x)]}{\sinh(\omega_v L)} + v_2 \frac{\sinh(\omega_v x)}{\sinh(\omega_v L)}, \quad \omega_v \equiv \sqrt{\sigma_v/D_v}, \quad (5.3.26)$$

where  $v_1 = V_e(0)$  and  $v_2 = V_e(L)$ . By setting  $\epsilon g(u_1, v_1) + k_v V_{ex}(0) = 0$  and  $\epsilon g(u_2, v_2) - k_v V_{ex}(L) = 0$ , we readily derive, in terms of a  $2 \times 2$  symmetric matrix  $\mathcal{A}$ , that

$$\mathcal{A} \begin{pmatrix} v_1 \\ v_2 \end{pmatrix} = z \begin{pmatrix} u_1 \\ u_2 \end{pmatrix}, \quad \mathcal{A} \equiv \begin{pmatrix} 1 + \frac{l_1}{l_0} \coth\left(\frac{L}{l_0}\right) & -\frac{l_1}{l_0} \operatorname{csch}\left(\frac{L}{l_0}\right) \\ -\frac{l_1}{l_0} \operatorname{csch}\left(\frac{L}{l_0}\right) & 1 + \frac{l_1}{l_0} \coth\left(\frac{L}{l_0}\right) \end{pmatrix}. \quad (5.3.27a)$$

Upon setting  $f(u_j, v_j) = 0$ ,  $j = 1, 2$ , we obtain a nonlinear algebraic system

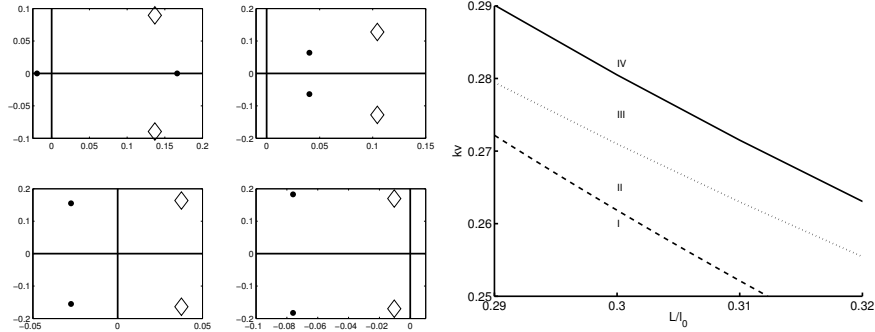


Figure 5.6: The spectrum  $\text{Im}(\lambda)$  versus  $\text{Re}(\lambda)$  (left panel) near the origin for the asynchronous (solid dots) and synchronous (diamonds) modes for a fixed  $L/l_0 = 0.3$ ,  $l_0 = 10$ ,  $q = 5$ ,  $z = 3.5$ ,  $\tau_v = 200$ , and  $\epsilon = 0.015$ , as the coupling strength  $k_v$  crosses various stability boundaries as shown in the right panel, representing a zoom of a portion of the  $k_v$  versus  $L/l_0$  plane of the right panel of Fig. 5.4. Top left  $k_v = 0.26$  (in the horseshoe-shaped region I):  $N = 1$  and  $N = 2$  for the anti-phase and in-phase modes, respectively. Top right:  $k_v = 0.265$  (outside the horseshoe, but before the asynchronous Hopf boundary: region II):  $N = 2$  for both anti-phase and in-phase modes. Bottom Left:  $k_v = 0.275$  (between the asynchronous and synchronous Hopf boundaries: region III):  $N = 0$  for the anti-phase and  $N = 2$  for the in-phase modes. Bottom Right:  $k_v = 0.282$  (above the synchronous Hopf boundary: region IV):  $N = 0$  for both the anti-phase and in-phase modes. These spectral results are all consistent with our stability theory.

for  $\mathbf{u} \equiv (u_1, u_2)^T$  given by  $\mathcal{N}(\mathbf{u}) = 0$ , where

$$\mathcal{N}(\mathbf{u}) \equiv -q \begin{pmatrix} (u_1 - 2)^3 \\ (u_2 - 2)^3 \end{pmatrix} + 4 \begin{pmatrix} 1 \\ 1 \end{pmatrix} + \mathbf{u} - z\mathcal{A}^{-1}\mathbf{u}. \quad (5.3.27b)$$

Since the matrix  $\mathcal{A}$  is symmetric and has a constant row sum, it follows that  $\mathbf{q}_1 \equiv (1, 1)^T$  (in-phase) and  $\mathbf{q}_2 \equiv (1, -1)^T$  (anti-phase) are its two eigenvectors. After some algebra, we obtain that the two corresponding eigenvalues are

$$\mathcal{A}\mathbf{q}_j = \mu_j\mathbf{q}_j; \quad \mu_1 = 1 + \frac{l_1}{l_0} \tanh\left(\frac{L}{2l_0}\right), \quad \mu_2 = 1 + \frac{l_1}{l_0} \coth\left(\frac{L}{2l_0}\right). \quad (5.3.28)$$

To recover the construction of the symmetric steady-state branch we use  $\mathbf{q}_1 \equiv (1, 1)^T$ , and look for a solution to (5.3.27b) with  $u_1 = u_2 \equiv u_e$ . Since  $z\mathcal{A}^{-1}\mathbf{q}_1 = z\mu_1^{-1}\mathbf{q}_1$ , and  $z\mu_1^{-1} = \beta$ , we readily identify that (5.3.27b) reduces to (5.3.3), where  $\beta$  is defined in (5.3.5). To determine whether there are any bifurcation points from this symmetric branch, we write  $\mathbf{u} = u_e(1, 1)^T + \delta\phi$ , where  $\delta \ll 1$  and  $\phi$  is a 2-vector. Upon linearizing (5.3.27b), we readily obtain that

$$\mathcal{A}\phi = \left( \frac{z}{1 - 3q(u_e - 2)^2} \right) \phi. \quad (5.3.29)$$

Bifurcation points correspond to where (5.3.29) has a nontrivial solution. Such points occur whenever

$$\begin{aligned} 1 - 3q(u_e - 2)^2 &= \beta, \quad (\text{in-phase}); \\ 1 - 3q(u_e - 2)^2 &= z \left[ 1 + \frac{l_1}{l_0} \coth\left(\frac{L}{2l_0}\right) \right]^{-1}, \quad (\text{anti-phase}). \end{aligned} \quad (5.3.30)$$

As shown previously, the in-phase equation above is inconsistent with any root of the cubic (5.3.3). In contrast, the anti-phase equation in (5.3.30) is precisely the condition  $b = b_-$ . Therefore, zero eigenvalue crossings for the asynchronous mode correspond to where branches of asymmetric steady-state solutions bifurcate from the symmetric steady-state branch.

In the left panel of Fig. 5.7 we plot a global bifurcation diagram versus the coupling strength  $k_v$  showing only the symmetric and asymmetric steady-state solution branches and the two bifurcation points off of the symmetric branch. This plot corresponds to taking a slice at fixed  $L/l_0$  through the phase diagram in the right panel of Fig. 5.4. It also corresponds to

### 5.3. One Diffusive Species in the Bulk

the solution set of the nonlinear algebraic system (5.3.27b). Although the bifurcation diagram can be obtained from (5.3.27b), we used the numerical bifurcation software XPPAUT [16] after first discretizing (5.3.1) into a large set of ODE's. In this way, the stability properties of the asymmetric steady-state branch was determined numerically. Our computations show that the asymmetric solution branch is unstable except in a narrow window of  $k_v$ . In the right panel of Fig. 5.7 we show results from full numerical solutions to the PDE-ODE system (5.3.1), computed using a method of lines approach, that verify this prediction of a stable window in  $k_v$  for the stability of the asymmetric steady-state solutions.

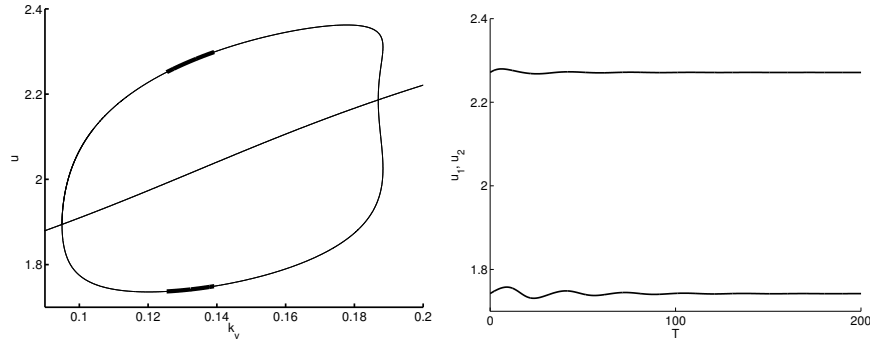


Figure 5.7: Left panel: Global bifurcation diagram of  $u_1$  and  $u_2$ , computed using XPPAUT [16], for the asymmetric and symmetric steady-state solutions to (5.3.1) showing the two bifurcation points off of the symmetric steady-state branch. The parameter values are  $l_0 = 10$ ,  $L/l_0 = 0.4$ ,  $q = 5$ ,  $z = 3.5$ ,  $\tau_v = 200$ , and  $\epsilon = 0.015$ . Thin curves represent unstable steady-state solutions while thick curves indicate stable ones. Right panel: Time evolution of  $u_1$ ,  $u_2$ , as computed from the full PDE-ODE system (5.3.1) using a method of lines approach. The parameter values are in left panel except that  $k_v = 0.13$  is chosen so that the asymmetric steady-state solution is stable. Initial conditions for (5.3.1) are chosen close to the stable asymmetric solution. As expected, the two  $u_i$  approach their steady-state values after a transient period.

In the left panel of Fig. 5.8, we plot a global bifurcation diagram of  $u_1$  versus  $k_v$ , computed using XPPAUT [16], showing only the local branching behavior of the synchronous periodic solution branch near the Hopf bifurcation point where it emerges from the symmetric steady-state branch. In the right panel of Fig. 5.8 we plot the corresponding period of the synchronous

### 5.3. One Diffusive Species in the Bulk

---

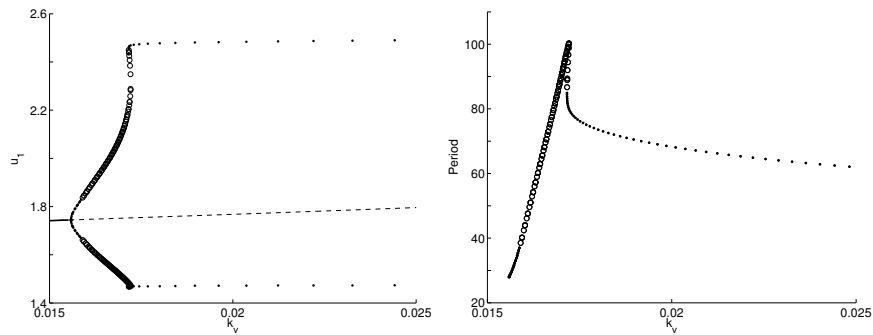


Figure 5.8: Left panel: The global bifurcation diagram of  $u_1$  versus  $k_v$ , computed using XPPAUT [16], for in-phase perturbations, showing the periodic solution branch of synchronous oscillations near the lower Hopf boundary for the synchronous mode in the right panel of Fig. 5.4. The other parameter values are  $L/l_0 = 1.0$ ,  $l_0 = 10$ ,  $q = 5$ ,  $z = 3.5$ ,  $\tau_v = 200$ , and  $\epsilon = 0.015$  corresponding to the parameter set (5.3.10a) of [23]. Right panel: The period of oscillations along the synchronous branch. The solid and open circles in both plots represent stable and unstable periodic solutions, respectively. The solid and dashed lines in the left panel are stable and unstable symmetric steady-state solutions, respectively.

### 5.3. One Diffusive Species in the Bulk

oscillations. The periodic solution branch is found to be supercritical at onset, with a narrow range of  $k_v$  where the branch is unstable. Stability is regained at some larger value of  $k_v$ . From the right panel of Fig. 5.8 the period of oscillations at onset is 27.99, which agrees rather well with the asymptotic result  $T = 2\pi/\lambda_I \approx 30.42$ , where we used  $\lambda_I \approx 0.2065$  as computed from (5.3.22a) for the synchronous mode.

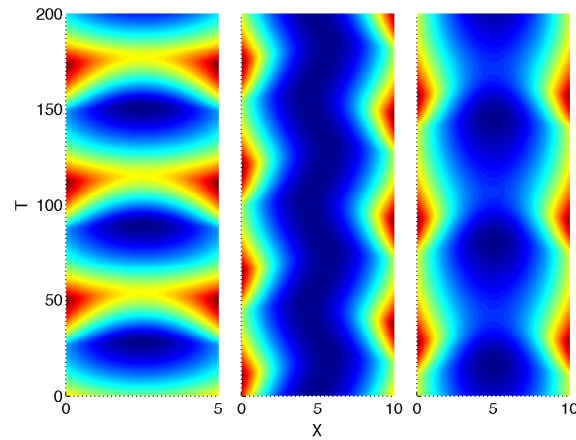


Figure 5.9: Full numerical simulations of the PDE-ODE system (5.3.1) for  $V(x, t)$ , with time running from bottom to top and space represented horizontally. The fixed parameter values are  $q = 5$ ,  $z = 3.5$ ,  $\tau_v = 200$ , and  $\epsilon = 0.015$ . The initial conditions used in the simulation are  $V(x) = 0.5$ ,  $u_1 = 1$ ,  $u_2 = 5$ . Left panel:  $L = 5$  with  $l_1/l_0 = 0.5$  and  $L/l_0 = 0.5$  showing stable synchronous oscillations. Middle panel:  $L = 10$  with  $l_1/l_0 = 0.25$  and  $L/l_0 = 1$  showing stable asynchronous oscillations. Right panel:  $L = 10$  with  $l_1/l_0 = 0.15$  and  $L/l_0 = 1$  corresponding to the parameter set (5.3.10a) of [23].

Finally, to illustrate the oscillatory dynamics, full time-dependent numerical solutions for  $V(x, t)$  from the coupled PDE-ODE system (5.3.1) were computed using a method of lines approach. We choose three parameter sets that are inside the region of the left panel of Fig. 5.4 where both oscillatory modes are unstable with  $N = 2$  unstable eigenvalues for each mode. In the left and middle panels in Fig. 5.9, representing contour plots of  $V(x, t)$ , we show the clear possibility of either stable synchronous or stable asynchronous oscillatory instabilities, depending on the particular point chosen within the instability region. For the right panel in Fig. 5.9, we use

the parameter set (5.3.10a) of [23], for which  $k_v = 0.0225$ , which is close to the stability boundary where a Hopf bifurcation occurs (see the marked point in the left panel of Fig. 5.4). For this parameter set, we observe from the right panel of Fig. 5.8 that the synchronous periodic solution is stable and that the period of oscillations is  $T \approx 64$ . The corresponding full numerical results computed from the PDE-ODE system (5.3.1) shown in the right plot of Fig. 5.9 reveal stable synchronous oscillations with a period close to this predicted value.

### 5.3.2 Stability Analysis for the $\epsilon = \mathcal{O}(1)$ Problem

Next, we study oscillatory dynamics for (5.3.1) when  $\epsilon = 0.3$ , which is a twenty-fold increase over the value used in §5.3.1. We use a combination of a numerical winding number computation, based on (5.3.9), to determine the stability properties of the symmetric steady-state, and Maple [50] to find the roots of (5.3.7) determining the eigenvalues of the linearization of (5.3.1) around the symmetric steady-state solution. Since for this larger value of  $\epsilon$  the PDE-ODE system (5.3.1) is not as computationally stiff as when  $\epsilon = 0.015$ , we are able to use XPPAUT [16] to calculate global branches of synchronous and asynchronous periodic solutions. Asymmetric steady-state branches and their bifurcations are also computed.

In the left panel of Fig. 5.10 we plot the Hopf bifurcation curves, computed from the roots of (5.3.7), in the  $l_1/l_0$  versus  $L/l_0$  plane when  $q = 5$ ,  $z = 3.5$ ,  $\tau_v = 200$ , and  $\epsilon = 0.3$ . In contrast to the similar plot in the left panel of Fig. 5.4 where  $\epsilon = 0.015$ , we observe from the left panel of Fig. 5.10 that the Hopf bifurcation thresholds for the synchronous and asynchronous modes are now rather distinct when  $L/l_0 < 0.5$ . The left horseshoe-shaped curve is the zero-eigenvalue crossing boundary for the asynchronous mode, as parametrized by (5.3.14).

For a fixed  $L/l_0 = 0.4$ , and with  $q = 5$ ,  $z = 3.5$ ,  $\tau_v = 200$ , and  $\epsilon = 0.3$ , in the right panel of Fig. 5.10 we plot the bifurcation diagram of  $u$  with respect to  $l_1/l_0$ , showing the primary solution branches and some secondary bifurcations. This plot corresponds to taking a vertical slice in the phase diagram given in the left panel of Fig. 5.10. There are several key features in this plot. Firstly, as  $l_1/l_0$  is increased from zero, the first bifurcation is to synchronous temporal oscillations. Our computations show that, except in very narrow ranges of  $l_1/l_0$ , the global branch of synchronous oscillations between the two membranes is stable. Secondly, we observe that the asynchronous branch of oscillations that bifurcates from the symmetric steady-state at  $l_1/l_0 \approx 0.41$  is mostly unstable, but exhibits a small region of bistability.

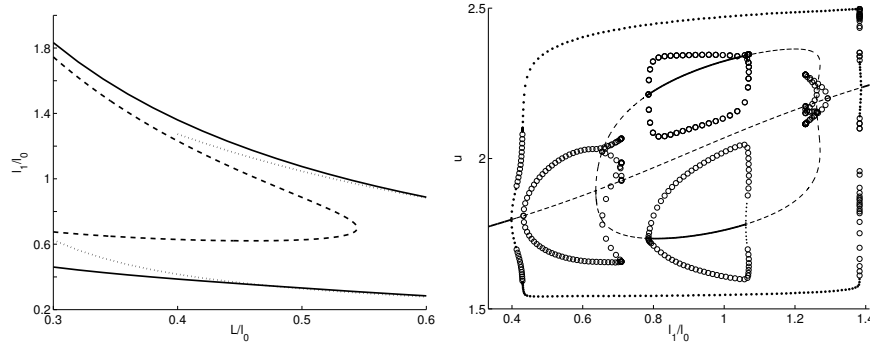


Figure 5.10: Left panel: The Hopf bifurcation boundaries for the synchronous (solid curves) and asynchronous (dotted curves) modes for the one-bulk species model (5.3.1), as computed from solving (5.3.7) with Maple [50] when  $q = 5$ ,  $z = 3.5$ ,  $\tau_v = 200$ , and  $\epsilon = 0.3$ . These Hopf bifurcation thresholds are distinct when  $L/l_0 < 0.5$ . The dashed curve is the zero-eigenvalue crossing for the asynchronous mode, given parametrically by (5.3.14). Right panel: Bifurcation diagram of  $u$  with respect to  $l_1/l_0$  for a fixed  $L/l_0 = 0.4$ . The solid and dashed curves indicate stable and unstable steady-states, respectively. The solid and open circles correspond to stable and unstable periodic solutions, respectively. The synchronous and asynchronous periodic solution branches first bifurcate from the symmetric steady-state at  $l_1/l_0 \approx 0.38$  and  $l_1/l_0 \approx 0.41$ , respectively. Asymmetric steady-state solution branches, that bifurcate from the symmetric steady-state solutions at the zero eigenvalue crossings, are also shown. Additional periodic solution branches, arising from Hopf bifurcations off of these asymmetric steady-states, also occur.

Thirdly, the asymmetric steady-state solution branch bifurcates from the symmetric steady-state branch at two values of  $l_1/l_0$ . These asymmetric steady-states are mostly unstable, but there is a range of  $l_1/l_0$  where they are stabilized. Unstable periodic solution branches, emerge from, and terminate on, the asymmetric steady-state branch. Overall, the bifurcation diagram is rather intricate, and it is beyond the scope of this study to classify and study all of these secondary bifurcations.

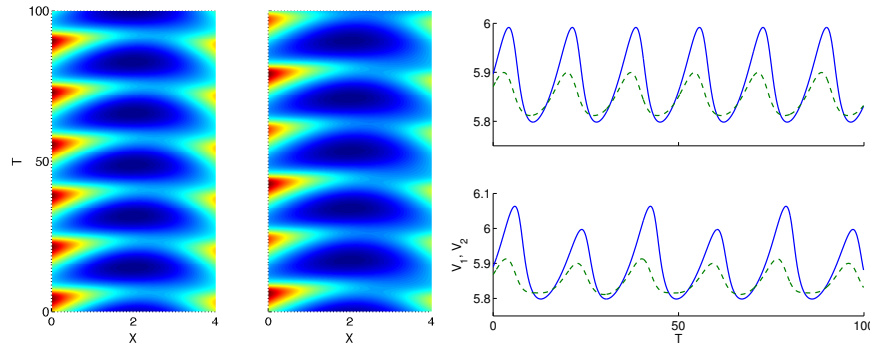


Figure 5.11: Left panel: Contour plot of  $V(x,t)$  computed numerically from the PDE-ODE system (5.3.1) for  $l_1/l_0 \approx 0.406$  ( $k_v = 1.22$ ) (left) and for  $l_1/l_0 \approx 0.41$  ( $k_v = 1.23$ ) (right). The initial condition is  $V(x,0) = 0.5$ ,  $u_1 = 1$ , and  $u_2 = 5$ , at  $t = 0$ . The system exhibits synchronized oscillations with unequal amplitude for  $l_1/l_0 \approx 0.406$ , and synchronized period-doubling oscillations for  $l_1/l_0 \approx 0.41$ . The other parameters are the same as in Fig. 5.10. Right panel: Time series of the inhibitor concentration  $v_1$  and  $v_2$  in the two membranes for  $l_1/l_0 \approx 0.406$  (top) and for  $l_1/l_0 \approx 0.41$  (bottom).

From the right panel in Fig. 5.10, we observe that although the synchronous periodic solution branch is stable in a large range of  $l_1/l_0$ , there is a narrow region  $0.413 < l_1/l_0 < 0.430$  predicted by XPPAUT [16] where the symmetric steady-state and the synchronous periodic solution branch are both unstable. As a result, in this narrow region we anticipate that (5.3.1) will exhibit rather complex dynamics. Due to the small numerical error associated with using XPPAUT on the spatially discretized version of (5.3.1), in our numerical simulations of the PDE-ODE system (5.3.1) shown in Fig. 5.11 we have observed qualitatively interesting dynamics in a slightly shifted interval of  $l_1/l_0$ . The results in Fig. 5.11 are for  $l_1/l_0 = 0.406$  and for

$l_1/l_0 = 0.41$ . From Fig. 5.11, we conclude that as  $l_1/l_0$  is increased through the narrow zone where the synchronous branch is unstable, the two membranes first exhibit synchronized oscillations with a significant distinction in their oscillating amplitudes. This is followed by period-doubling behavior. As  $l_1/l_0$  increases further, the periodic-doubling behavior disappears and the two membranes return to synchronous oscillations with unequal amplitudes.

## 5.4 Two Diffusive Species in the Bulk

In §5.3 we considered the case where only the inhibitor can detach from the membrane and diffuse in the bulk. In this section, we consider the full model (5.1.1) where both the activator and inhibitor undergo bulk diffusion. To partially restrict the wide parameter space for (5.1.1), we will study (5.1.1) for the fixed parameter values

$$D_v = 0.5, \quad D_u = 1.5, \quad \sigma_v = 0.008, \quad \sigma_u = 0.01, \quad z = 3.5, \quad q = 5, \quad (5.4.1a)$$

and we will impose equal coupling strengths so that  $k \equiv k_u = k_v$ . We will vary the domain length  $L$  and  $k$ . We then introduce the diffusion lengths  $l_0$  and  $l_u$ , the ratio of diffusion lengths  $\alpha_u$ , and the two time-constants  $\tau_v$  and  $\tau_u$ , by

$$\begin{aligned} l_0 &\equiv \sqrt{\frac{D_v}{\sigma_v}} \approx 7.9057, & l_u &\equiv \sqrt{\frac{D_u}{\sigma_u}} \approx 12.247, \\ \alpha_u &\equiv \frac{l_0}{l_u} \approx 0.6455, & \tau_v &\equiv \frac{1}{\sigma_v} = 125, & \tau_u &\equiv \frac{1}{\sigma_u} = 100. \end{aligned} \quad (5.4.1b)$$

To determine the stability of the unique symmetric steady-state solution, we first nondimensionalize (5.2.18), in a similar way as was done in (5.3.7) for the one-bulk species model. We obtain that the number  $N$  of eigenvalues  $\lambda$  of the linearization of (5.1.1) in  $\text{Re}(\lambda) > 0$  is

$$N = P + \frac{1}{\pi} [\arg \mathcal{F}_{\pm}^0]_{\Gamma_+}, \quad (5.4.2a)$$

where

$$P = \begin{cases} 2 & \text{if } b = \text{tr} J_e > 0 \\ 0 & \text{if } b = \text{tr} J_e < 0 \end{cases}, \quad b \equiv 1 - \epsilon - 3q(u_e - 2)^2, \quad (5.4.2b)$$

#### 5.4. Two Diffusive Species in the Bulk

---

where  $u_e$  is the unique root of the cubic (5.2.3a), and where  $\mathcal{F}_\pm^0(\lambda)$  is defined by

$$\begin{aligned} \mathcal{F}_\pm^0(\lambda) \equiv & \frac{l_0}{l_1 q_\pm} - \frac{\epsilon \sqrt{1 + \tau_v \lambda} (b + \epsilon - \lambda)}{\det(J_e - \lambda I)} + \frac{\epsilon \alpha_u \sqrt{1 + \tau_u \lambda} (\epsilon + \lambda)}{\det(J_e - \lambda I)} \left( \frac{p_\pm}{q_\pm} \right) \\ & + \left( \frac{\epsilon^2 \alpha_u l_1}{l_0} \right) p_\pm \frac{\sqrt{1 + \tau_v \lambda} \sqrt{1 + \tau_u \lambda}}{\det(J_e - \lambda I)}. \end{aligned} \quad (5.4.3a)$$

Here  $\det(J_e - \lambda I) = \lambda^2 - b\lambda + \epsilon(z - \epsilon - b)$ ,  $q_\pm$  are given in (5.3.8), and  $p_\pm$  are defined by

$$p_+ = \tanh \left( \alpha_u \sqrt{1 + \tau_u \lambda} \frac{L}{2l_0} \right), \quad p_- = \coth \left( \alpha_u \sqrt{1 + \tau_u \lambda} \frac{L}{2l_0} \right). \quad (5.4.3b)$$

We observe that the first two-terms in (5.4.3a) are the same as in (5.3.7), with the last two terms arising from the additional coupling with the activator. As in §5.3.1, it is possible to study (5.4.3) in the limit  $\epsilon \rightarrow 0$  to determine  $N$  analytically for both the synchronous and asynchronous modes, and to asymptotically calculate the Hopf bifurcation frequencies near onset. However, in this section, we will consider the finite  $\epsilon$  problem with  $\epsilon = 0.15$  and use Maple [50] to numerically compute both the roots of (5.4.3) and the winding number in (5.4.2a), which gives  $N$ .

In this way, in the left panel of Fig. 5.12 we show a phase diagram in the  $l_1/l_0$  versus  $L/l_0$  parameter space, where  $l_1 = k/\epsilon$  and  $\epsilon = 0.15$ , with  $k \equiv k_v = k_u$ . The Hopf bifurcation boundaries for the synchronous and asynchronous modes are the solid and dashed curves, respectively. Inside the region bounded by the disjoint solid curves, the synchronous mode is unstable with two unstable eigenvalues. Inside the open loop bounded by the dashed curve, the asynchronous mode is unstable with  $N = 2$ . In contrast to the phase diagrams for the one-bulk species case, no zero-eigenvalue crossings were detected for the parameter set (5.4.1). This aspect is discussed further at the end of this section.

By using XPPAUT [16], in the right panel of Fig. 5.12 we plot the global bifurcation diagram of  $u$  with respect to  $l_1/l_0$  for a fixed vertical slice with  $L = 4$  through the phase diagram in the left panel of Fig. 5.12, so that  $L/l_0 \approx 0.505$ . This plot shows that the synchronous mode first loses stability to a stable periodic solution at  $l_1/l_0 \approx 0.36$ , and that there is a subsequent Hopf bifurcation to the asynchronous mode at  $l_1/l_0 \approx 0.39$ . The key feature in this plot is that the synchronous branch of periodic solutions is almost

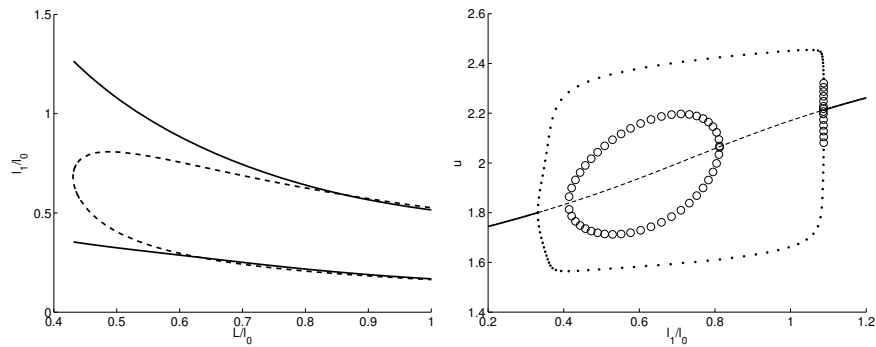


Figure 5.12: Left panel: The Hopf bifurcation boundaries for the synchronous mode (solid curves) and asynchronous mode (dashed curves) for the two-bulk species model (5.1.1), as computed from (5.4.3) with Maple [50] when  $\epsilon = 0.15$  and for the parameters of (5.4.1). Inside the region bounded by the solid curves, the synchronous mode is unstable, while inside the region bounded by the dashed loop the asynchronous mode is unstable. Right panel: Global bifurcation diagram of  $u$  with respect to  $l_1/l_0$  for fixed  $L = 4$  so that  $L/l_0 \approx 0.505$ . The solid/dashed lines are stable/unstable symmetric steady-states. The outer loop, which is almost entirely stable, corresponds to the branch of synchronous oscillations. The inner loop is the unstable branch of asynchronous oscillations.

entirely stable, while the asynchronous branch is unstable. No asymmetric steady-state solutions bifurcating from the symmetric steady-state branch were detected. As a partial confirmation of these theoretical predictions, in Fig. 5.13 we show a contour plot of  $V(x, t)$  computed from the PDE-ODE system (5.1.1) for the parameters of (5.4.1) and with  $\epsilon = 0.15$ ,  $L = 4$ ,  $k = 0.7$ , so that  $L/l_0 \approx 0.505$  and  $l_1/l_0 \approx 0.59$ . With a random initial condition, this plot shows the eventual synchronization of the oscillations in the two membranes. This simulation confirms the prediction of the right panel of Fig. 5.12 that only the synchronous mode is stable for this parameter choice.

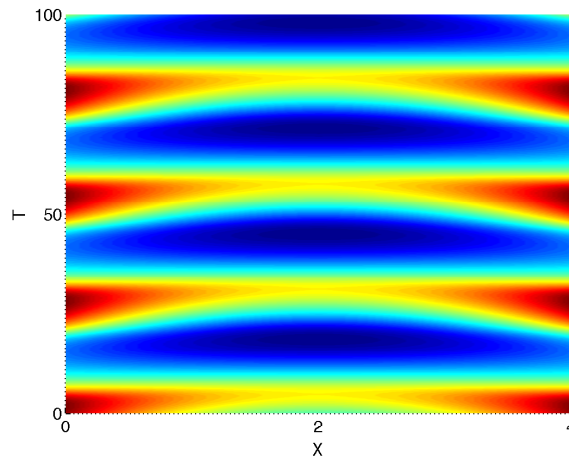


Figure 5.13: Full numerical solution of  $V(x, t)$  computed from the PDE-ODE system (5.1.1) showing stable synchronous oscillations for the parameter values of (5.4.1) and with  $\epsilon = 0.15$ ,  $L = 4$ ,  $k = 0.7$ , so that  $L/l_0 \approx 0.505$  and  $l_1/l_0 \approx 0.59$ . The initial condition for (5.1.1) was  $V(x, 0) = 0.8$  and  $U(x, 0) = 2$ .

We remark that richer spatio-temporal dynamics can occur if we choose a vertical slice through the phase diagram in the left panel of Fig. 5.12 for the larger value  $L = 5.5$ , so that  $L/l_0 \approx 0.70$ . In the right panel of Fig. 5.14 we plot the global bifurcation diagram of  $u$  versus  $l_1/l_0$  for this vertical slice. In contrast to the case where  $L = 4$  in the right panel of Fig. 5.12, we observe from Fig. 5.14 that, as we increase the value of  $l_1/l_0$  from 0.2, the asynchronous mode loses its stability before the synchronous mode. However, as  $l_1/l_0$  is decreased from 0.8, the synchronous mode loses

#### 5.4. Two Diffusive Species in the Bulk

---

its stability at  $l_1/l_0 \approx 0.76$  before the asynchronous mode at  $l_1/l_0 \approx 0.70$ . We again find that the synchronous mode is stable for a wide range of  $l_1/l_0$ . However, in the rather narrow parameter range  $0.290 < l_1/l_0 < 0.305$  both the synchronous and asynchronous modes are unstable. To examine the behavior of the full PDE-ODE system (5.1.1) in this range of  $l_1/l_0$ , in the left panel of Fig. 5.14 we plot the numerically computed time evolution of  $v_2(t) = V(L, t)$  for (5.1.1) when  $l_1/l_0 = 0.30$ . The initial conditions used in the simulation are the same as given in the caption of Fig 5.13. The resulting time-series for  $v_2(t)$  shows the presence of two distinct periods, which is indicative of a torus bifurcation. We expect similar analysis as shown in chapter §3 could be applied here for the initiation of the torus but we will omit it here.

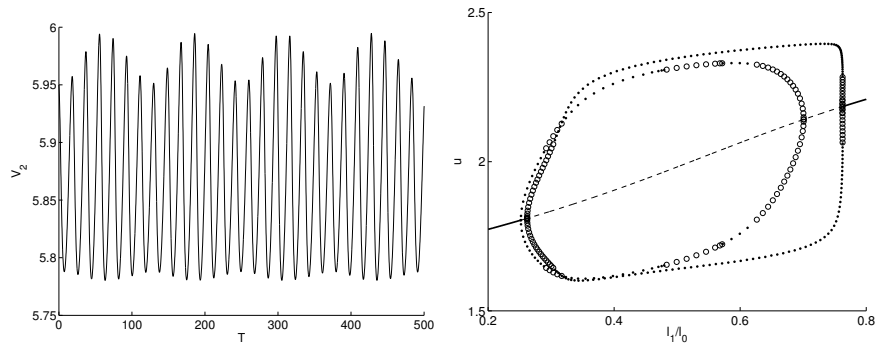


Figure 5.14: Left panel: Plot  $v_2(t) = V(L, t)$  versus  $t$  computed from full PDE-ODE system (5.1.1) for the parameter values of (5.4.1) and with  $\epsilon = 0.15$ ,  $L = 5.5$ ,  $k = 0.35$ , so that  $L/l_0 \approx 0.7$  and  $l_1/l_0 \approx 0.30$ . The resulting time series has two distinct periods, which indicates a possible torus bifurcation where the in-phase and anti-phase periodic solutions change from stable (unstable) to unstable (stable). Right panel: Global bifurcation diagram of  $u$  with respect to  $l_1/l_0$  for fixed  $L = 5.5$ , so that  $L/l_0 \approx 0.7$ . The labeling of the branches and their stability is the same as in the right panel of Fig. 5.12. The closed, primarily outer, loop is the synchronous branch, while the other closed loop is the asynchronous branch, which is mostly unstable. The synchronous branch is again mostly stable. In the window  $0.290 < l_1/l_0 < 0.305$  both the synchronous and asynchronous branches of periodic solutions are unstable. No secondary bifurcations are shown.

Finally, we confirm theoretically that there are no zero-eigenvalue crossings, corresponding to the bifurcation of asymmetric steady-state solutions

#### 5.4. Two Diffusive Species in the Bulk

---

from the symmetric steady-state branch. Proceeding similarly as in (5.3.26)–(5.3.27b) of §5.3.1, we obtain in place of (5.3.27b) that, for any asymmetric steady-state solution of (5.1.1),  $\mathbf{u} = (u_1, u_2)^T$  now satisfies

$$\mathcal{N}(\mathbf{u}) \equiv -q \begin{pmatrix} (u_1 - 2)^3 \\ (u_2 - 2)^3 \end{pmatrix} + 4 \begin{pmatrix} 1 \\ 1 \end{pmatrix} + \mathbf{u} - z\mathcal{A}^{-1}\mathbf{u} - \frac{k}{l_u}\mathcal{B}\mathbf{u} = 0. \quad (5.4.4)$$

where  $\mathcal{A}$  is defined in (5.3.27a) and the symmetric matrix  $\mathcal{B}$  is defined by

$$\mathcal{B} \equiv \begin{pmatrix} \coth\left(\frac{L}{l_u}\right) & -\operatorname{csch}\left(\frac{L}{l_u}\right) \\ -\operatorname{csch}\left(\frac{L}{l_u}\right) & \coth\left(\frac{L}{l_u}\right) \end{pmatrix}. \quad (5.4.5)$$

Since  $\mathcal{B}$  is symmetric with a constant row sum, the eigenvectors  $\mathbf{q}_1 = (1, 1)^T$  and  $\mathbf{q}_2 = (1, -1)^T$  are common to both  $\mathcal{A}$  and  $\mathcal{B}$ . We readily calculate that the two eigenvalues  $\xi_j$  for  $j = 1, 2$  of  $\mathcal{B}$  are  $\xi_1 = \tanh(L/(2l_u))$  and  $\xi_2 = \coth(L/(2l_u))$ .

The symmetric steady-state solution is recovered by seeking a solution to (5.4.4) of the form  $\mathbf{u} = u_e\mathbf{q}_1$ . By using the explicit expressions for the eigenvalues  $\xi_1$  and  $\mu_1$  of  $\mathcal{B}$  and  $\mathcal{A}$ , respectively, where  $\mu_1$  is given in (5.3.28), we readily derive that  $u_e$  satisfies the cubic (5.2.3a). To determine whether there are any bifurcation points from this branch we write  $\mathbf{u} = u_e(1, 1)^T + \delta\phi$  for  $\delta \ll 1$ , and linearize (5.4.4). We conclude that bifurcation points occur whenever

$$-3q(u_e - 2)^2\phi + \phi - z\mathcal{A}^{-1}\phi - \frac{k}{l_u}\mathcal{B}\phi = 0, \quad (5.4.6)$$

has a nontrivial solution  $\phi$ . For the in-phase mode  $\phi = \mathbf{q}_1$ , we use the explicit expressions for  $\xi_1$  and  $\mu_1$  to derive from (5.4.6) that any such a bifurcation point must satisfy  $\beta + a_u - 1 = -3q(u_e - 2)^2$ , where  $\beta$  and  $a_u$  are defined in (5.2.3b). By an identical proof as in §5.3.1, this condition is inconsistent with any root  $u_e$  to the cubic (5.2.3a). Thus, no zero-eigenvalue crossing of the in-phase mode from the symmetric steady-state branch can occur.

For the anti-phase mode  $\phi = \mathbf{q}_2$ , we use the explicit expressions for the eigenvalues  $\xi_2$  and  $\mu_2$  in (5.4.6) to obtain that there is a bifurcation point to an asymmetric steady-state whenever

$$-3q(u_e - 2)^2 + 1 - \frac{k}{l_u}\coth\left(\frac{L}{2l_u}\right) = \frac{z}{1 + \frac{l_1}{l_0}\coth\left(\frac{L}{2l_0}\right)},$$

#### 5.4. Two Diffusive Species in the Bulk

---

has a solution, where  $u_e$  is a root of the cubic (5.2.3a). For the parameter set (5.4.1), we verified numerically that no such solution exists for any point in the phase diagram in the left panel of Fig. 5.12. However, we remark that for other parameter sets, notably when  $\epsilon$  is decreased from  $\epsilon = 0.15$ , such bifurcation points should be possible.

## Chapter 6

# Models in a Two-Dimensional Domain

In previous chapters we have studied coupled bulk-membrane models where the membranes or cells are coupled by diffusive signals in a one-dimensional domain. In this chapter, we formulate a class of coupled cell-bulk models in a two-dimensional domain, which provides a more realistic geometry for modeling experimental observations relating to quorum sensing behavior in thin petri dishes. In our analysis we will not focus on a specific biological application, but rather will formulate and provide a theoretical framework to construct the steady-states and to analyze their linear stability properties for a general class of cell-bulk models, with the aim to predict when synchronous oscillations can be triggered by the cell-bulk coupling. The theory will be illustrated for some specific choices of the intracellular kinetics.

The outline of this chapter is as follows. We first formulate the coupled cell-bulk model with one signaling compartment in a two-dimensional bounded domain in §6.1. Our modeling framework is closely related to the study of quorum sensing behavior in bacteria done in [54] and [55] through the formulation and analysis of similar coupled cell-bulk models in  $\mathbb{R}^3$ . For this 3-D case, in [54] and [55] steady-state solutions were constructed and large-scale dynamics studied in the case where the signaling compartments have small radius of order  $\mathcal{O}(\epsilon)$ . However, due to the rapid  $1/r$  decay of the free-space Green's function for the Laplacian in 3-D, it was shown in [54] and [55] that the release of the signaling molecule leads to only a rather weak communication between the cells of the same  $\mathcal{O}(\epsilon)$  order of the cell radius. As a result, small cells in 3-D are primarily influenced by their own signal, and hence no robust mechanism to trigger collective synchronous oscillations in the cells due to Hopf bifurcations was observed in [54] and [55]. We emphasize that the models of [54] and [55] are based on postulating a diffusive coupling mechanism between distinct, spatially segregated, dynamically active sites. Other approaches for studying quorum sensing behavior, such as in [58], are based on reaction-diffusion (RD) systems, which adopt a homogenization theory approach to treat large populations or colonies of

individual cells as a continuum density, rather than as discrete units as in [54] and [55].

Next in §6.2 we use the method of matched asymptotic expansions to construct steady-state solutions to our 2-D multi-cell-bulk model (6.2.1), and we derive a globally coupled eigenvalue problem whose spectrum characterizes the stability properties of the steady-state. In our 2-D analysis, the interaction between the cells is of order  $\nu \equiv -1/\log \epsilon$ , where  $\epsilon \ll 1$  is the assumed common radius of the small circular cells. In the distinguished limit where the bulk diffusion coefficient  $D$  is of the asymptotic order  $D = \mathcal{O}(\nu^{-1})$ , in §6.3 we show that the leading order approximate steady-state solution and the associated linear stability problem are both independent of the spatial configurations of cells and the shape of the domain. In this regime, we then show that the steady-state solution can be destabilized by either a synchronous perturbation in the cells or by  $m - 1$  possible asynchronous modes of instability. In §6.3 leading-order-in- $\nu$  limiting spectral problems when  $D = D_0/\nu$ , with  $\nu \ll 1$ , for both these classes of instabilities are derived. In §6.4, we illustrate our theory for various intracellular dynamics. When there is only a single dynamically active intracellular component, we show that no triggered oscillations can occur. For two specific intracellular reaction kinetics involving two local species, modeled either by Sel'kov or Fitzhugh-Nagumo (FN) dynamics, in §6.4 we perform detailed analysis to obtain Hopf bifurcation boundaries, corresponding to the onset of either synchronous or asynchronous oscillations, in various parameter planes. In addition to this detailed stability analysis for the  $D = \mathcal{O}(\nu^{-1})$  regime, in §6.5 we show for the case of one cell that when  $D \gg \mathcal{O}(\nu^{-1})$  the coupled cell-bulk model is effectively well-mixed and its solutions can be well-approximated by a finite-dimensional system of nonlinear ODEs. The analytical and numerical study of these limiting ODEs in §6.5 reveals that their steady-states can be destabilized through a Hopf bifurcation. Numerical bifurcation software is then used to show the existence of globally stable time-periodic solution branches that are intrinsically due to the cell-bulk coupling. For the  $D = \mathcal{O}(1)$  regime, where the spatial configuration of the cells in the domain is an important factor, in §6.6 we perform a detailed stability analysis for a ring-shaped pattern of cells that is concentric within the unit disk. For this simple spatial configuration of cells, phase diagrams in the  $\tau$  versus  $D$  parameter space, for various ring radii, characterizing the existence of either synchronous or asynchronous oscillatory instabilities, are obtained for the case of Sel'kov intracellular dynamics. These phase diagrams show that triggered synchronous oscillations can occur when cells become more spatially clustered. In §6.6 we also provide a clear example of quorum sensing

behavior, characterized by the triggering of collective dynamics only when the number of cells exceeds a critical threshold.

Our analysis of synchronous and asynchronous instabilities for (6.2.1) in the  $D = \mathcal{O}(\nu^{-1})$  regime, where the stability thresholds are, to leading-order, independent of the spatial configuration of cells, has some similarities with the stability analysis of [77], [78], [65], and [9] (see also the references therein) for localized spot solutions to various activator-inhibitor RD systems with short range activation and long-range inhibition. In this RD context, when the inhibitor diffusivity is of the order  $\mathcal{O}(\nu^{-1})$ , localized spot patterns can be destabilized by either synchronous or asynchronous perturbations, with the stability thresholds being, to leading-order in  $\nu$ , independent of the spatial configuration of the spots in the domain. The qualitative reason for this similarity between the coupled cell-bulk and localized spot problems is intuitively rather clear. In the RD context, the inhibitor diffusion field is the long-range “bulk” diffusion field, which mediates the interaction between the “dynamically active units”, consisting of  $m$  spatially segregated localized regions of high activator concentration, each of which is self-activating. In this RD context, asynchronous instabilities lead to asymmetric spot patterns, while synchronous oscillatory instabilities lead to collective temporal oscillations in the amplitudes of the localized spots (cf. [77], [78], [65], and [9]).

Finally, we remark that the asymptotic framework for the construction of steady-state solutions to the cell-bulk model (6.2.1), and the analysis of their linear stability properties, relies heavily on the methodology of strong localized perturbation theory (cf. [76]). Related problems where such techniques are used include [37], [63], [45], and [46].

## 6.1 Formulation of a 2-D Coupled Cell-Bulk System

We first formulate and non-dimensionalize our coupled cell-bulk model assuming that there is only one signalling compartment  $\Omega_0$  inside the two-dimensional domain  $\Omega$ . We assume that the cell can release a specific signaling molecule into the bulk region exterior to the cell, and that this secretion is regulated by both the extracellular concentration of the molecule together with its number density inside the cell. If  $\mathcal{U}(\mathbf{X}, T)$  represents the concentration of the signaling molecule in the bulk region  $\Omega \setminus \Omega_0$ , then its spatial-temporal evolution in this region is assumed to be governed by the

### 6.1. Formulation of a 2-D Coupled Cell-Bulk System

---

PDE model

$$\begin{aligned} \mathcal{U}_T &= D_B \Delta_{\mathbf{X}} \mathcal{U} - k_B \mathcal{U}, & \mathbf{X} &\in \Omega \setminus \Omega_0, \\ \partial_{n_{\mathbf{X}}} \mathcal{U} &= 0, & \mathbf{X} &\in \partial\Omega, \\ D_B \partial_{n_{\mathbf{X}}} \mathcal{U} &= \beta_1 \mathcal{U} - \beta_2 \mu^1, & \mathbf{X} &\in \partial\Omega_0, \end{aligned} \quad (6.1.1a)$$

where, for simplicity, we assume that the signalling compartment  $\Omega_0 \in \Omega$  is a disk of radius  $\sigma$  centered at some  $\mathbf{X}_0 \in \Omega$ .

Next, we suppose that inside the cell there are  $n$  interacting species  $\boldsymbol{\mu} \equiv (\mu^1, \dots, \mu^n)$  whose dynamics are governed by  $n$ -ODEs of the form

$$\frac{d\boldsymbol{\mu}}{dT} = k_R \mu_c \mathbf{F}(\boldsymbol{\mu}/\mu_c) + \mathbf{e}_1 \int_{\partial\Omega_0} (\beta_1 \mathcal{U} - \beta_2 \mu^1) dS_{\mathbf{X}}, \quad (6.1.1b)$$

where  $\mathbf{e}_1 \equiv (1, 0, \dots, 0)^T$ . Here  $\boldsymbol{\mu} = (\mu^1, \dots, \mu^n)^T$  represents the total amount of the  $n$  species inside the cell, while  $k_R > 0$  is the reaction rate for the intracellular dynamics. The scaling constant  $\mu_c > 0$  is a dimensional constant measuring a typical value for  $\boldsymbol{\mu}$  inside the compartment. The dimensionless function  $\mathbf{F}(\mathbf{u})$  models the reaction dynamics for the local species within the cell. We remark that the integration in (6.1.1b) is over the boundary  $dS_{\mathbf{X}}$  of the cell.

In this coupled cell-bulk model,  $D_B > 0$  is the diffusion coefficient for the bulk process,  $k_B$  is the rate at which the signalling molecule is degraded in the bulk, while  $\beta_1 > 0$  and  $\beta_2 > 0$  are the dimensional influx (efflux) constants modeling the permeability of the cell wall. In addition,  $\partial_{n_{\mathbf{X}}}$  denotes either the outer normal derivative of  $\Omega$ , or the outer normal to  $\Omega_0$  (which points inside the bulk region). The flux  $\beta_1 \mathcal{U} - \beta_2 \mu^1$  on the cell membrane models the influx of the signaling molecule into the extracellular bulk region, which depends on both the external bulk concentration  $\mathcal{U}(\mathbf{X}, T)$  at the cell membrane  $\partial\Omega_0$  as well as on the intracellular concentration  $\mu^1$  within the cell. Only one of the intracellular species,  $\mu^1$ , is capable of leaving the cell into the bulk.

If we let  $[\gamma]$  denote the dimensions of the variable  $\gamma$ , then the dimensions of the various quantities in (6.1.1) are as follows:

$$\begin{aligned} [\mathcal{U}] &= \frac{\text{moles}}{(\text{length})^2}, & [\boldsymbol{\mu}] &= \text{moles}, & [\mu_c] &= \text{moles}, & [D_B] &= \frac{(\text{length})^2}{\text{time}}, \\ [k_B] &= [k_R] = \frac{1}{\text{time}}, & [\beta_1] &= \frac{\text{length}}{\text{time}}, & [\beta_2] &= \frac{1}{\text{length} \times \text{time}}. \end{aligned} \quad (6.1.2)$$

### 6.1. Formulation of a 2-D Coupled Cell-Bulk System

---

We now nondimensionalize this model by introducing the dimensionless variables  $t$ ,  $\mathbf{x}$ ,  $U$ , and  $\mathbf{u}$  defined by

$$t = T/t_R, \quad \mathbf{x} = \mathbf{X}/L, \quad U = \frac{L^2}{\mu_c} \mathcal{U}, \quad \mathbf{u} = \frac{\boldsymbol{\mu}}{\mu_c}, \quad (6.1.3)$$

where  $L$  is a typical radius of  $\Omega$ . In terms of these variables, (6.1.1) becomes

$$\begin{aligned} \frac{1}{k_B t_R} U_t &= \frac{D_B}{k_B L^2} \Delta_{\mathbf{x}} U - U, & \mathbf{x} \in \tilde{\Omega} \setminus \tilde{\Omega}_0, \\ \partial_{n_{\mathbf{x}}} U &= 0, & \mathbf{x} \in \partial \tilde{\Omega}, \\ \frac{D_B}{L^3} \partial_{n_{\mathbf{x}}} U &= \frac{\beta_1}{L^2} U - \beta_2 u^1, & \mathbf{x} \in \partial \tilde{\Omega}_0, \end{aligned} \quad (6.1.4a)$$

which is coupled to the intracellular dynamics

$$\frac{1}{k_R t_R} \frac{d\mathbf{u}}{dt} = \mathbf{F}(\mathbf{u}) + \frac{L \mathbf{e}_1}{k_R} \int_{\partial \tilde{\Omega}_0} \left( \frac{\beta_1}{L^2} U - \beta_2 u^1 \right) dS_{\mathbf{x}}. \quad (6.1.4b)$$

Here  $\tilde{\Omega}_0$  is a sphere centered at some  $\mathbf{x}_0$  of radius  $\sigma/L$ .

We then choose  $t_R$  based on the time-scale of the reaction kinetics, and introduce an effective dimensionless diffusivity  $D$ , both which are defined by

$$t_R \equiv \frac{1}{k_R}, \quad D \equiv \frac{D_B}{k_B L^2}. \quad (6.1.5)$$

Then, (6.1.4) can be written as

$$\begin{aligned} \frac{k_R}{k_B} U_t &= D \Delta_{\mathbf{x}} U - U, & \mathbf{x} \in \tilde{\Omega} \setminus \tilde{\Omega}_0, \\ \partial_{n_{\mathbf{x}}} U &= 0, & \mathbf{x} \in \partial \tilde{\Omega}, \\ D \partial_{n_{\mathbf{x}}} U &= \frac{\beta_1}{k_B L} U - \frac{\beta_2 L}{k_B} u^1, & \mathbf{x} \in \partial \tilde{\Omega}_0, \end{aligned} \quad (6.1.6a)$$

which is coupled to the intracellular dynamics

$$\frac{d\mathbf{u}}{dt} = \mathbf{F}(\mathbf{u}) + \frac{k_B \mathbf{e}_1}{k_R} \int_{\partial \tilde{\Omega}_0} \left( \frac{\beta_1}{k_B L} U - \frac{\beta_2 L}{k_B} u^1 \right) dS_{\mathbf{x}}. \quad (6.1.6b)$$

We now introduce our scaling assumption that the radius of the cell is small compared to the radius of the domain, so that  $\epsilon \equiv \sigma/L \ll 1$ . However, in order that the signalling compartment has a non-negligible effect on the

### 6.1. Formulation of a 2-D Coupled Cell-Bulk System

---

bulk process, we need to assume that  $\beta_1$  and  $\beta_2$  are both  $\mathcal{O}(\epsilon^{-1}) \gg 1$  as  $\epsilon \rightarrow 0$ . In this way, (6.1.6) reduces to the dimensionless coupled system

$$\begin{aligned} \tau U_t &= D \Delta_{\mathbf{x}} U - U, & \mathbf{x} &\in \tilde{\Omega} \setminus \tilde{\Omega}_0, \\ \partial_{n_{\mathbf{x}}} U &= 0, & \mathbf{x} &\in \partial \tilde{\Omega}, \\ \epsilon D \partial_{n_{\mathbf{x}}} U &= d_1 U - d_2 u^1, & \mathbf{x} &\in \partial \tilde{\Omega}_0, \end{aligned} \quad (6.1.7a)$$

where  $\tilde{\Omega}_0$  is a disk of radius  $\epsilon \ll 1$  centered at some  $x_0 \in \tilde{\Omega}$ . This bulk process is coupled to the intracellular dynamics described by

$$\frac{d\mathbf{u}}{dt} = \mathbf{F}(\mathbf{u}) + \frac{\mathbf{e}_1}{\tau \epsilon} \int_{\partial \tilde{\Omega}_0} (d_1 U - d_2 u^1) dS_{\mathbf{x}}. \quad (6.1.7b)$$

The key  $\mathcal{O}(1)$  dimensionless parameters in (6.1.7) are  $\tau$ ,  $D$ ,  $d_1$ , and  $d_2$ , defined by

$$\tau \equiv \frac{k_R}{k_B}, \quad D \equiv \frac{D_B}{k_B L^2}, \quad \beta_1 \equiv (k_B L) \frac{d_1}{\epsilon}, \quad \beta_2 \equiv \left( \frac{k_B}{L} \right) \frac{d_2}{\epsilon}. \quad (6.1.8)$$

We remark that the limit  $\tau \ll 1$  ( $\tau \gg 1$ ) corresponds to when the intracellular dynamics is very slow (fast) with respect to the time-scale of degradation of the signalling molecule in the bulk. The limit  $D \gg 1$  corresponds to when the bulk diffusion length  $\sqrt{D_B/k_B}$  is large compared to the length-scale  $L$  of the overall domain. Finally, we remark that upon using the divergence theorem, we can readily establish that

$$\frac{d}{dt} \left( \int_{\tilde{\Omega} \setminus \tilde{\Omega}_0} U d\mathbf{x} + \mathbf{e}^T \mathbf{u} \right) = -\frac{1}{\tau} \int_{\tilde{\Omega} \setminus \tilde{\Omega}_0} U d\mathbf{x} + \mathbf{e}^T \mathbf{F}(\mathbf{u}), \quad (6.1.9)$$

where  $\mathbf{e} \equiv (1, \dots, 1)^T$ . The left-hand side of this expression is the total amount of material inside the cells and in the bulk, while the right-hand side characterizes the bulk degradation and production within the cell.

Our analysis of the 2-D coupled cell-bulk model (6.1.7), and its multi-cell counterpart (6.2.1), which extends the 3-D modeling paradigm of [54] and [55], has the potential of providing a theoretical framework to model quorum sensing behavior in experiments performed in petri dishes, where cells live on a thin substrate. In contrast to the assumption of only one active intracellular component used in [54] and [55], in our study we will allow for  $m$  small spatially segregated cells with multi-component intracellular dynamics. We will show for our 2-D case that the communication between small

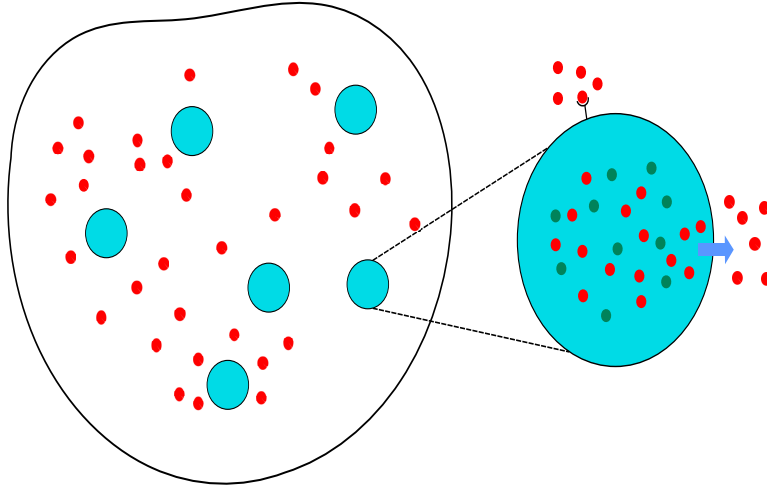


Figure 6.1: Schematic diagram showing the internal molecule reactions and external passive diffusion of the signal. The small shaded regions are the signalling compartments or cells.

cells through the diffusive medium is much stronger than in 3-D, and leads in certain parameter regimes to the triggering of synchronous oscillations, which otherwise would not be present in the absence of any cell-bulk coupling. In addition, when  $D = \mathcal{O}(1)$ , we show that the spatial configuration of small cells in the domain is an important factor in triggering collective synchronous temporal instabilities in the cells.

## 6.2 Analysis of the Dimensionless 2-D Cell-Bulk System

With the motivation provided in §6.1, in this section we analyze a general class of dimensionless coupled cell-bulk dynamics, in a two-dimensional bounded domain  $\Omega$  that contains  $m$  small, disjoint, cells or compartments that are scattered inside  $\Omega$ . We assume that each cell is a small region of radius  $\mathcal{O}(\epsilon) \ll 1$ , and that both the diameter of  $\Omega$  and the distance between any two cells is  $\mathcal{O}(1)$  as  $\epsilon \rightarrow 0$ . A schematic plot of the geometry is shown in Fig. 6.1.

In analogy with the dimensional reasoning provided in §6.1, if  $U(\mathbf{x}, t)$  represents the dimensionless concentration of the signaling molecule in the

## 6.2. Analysis of the Dimensionless 2-D Cell-Bulk System

---

bulk region between the cells, then its spatial-temporal evolution in this region is governed by the dimensionless PDE model

$$\begin{aligned} \tau U_t &= D\Delta U - U, & \mathbf{x} &\in \Omega \setminus \cup_{j=1}^m \Omega_{\epsilon_j}, \\ \partial_n U &= 0, & \mathbf{x} &\in \partial\Omega, \\ \epsilon D \partial_{n_j} U &= d_1 U - d_2 u_j^1, & \mathbf{x} &\in \partial\Omega_{\epsilon_j}, \quad j = 1, \dots, m. \end{aligned} \quad (6.2.1a)$$

Here  $D > 0$  is the diffusion coefficient of the bulk,  $d_1 > 0$ ,  $d_2 > 0$  are the dimensionless influx (efflux) constants modeling the permeability of the cell wall,  $\partial_n$  denotes the outer normal derivative of  $\Omega$ , and  $\partial_{n_j}$  denotes the outer normal to each  $\Omega_{\epsilon_j}$ , which points inside the bulk region. We assume that  $\Omega_{\epsilon_j}$  is a domain of radius  $\mathcal{O}(\epsilon)$  that shrinks uniformly to a point  $\mathbf{x}_j \in \Omega$  as  $\epsilon \rightarrow 0$  for each  $j = 1, \dots, m$ . The signalling cell, or compartment,  $\Omega_{\epsilon_j}$  is assumed to lie entirely within  $\Omega$ . The flux  $d_1 U - d_2 u_j^1$  on each cell membrane models the influx of the signaling molecule into the extracellular bulk region, which depends on both the external bulk concentration  $U(\mathbf{x}, t)$  at the cell membrane  $\partial\Omega_{\epsilon_j}$  as well as on the amount  $u_j^1$  of the intracellular species within the  $j$ -th cell.

We suppose that inside each of the  $m$  cells there are  $n$  species that can interact with each other, and that their dynamics are governed by  $n$ -ODEs of the form

$$\frac{d\mathbf{u}_j}{dt} = \mathbf{F}_j(\mathbf{u}_j) + \frac{1}{\epsilon\tau} \int_{\partial\Omega_{\epsilon_j}} (d_1 U - d_2 u_j^1) ds \mathbf{e}_1, \quad (6.2.1b)$$

where  $\mathbf{e}_1 \equiv (1, 0, \dots, 0)^T$ . Here  $\mathbf{u}_j = (u_j^1, \dots, u_j^n)^T$  represents the concentration of the  $n$  species inside the  $j$ -th cell and  $\mathbf{F}_j(\mathbf{u}_j)$  is the vector nonlinearity modeling the chemical dynamics for these local species within the  $j$ -th cell. We remark that the integration in (6.2.1b) is over the boundary of the compartment. Since the perimeter of the compartmental boundary  $\partial\Omega_{\epsilon_j}$  has length  $|\partial\Omega_{\epsilon_j}| = \mathcal{O}(\epsilon)$ , the source term for the ODE in (6.2.1b), arising from the integration over the perimeter, is  $\mathcal{O}(1)$ .

The dimensionless constants  $D$ ,  $\tau$ ,  $d_1$ , and  $d_2$ , are related to their dimensional counterparts by (6.1.8). From (6.1.8), we conclude that when  $\tau \ll 1$  the intracellular dynamics occurs on a much slower time-scale than the time-scale associated with bulk decay. The limit  $D \gg 1$  corresponds to where the diffusion length induced by the bulk diffusivity and the bulk decay rate is much larger than the overall length-scale of the confining domain  $\Omega$ . These simple qualitative will serve as a guide for interpreting our stability results obtained below.

### 6.2.1 The Steady-State Solution for the $m$ Cells System

We first construct an equilibrium solution to (6.2.1) with  $m$  cells scattered in the two-dimensional domain  $\Omega$ . In the next sub-section we will formulate the linear stability problem for this steady-state solution. We assume that the cells are well-separated in the sense that  $\text{dist}(\mathbf{x}_i, \mathbf{x}_j) = \mathcal{O}(1)$  for  $i \neq j$  and  $\text{dist}(\mathbf{x}_j, \partial\Omega) = \mathcal{O}(1)$  for  $j = 1, \dots, m$ .

In our analysis below, for simplicity we assume that each  $\Omega_{\epsilon_j}$  is a circular domain of radius  $\epsilon$  centered at  $\mathbf{x}_j \in \Omega$  for each  $j = 1, \dots, m$ . With such an assumption we are able to provide an explicit approximate solution in the vicinity of each cell. However, as we will remark below, this assumption that each cell has a circular shape is readily extended to the case where the small cells have an arbitrary shape.

Since in an  $\mathcal{O}(\epsilon)$  neighborhood near each cell the solution  $U$  changes rapidly and has a sharp spatial gradient, we will use the method of matched asymptotic expansions to construct the equilibrium solution to (6.2.1). In the inner region near the  $j$ -th cell, we introduce the local variables  $U_j$  and  $\mathbf{y}$ , which are defined by

$$\mathbf{y} = \epsilon^{-1}(\mathbf{x} - \mathbf{x}_j), \quad U_j(\mathbf{y}) = U(\mathbf{x}_j + \epsilon\mathbf{y}). \quad (6.2.2)$$

In terms of these local variables (6.2.1a) transforms to

$$\begin{aligned} D\Delta_{\mathbf{y}}U_j - \epsilon^2U_j &= 0, & |\mathbf{y}| > 1, \\ D\partial_{n_j}U_j &= d_1U_j - d_2u_j^1, & |\mathbf{y}| = 1. \end{aligned} \quad (6.2.3)$$

We look for a radially symmetric solution to (6.2.3) of the form  $U_j = U_j(\rho)$ , where  $\rho \equiv |\mathbf{y}|$  and  $\Delta_{\mathbf{y}} = \partial_{\rho\rho} + \rho^{-1}\partial_{\rho}$  denotes the radially symmetric part of the Laplacian. Then, at the leading order, we seek a radially symmetric solution to

$$\partial_{\rho\rho}U_j + \rho^{-1}\partial_{\rho}U_j = 0, \quad 1 < \rho < \infty, \quad (6.2.4a)$$

subject to the boundary condition

$$D\frac{\partial U_j}{\partial \rho} = d_1U_j - d_2u_j^1, \quad \rho = 1. \quad (6.2.4b)$$

The solution to (6.2.4a), which has logarithmic growth at infinity, is

$$U_j = S_j \log \rho + \chi_j, \quad (6.2.5)$$

where  $\chi_j = U_j(1)$  is to be determined. We refer to  $S_j$  as the *source strength* of the  $j$ -th cell. By satisfying the boundary condition (6.2.4b) at  $\rho = 1$ , we

determine  $\chi_j$  in terms of  $S_j$  and  $u_j^1$  as

$$\chi_j = \frac{1}{d_1}(DS_j + d_2u_j^1), \quad j = 1, \dots, m. \quad (6.2.6)$$

With the inner dynamics (6.2.1b) inside each cell, we find that the source strength  $S_j$  and the steady-state solution  $\mathbf{u}_j$  satisfy the nonlinear algebraic system of equations

$$\mathbf{F}_j(\mathbf{u}_j) + \frac{2\pi D}{\tau}S_j\mathbf{e}_1 = 0, \quad (6.2.7)$$

which, with  $\mathbf{F}_j \equiv (F_j^1, \dots, F_j^n)^T$ , is equivalent to the following system written in component form:

$$F_j^1(u_j^1, \dots, u_j^n) + \frac{2\pi D}{\tau}S_j = 0; \quad F_j^i(u_j^1, \dots, u_j^n) = 0, \quad i = 2, \dots, n.$$

In principle, we can determine  $u_j^1$  from this system in terms of the unknown  $S_j$  as  $u_j^1 = u_j^1(S_j)$ . The remaining steady-state values  $u_2^j, \dots, u_n^j$  also depend on  $S_j$ . Next, in terms of  $u_j^1$ , we derive a system of algebraic equations for  $S_1, \dots, S_m$ , which is then coupled to (6.2.7).

Upon matching the far-field behavior of the inner solution (6.2.5) to the outer solution, we obtain that the outer problem for  $U$  is

$$\begin{aligned} \Delta U - \varphi_0^2 U &= 0, & \mathbf{x} &\in \Omega \setminus \{\mathbf{x}_1, \dots, \mathbf{x}_m\}, \\ \partial_n U &= 0, & \mathbf{x} &\in \partial\Omega, \\ U &\sim S_j \log|\mathbf{x} - \mathbf{x}_j| + \frac{S_j}{\nu} + \chi_j, & \text{as } \mathbf{x} &\rightarrow \mathbf{x}_j, \quad j = 1, \dots, m, \end{aligned} \quad (6.2.8)$$

where we have defined  $\varphi_0$  and  $\nu \ll 1$  by

$$\varphi_0 \equiv 1/\sqrt{D}, \quad \nu \equiv -1/\log \epsilon. \quad (6.2.9)$$

We remark that the singularity condition in (6.2.8) for  $U$  as  $\mathbf{x} \rightarrow \mathbf{x}_j$  is derived by matching the outer solution for  $U$  to the far field behavior of the inner solution (6.2.5). To solve (6.2.8), we introduce the reduced-wave Green's function  $G(\mathbf{x}; \mathbf{x}_j)$ , which satisfies

$$\Delta G - \varphi_0^2 G = -\delta(\mathbf{x} - \mathbf{x}_j), \quad \mathbf{x} \in \Omega; \quad \partial_n G = 0, \quad \mathbf{x} \in \partial\Omega. \quad (6.2.10a)$$

As  $\mathbf{x} \rightarrow \mathbf{x}_j$ , this Green's function has the local behavior

$$G(\mathbf{x}; \mathbf{x}_j) \sim -\frac{1}{2\pi} \log|\mathbf{x} - \mathbf{x}_j| + R_j + o(1), \quad \mathbf{x} \rightarrow \mathbf{x}_j, \quad (6.2.10b)$$

where  $R_j = R_j(\mathbf{x}_j)$  is called the regular part of  $G(\mathbf{x}; \mathbf{x}_j)$  at  $\mathbf{x} = \mathbf{x}_j$ . In terms of  $G(\mathbf{x}; \mathbf{x}_j)$  we can represent the outer solution for  $U$  in (6.2.8) as

$$U(\mathbf{x}) = -2\pi \sum_{i=1}^m S_i G(\mathbf{x}, \mathbf{x}_i). \quad (6.2.11)$$

By expanding  $U$  as  $\mathbf{x} \rightarrow \mathbf{x}_j$ , and equating the resulting expression with the required singularity behavior in (6.2.8), we obtain the following nonlinear algebraic system for  $S_1, \dots, S_m$ :

$$S_j + \frac{\nu}{d_1} \left( DS_j + d_2 u_j^1 \right) + 2\pi\nu \left( S_j R_j + \sum_{i \neq j}^m S_i G_{ji} \right) = 0, \quad j = 1, \dots, m, \quad (6.2.12)$$

where  $G_{ji} \equiv G(\mathbf{x}_j; \mathbf{x}_i)$ . This system is coupled to (6.2.7), which determines  $u_j^1$  in terms of  $S_j$ .

It is convenient to write (6.2.12) in matrix form. To do so, we define the Green's matrix  $\mathcal{G}$ , the vector of source strengths  $\mathbf{S}$  and the vector  $\mathbf{u}^1$ , whose  $j$ -th element is the first local variable in the  $j$ -th cell, by

$$\mathcal{G} \equiv \begin{pmatrix} R_1 & G_{12} & \cdots & G_{1m} \\ G_{21} & R_2 & \cdots & G_{2m} \\ \vdots & \vdots & \ddots & \vdots \\ G_{m1} & G_{m2} & \cdots & R_m \end{pmatrix}, \quad \mathbf{S} \equiv \begin{pmatrix} S_1 \\ S_2 \\ \vdots \\ S_m \end{pmatrix}, \quad \mathbf{u}^1 \equiv \begin{pmatrix} u_1^1 \\ u_2^1 \\ \vdots \\ u_m^1 \end{pmatrix}.$$

By the reciprocity of the Green's function, we have that  $G_{ji} = G_{ij}$ , so that  $\mathcal{G}$  is a symmetric matrix. In terms of this matrix notation, (6.2.12) can be written as

$$\left( 1 + \frac{D\nu}{d_1} \right) \mathbf{S} + 2\pi\nu \mathcal{G} \mathbf{S} = -\frac{d_2}{d_1} \nu \mathbf{u}^1. \quad (6.2.13)$$

Together with (6.2.7), (6.2.13) provides an approximate steady-state solution for  $\mathbf{u}$ , which is coupled to the source strengths  $\mathbf{S}$ . It is rather intractable analytically to write general conditions on the nonlinear kinetics to ensure the existence of a solution to the coupled algebraic system (6.2.7) and (6.2.13). As such, in subsequent sub-sections below we will analyze in detail the solvability of this system for some specific choices for the nonlinear kinetics. We remark that even if we make the assumption that the nonlinear kinetics in the cells are identical, so that  $\mathbf{F}_j = \mathbf{F}$  for  $j = 1, \dots, m$ , we still

have that  $S_j$  and  $\mathbf{u}^1$  depend on  $j$  through as a result of the Green's interaction matrix  $\mathcal{G}$ , which depends on the spatial configuration  $\{\mathbf{x}_1, \dots, \mathbf{x}_m\}$  of the cells.

In summary, after solving the nonlinear algebraic system (6.2.7) and (6.2.13), the approximate steady-state solution for  $U$  is given by (6.2.11) in the outer region, defined at  $\mathcal{O}(1)$  distances from the cells, and (6.2.5) in the neighborhood of each cell. We remark that this approximate steady-state solution is accurate to all orders in  $\nu$ , and our analysis has effectively summed an infinite order logarithmic expansion in powers of  $\nu$  for the steady-state solution. Related 2-D problems involving logarithmic expansions, such as the calculation of the mean first passage time for diffusion in 2-D domains, are studied in [37] and [63] (see also the references therein).

Lastly, we remark on how the analysis can be extended to study the case where the small cells have an arbitrary shape. In this case, the inner problem near the  $j$ -th cell is

$$\begin{aligned} \Delta_{\mathbf{y}} U_j &= 0, & \mathbf{y} &\notin \Omega_j; & D\partial_{n_j} U_j &= d_1 U_j - d_2 u_j^1, & \mathbf{y} &\in \partial\Omega_j, \\ U_j &\sim S_j \log |\mathbf{y}|, & |\mathbf{y}| &\rightarrow \infty. \end{aligned} \tag{6.2.14}$$

Here  $\Omega_j = \epsilon^{-1}\Omega_{\epsilon_j}$  denotes the  $j$ -th cell region when magnified by  $\epsilon^{-1}$ , while  $\partial_{n_j}$  now denotes the outward normal derivative to  $\Omega_j$  as written in the  $\mathbf{y}$  variable. The solution to (6.2.14) can be conveniently decomposed as

$$U_j = \frac{d_2}{d_1} u_j^1 + V_j S_j,$$

where  $V_j$  is the unique solution to

$$\begin{aligned} \Delta_{\mathbf{y}} V_j &= 0, & \mathbf{y} &\notin \Omega_j; & D\partial_{n_j} V_j &= d_1 V_j, & \mathbf{y} &\in \partial\Omega_j, \\ V_j &\sim \log |\mathbf{y}|, & |\mathbf{y}| &\rightarrow \infty. \end{aligned} \tag{6.2.15a}$$

In terms of this solution, we identify the constant  $\xi$  in the far-field behavior of  $V_j$ , which depends on the shape of  $\Omega_j$  and the ratio  $d_1/D$ , by

$$V_j \sim \log |\mathbf{y}| - \log \xi + o(1), \quad |\mathbf{y}| \rightarrow \infty. \tag{6.2.15b}$$

In general  $\xi$  must be calculated numerically from a boundary integral formulation of (6.2.15a). This yields the following far-field behavior of the inner solution  $U_j$  when written in outer variables:

$$U_j \sim S_j \log |\mathbf{x} - \mathbf{x}_j| + \frac{S_j}{\tilde{\nu}} + \frac{d_2 u_j^1}{d_1}, \quad \tilde{\nu} \equiv -1/\log(\epsilon\xi). \tag{6.2.16}$$

By using the divergence theorem in the region between  $\partial\Omega_j$  and a large disk, we can readily verify that (6.2.7) still holds, and that (6.2.8) also holds if we replace  $\nu$  and  $\chi_j$  in (6.2.8) with  $\tilde{\nu}$  and  $d_2 u_j^1/d_1$ , respectively. By repeating our previous analysis, it is clear that we can readily determine a system very similar to (6.2.29). The only essential difference is that one must numerically compute the constant  $\xi$  from the PDE (6.2.15a). This constant defines the gauge function  $\tilde{\nu}$  from (6.2.16). Rather than proceed with this general case, in the next sub-section we study the linearized stability problem for the simpler case where all the cells are circular with a common radius  $\epsilon$ .

### 6.2.2 Formulation of the Linear Stability Problem

Next, we consider the linear stability of the steady-state solution constructed in the previous subsection. We perturb this steady-state solution, denoted here by  $U_e(\mathbf{x})$  in the bulk region, and  $\mathbf{u}_{e,j}$  in the  $j$ -th cell as

$$U = U_e + e^{\lambda t} \eta(\mathbf{x}), \quad \mathbf{u}_j = \mathbf{u}_{e,j} + e^{\lambda t} \phi_j.$$

Upon substituting this perturbation into (6.2.1), we obtain in the bulk region that

$$\begin{aligned} \tau \lambda \eta &= D \Delta \eta - \eta, & \mathbf{x} &\in \Omega \setminus \cup_{j=1}^m \Omega_{\epsilon_j}, \\ \partial_n \eta &= 0, & \mathbf{x} &\in \partial\Omega, \\ \epsilon D \partial_{n_j} \eta &= d_1 \eta - d_2 \phi_j^1, & \mathbf{x} &\in \partial\Omega_{\epsilon_j}. \end{aligned} \quad (6.2.17a)$$

Within the  $j$ -th cell the linearized problem is

$$\lambda \phi_j = J_j \phi_j + \frac{1}{\epsilon \tau} \mathbf{e}_1 \int_{\partial\Omega_{\epsilon_j}} (d_1 \eta - d_2 \phi_j^1) ds, \quad (6.2.17b)$$

where  $J_j$  denotes the Jacobian matrix of the nonlinear kinetics  $\mathbf{F}_j$  evaluated at  $\mathbf{u}_{e,j}$ . We now study (6.2.17) in the limit  $\epsilon \rightarrow 0$  using the method of matched asymptotic expansions. The analysis will provide a limiting globally coupled eigenvalue problem for  $\lambda$ , from which we can investigate possible instabilities.

In the inner region near the  $j$ -th cell, we introduce the local variables  $\mathbf{y} = \epsilon^{-1}(\mathbf{x} - \mathbf{x}_j)$ , with  $\rho = |\mathbf{y}|$ , and let  $\eta_j(\mathbf{y}) = \eta(\mathbf{x}_j + \epsilon \mathbf{y})$ . We will look for the radially symmetric eigenfunction  $\eta_j$  in the inner variable  $\rho$ . Then, from (6.2.17a), upon neglecting higher order algebraic terms in  $\epsilon$ , the inner problem becomes

$$\partial_{\rho\rho} \eta_j + \rho^{-1} \partial_{\rho} \eta_j = 0, \quad 1 < \rho < \infty, \quad (6.2.18a)$$

with boundary condition

$$D \frac{\partial \eta_j}{\partial \rho} = d_1 \eta_j - d_2 \phi_j^1, \quad \rho = 1. \quad (6.2.18b)$$

The solution to this problem is

$$\eta_j = c_j \log \rho + B_j, \quad (6.2.19)$$

where  $c_j$  and  $B_j$  both are unknown constants. Upon satisfying the boundary condition in (6.2.18b), we determine  $B_j$  in terms of  $c_j$  as

$$B_j = \frac{1}{d_1} (D c_j + d_2 \phi_j^1). \quad (6.2.20)$$

Then, upon substituting (6.2.19) and (6.2.20) into (6.2.17b), we obtain that

$$(J_j - \lambda I) \phi_j + 2\pi \frac{D}{\tau} c_j \mathbf{e}_1 = 0, \quad j = 1, \dots, m. \quad (6.2.21)$$

In the outer region, defined at  $\mathcal{O}(1)$  distances from the cells, the outer problem for the eigenfunction  $\eta(\mathbf{x})$  is

$$\begin{aligned} \Delta \eta - \frac{(1 + \tau \lambda)}{D} \eta &= 0, & \mathbf{x} \in \Omega \setminus \{\mathbf{x}_1, \dots, \mathbf{x}_m\}, \\ \partial_n \eta &= 0, & \mathbf{x} \in \partial \Omega, \\ \eta &\sim c_j \log |\mathbf{x} - \mathbf{x}_j| + \frac{c_j}{\nu} + B_j, & \mathbf{x} \rightarrow \mathbf{x}_j, \quad j = 1, \dots, m, \end{aligned} \quad (6.2.22)$$

where  $\nu \equiv -1/\log \epsilon$ . We remark that the singularity condition in (6.2.22) as  $\mathbf{x} \rightarrow \mathbf{x}_j$  is derived by matching the outer solution for  $\eta$  to the far field behavior of the inner solution (6.2.19). To solve (6.2.22), we introduce the Green's function  $G_\lambda(\mathbf{x}; \mathbf{x}_j)$  which satisfies

$$\begin{aligned} \Delta G_\lambda - \varphi_\lambda^2 G_\lambda &= -\delta(\mathbf{x} - \mathbf{x}_j), & \mathbf{x} \in \Omega, \\ \partial_n G_\lambda &= 0, & \mathbf{x} \in \partial \Omega, \\ G_\lambda(\mathbf{x}; \mathbf{x}_j) &\sim -\frac{1}{2\pi} \log |\mathbf{x} - \mathbf{x}_j| + R_{\lambda,j} + o(1), & \mathbf{x} \rightarrow \mathbf{x}_j, \end{aligned} \quad (6.2.23)$$

where  $R_{\lambda,j} \equiv R_\lambda(\mathbf{x}_j)$  is the regular part of  $G_\lambda$  at  $\mathbf{x}_j$ . Here we have defined  $\varphi_\lambda$  by

$$\varphi_\lambda \equiv \sqrt{\frac{1 + \tau \lambda}{D}}. \quad (6.2.24)$$

We will choose the principal branch of  $\varphi_\lambda$ , which ensures that  $\varphi_\lambda$  is analytic in  $\text{Re}(\lambda) > 0$ . For the case of an asymptotically large domain  $\Omega$ , this choice for the branch cut also ensures that  $G_\lambda$  decays as  $|\mathbf{x} - \mathbf{x}_j| \rightarrow \infty$ .

In terms of  $G_\lambda(\mathbf{x}; \mathbf{x}_j)$ , we can represent the outer solution  $\eta(\mathbf{x})$ , which satisfies (6.2.22), as

$$\eta(\mathbf{x}) = -2\pi \sum_{i=1}^m c_i G_\lambda(\mathbf{x}, \mathbf{x}_i). \quad (6.2.25)$$

By matching the singularity condition at  $\mathbf{x} \rightarrow \mathbf{x}_j$ , we obtain a system of equations for  $c_j$  as

$$\frac{c_j}{\nu} + B_j = -2\pi \left( c_j R_{\lambda,j} + \sum_{i \neq j}^m c_i G_{\lambda,ij} \right), \quad j = 1, \dots, m, \quad (6.2.26)$$

where  $G_{\lambda,ij} \equiv G_\lambda(\mathbf{x}_j; \mathbf{x}_i)$ . Upon recalling that  $B_j = \frac{1}{d_1}(Dc_j + d_2\phi_j^1)$  from (6.2.20), we can rewrite (6.2.26) as

$$\frac{c_j}{\nu} + \frac{1}{d_1}(Dc_j + d_2\phi_j^1) + 2\pi(c_j R_{\lambda,j} + \sum_{i \neq j}^m c_i G_{\lambda,ji}) = 0. \quad (6.2.27)$$

It is convenient to write (6.2.27) in matrix notation. To this end, we define the Green's matrix  $\mathcal{G}_\lambda$  and the vectors  $\mathbf{c}$  and  $\boldsymbol{\phi}^1$  by

$$\mathcal{G}_\lambda \equiv \begin{pmatrix} R_{\lambda,1} & G_{\lambda,12} & \cdots & G_{\lambda,1m} \\ G_{\lambda,21} & R_{\lambda,2} & \cdots & G_{\lambda,2m} \\ \vdots & \vdots & \ddots & \vdots \\ G_{\lambda,m1} & G_{\lambda,m2} & \cdots & R_{\lambda,m} \end{pmatrix}, \quad \mathbf{c} \equiv \begin{pmatrix} c_1 \\ c_2 \\ \vdots \\ c_m \end{pmatrix}, \quad \boldsymbol{\phi}^1 \equiv \begin{pmatrix} \phi_1^1 \\ \phi_2^1 \\ \vdots \\ \phi_m^1 \end{pmatrix}. \quad (6.2.28)$$

We observe that the  $j$ -th entry in the vector  $\boldsymbol{\phi}^1 = (\phi_1^1, \dots, \phi_m^1)^T$  is simply the first element in the eigenvector for the  $j$ -th cell. In this way, (6.2.27) can be written in matrix form as

$$\left( 1 + \frac{D\nu}{d_1} \right) \mathbf{c} + \frac{d_2}{d_1} \nu \boldsymbol{\phi}^1 + 2\pi\nu \mathcal{G}_\lambda \mathbf{c} = 0. \quad (6.2.29)$$

Together with (6.2.21), (6.2.29) will yield an eigenvalue problem for  $\lambda$  with eigenvector  $\mathbf{c}$ .

We now determine this eigenvalue problem in a more explicit form by first calculating  $\phi_1$  in terms of  $\mathbf{c}$  from (6.2.21) and then substituting the resulting expression into (6.2.29). If  $\lambda$  is not an eigenvalue of  $J_j$ , we obtain from (6.2.21) that

$$\phi_j = \frac{2\pi D}{\tau} (\lambda I - J_j)^{-1} c_j \mathbf{e}_1,$$

where  $\mathbf{e}_1$  is the  $n$ -vector  $\mathbf{e}_1 = (1, 0, \dots, 0)^T$ . Upon taking the dot product with  $\mathbf{e}_1$ , we isolate  $\phi_j^1$  as

$$\phi_j^1 = \frac{2\pi D}{\tau} c_j \mathbf{e}_1^T (\lambda I - J_j)^{-1} \mathbf{e}_1.$$

This then yields that

$$\phi^1 = 2\pi \frac{D}{\tau} \mathcal{K} \mathbf{c}, \quad (6.2.30a)$$

where  $\mathcal{K} = \mathcal{K}(\lambda)$  is the  $m \times m$  diagonal matrix with diagonal entries

$$\mathcal{K}_j = \mathbf{e}_1^T (\lambda I - J_j)^{-1} \mathbf{e}_1 = \frac{1}{\det(\lambda I - J_j)} \mathbf{e}_1 M_j^T \mathbf{e}_1 = \frac{M_{j,11}}{\det(\lambda I - J_j)}. \quad (6.2.30b)$$

Here  $M_j$  is the  $n \times n$  matrix of cofactors of the matrix  $\lambda I - J_j$ , with  $M_{j,11}$  denoting the matrix entry in the first row and first column of  $M_j$ , given explicitly by

$$M_{j,11} = M_{j,11}(\lambda) \equiv \det \begin{pmatrix} \lambda - \frac{\partial F_j^2}{\partial u_2} \Big|_{\mathbf{u}=\mathbf{u}_{e,j}} & \cdots & -\frac{\partial F_j^2}{\partial u_n} \Big|_{\mathbf{u}=\mathbf{u}_{e,j}} \\ \cdots & \cdots & \cdots \\ -\frac{\partial F_j^n}{\partial u_2} \Big|_{\mathbf{u}=\mathbf{u}_{e,j}} & \cdots & \lambda - \frac{\partial F_j^n}{\partial u_n} \Big|_{\mathbf{u}=\mathbf{u}_{e,j}} \end{pmatrix}. \quad (6.2.31)$$

Here  $F_j^2, \dots, F_j^n$  denote the components of the vector  $\mathbf{F}_j \equiv (F_j^1, \dots, F_j^n)^T$ , characterizing the membrane kinetics.

Next, upon substituting (6.2.30a) into (6.2.29), we obtain the homogeneous  $m \times m$  linear system

$$\mathcal{M} \mathbf{c} = \mathbf{0}, \quad (6.2.32a)$$

where  $\mathcal{M} = \mathcal{M}(\lambda)$  is defined by

$$\mathcal{M} \equiv \left( 1 + \frac{D\nu}{d_1} \right) I + 2\pi\nu \frac{d_2}{d_1\tau} D\mathcal{K} + 2\pi\nu \mathcal{G}_\lambda, \quad (6.2.32b)$$

### 6.3. The Distinguished Limit of $D = \mathcal{O}(\nu^{-1}) \gg 1$

---

where the diagonal matrix  $\mathcal{K}$  has diagonal entries (6.2.30b), and  $\mathcal{G}_\lambda$  is the Green's interaction matrix defined in (6.2.28), which depends on  $\lambda$  as well as on the spatial configuration  $\{\mathbf{x}_1, \dots, \mathbf{x}_m\}$  of the small cells.

We refer to (6.2.32) as the globally coupled eigenvalue problem (GCEP). In the limit  $\epsilon \rightarrow 0$ , we conclude that  $\lambda$  is a discrete eigenvalue of the linearized problem (6.2.17) if and only if  $\lambda$  is a root of the transcendental equation

$$\det \mathcal{M} = 0. \quad (6.2.33)$$

To determine the region of stability, we must seek conditions on the parameters for which any such eigenvalue satisfies  $\text{Re}(\lambda) < 0$ . The corresponding eigenvector  $\mathbf{c}$  of (6.2.32) associated with a root of (6.2.33) gives the spatial information for the eigenfunction in the bulk via (6.2.25).

We now make some remarks on the form of the GCEP. We first observe from (6.2.32b) that when  $D = \mathcal{O}(1)$ , then to leading-order in  $\nu \ll 1$ , we have that  $\mathcal{M} \sim I + \mathcal{O}(\nu)$ . As such, when  $D = \mathcal{O}(1)$ , we conclude that to leading order in  $\nu$  there are no discrete eigenvalues of the linearized problem with  $\lambda = \mathcal{O}(1)$ , and hence no  $\mathcal{O}(1)$  time-scale instabilities. However, since  $\nu = -1/\log \epsilon$  is not very small unless  $\epsilon$  is extremely small, this prediction of no instability in the  $D = \mathcal{O}(1)$  regime may be somewhat misleading at small finite  $\epsilon$ . Instead of finding the roots of (6.2.33) using numerical methods, without first assuming  $\nu \ll 1$ , in the next sub-section we will consider the distinguished limit  $D = \mathcal{O}(\nu^{-1}) \gg 1$  for (6.2.32b) where the linearized stability problem becomes highly tractable analytically. In another, somewhat related, context this large  $D$  distinguished limit regime was found in [77], [78], and [65] (see the references therein) to play a central role in calculating stability thresholds associated with localized spot patterns for certain two-component reaction-diffusion systems in the plane.

### 6.3 The Distinguished Limit of $D = \mathcal{O}(\nu^{-1}) \gg 1$

In the previous section we considered the general case where there are  $m$  dynamically active cells in a two dimensional bounded domain  $\Omega$  with bulk diffusion. For  $\epsilon \rightarrow 0$ , we constructed the steady-state solution for this problem and derived the spectral problem that characterizes the linear stability of this solution.

In this section, we consider the distinguished limit where the signaling molecule in the bulk diffuses rapidly, so that  $D \gg 1$ . More specifically, we will consider the distinguished limit where  $D = \mathcal{O}(\nu^{-1})$ , and hence for some

$D_0 = \mathcal{O}(1)$ , we set

$$D = \frac{D_0}{\nu}. \quad (6.3.1)$$

Under this assumption, we will obtain a leading order approximation to the steady-state solution. We will then analyze the corresponding spectral problem.

Since the reduced-wave Green's function depends on  $D$ , we first approximate it for large  $D$ . We write (6.2.10a) as

$$\Delta G - \frac{\nu}{D_0} G = -\delta(\mathbf{x} - \mathbf{x}_j), \quad \mathbf{x} \in \Omega; \quad \partial_n G = 0, \quad \mathbf{x} \in \partial\Omega. \quad (6.3.2)$$

This problem has no solution when  $\nu = 0$ . Therefore, we expand  $G = G(\mathbf{x}; \mathbf{x}_j)$  for  $D \gg 1$  as

$$G = \frac{1}{\nu} G_{-1} + G_0 + \nu G_1 + \dots \quad (6.3.3)$$

Upon substituting (6.3.3) into (6.3.2), and equating powers of  $\nu$ , we obtain a sequence of problems for  $G_i$  for  $i = -1, 0, 1$ . To leading-order  $\mathcal{O}(\nu^{-1})$ , we get that  $G_{-1}$  satisfies

$$\Delta G_{-1} = 0, \quad \mathbf{x} \in \Omega; \quad \partial_n G_{-1} = 0, \quad \mathbf{x} \in \partial\Omega. \quad (6.3.4)$$

This gives that  $G_{-1}$  is a constant. The  $\mathcal{O}(1)$  system for  $G_0$  is

$$\Delta G_0 = \frac{1}{D_0} G_{-1} - \delta(\mathbf{x} - \mathbf{x}_j), \quad \mathbf{x} \in \Omega; \quad \partial_n G_0 = 0, \quad \mathbf{x} \in \partial\Omega. \quad (6.3.5)$$

Similarly the  $\mathcal{O}(\nu)$  problem satisfied by  $G_1$  is

$$\Delta G_1 = \frac{1}{D_0} G_0, \quad \mathbf{x} \in \Omega; \quad \partial_n G_1 = 0, \quad \mathbf{x} \in \partial\Omega. \quad (6.3.6)$$

The divergence theorem applied to (6.3.5) and (6.3.6) yields that

$$G_{-1} = \frac{D_0}{|\Omega|}, \quad \int_{\Omega} G_0 d\mathbf{x} = 0.$$

In this way, we obtain the following two-term expansion for the reduced-wave Green's function and its regular part  $R_j$  in the limit  $D = D_0/\nu \gg 1$ :

$$G(\mathbf{x}; \mathbf{x}_j) = \frac{D_0}{\nu|\Omega|} + G_0(\mathbf{x}; \mathbf{x}_j) + \dots, \quad R_j = \frac{D_0}{\nu|\Omega|} + R_{0,j} + \dots \quad (6.3.7)$$

6.3. The Distinguished Limit of  $D = \mathcal{O}(\nu^{-1}) \gg 1$

---

Here  $G_0(\mathbf{x}; \mathbf{x}_j)$ , with regular part  $R_{0j}$ , is the Neumann Green's function defined as the unique solution to

$$\begin{aligned} \Delta G_0 &= \frac{1}{|\Omega|} - \delta(\mathbf{x} - \mathbf{x}_j), & \mathbf{x} \in \Omega; \\ \partial_n G_0 &= 0, & \mathbf{x} \in \partial\Omega; & \int_{\Omega} G_0 d\mathbf{x} = 0, \\ G_0(\mathbf{x}; \mathbf{x}_j) &\sim -\frac{1}{2\pi} \log|\mathbf{x} - \mathbf{x}_j| + R_{0j}, & \mathbf{x} \rightarrow \mathbf{x}_j. \end{aligned} \quad (6.3.8)$$

We then substitute the expansion (6.3.7) and  $D = D_0/\nu$  into the nonlinear algebraic system (6.2.7) and (6.2.13), which is associated with the steady-state problem, to obtain that

$$\begin{aligned} \left(1 + \frac{D_0}{d_1}\right) \mathbf{S} + \frac{2\pi m D_0}{|\Omega|} \mathcal{E} \mathbf{S} + 2\pi\nu \mathcal{G}_0 \mathbf{S} &= -\frac{d_2}{d_1} \nu \mathbf{u}^1; \\ \mathbf{F}_j(\mathbf{u}_j) + \frac{2\pi D_0}{\tau\nu} S_j \mathbf{e}_1 &= 0, \quad j = 1, \dots, m, \end{aligned} \quad (6.3.9)$$

where  $\mathcal{E}$  and the Neumann Green's matrix  $\mathcal{G}_0$  are the  $m \times m$  matrices defined by

$$\mathcal{E} \equiv \frac{1}{m} \mathbf{e} \mathbf{e}^T = \frac{1}{m} \begin{pmatrix} 1 & \cdots & 1 \\ \vdots & \ddots & \vdots \\ 1 & \cdots & 1 \end{pmatrix}, \quad \mathcal{G}_0 \equiv \begin{pmatrix} R_{0,1} & G_{0,12} & \cdots & G_{0,1m} \\ G_{0,21} & R_{0,2} & \cdots & G_{0,2m} \\ \vdots & \vdots & \ddots & \vdots \\ G_{0,m1} & G_{0,m2} & \cdots & R_{0,m} \end{pmatrix}. \quad (6.3.10)$$

Here  $\mathbf{e}$  is the  $m \times 1$  vector  $\mathbf{e} \equiv (1, \dots, 1)^T$ .

The leading-order solution to (6.3.9) when  $\nu \ll 1$  has the form

$$\mathbf{S} = \nu \mathbf{S}_0 + \mathcal{O}(\nu^2), \quad \mathbf{u}_j = \mathbf{u}_{j0} + \mathcal{O}(\nu). \quad (6.3.11)$$

From (6.3.9) we conclude that  $\mathbf{S}_0$  and  $\mathbf{u}_{j0}$  satisfy the limiting leading-order nonlinear algebraic system

$$\begin{aligned} \left(1 + \frac{D_0}{d_1}\right) \mathbf{S}_0 + \frac{2\pi m D_0}{|\Omega|} \mathcal{E} \mathbf{S}_0 &= -\frac{d_2}{d_1} \mathbf{u}_0^1; \\ \mathbf{F}_j(\mathbf{u}_{j0}) + \frac{2\pi D_0}{\tau} S_{0j} \mathbf{e}_1 &= 0, \quad j = 1, \dots, m. \end{aligned} \quad (6.3.12)$$

6.3. The Distinguished Limit of  $D = \mathcal{O}(\nu^{-1}) \gg 1$

---

Since this leading order system does not involve the Neumann Green's matrix  $\mathcal{G}_0$ , we conclude that  $\mathbf{S}_0$  is independent of the spatial configuration of the cells in  $\Omega$ .

For the special case where the reaction kinetics  $\mathbf{F}_j$  is identical for each cell, so that  $\mathbf{F}_j = \mathbf{F}$  for  $j = 1, \dots, m$ , we will look for a solution to (6.3.12) with identical source strengths, so that  $S_{0j}$  is independent of  $j$  and  $\mathbf{u}_{0j} = \mathbf{u}_0$  is independent of  $j$ . Therefore, we write

$$\mathbf{S}_0 = S_{0c} \mathbf{e}, \quad (6.3.13)$$

where  $S_{0c}$  is the common source strength. From (6.3.12), where we use  $\mathcal{E} \mathbf{e} = \mathbf{e}$ , this yields that  $S_{0c}$  and  $\mathbf{u}_0$  satisfy the  $m + 1$  dimensional nonlinear algebraic system

$$\left(1 + \frac{D_0}{d_1} + \frac{2\pi m D_0}{|\Omega|}\right) S_{0c} = -\frac{d_2}{d_1} u_0^1, \quad \mathbf{F}(\mathbf{u}_0) + \frac{2\pi D_0}{\tau} S_{0c} \mathbf{e}_1 = 0, \quad (6.3.14)$$

where  $u_0^1$  is the first component of  $\mathbf{u}_0$ . This simple limiting system will be studied in detail in the next section for various choices of the nonlinear kinetics  $\mathbf{F}(\mathbf{u}_0)$ .

Next, we will simplify the globally coupled eigenvalue problem (GCEP), given by (6.2.32), when  $D = D_0/\nu \gg 1$ , and under the assumption that the reaction kinetics are the same in each cell. In the same way as was derived in (6.3.2)–(6.3.7), we let  $D = D_0/\nu \gg 1$  and approximate the  $\lambda$ -dependent reduced Green's function  $G_\lambda(\mathbf{x}; \mathbf{x}_j)$ , which satisfies (6.2.23). For  $\tau = \mathcal{O}(1)$ , we calculate, in place of (6.3.7), that

$$G_\lambda(\mathbf{x}; \mathbf{x}_j) = \frac{D_0}{\nu(1 + \tau\lambda)|\Omega|} + G_0(\mathbf{x}; \mathbf{x}_j) + \mathcal{O}(\nu),$$

$$R_{\lambda,j} = \frac{D_0}{\nu(1 + \tau\lambda)|\Omega|} + R_{0,j} + \mathcal{O}(\nu),$$

where  $G_0(\mathbf{x}; \mathbf{x}_j)$ , with regular part  $R_{0,j}$ , is the Neumann Green's function satisfying (6.3.8). It follows that for  $D = D_0/\nu \gg 1$  and  $\tau = \mathcal{O}(1)$ , we have

$$\mathcal{G}_\lambda = \frac{m D_0}{\nu(1 + \tau\lambda)|\Omega|} \mathcal{E} + \mathcal{G}_0 + \mathcal{O}(\nu), \quad (6.3.15)$$

where  $\mathcal{E}$ , and the Neumann Green's matrix  $\mathcal{G}_0$ , are defined in (6.3.10).

We substitute (6.3.15) into (6.2.32b), and set  $D = D_0/\nu$ . In (6.2.32b), we calculate to leading order in  $\nu$  that the matrix  $\mathcal{K}(\lambda)$ , defined in (6.2.30b), reduces to

$$\mathcal{K} \sim \frac{M_{11}}{\det(\lambda I - J)} + \mathcal{O}(\nu), \quad (6.3.16)$$

### 6.3. The Distinguished Limit of $D = \mathcal{O}(\nu^{-1}) \gg 1$

---

where  $J$  is the Jacobian of  $\mathbf{F}$  evaluated at the solution  $\mathbf{u}_0$  to the limiting problem (6.3.14), and  $M_{11}$  is the cofactor of  $\lambda I - J$  associated with its first row and first column. The  $\mathcal{O}(\nu)$  correction in  $\mathcal{K}(\lambda)$  arises from the higher order terms in the Jacobian resulting from the solution to the full system (6.3.9). In this way, the matrix  $\mathcal{M}$ , defined in (6.2.32b), associated with the GCEP reduces to leading order to

$$\mathcal{M} = a(\lambda)I + b(\lambda)\mathcal{E} + \mathcal{O}(\nu), \quad (6.3.17a)$$

where  $a(\lambda)$  and  $b(\lambda)$  are defined by

$$a(\lambda) = 1 + \frac{D_0}{d_1} + \frac{2\pi d_2}{d_1 \tau} \frac{D_0 M_{11}}{\det(\lambda I - J)}, \quad b(\lambda) = \frac{2\pi m D_0}{(1 + \tau\lambda)|\Omega|}. \quad (6.3.17b)$$

We remark that the  $\mathcal{O}(\nu)$  correction terms in (6.3.17a) arises from both  $2\pi\nu\mathcal{G}_0$ , which depends on the spatial configuration of the cells, and the  $\mathcal{O}(\nu)$  term in  $\mathcal{K}$  as written in (6.3.16).

Therefore, when  $D = D_0/\nu$ , it follows from (6.3.17a) and the criterion (6.2.33) of the GCEP that  $\lambda$  is a discrete eigenvalue of the linearization if and only if there exists a nontrivial solution  $\mathbf{c}$  to

$$(a(\lambda)I + b(\lambda)\mathcal{E})\mathbf{c} = \mathbf{0}, \quad (6.3.18)$$

where  $a(\lambda)$  and  $b(\lambda)$  are defined in (6.3.17b). Any such eigenvalue with  $\text{Re}(\lambda) > 0$  leads to a linear instability of the steady-state solution on the regime  $D = \mathcal{O}(\nu^{-1})$ .

Explicit equations for  $\lambda$  are readily derived from (6.3.18) by using the key property that  $\mathcal{E}\mathbf{e} = \mathbf{e}$  and  $\mathcal{E}\mathbf{q}_j = \mathbf{0}$  for  $j = 2, \dots, m$ , where  $\mathbf{q}_j$  for  $j = 2, \dots, m$  are an orthogonal basis of the  $m - 1$  dimensional perpendicular subspace to  $\mathbf{e}$ , i.e  $\mathbf{q}_j^T \mathbf{e} = 0$ .

In this way, we obtain that  $\lambda$  is a discrete eigenvalue for the *synchronous mode*, corresponding to  $\mathbf{c} = \mathbf{e}$ , whenever  $\lambda$  satisfies

$$a(\lambda) + b(\lambda) \equiv 1 + \frac{D_0}{d_1} + \frac{2\pi d_2}{d_1 \tau} \frac{D_0 M_{11}}{\det(\lambda I - J)} + \frac{2\pi m D_0}{(1 + \tau\lambda)|\Omega|} = 0. \quad (6.3.19)$$

This expression can be conveniently written as

$$\frac{M_{11}}{\det(\lambda I - J)} = -\frac{\tau}{2\pi d_2} \left( \frac{\kappa_1 \tau \lambda + \kappa_2}{\tau \lambda + 1} \right), \text{ where } \kappa_1 \equiv \frac{d_1}{D_0} + 1, \kappa_2 \equiv \kappa_1 + \frac{2m\pi d_1}{|\Omega|}. \quad (6.3.20)$$

#### 6.4. Examples of the Theory: Finite Domain With $D = \mathcal{O}(\nu^{-1})$

---

In contrast,  $\lambda$  is a discrete eigenvalue for the *asynchronous or competition modes*, corresponding to  $\mathbf{c} = \mathbf{q}_j$  for  $j = 2, \dots, m$ , whenever  $\lambda$  satisfies  $a(\lambda) = 0$ , which yields

$$\frac{M_{11}}{\det(\lambda I - J)} = -\frac{\tau}{2\pi d_2} \left( \frac{d_1}{D_0} + 1 \right). \quad (6.3.21)$$

We remark that the synchronous mode depends on the total number  $m$  of cells. In contrast, the asynchronous mode is independent of  $m$ , but does require that  $m \geq 2$ .

Any discrete eigenvalue for either the synchronous or asynchronous modes that satisfies  $\text{Re}(\lambda) > 0$  leads to an instability. If all such eigenvalues satisfy  $\text{Re}(\lambda) < 0$ , then the steady-state solution for the regime  $D = D_0/\nu$  is linearly stable on an  $\mathcal{O}(1)$  time-scale.

### 6.4 Examples of the Theory: Finite Domain With $D = \mathcal{O}(\nu^{-1})$

In this section we will study the leading-order steady-state problem (6.3.14), and its associated spectral problem (6.3.19) and (6.3.21), for various special cases and choices of the reaction kinetics  $\mathbf{F}$ . We would like to investigate the stability properties of the steady-state (6.3.14) as parameters are varying, and in particular, find conditions for Hopf bifurcations to occur.

#### 6.4.1 Example 1: $m$ Cells; One Local Component

To illustrate the asymptotic theory, we first consider a system with  $m$  cells in a two-dimensional bounded domain  $\Omega$  such that the local dynamics inside each cell consists of only a single component with arbitrary scalar kinetics  $F$ . For this case, the steady-state problem for  $\mathbf{u}_0 = u_0$  and  $S$ , given by (6.3.14), reduces to two algebraic equations. We now show that no matter what  $F(u)$  is, the steady-state can never be destabilized by a Hopf bifurcation.

We will study the stability problem for both the synchronous and asynchronous modes. In the one component case, we calculate  $M_{11} = 1$  and  $\det(\lambda I - J) = \lambda - F_u^e$ , where  $F_u^e$  is defined as the derivative of  $F(u)$  evaluated at the steady-state  $u_0$ . It is easily shown that the spectral problem (6.3.20) for the synchronous mode reduces to

$$\lambda^2 - \lambda p_1 + p_2 = 0, \quad p_1 \equiv F_u^e - \frac{\gamma}{\tau} - \frac{\zeta}{\tau}, \quad p_2 \equiv \frac{1}{\tau} \left( \frac{\gamma}{\tau} - \zeta F_u^e \right) = 0, \quad (6.4.1a)$$

#### 6.4. Examples of the Theory: Finite Domain With $D = \mathcal{O}(\nu^{-1})$

---

where

$$\gamma \equiv \frac{2\pi d_2 D_0}{d_1 + D_0} > 0, \quad \zeta \equiv 1 + \frac{2\pi m d_1 D_0}{|\Omega|(d_1 + D_0)} > 1. \quad (6.4.1b)$$

For a Hopf bifurcation to occur we need  $p_1 = 0$  and  $p_2 > 0$ . Upon setting  $p_1 = 0$ , we get

$$F_u^e = \frac{1}{\tau} (\gamma + \zeta) > 0. \quad (6.4.2)$$

Upon substituting (6.4.2) into the expression for  $p_2$  in (6.4.1a) we get

$$p_2 = \frac{1}{\tau} \left( \frac{\gamma}{\tau} - \zeta F_u^e \right) = \frac{1}{\tau^2} (\gamma(1 - \zeta) - \zeta^2) < 0, \quad (6.4.3)$$

since  $\tau > 0$ ,  $\gamma > 0$  and  $\zeta > 1$ . Therefore, there can be no Hopf bifurcation for the synchronous mode. The following result characterizes the stability properties for the synchronous mode:

**Proposition 6.4.1** *Consider the synchronous mode. Suppose that*

$$F_u^e < \frac{\gamma}{\zeta\tau} = \frac{2\pi d_2}{\tau} \left[ 1 + \frac{d_1}{D_0} + \frac{2\pi m d_1}{|\Omega|} \right]^{-1}, \quad (6.4.4)$$

*then we have  $\text{Re}(\lambda) < 0$ , and so the steady-state is linearly stable to synchronous perturbations. If  $F_u^e > \gamma/[\zeta\tau]$ , the linearization has exactly one positive eigenvalue.*

To show this, we note that the steady-state solution is stable to synchronous perturbations if and only if  $p_1 < 0$  and  $p_2 > 0$ . From (6.4.1a),  $p_1 < 0$  and  $p_2 > 0$  when

$$\tau F_u^e < \zeta + \gamma, \quad \tau F_u^e < \gamma/\zeta, \quad (6.4.5)$$

respectively, which implies that we must have  $\tau F_u^e < \min(\zeta + \gamma, \gamma/\zeta)$ . Since  $\zeta > 1$ , the two inequalities in (6.4.5) hold simultaneously only when  $\tau F_u^e < \gamma/\zeta$ . This yields that  $\text{Re}(\lambda) < 0$  when (6.4.4) holds. Finally, when  $F_u^e > \gamma/[\zeta\tau]$ , then  $p_2 < 0$ , and so there is a unique positive eigenvalue.

This result shows that the effect of cell-bulk coupling is that the steady-state of the coupled system can be linearly stable even when the reaction kinetics is self-activating in the sense that  $F_u^e > 0$ . We observe that the stability threshold  $\gamma/\zeta$  is a monotone increasing function of  $D_0$ , with  $\gamma/\zeta \rightarrow 0$  as  $D_0 \rightarrow 0$  and  $\gamma/\zeta$  tending to a limiting value as  $D_0 \rightarrow \infty$ . This shows that as  $D_0$  is decreased, corresponding to when the cells are effectively more

#### 6.4. Examples of the Theory: Finite Domain With $D = \mathcal{O}(\nu^{-1})$

---

isolated from each other, there is a smaller range of  $F_u^e > 0$  where stability can still be achieved.

Next, we will consider the spectral problem for the asynchronous mode. From (6.3.21), we get

$$\frac{1}{\lambda - F_u^e} = -\frac{\tau}{\gamma}, \quad (6.4.6)$$

where  $\gamma$  is defined in (6.4.1b). Therefore,  $\lambda = F_u^e - \gamma/\tau$ , and so  $\lambda$  is real and no Hopf bifurcation can occur. This asynchronous mode is stable if  $F_u^e < \gamma/\tau$ . Since  $\zeta > 1$ , we observe, upon comparing this threshold with that for the synchronous mode in (6.4.4), that the stability criterion for the synchronous mode is the more restrictive of the two stability thresholds.

In summary, we conclude that a Hopf bifurcation is impossible for (6.2.1a) in the parameter regime  $D = D_0/\nu$  when there is only one dynamically active species inside each of  $m$  small cells. Moreover, if  $F_u^e < \gamma/[\zeta\tau]$ , where  $\gamma$  and  $\zeta$  are defined in (6.4.1b), then the steady-state solution is linearly stable to both the synchronous and asynchronous modes.

#### 6.4.2 Example 2: $m$ Cells; Two Local Components

Next we consider  $m$  cells in  $\Omega$ , but now we assume that there are two dynamically active local species inside each cell. Without causing any confusion, we write the intracellular variable as  $\mathbf{u} = (v, w)^T$  and the local kinetics as  $\mathbf{F}(v, w) = (F(v, w), G(v, w))^T$ . In this way, the steady-state problem (6.3.14) becomes

$$\left(1 + \frac{D_0}{d_1} + \frac{2\pi m D_0}{|\Omega|}\right) S_{0c} = -\frac{d_2}{d_1} v_e, \quad F(v_e, w_e) + \frac{2\pi D_0}{\tau} S_{0c} = 0, \quad G(v_e, w_e) = 0. \quad (6.4.7)$$

Given specific forms for  $F$  and  $G$ , we can solve the steady-state problem (6.4.7) either analytically or numerically.

To analyze the stability problem, in a similar way as for the one-species case, we first calculate the cofactor  $M_{11}$  as  $M_{11} = \lambda - G_w^e$  and  $\det(\lambda I - J) = \lambda^2 - \text{tr}(J)\lambda + \det(J)$ , where  $\text{tr}(J)$  and  $\det(J)$  are the trace and determinant of the Jacobian of  $\mathbf{F}$ , given by

$$\text{tr}(J) = F_v^e + G_w^e, \quad \det(J) = F_v^e G_w^e - F_w^e G_v^e. \quad (6.4.8)$$

Here  $F_i^e, G_i^e$  are partial derivatives of  $F, G$  with respect to  $i$ , with  $i \in (v, w)$ , evaluated at the solution to (6.4.7).

Next, we analyze the stability of the steady-state solution with respect to either synchronous or asynchronous perturbations. For the synchronous

#### 6.4. Examples of the Theory: Finite Domain With $D = \mathcal{O}(\nu^{-1})$

---

mode, we obtain, after some algebra, that (6.3.20) can be reduced to the study of the following cubic polynomial in  $\lambda$ :

$$\mathcal{H}(\lambda) \equiv \lambda^3 + \lambda^2 p_1 + \lambda p_2 + p_3 = 0, \quad (6.4.9a)$$

where we have defined  $p_1$ ,  $p_2$ , and  $p_3$  by

$$\begin{aligned} p_1 &\equiv \frac{\gamma}{\tau} + \frac{\zeta}{\tau} - \text{tr}(J), \\ p_2 &\equiv \det(J) - \frac{\gamma}{\tau} G_w^e + \frac{1}{\tau} \left( \frac{\gamma}{\tau} - \zeta \text{tr}(J) \right), \\ p_3 &\equiv \frac{1}{\tau} (\zeta \det(J) - \frac{\gamma}{\tau} G_w^e). \end{aligned} \quad (6.4.9b)$$

Here  $\gamma$  and  $\zeta$  are defined in (6.4.1b).

To determine whether there is any eigenvalue lying in the right-half of the complex  $\lambda$ -plane, and to detect any Hopf bifurcation boundary in the parameter space, we will use the *Routh-Hurwitz criterion* for a cubic function. This criterion gives necessary and sufficient conditions for all of the roots of the cubic polynomial with real coefficients to lie in  $\text{Re}(\lambda) < 0$ . Given a cubic polynomial  $\mathcal{H}(\lambda)$ , the criterion states that a necessary and sufficient condition for all its roots to satisfy  $\text{Re}(\lambda) < 0$  is that the following three conditions on the coefficients hold:

$$p_1 > 0, \quad p_3 > 0, \quad p_1 p_2 > p_3. \quad (6.4.10)$$

To find the conditions that parameters should satisfy on a Hopf bifurcation boundary, we need only consider a special cubic equation which has roots  $\lambda_1 = a < 0$  and  $\lambda_{2,3} = \pm i\omega$ . Thus, such a cubic equation has the form

$$(\lambda - a)(\lambda - i\omega)(\lambda + i\omega) = \lambda^3 - a\lambda^2 + \omega^2\lambda - a\omega^2 = 0. \quad (6.4.11)$$

Comparing this expression with (6.4.9a) and together with *Routh-Hurwitz criterion*, we conclude that the Hopf bifurcation boundary lies in the parameter regime where

$$p_1 > 0, \quad p_3 > 0, \quad (6.4.12a)$$

with the Hopf bifurcation boundary given by

$$p_1 p_2 = p_3. \quad (6.4.12b)$$

We will return to criterion in the next two subsections when we study two specific models for the local kinetics ( $F, G$ ).

#### 6.4. Examples of the Theory: Finite Domain With $D = \mathcal{O}(\nu^{-1})$

---

Next, we consider the spectral problem for the asynchronous mode. Upon substituting the expressions of  $M_{11}$  and  $\det(\lambda I - J)$  into (6.3.21) and reorganizing it, (6.3.21) becomes a quadratic equation in  $\lambda$  given by

$$\lambda^2 - \lambda q_1 + q_2 = 0, \quad q_1 \equiv \text{tr}(J) - \frac{\gamma}{\tau}, \quad q_2 \equiv \det(J) - \frac{\gamma}{\tau} G_w^e. \quad (6.4.13)$$

For a Hopf bifurcation to occur, we require that  $q_1 = 0$  and  $q_2 > 0$ , which yields that

$$\frac{\gamma}{\tau} = \text{tr}(J) = F_v^e + G_w^e, \quad (6.4.14a)$$

provided the inequality

$$\det(J) - \frac{\gamma}{\tau} G_w^e = -G_v^e F_w^e - (G_w^e)^2 > 0, \quad (6.4.14b)$$

holds. Finally, we conclude that  $\text{Re}(\lambda) < 0$  for the asynchronous modes if and only if

$$\text{tr}(J) < \gamma/\tau, \quad \text{and} \quad \det(J) - \frac{\gamma}{\tau} G_w^e > 0. \quad (6.4.15)$$

To write the stability problem for the asynchronous mode in terms of  $D_0$ , we use (6.4.1b) for  $\gamma$  in terms of  $D_0$  to obtain from the conditions (6.4.14a) and (6.4.14b) that the Hopf bifurcation threshold for the asynchronous mode is given by the transcendental equation

$$D_0 = \frac{\tau d_1 \text{tr}(J)}{2\pi d_2 - \tau \text{tr}(J)}, \quad (6.4.16a)$$

provided that the inequality

$$D_0 \left( \frac{2\pi d_2}{\tau} G_w^e - \det(J) \right) < d_1 \det(J), \quad (6.4.16b)$$

is satisfied. We observe that in this formulation, both  $\text{tr}(J)$  and  $\det(J)$  depend on the form of the local kinetics and the steady-state solution, which depends on  $D_0$  and  $\tau$ .

In the next two subsections we study in some detail two specific choices for the local kinetics, and we show phase diagrams where oscillatory instabilities can occur.

### Local Kinetics Described by the Sel'kov Model

We first consider the Sel'kov model, used in simple models of glycolysis, where the functions  $F(v, w)$  and  $G(v, w)$  are given in terms of parameters  $\alpha > 0$ ,  $\mu > 0$ , and  $\epsilon_0 > 0$  by

$$F(v, w) = \alpha w + wv^2 - v, \quad G(v, w) = \epsilon_0 \left( \mu - (\alpha w + wv^2) \right). \quad (6.4.17)$$

First, we determine the approximate steady-state solution by substituting (6.4.17) into (6.4.7). This system can be solved analytically to obtain the steady-state solution

$$v_e = \frac{\mu}{[1 + 2\pi D_0 \beta / \tau]}, \quad w_e = \frac{\mu}{\alpha + v_e^2}, \quad S_{0c} = \beta v_e, \quad (6.4.18a)$$

where we have defined  $\beta > 0$  by

$$\beta \equiv \frac{d_2}{d_1 + D_0 + 2\pi m d_1 D_0 / |\Omega|}. \quad (6.4.18b)$$

As needed below, we first calculate the partial derivatives of  $F$  and  $G$  evaluated at the steady-state solution as

$$F_v^e = 2v_e w_e - 1, \quad F_w^e = \alpha + v_e^2, \quad G_v^e = -2\epsilon_0 v_e w_e, \quad G_w^e = -\epsilon_0(\alpha + v_e^2), \quad (6.4.19a)$$

which yields

$$\det(J) = \epsilon_0 \left( \alpha + v_e^2 \right) > 0, \quad \text{tr}(J) = 2v_e w_e - 1 - \epsilon_0 \left( \alpha + v_e^2 \right). \quad (6.4.19b)$$

To study possible synchronous oscillations of the  $m$  cells, we compute the Hopf bifurcation boundaries as given in (6.4.12), where we use (6.4.19). For the parameter set  $\tau = 1$ ,  $D_0 = 1$ ,  $|\Omega| = 10$ ,  $\mu = 2$ ,  $\alpha = 0.9$ , and  $\epsilon_0 = 0.15$ , we obtain the Hopf bifurcation boundary in the  $d_1$  versus  $d_2$  parameter plane as shown by the solid curves in Fig. 6.2 for  $m = 1, 2, 3$ .

Next, to obtain instability thresholds corresponding to asynchronous mode, we substitute (6.4.19a) into (6.4.14) and obtain that, the Hopf bifurcation boundary is given by

$$\gamma = \tau \text{tr}(J) \equiv \tau \left[ 2v_e w_e - 1 - \epsilon_0(\alpha + v_e^2) \right], \quad (6.4.20)$$

provided that  $\det(J) - \text{tr}(J)G_w^e > 0$ . This latter condition can be written, using (6.4.19a), as  $\epsilon_0(\alpha + v_e^2) (1 + \text{tr}(J)) > 0$ , and so is satisfied provided

#### 6.4. Examples of the Theory: Finite Domain With $D = \mathcal{O}(\nu^{-1})$

---

that  $\text{tr}(J) > -1$ . Since  $\gamma > 0$  from (6.4.20), we must have  $\text{tr}(J) > 0$ , which guarantees that  $\det(J) - \text{tr}(J)G_w^e > 0$  always holds at a Hopf bifurcation. In this way, and by substituting (6.4.18) for  $w_e$  into (6.4.20), we obtain that the asynchronous mode has a pure imaginary pair of complex conjugate eigenvalues when

$$\gamma = \tau \left[ \frac{2v_e\mu}{\alpha + v_e^2} - 1 - \epsilon_0 \left( \alpha + v_e^2 \right) \right], \quad \text{where} \quad v_e = \frac{\mu}{\left[ 1 + 2\pi D_0 \beta / \tau \right]}, \quad (6.4.21)$$

where  $\gamma$  and  $\beta$ , depending on  $d_1$ ,  $d_2$ ,  $m$ ,  $|\Omega|$ , and  $D_0$ , are defined in (6.4.1b) and (6.4.18b), respectively. By using these expressions for  $\gamma$  and  $\beta$ , we can readily determine a parametric form for the Hopf bifurcation boundary in the  $d_1$  versus  $d_2$  plane as the solution to a linear algebraic system for  $d_1$  and  $d_2$  in terms of the parameter  $v_e$  with  $0 < v_e < \mu$ . Some simple algebra yields that

$$d_1 = \frac{D_0(a_{12} - a_{22})}{a_{11}a_{22} - a_{21}a_{12}}, \quad d_2 = \frac{D_0(a_{21} - a_{11})}{a_{11}a_{22} - a_{21}a_{12}}, \quad (6.4.22a)$$

where  $a_{11}$ ,  $a_{12}$ ,  $a_{22}$ , and  $a_{21}$ , are defined in terms of the parameter  $v_e$  by

$$a_{11} \equiv 1 + \frac{2\pi m D_0}{|\Omega|}, \quad a_{12} \equiv -\frac{1}{\beta(v_e)}, \quad a_{21} \equiv 1, \quad a_{22} \equiv -\frac{2\pi D_0}{\gamma(v_e)}, \quad (6.4.22b)$$

where

$$\gamma(v_e) \equiv \tau \left[ \frac{2v_e\mu}{\alpha + v_e^2} - 1 - \epsilon_0 \left( \alpha + v_e^2 \right) \right], \quad \beta(v_e) \equiv \tau \frac{(\mu - v_e)}{2\pi D_0 v_e}. \quad (6.4.22c)$$

By varying  $v_e$ , with  $0 < v_e < \mu$ , and retaining only the portion of the curve for which  $d_1 > 0$  and  $d_2 > 0$ , we obtain a parametric form for the Hopf bifurcation boundary for the asynchronous mode in the  $d_1$  versus  $d_2$  parameter plane. For  $m = 2$  and  $m = 3$ , these are the dashed curves shown in Fig. 6.2.

6.4. Examples of the Theory: Finite Domain With  $D = \mathcal{O}(\nu^{-1})$

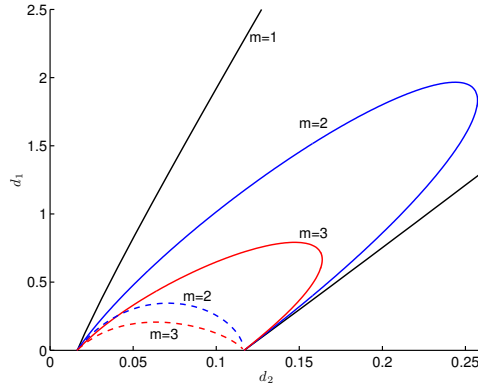


Figure 6.2: Hopf bifurcation boundaries for the synchronous (solid curve) and asynchronous (dashed curve) modes for the Sel'kov model with various number  $m$  of cells in the  $d_1$  versus  $d_2$  parameter plane. The synchronous mode for  $m = 1$  between the two black lines is unstable. For  $m = 2$  and  $m = 3$  the synchronous mode is unstable in the horseshoe-shaped region bounded by the blue and red solid curves, respectively. Inside the dotted regions for  $m = 2$  and  $m = 3$  the asynchronous mode is unstable. For the asynchronous mode, the boundary of these regions is given parametrically by (6.4.22). The parameters used are  $\mu = 2$ ,  $\alpha = 0.9$ ,  $\epsilon_0 = 0.15$ ,  $\tau = 1$ ,  $D_0 = 1$ , and  $|\Omega| = 10$ .

We now discuss qualitative aspects of the Hopf bifurcation boundaries for both synchronous and asynchronous modes for various choices of  $m$  as seen in Fig. 6.2. For  $m = 1$ , we only need to consider the synchronous instability. The Hopf bifurcation boundary is given by the two black lines, and the region with unstable oscillatory dynamics is located between these two lines. For  $m = 2$ , inside the region bounded by the blue solid curve, the synchronous mode is unstable and under the blue dashed curve, the asynchronous mode is unstable. Similar notation applies to the case with  $m = 3$ , where the Hopf bifurcation boundaries for synchronous/asynchronous mode are denoted by red solid/dashed curves.

One key qualitative feature we can observe from Fig. 6.2 is that the oscillatory region for a larger value of  $m$  lies completely within the unstable region for smaller  $m$  for both the synchronous and asynchronous modes. This suggests that if a coupled system with  $m_1$  cells is unstable to synchronous perturbations, then a system with  $m_2 < m_1$  cells will also be unstable to such perturbations. However, if a two-cell system is unstable, it is possible

6.4. Examples of the Theory: Finite Domain With  $D = \mathcal{O}(\nu^{-1})$

that a system with three cells, with the same parameter set, can be stable. Finally, we observe qualitatively that the Hopf bifurcation boundary of the asynchronous mode always lies between that of the synchronous mode. This suggests that as we vary  $d_1$  and  $d_2$  from a stable parameter region into an unstable parameter region, we will always first trigger a synchronous oscillatory instability rather than an asynchronous instability. It is an open problem to show that these qualitative observations still hold for a wide range of other parameter sets.

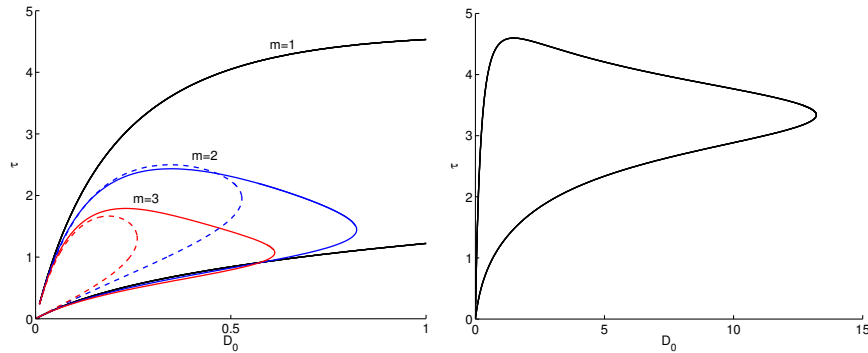


Figure 6.3: Left panel: Hopf bifurcation boundaries for the synchronous (solid curves) and asynchronous (dashed curves) modes for the Sel'kov model with various number  $m$  of cells in the  $\tau$  versus  $D_0$  plane. Only inside the region bounded by the two black solid curves, the synchronous mode is unstable for  $m = 1$ . Similarly, in the lobe formed by the blue solid and red solid curves the synchronous mode is unstable for  $m = 2$  (blue) and  $m = 3$  (red), respectively. In the region enclosed by the blue (red) dashed curve, the asynchronous mode is unstable for  $m = 2$  ( $m = 3$ ). Right panel: Hopf bifurcation boundaries for the synchronous mode with  $m = 1$  shown in a larger region of the  $\tau$  versus  $D_0$  plane. Parameters used are  $\mu = 2$ ,  $\alpha = 0.9$ ,  $\epsilon_0 = 0.15$ ,  $d_1 = 0.5$ ,  $d_2 = 0.2$  and  $|\Omega| = 10$ . With these choices of  $\mu$ ,  $\alpha$  and  $\epsilon_0$ , the uncoupled system has a stable steady-state for the intracellular kinetics.

Next, we show the region where oscillatory instabilities can occur in the  $\tau$  versus  $D_0$  parameter plane for the synchronous and asynchronous modes. We fix the Sel'kov parameter values as  $\mu = 2$ ,  $\alpha = 0.9$ , and  $\epsilon_0 = 0.15$ , so that the uncoupled intracellular kinetics has a stable steady-state. We then take  $d_1 = 0.5$ ,  $d_2 = 0.2$ , and  $|\Omega| = 10$ . For this parameter set, we solve the Hopf bifurcation conditions (6.4.12) by a root finder. In this way, in the left panel

#### 6.4. Examples of the Theory: Finite Domain With $D = \mathcal{O}(\nu^{-1})$

---

of Fig. 6.3 we plot the Hopf bifurcation boundaries for the synchronous mode in the  $\tau$  versus  $D_0$  plane for  $m = 1, 2, 3$ . Similarly, upon using (6.4.16), in the left panel of Fig. 6.3 we also plot the Hopf bifurcation boundaries for the asynchronous mode. In the right panel of Fig. 6.3, where we plot in a larger region of the  $\tau$  versus  $D$  plane, we show that the instability lobe for the  $m = 1$  case is indeed closed. We observe for  $m = 2$  and  $m = 3$  that, for this parameter set, the lobes of instability of the asynchronous mode are almost entirely contained inside the instability lobes for the synchronous mode.

Finally, we consider the effect of changing  $d_1$  and  $d_2$  to  $d_1 = 0.1$  and  $d_2 = 0.2$ , while fixing the Sel'kov parameters as  $\mu = 2$ ,  $\alpha = 0.9$ , and  $\epsilon_0 = 0.15$ , and keeping  $|\Omega| = 10$ . In Fig. 6.4 we plot the Hopf bifurcation curve for the synchronous mode when  $m = 1$ , computed using (6.4.12), in the  $\tau$  versus  $D_0$  plane. We observe that there is no longer any closed lobe of instability. In this figure we also show the two Hopf bifurcation values, derived below in §6.5, that corresponds to taking the limit  $D_0 \gg 1$ . These latter values are Hopf bifurcation points associated with the linearization of the ODE system (6.5.16) around its steady-state value. This ODE system (6.5.16), which will be derived in the next section, describes large-scale cell-bulk dynamics in the regime  $D \gg \mathcal{O}(\nu)$ .

#### Local Kinetics Described by a Fitzhugh-Nagumo Type System

Next, we will consider another form for the local kinetics, taken from [23], that is of Fitzhugh-Nagumo (FN) type. The functions  $F(v, w)$  and  $G(v, w)$ , have the form

$$F(v, w) = \epsilon_0(wz - v), \quad G(v, w) = w - q(w - 2)^3 + 4 - v, \quad (6.4.23)$$

where the parameters satisfy  $\epsilon_0 > 0$ ,  $q > 0$ , and  $z > 1$ .

Upon substituting (6.4.23) into (6.4.7) we calculate that the steady-state solution  $w_e > 0$  is given by the unique real positive root of the cubic  $\mathcal{C}(w) = 0$  given by

$$\mathcal{C}(w) \equiv qw^3 - 6qw^2 + w(12q - 1 + \Lambda) - (8q + 4), \quad (6.4.24a)$$

where  $\Lambda$  is defined as

$$\Lambda \equiv \frac{\epsilon_0 z}{[\epsilon_0 + 2\pi D_0 \beta / \tau]}, \quad (6.4.24b)$$

and  $\beta$  is defined in (6.4.18b). The uniqueness of the positive root of this cubic for any  $\Lambda > 0$  was proved previously in our 1-D analysis of membrane-bulk coupling with FN membrane dynamics. In terms of the solution  $w_e > 0$

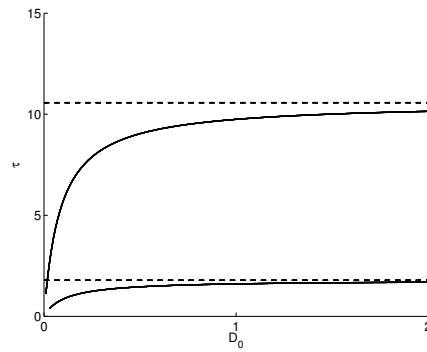


Figure 6.4: Hopf bifurcation boundaries for the synchronous mode for the Sel'kov model with  $m = 1$  in the  $\tau$  versus  $D_0$  plane when  $d_1 = 0.1$  and  $d_2 = 0.2$ . The other parameters are the same as in Fig. 6.3. Inside the region bounded by the two black solid curves, which were computed using (6.4.12), the synchronous mode is unstable. The instability region is no longer a closed lobe as in Fig. 6.3. The dashed lines represent the two Hopf bifurcation points that are obtained by a numerical path following using XPPAUT [16] of the steady-states of the ODE system (6.5.16). We observe that as  $D_0$  increases, the Hopf bifurcation thresholds in  $\tau$  gradually approach that obtained by the large  $D$  approximation.

#### 6.4. Examples of the Theory: Finite Domain With $D = \mathcal{O}(\nu^{-1})$

---

to the cubic equation, we can calculate  $v_e$  by  $v_e = \Lambda w_e$  and the common source strength by  $S_{0c} = -\beta \Lambda w_e$ .

As needed below, we first calculate the partial derivatives of  $F$  and  $G$  at the steady-state solution as

$$F_v^e = -\epsilon_0, \quad F_w^e = \epsilon_0 z, \quad G_v^e = -1, \quad G_w^e = 1 - 3q(w_e - 2)^2, \quad (6.4.25a)$$

which yields

$$\det(J) = \epsilon_0 \left[ z - 1 + 3q(w_e - 2)^2 \right] > 0, \quad \text{tr}(J) = -\epsilon_0 + 1 - 3q(w_e - 2)^2. \quad (6.4.25b)$$

To determine conditions for which the synchronous oscillation mode has a Hopf bifurcation we first substitute (6.4.25a) into (6.4.9b). Then, from the conditions in (6.4.12), to obtain purely imaginary roots of (6.4.9a), we need to numerically compute the parameter regime where  $p_1 p_2 = p_3$ , with  $p_1 > 0$  and  $p_3 > 0$ .

Similarly, to study instabilities associated with the asynchronous oscillatory mode we substitute (6.4.25a) into (6.4.14) to obtain that the Hopf bifurcation boundary is given by

$$\gamma = \tau \left[ -\epsilon_0 + 1 - 3q(w_e - 2)^2 \right], \quad (6.4.26a)$$

provided that

$$\det(J) - \frac{\gamma}{\tau} G_w^e = -G_v^e F_w^e - (G_w^e)^2 = \epsilon_0 z - \left[ 1 - 3q(w_e - 2)^2 \right]^2 > 0, \quad (6.4.26b)$$

where  $w_e$  is the positive root of the cubic (6.4.24a). In a similar way as was done for the Sel'kov model in §6.4.2, the Hopf bifurcation boundary for the asynchronous mode in the  $d_1$  versus  $d_2$  parameter plane can be parametrized as in (6.4.22a) where where  $a_{11}$ ,  $a_{12}$ ,  $a_{22}$ , and  $a_{21}$ , are now defined in terms of the parameter  $w_e > 0$  by

$$a_{11} \equiv 1 + \frac{2\pi m D_0}{|\Omega|}, \quad a_{12} \equiv -\frac{1}{\beta(w_e)}, \quad a_{21} \equiv 1, \quad a_{22} \equiv -\frac{2\pi D_0}{\gamma(w_e)}, \quad (6.4.27a)$$

where

$$\beta(w_e) \equiv \tau \frac{\epsilon_0}{2\pi D_0} \left( \frac{z}{\Lambda(w_e)} - 1 \right), \quad \text{with} \quad \Lambda(w_e) \equiv -\frac{q(w_e - 2)^3}{w_e} + 1 + \frac{4}{w_e},$$

$$\gamma(w_e) \equiv \tau \left[ -\epsilon_0 + 1 - 3q(w_e - 2)^2 \right]. \quad (6.4.27b)$$

#### 6.4. Examples of the Theory: Finite Domain With $D = \mathcal{O}(\nu^{-1})$

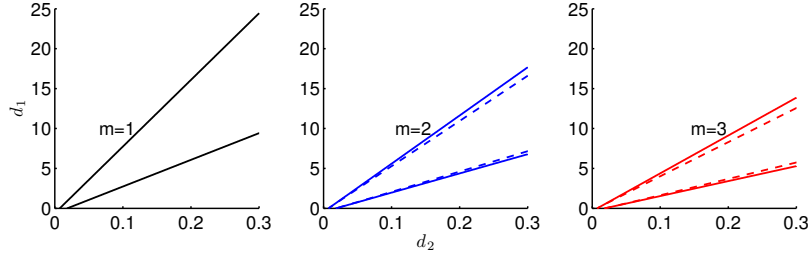


Figure 6.5: Hopf bifurcation boundaries for the synchronous (solid curve) and asynchronous (dashed curve) modes for the FN system (6.4.23) with various number  $m$  of cells in the  $d_1$  versus  $d_2$  parameter plane. Between the solid lines the synchronous mode is unstable, whereas between the dashed lines the asynchronous mode is unstable. Notice that the region of instability for the asynchronous mode is contained within the instability region for the synchronous mode. Parameters used are  $z = 3.5$ ,  $q = 5$ ,  $\epsilon_0 = 0.5$ ,  $\tau = 1$ ,  $D_0 = 1$ , and  $|\Omega| = 10$ .

By varying  $w_e > 0$  and retaining only the portion of the curve for which  $d_1 > 0$  and  $d_2 > 0$ , and ensuring that the constraint (6.4.26b) holds, we obtain a parametric form for the Hopf bifurcation boundary for the asynchronous mode in the  $d_1$  versus  $d_2$  parameter plane. For  $m = 2$  and  $m = 3$ , these are the dashed curves shown in Fig. 6.5.

In this way, in Fig. 6.5 we plot the Hopf bifurcation boundaries for the synchronous mode (solid curves) and asynchronous mode (dashed curves) for various values of  $m$  for the parameter set  $z = 3.5$ ,  $q = 5$ ,  $\epsilon_0 = 0.5$ ,  $\tau = 1$ ,  $D_0 = 1$ , and  $|\Omega| = 10$ . As compared to Fig. 6.2, we notice that the unstable regions for both modes are not only shrinking but also the boundaries shift as the number  $m$  of cells increases. This feature does not appear in the previous Sel'kov model.

Next, in Fig. 6.6 we show the region of oscillatory instabilities for the synchronous and asynchronous modes for  $m = 1, 2, 3$  in the  $\tau$  versus  $D_0$  plane. These Hopf bifurcation boundaries are computed by finding roots of (6.4.12) for the synchronous mode or (6.4.26) for the asynchronous mode for various values of  $D_0$ . The other parameter values are the same as those used for Fig. 6.5 except  $d_1 = 10$  and  $d_2 = 0.2$ . Inside the region bounded by the solid curves the synchronous mode is unstable, while inside the region bounded by the dashed curves, the asynchronous mode is unstable. Similar

to that shown in Fig. 6.5, the regions of instability are shrinking, at the same time as the Hopf bifurcation boundaries shift, as  $m$  increases. For these parameter values of  $d_1$  and  $d_2$ , the Hopf bifurcation still occurs for large value of  $D_0$ .

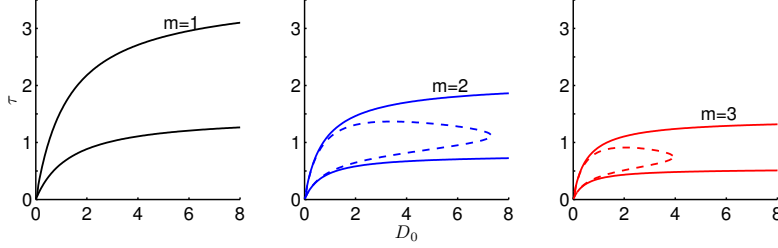


Figure 6.6: Hopf bifurcation boundaries for the synchronous (solid curves) and asynchronous (dashed curves) modes for the FN system (6.4.23) with various number  $m$  of cells in the  $\tau$  versus  $D_0$  parameter plane. Between the solid lines the synchronous mode is unstable, whereas between the dashed lines the asynchronous mode is unstable. Parameters used are  $z = 3.5$ ,  $q = 5$ ,  $\epsilon_0 = 0.5$ ,  $d_1 = 10$ ,  $d_2 = 0.2$ , and  $|\Omega| = 10$ .

## 6.5 Finite Domain: Reduction to ODEs for $D \gg \mathcal{O}(\nu^{-1})$

In this section we will consider our basic model with one small cell circular  $\Omega_\epsilon$  centered in a bounded two-dimensional domain  $\Omega$  under the assumption that the diffusion coefficient  $D$  satisfies  $D \gg \mathcal{O}(\nu^{-1})$ , with  $\nu = -1/\log \epsilon$ . In this limit, in which the bulk region is effectively well-mixed, we show that we can reduce the dynamics in the coupled cell-bulk model to a system of nonlinear ODEs for the time history of the bulk and cell concentrations.

For the case of one cell, the basic model is formulated as

$$\begin{aligned} \tau U_t &= D\Delta U - U, & \mathbf{x} \in \Omega \setminus \Omega_\epsilon; & & \partial_n U &= 0, & \mathbf{x} \in \partial\Omega, \\ \epsilon D \partial_n U &= d_1 U - d_2 u^1, & \mathbf{x} \in \partial\Omega_\epsilon, & \end{aligned} \quad (6.5.1a)$$

which is coupled to the cell dynamics by

$$\frac{d\mathbf{u}}{dt} = \mathbf{F}(\mathbf{u}) + \frac{1}{\epsilon\tau} \int_{\partial\Omega_\epsilon} (d_1 U - d_2 u_1) ds \mathbf{e}_1, \quad (6.5.1b)$$

6.5. Finite Domain: Reduction to ODEs for  $D \gg \mathcal{O}(\nu^{-1})$

---

where  $\mathbf{e}_1 \equiv (1, 0, \dots, 0)^T$ . Here  $\mathbf{u} = (u_1, \dots, u_n)^T$  represents the concentration of the  $n$  species inside the cell with intracellular reaction kinetics  $\mathbf{F}(\mathbf{u})$ .

We will assume that  $D \gg 1$ , and in the bulk region expand

$$U = U_0 + \frac{1}{D}U_1 + \dots \quad (6.5.2)$$

Upon substituting this expansion into (6.5.1a), and noting that  $\Omega_\epsilon \rightarrow \mathbf{x}_0$  as  $\epsilon \rightarrow 0$ , we obtain to leading order in  $1/D$  that  $\Delta U_0 = 0$  with  $\partial_{\mathbf{n}} U_0 = 0$  on  $\partial\Omega$ . As such, we have  $U_0 = U_0(t)$ . At next order, we have that  $U_1$  satisfies

$$\Delta U_1 = U_0 + \tau U_{0t}, \quad \mathbf{x} \in \Omega \setminus \{\mathbf{x}_0\}; \quad \partial_{\mathbf{n}} U_1 = 0, \quad \mathbf{x} \in \partial\Omega. \quad (6.5.3)$$

The formulation of this problem is complete once we determine a matching condition for  $U_1$  as  $\mathbf{x} \rightarrow \mathbf{x}_0$ .

To obtain this matching condition, we must consider the inner region defined at  $\mathcal{O}(\epsilon)$  distances outside the cell. In this inner region we introduce the new variables  $\mathbf{y} = \epsilon^{-1}(\mathbf{x} - \mathbf{x}_0)$  and  $\hat{U}(\mathbf{y}, t) = U(\mathbf{x}_0 + \epsilon\mathbf{y}, t)$ . From (6.5.1a), we obtain that

$$\tau \hat{U}_t = \frac{D}{\epsilon^2} \Delta_{\mathbf{y}} \hat{U} - \hat{U}, \quad \rho = |\mathbf{y}| \geq 1; \quad D \frac{\partial \hat{U}}{\partial \rho} = d_1 \hat{U} - d_2 u_1, \quad \text{on } \rho = 1.$$

For  $D \gg 1$ , we then seek a radially symmetric solution to this inner problem in the form

$$\hat{U}(\rho, t) = \hat{U}_0(\rho, t) + \frac{1}{D} \hat{U}_1(\rho, t) + \dots \quad (6.5.4)$$

To leading order we obtain that

$$\Delta_\rho \hat{U}_0 = 0, \quad \rho \geq 1; \quad \frac{\partial \hat{U}_0}{\partial \rho} = 0, \quad \rho = 1,$$

subject to the matching condition to the bulk that  $\hat{U}_0 \rightarrow U_0$  as  $\rho \rightarrow \infty$ . We conclude that  $\hat{U}_0 = U_0$ . At next order, the problem for  $\hat{U}_1$  is that

$$\Delta_\rho \hat{U}_1 = 0, \quad \rho \geq 1; \quad \frac{\partial \hat{U}_1}{\partial \rho} = d_1 U_0 - d_2 u_1, \quad \rho = 1. \quad (6.5.5)$$

Allowing for logarithmic growth at infinity, the solution to this problem is

$$\hat{U}_1 = (d_1 U_0 - d_2 u_1) \log \rho + C, \quad (6.5.6)$$

6.5. Finite Domain: Reduction to ODEs for  $D \gg \mathcal{O}(\nu^{-1})$

---

where  $C$  is a constant to be found. Then, by writing (6.5.6) in outer variables, and recalling (6.5.4), we obtain that the far field behavior of the inner expansion is

$$\hat{U} \sim U_0 + \frac{1}{D} \left[ (d_1 U_0 - d_2 u_1) \log |\mathbf{x} - \mathbf{x}_0| + \frac{1}{\nu} (d_1 U_0 - d_2 u_1) + C \right] + \dots \quad (6.5.7)$$

From (6.5.7) we observe that the term proportional to  $1/D$  is smaller than the first term provided that  $D \gg \mathcal{O}(\nu^{-1})$ . This specifies the asymptotic range of  $D$  for which our analysis will hold. From asymptotic matching of the bulk and inner solutions, the far-field behavior of the inner solution (6.5.7) provides the required singular behavior as  $\mathbf{x} \rightarrow \mathbf{x}_0$  for the outer bulk solution. In this way, we find from (6.5.7) and (6.5.2) that  $U_1$  satisfies (6.5.3) subject to the singular behavior

$$U_1 \sim (d_1 U_0 - d_2 u_1) \log |\mathbf{x} - \mathbf{x}_0|, \quad \text{as } \mathbf{x} \rightarrow \mathbf{x}_0. \quad (6.5.8)$$

Then, (6.5.3) together with (6.5.8) determines  $U_1$  uniquely. Finally, in terms of this solution, we identify that the constant  $C$  in (6.5.7) and (6.5.6) is obtained from

$$\lim_{\mathbf{x} \rightarrow \mathbf{x}_0} [U_1 - (d_1 U_0 - d_2 u_1) \log |\mathbf{x} - \mathbf{x}_0|] = \nu^{-1} (d_1 U_0 - d_2 u_1) + C. \quad (6.5.9)$$

We now carry out the details of the analysis. We can write the problem (6.5.3) and (6.5.8) for  $U_1$  as

$$\Delta U_1 = U_0 + \tau U_{0t} + 2\pi (d_1 U_0 - d_2 u_1) \delta(\mathbf{x} - \mathbf{x}_0), \quad \mathbf{x} \in \Omega; \quad \partial_n U_1 = 0, \quad \mathbf{x} \in \partial\Omega. \quad (6.5.10)$$

By the divergence theorem, this problem has a solution only if  $(U_0 + \tau U_{0t}) |\Omega| = -2\pi(d_1 U_0 - d_2 u_1)$ . This leads to the following ODE for the leading-order bulk solution  $U_0(t)$ :

$$U_0' = -\frac{1}{\tau} \left( 1 + \frac{2\pi d_1}{|\Omega|} \right) U_0 + \frac{2\pi d_2}{\tau |\Omega|} u_1. \quad (6.5.11)$$

Without loss of generality we can impose that  $\int_{\Omega} U_1 d\mathbf{x} = 0$  so that  $U_0$  describes the spatial average of  $U$ . The solution to (6.5.10) is then simply

$$U_1 = -2\pi (d_1 U_0 - d_2 u_1) G_0(\mathbf{x}; \mathbf{x}_0), \quad (6.5.12)$$

where  $G_0(\mathbf{x}; \mathbf{x}_0)$  is the Neumann Green's function defined uniquely by (6.3.8). We then expand (6.5.12) as  $\mathbf{x} \rightarrow \mathbf{x}_0$ , and use (6.5.9) to identify  $C$  as

$$C = - (d_1 U_0 - d_2 u_1) \left( \nu^{-1} + 2\pi R_0 \right), \quad (6.5.13)$$

6.5. Finite Domain: Reduction to ODEs for  $D \gg \mathcal{O}(\nu^{-1})$

---

where  $R_0$  is the regular part of the Neumann Green's function defined in (6.3.8).

In summary, by using (6.5.4), (6.5.6), and (6.5.13), the two-term inner expansion near the cell is given by

$$\hat{U} \sim U_0 + \frac{1}{D} (d_1 U_0 - d_2 u_1) \left( \log \rho - \frac{1}{\nu} - 2\pi R_0 \right) + \dots \quad (6.5.14)$$

From (6.5.2) and (6.5.12), we obtain the corresponding two-term expansion of the outer bulk solution

$$U \sim U_0 - \frac{2\pi}{D} (d_1 U_0 - d_2 u_1) G_0(\mathbf{x}; \mathbf{x}_0), \quad (6.5.15)$$

where  $U_0(t)$  satisfies the ODE (6.5.11).

The final step in the analysis is to use (6.5.1b) to derive the dynamics inside the cell. We readily calculate that

$$\frac{1}{\epsilon\tau} \int_{\partial\Omega_\epsilon} (d_1 U - d_2 u_1) ds \sim \frac{2\pi}{\tau} (d_1 U_0 - d_2 u_1),$$

which determines the dynamics inside the cell from (6.5.1b).

This leads to our main result that, for  $D \gg \mathcal{O}(\nu^{-1})$ , the coupled PDE model (6.5.1) reduces to the study of the coupled  $(n+1)$  dimensional ODE system for the leading-order average bulk concentration  $U_0(t)$  and cell dynamics  $\mathbf{u}$  given by

$$U_0' = -\frac{1}{\tau} \left( 1 + \frac{2\pi d_1}{|\Omega|} \right) U_0 + \frac{2\pi d_2}{\tau |\Omega|} u_1, \quad \mathbf{u}' = \mathbf{F}(\mathbf{u}) + \frac{2\pi}{\tau} [d_1 U_0 - d_2 u_1] \mathbf{e}_1. \quad (6.5.16)$$

Before studying (6.5.16) for some specific reaction kinetics, we first examine conditions for the existence of steady-state solutions for (6.5.16) and we derive the spectral problem characterizing the linear stability of these steady-states.

A steady-state solution  $U_{0e}$  and  $\mathbf{u}_e$  of (6.5.16), if it exists, is a solution to the nonlinear algebraic system

$$\mathbf{F}(\mathbf{u}_e) + \frac{2\pi}{\tau} (d_1 U_{0e} - d_2 \mathbf{u}_{1e}) \mathbf{e}_1 = 0, \quad r U_{0e} = s u_{1e}, \quad (6.5.17a)$$

where  $r$  and  $s$  are defined by

$$r \equiv 1 + \frac{2\pi d_1}{|\Omega|}, \quad s \equiv \frac{2\pi d_2}{|\Omega|}. \quad (6.5.17b)$$

6.5. Finite Domain: Reduction to ODEs for  $D \gg \mathcal{O}(\nu^{-1})$

---

To examine the linearized stability of such a steady-state, we substitute

$$U_0 = U_{0e} + e^{\lambda t} \eta, \quad \mathbf{u} = \mathbf{u}_e + e^{\lambda t} \phi.$$

into (6.5.16) and linearize. This yields that  $\eta$  and  $\phi$  satisfy

$$\lambda \phi = J \phi + \frac{2\pi}{\tau} (d_1 \eta - d_2 \phi_1) \mathbf{e}_1, \quad \tau \lambda \eta = -r \eta + s \phi_1,$$

where  $J$  is the Jacobian of  $\mathbf{F}$  evaluated at the steady-state  $\mathbf{u} = \mathbf{u}_e$ . Upon solving the second equation for  $\eta$ , and substituting the resulting expression into the first equation, we readily derive the homogeneous linear system

$$[(\lambda I - J) - \mu \mathcal{E}_1] \phi = 0, \quad \text{where} \quad \mu \equiv \frac{2\pi}{\tau} \left( \frac{d_1 s}{\tau \lambda + r} - d_2 \right), \quad (6.5.18)$$

where  $\mathcal{E}_1$  is the rank-one matrix  $\mathcal{E}_1 = \mathbf{e}_1 \mathbf{e}_1^T$ .

By using the matrix determinant lemma we conclude that  $\lambda$  is an eigenvalue of the linearization if and only if  $\lambda$  satisfies  $\mathbf{e}_1^T (\lambda I - J)^{-1} \mathbf{e}_1 = 1/\mu$ , where  $\mu$  is defined in (6.5.18). From this expression, and by using  $d_1 s - d_2 r = -d_2$  as obtained from (6.5.17b), we conclude that  $\lambda$  must be a root of  $\mathcal{Q}(\lambda) = 0$ , where

$$\mathcal{Q}(\lambda) \equiv -\frac{\tau(r + \tau\lambda)}{2\pi d_2(1 + \tau\lambda)} - \frac{M_{11}}{\det(\lambda I - J)}, \quad (6.5.19)$$

where  $r$  is defined in (6.5.17b). Here  $M_{11}$  is the cofactor of the element in the first row and first column of  $\lambda I - J$ .

We use the argument principle to determine the number  $N$  of roots of  $\mathcal{Q}(\lambda)$  in  $\text{Re}(\lambda) > 0$ . We first observe that  $[\arg \mathcal{Q}(\lambda)]_{\Gamma_R} \rightarrow 0$  as  $R \rightarrow \infty$ , where  $\Gamma_R$  is the semi-circle  $\lambda = R e^{i\theta}$  with  $|\theta| \leq \pi/2$  and the square brackets indicate the change in the argument over  $\Gamma_R$ . Assuming that there are no zeroes on the imaginary axis, we readily obtain that

$$N = \frac{1}{\pi} [\arg \mathcal{Q}(\lambda)]_{\Gamma_{I+}} + P, \quad (6.5.20)$$

where  $P$  is the number of zeroes of  $\det(\lambda I - J)$  in  $\text{Re}(\lambda) > 0$ , and  $\Gamma_{I+}$  denotes the positive imaginary axis  $\lambda = i\lambda_I$  with  $\lambda_I > 0$  traversed in the downwards direction.

Next, we show that (6.5.19), which characterizes the stability of a steady-state solution of the ODE dynamics (6.5.16), can also be derived by taking the limit  $D_0 \gg 1$  in the stability results obtained in (6.3.19) of §6.3 for the

$D = \mathcal{O}(\nu^{-1})$  regime where we set  $D = D_0/\nu$ . Recall from the analysis in §6.3 for  $D = D_0/\nu$ , that when  $m = 1$  only the synchronous mode can occur, and that the linearized eigenvalue satisfies (6.3.20). By formally letting  $D_0 \rightarrow \infty$  in (6.3.20) we readily recover (6.5.19).

We now give some examples of our stability theory.

### 6.5.1 Large D Theory: Analysis of Reduced Dynamics

We first consider the case where there is exactly one dynamical species in the cell so that  $n = 1$ . From (6.5.17) with  $n = 1$  we obtain that the steady-state  $u_e$  is any solution of

$$F(u_e) - \frac{2\pi d_2}{\tau} \left[ 1 + \frac{2\pi d_1}{|\Omega|} \right]^{-1} u_e = 0, \quad U_{0e} = \frac{2\pi d_2}{|\Omega|} \left[ 1 + \frac{2\pi d_1}{|\Omega|} \right]^{-1} u_e = 0. \quad (6.5.21)$$

In the stability criterion (6.5.19) we set  $M_{11} = 1$  and  $\det(\lambda I - J) = \lambda - F'_e$ , where  $F'_u \equiv dF/du|_{u=u_e}$ , to conclude that the stability of this steady-state is determined by the roots of the quadratic

$$\lambda^2 - \lambda p_1 + p_2 = 0, \quad (6.5.22a)$$

where  $p_1$  and  $p_2$  are defined by

$$p_1 = -\frac{1}{\tau} \left( 1 + \frac{2\pi d_1}{|\Omega|} \right) + F'_u - \frac{2\pi d_2}{\tau}, \quad p_2 = -\frac{F'_u}{\tau} \left( 1 + \frac{2\pi d_1}{|\Omega|} \right) + \frac{2\pi d_2}{\tau^2}. \quad (6.5.22b)$$

We now establish the following simple result based on (6.5.22).

**Proposition 6.5.1** *Let  $n = 1$ . Then, no steady-state solution of (6.5.16) can undergo a Hopf bifurcation. Furthermore, if*

$$F'_u < F_{th} \equiv \frac{2\pi d_2}{\tau} \left[ 1 + \frac{2\pi d_1}{|\Omega|} \right]^{-1}, \quad (6.5.23)$$

*then  $\text{Re}(\lambda) < 0$ , and so the steady-state is linearly stable. If  $F'_u > F_{th}$ , the linearization has exactly one positive eigenvalue.*

We first prove that no Hopf bifurcations are possible for the steady-state. From (6.5.22a) it is clear that there exists a Hopf bifurcation if and only if  $p_1 = 0$  and  $p_2 > 0$  in (6.5.22b). Upon setting  $p_1 = 0$ , we get

6.5. Finite Domain: Reduction to ODEs for  $D \gg \mathcal{O}(\nu^{-1})$

---

$F_u^e = 2\pi d_2 \tau^{-1} + \tau^{-1} (1 + 2\pi d_1 / |\Omega|)$ . Upon substituting this expression into (6.5.22b) for  $p_2$ , we get that

$$p_2 = \frac{1}{\tau} \left[ -\frac{4\pi^2 d_2^2}{\tau |\Omega|} - \frac{1}{\tau} \left( 1 + \frac{2\pi d_1}{|\Omega|} \right) \left( 1 + \frac{2\pi d_2}{|\Omega|} \right) \right] < 0.$$

Since  $p_2 < 0$  whenever  $p_1 = 0$ , we conclude that no Hopf bifurcations for the steady-state are possible.

The second result follows by establishing that  $p_1 < 0$  and  $p_2 > 0$  when  $F_u^e < F_{\text{th}}$ . From (6.5.22b) it follows that  $p_1 < 0$  and  $p_2 > 0$  when

$$\frac{2\pi d_2}{\tau} - F_u^e + \frac{1}{\tau} \left( 1 + \frac{2\pi d_1}{|\Omega|} \right) > 0, \quad \frac{2\pi d_2}{\tau} - F_u^e - \frac{2\pi d_1}{|\Omega|} F_u^e > 0. \quad (6.5.24)$$

These two inequalities hold simultaneously only when the second relation is satisfied. This yields that when (6.5.23) holds, we have  $\text{Re}(\lambda) < 0$ . Finally, when  $F_u^e > F_{\text{th}}$ , we have  $p_2 < 0$ , and so there is a unique positive eigenvalue.

This result qualitatively shows that the effect of cell-bulk coupling is that the steady-state of the ODE dynamics (6.5.16) can be linearly stable even when the reaction kinetics is self-activating in the sense that  $F_u^e > 0$ . Moreover, we observe that as  $\tau$  increases, corresponding to the situation where the membrane kinetics has faster dynamics than the time scale for bulk decay, then the stability threshold  $F_{\text{th}}$  decreases. Therefore, for fast cell dynamics there is a smaller parameter range where self-activation of the intracellular dynamics can occur while still maintaining stability of the steady-state to the coupled system.

Next, we consider the case  $n = 2$ , where  $\mathbf{F}(\mathbf{u}) = (F(u_1, u_2), G(u_1, u_2))^T$ . We readily derive that any steady-state of the ODEs (6.5.16) must satisfy

$$F(u_{1e}, u_{2e}) - \frac{2\pi d_2}{r\tau} u_{1e} = 0, \quad G(u_{1e}, u_{2e}) = 0, \quad U_{0e} = \frac{s}{r} u_{1e}, \quad (6.5.25)$$

where  $r$  and  $s$  are defined in (6.5.17b). We then observe that the roots of  $\mathcal{Q}(\lambda) = 0$  in (6.5.19) are roots to a cubic polynomial in  $\lambda$ . Since  $M_{11} = \lambda - G_{u_2}^e$ ,  $\det(\lambda I - J) = \lambda^2 - \text{tr}(J)\lambda + \det J$ , where

$$\text{tr}(J) = F_{u_1}^e + G_{u_2}^e, \quad \det J = F_{u_1}^e G_{u_2}^e - F_{u_2}^e G_{u_1}^e, \quad (6.5.26)$$

and  $F_v^e, G_v^e$  are partial derivatives of  $F$  or  $G$  with respect to  $v \in (u_1, u_2)$  evaluated at the steady-state, we conclude that the linear stability of the steady-state is characterized by the roots of the cubic

$$\lambda^3 + p_1 \lambda^2 + p_2 \lambda + p_3 = 0, \quad (6.5.27a)$$

where  $p_1$ ,  $p_2$  and  $p_3$  are defined as

$$\begin{aligned}
 p_1 &\equiv \frac{2\pi d_2}{\tau} + \frac{1}{\tau} \left( 1 + \frac{2\pi d_1}{|\Omega|} \right) - \text{tr}(J), \\
 p_2 &\equiv \det J - \frac{2\pi d_2}{\tau} G_{u_2}^e + \frac{1}{\tau} \left( \frac{2\pi d_2}{\tau} - \left( 1 + \frac{2\pi d_1}{|\Omega|} \right) \text{tr}(J) \right), \\
 p_3 &\equiv \frac{1}{\tau} \left( \left( 1 + \frac{2\pi d_1}{|\Omega|} \right) \det J - \frac{2\pi d_2}{\tau} G_{u_2}^e \right).
 \end{aligned} \tag{6.5.27b}$$

By taking  $m = 1$  and letting  $D_0 \rightarrow \infty$  in (6.4.9b), it is readily verified that the expressions above for  $p_i$ , for  $i = 1, 2, 3$ , agree exactly with those in (6.4.9b). Then, by satisfying the Routh-Hurwitz conditions (6.4.12), we can plot the Hopf bifurcation boundaries in different parameter planes.

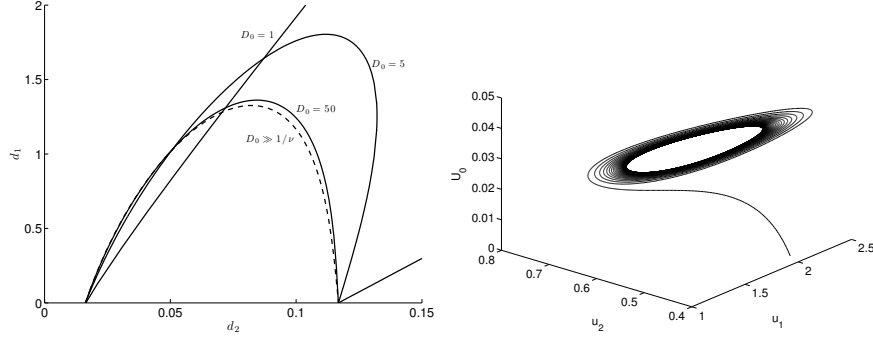
**Example: One Cell With Sel'kov Dynamics**


Figure 6.7: Left panel: Comparison of the Hopf bifurcation boundaries for the synchronous mode for the Sel'kov model (6.4.17) in the  $d_1$  versus  $d_2$  parameter plane with  $D_0 = 1, 5, 50$  (solid), as obtained from (6.4.9), and the large  $D$  approximation (dashed), as obtained from (6.5.27). Between the outer two black curves, the synchronous mode is unstable for  $D_0 = 1$ , whereas in the region bounded by the solid/dashed curve the synchronous mode is unstable. We observe that as  $D_0$  increases, the Hopf boundaries obtained from (6.4.9) gradually approaches the one obtained from (6.5.27) from the large  $D$  approximation. Right panel: Numerical simulation for the ODE system (6.5.16), showing sustained oscillations. In the left and right panels we fixed  $\mu = 2$ ,  $\alpha = 0.9$ ,  $\epsilon_0 = 0.15$ ,  $\tau = 1$ , and  $|\Omega| = 10$ , and in the right panel we took  $d_1 = 0.8$  and  $d_2 = 0.05$  corresponding to a point where the steady-state solution of the ODEs (6.5.16) is unstable.

Next, we apply our theory for the  $D \gg \mathcal{O}(\nu^{-1})$  regime to the case where the local kinetics is described by the Sel'kov model, where the nonlinearities  $F$  and  $G$  are given in (6.4.17). From (6.5.25) we obtain that the steady-state solution of the ODE dynamics (6.5.16) under Sel'kov kinetics is

$$u_1^e = \frac{r\mu}{[r + 2\pi d_2/\tau]}, \quad u_2^e = \frac{\mu}{\alpha + (u_1^e)^2}, \quad U_{0e} = \frac{s\mu}{r + 2\pi d_2}, \quad (6.5.28)$$

where  $r$  and  $s$  are defined in (6.5.17b). The partial derivatives of  $F$  and  $G$  can be calculated as in (6.4.19a).

In the left panel of Fig. 6.7 we plot the Hopf bifurcation boundary in the  $d_1$  versus  $d_2$  plane associated with linearizing the ODEs (6.5.16) about this steady-state solution. In this figure we also plot the Hopf bifurcation

6.5. Finite Domain: Reduction to ODEs for  $D \gg \mathcal{O}(\nu^{-1})$

boundary for different values of  $D_0$ , with  $D = D_0/\nu$ , as obtained from our stability formulation (6.4.9) of §6.4 for the  $D = \mathcal{O}(\nu^{-1})$  regime. We observe from this figure that the stability boundary with  $D_0 = 50$  closely approximates that obtained from (6.5.27), which corresponds to the  $D_0 \rightarrow \infty$  limit of (6.4.9).

We emphasize that since in the distinguished limit  $D \gg \mathcal{O}(\nu^{-1})$  we can approximate the original coupled PDE system by the system (6.5.16) of ODEs, a numerical solution of the approximate system to show large-scale time dynamics away from the steady-state becomes possible. In the right panel of Fig. 6.7, we plot the numerical solution to (6.5.16) with Sel'kov dynamics (6.4.17), where the initial condition is  $u_1(0) = 0.01$ ,  $u_2(0) = 0.2$  and  $U_0(0) = 0.5$ . We observe that by choosing  $d_1$  and  $d_2$  inside the region bounded by the dashed curve in the left panel of Fig. 6.7, where the steady-state is unstable, the full ODE system (6.5.16) exhibits a stable periodic orbit, indicating a limit cycle behavior.

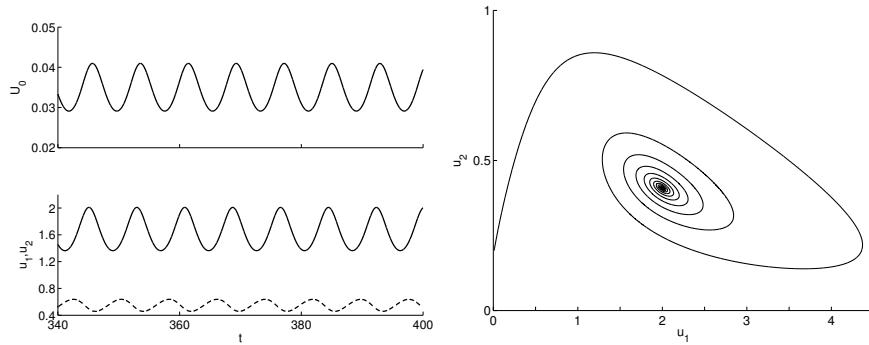


Figure 6.8: Left: Plot of  $u_1$ ,  $u_2$  and  $U_0$  versus time showing sustained oscillatory dynamics. Parameters used are  $\mu = 2$ ,  $\alpha = 0.9$ ,  $\epsilon_0 = 0.15$ ,  $\tau = 1$ ,  $|\Omega| = 10$ ,  $d_1 = 0.8$  and  $d_2 = 0.05$ . Right: Plot of  $u_1$  versus  $u_2$  when the local kinetics is decoupled from the bulk. There is decaying oscillations towards the stable steady-state solution at  $u_1 = \mu$  and  $u_2 = \mu/(\alpha + u_1^2)$ . The initial condition is  $u_1(0) = 0.01$  and  $u_2(0) = 0.2$ . The parameter values of  $\mu$ ,  $\epsilon_0$  and  $\alpha$  are the same as that used for the left panel.

In addition, in the left panel of Fig. 6.8 we plot the time evolution of  $u_1$ ,  $u_2$  and  $U_0$ , showing clearly the sustained periodic oscillations. For comparison, fixing the same parameter set for the Sel'kov kinetics (6.4.17), in the right panel of Fig. 6.8 we plot the phase plane of  $u_2$  versus  $u_1$  when there is no coupling between the local kinetics and the bulk. We now observe that

without this cell-bulk coupling the Sel'kov model (6.4.17) exhibits transient decaying oscillatory dynamics, with a spiral behavior in the phase-plane towards the linearly stable steady-state.

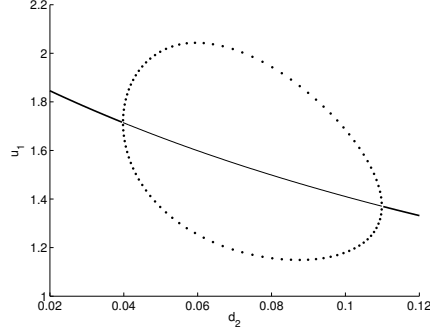


Figure 6.9: Global bifurcation diagram of  $u_1$  with respect to  $d_2$  at a fixed  $d_1 = 0.8$  as computed using XPPAUT [16] from the ODE system (6.5.16) for the Sel'kov kinetics (6.4.17). The thick/thin solid line represents stable/unstable steady-state solutions of  $u_1$ , while the solid dots indicate stable synchronous periodic solution. The parameters used are  $\mu = 2$ ,  $\alpha = 0.9$ ,  $\epsilon_0 = 0.15$ ,  $\tau = 1$ , and  $|\Omega| = 10$ .

Finally, we use the numerical bifurcation software XPPAUT [16] to confirm the existence of a stable large amplitude periodic solution to (6.5.16) with Sel'kov kinetics when  $d_1$  and  $d_2$  are in the unstable region of the left panel of Fig. 6.7. In Fig. 6.9 we plot a global bifurcation diagram of  $u_1$  versus  $d_2$  for  $d_1 = 0.8$ , corresponding to taking a horizontal slice at fixed  $d_2 = 0.8$  through the stability boundaries in the  $d_2$  versus  $d_1$  plane shown in Fig. 6.7. The two computed Hopf bifurcation points at  $d_2 \approx 0.0398$  and  $d_1 \approx 0.1098$  agree with the theoretically predicted values in Fig. 6.7.

### Example: One Cell With Fitzhugh-Nagumo Dynamics

Finally, we apply our large  $D$  theory to the case where the intracellular dynamics is governed by the FN kinetics (6.4.23). From (6.5.25) we obtain that the steady-state solution of the ODEs (6.5.16) with the kinetics (6.4.23) is

$$u_1^e = \Lambda u_2^e, \quad U_{0e} = \frac{su_1^e}{r}, \quad \text{where} \quad \Lambda \equiv \frac{\epsilon_0 z r}{[\epsilon_0 r + 2\pi d_2 / \tau]}. \quad (6.5.29)$$

### 6.5. Finite Domain: Reduction to ODEs for $D \gg \mathcal{O}(\nu^{-1})$

Here  $r$  and  $s$  are defined in (6.5.17b), and  $u_{2e} > 0$  is the unique root of the cubic (6.4.24a) where  $\Lambda$  in (6.4.24a) is now defined in (6.5.29). The partial derivatives of  $F$  and  $G$  can be calculated as in (6.4.25).

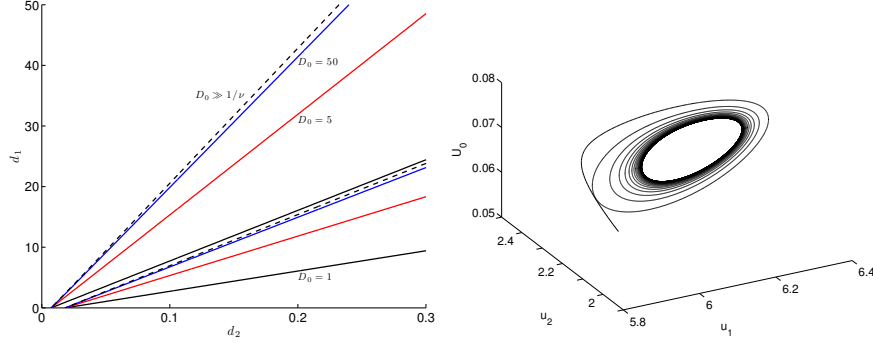


Figure 6.10: Left panel: Comparison of the Hopf bifurcation boundaries for the synchronous mode with FN kinetics (6.4.23) in the  $d_1$  versus  $d_2$  parameter plane with  $D_0 = 1, 5, 50$  (solid), as obtained from (6.4.9), and the large  $D$  approximation (dashed), as obtained from (6.5.27). In the wedge-shaped regions bounded by the solid curves the synchronous mode is unstable for the finite values of  $D_0$ . As  $D_0$  increases, the Hopf boundaries obtained from (6.4.9) becomes rather close to the dashed one obtained from (6.5.27) from the large  $D$  approximation. Right panel: Numerical simulation for the ODE system (6.5.16), showing sustained oscillations, with initial conditions  $u_1(0) = 6.0$ ,  $u_2(0) = 2.3$ , and  $U_0(0) = 0.05$ . In the left and right panels we fixed  $z = 3.5$ ,  $q = 5$ ,  $\epsilon_0 = 0.5$ ,  $\tau = 1$ , and  $|\Omega| = 10$ , and in the right panel we took  $d_1 = 15.6$  and  $d_2 = 0.2$  corresponding to a point where the steady-state solution of the ODEs (6.5.16) is unstable.

In the left panel of Fig. 6.10 we plot by the dashed curve the Hopf bifurcation boundary in the  $d_1$  versus  $d_2$  plane associated with linearizing the ODEs (6.5.16) about this steady-state solution. This curve was obtained by setting  $p_1 p_2 = p_3$  with  $p_1 > 0$  and  $p_3 > 0$  in (6.5.27). In this figure the Hopf bifurcation boundaries for different values of  $D_0$ , with  $D = D_0/\nu$ , are also shown. These latter curves were obtained from our stability formulation (6.4.9) of §6.4. Similar to what we found for the Sel'kov model, the stability boundary for  $D_0 = 50$  is very close to that for the infinite  $D$  result obtained from (6.5.27). In the right panel of Fig. 6.10 we plot the numerical solution to (6.5.16) with FN dynamics (6.4.23) for the parameter set  $d_1 = 15.6$  and  $d_2 = 0.2$ , which is inside the unstable region bounded by the dashed

6.6. *The Effect of the Spatial Configuration of the Small Cells: The  $D = \mathcal{O}(1)$  Regime*

---

curves in the left panel of Fig. 6.10. With the initial condition  $u_1(0) = 6.0$ ,  $u_2(0) = 2.3$  and  $U_0(0) = 0.05$ , the numerical computations of the full ODE system (6.5.16) reveal a sustained and stable periodic solution.

Finally, we use XPPAUT [16] on (6.5.16) to compute a global bifurcation of  $u_1$  versus  $d_1$  for fixed  $d_2 = 0.2$  for FN kinetics. This plot corresponds to taking a vertical slice at fixed  $d_2 = 0.2$  through the stability boundaries in the  $d_2$  versus  $d_1$  plane shown in Fig. 6.10. The two computed Hopf bifurcation points at  $d_1 \approx 15.389$  and  $d_1 \approx 42.842$  agree with the theoretically predicted values in Fig. 6.10. These results confirm the existence of a stable periodic solution branch induced by the cell-bulk coupling.

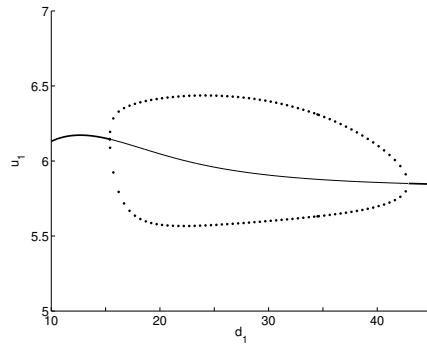


Figure 6.11: Global bifurcation diagram of  $u_1$  versus  $d_1$  at a fixed  $d_2 = 0.2$ , as computed using XPPAUT [16] from the ODE system (6.5.16) for the FN kinetics (6.4.23). The thick/thin solid line represents stable/unstable steady-state solutions of  $u_1$ , while the solid dots indicate a stable periodic solution. The other parameter values are  $z = 3.5$ ,  $q = 5$ ,  $\epsilon_0 = 0.5$ ,  $\tau = 1$ , and  $|\Omega| = 10$ .

## 6.6 The Effect of the Spatial Configuration of the Small Cells: The $D = \mathcal{O}(1)$ Regime

In this section we construct steady-state solutions and study their linear stability properties in the  $D = \mathcal{O}(1)$  regime, where both the number of cells and their spatial distribution in the domain are important factors. For simplicity, we consider a special spatial configuration of the cells inside the unit disk  $\Omega$  for which the Green's matrix  $\mathcal{G}$  has a cyclic structure. More specifically, on a ring of radius  $r_0$ , with  $0 < r_0 < 1$ , we place  $m$  equally-

6.6. *The Effect of the Spatial Configuration of the Small Cells: The  $D = \mathcal{O}(1)$  Regime*

---

spaced cells whose centers are at

$$\mathbf{x}_j = r_0 \left( \cos \left( \frac{2\pi j}{m} \right), \sin \left( \frac{2\pi j}{m} \right) \right)^T, \quad j = 1, \dots, m. \quad (6.6.1)$$

This ring of cells is concentric with respect to the unit disk  $\Omega \equiv \{\mathbf{x} \mid |\mathbf{x}| \leq 1\}$ . A schematic diagram for this system with  $m = 5$  is shown in Fig. 6.12.

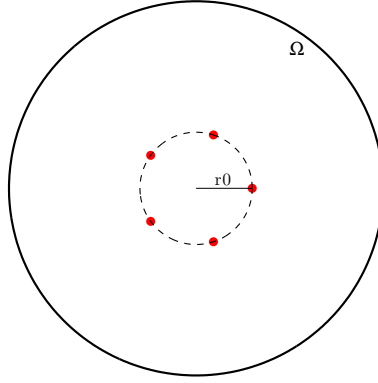


Figure 6.12: Schematic diagram showing five cells evenly spaced on 2D ring with radius  $r_0 = 0.3$  inside the unit disk. The red dots denotes signaling compartments or cells

We also assume that the intracellular kinetics is the same within each cell, so that  $\mathbf{F}_j = \mathbf{F}$  for  $j = 1, \dots, m$ . A related type of analysis characterizing the stability of localized spot solutions for the Gray-Scott RD model, where localized spots are equally-spaced on a ring concentric with the unit disk, was performed in [9].

For the unit disk, the Green's function  $G(\mathbf{x}; \boldsymbol{\xi})$  satisfying (6.2.10) can be written as an infinite sum involving the modified Bessel functions of the first and second kind  $I_n(z)$  and  $K_n(z)$ , respectively, in the form (see Appendix A.1 of [9])

$$\begin{aligned} G(\mathbf{x}; \boldsymbol{\xi}) &= \frac{1}{2\pi} K_0(\theta_0 |\mathbf{x} - \boldsymbol{\xi}|) \\ &\quad - \frac{1}{2\pi} \sum_{n=0}^{\infty} \sigma_n \cos(n(\psi - \psi_0)) \frac{K'_n(\theta_0)}{I'_n(\theta_0)} I_n(\theta_0 r) I_n(\theta_0 r_0); \quad (6.6.2) \\ &\quad \sigma_0 = 1, \quad \sigma_n = 2, \quad n \geq 1. \end{aligned}$$

6.6. *The Effect of the Spatial Configuration of the Small Cells: The  $D = \mathcal{O}(1)$  Regime*

---

Here  $\theta_0 \equiv D^{-1/2}$ ,  $\mathbf{x} = r e^{i\psi}$ ,  $\boldsymbol{\xi} = r_0 e^{i\psi_0}$ , and

$$|\mathbf{x} - \boldsymbol{\xi}| = \sqrt{r^2 + r_0^2 - 2rr_0 \cos(\psi - \psi_0)}.$$

By using the local behavior  $K_0(z) \sim -\log z + \log 2 - \gamma_e + o(1)$  as  $z \rightarrow 0^+$ , where  $\gamma_e$  is Euler's constant, we can extract the regular part  $R$  of  $G(\mathbf{x}; \boldsymbol{\xi})$  as  $\mathbf{x} \rightarrow \boldsymbol{\xi}$ , as identified in (6.2.10b), as

$$R = \frac{1}{2\pi} \left( \log 2 - \gamma_e + \frac{1}{2} \log D \right) - \frac{1}{2\pi} \sum_{n=0}^{\infty} \sigma_n \frac{K'_n(\theta_0)}{I'_n(\theta_0)} [I_n(\theta_0 r_0)]^2. \quad (6.6.3)$$

For this spatial configuration of cells, the Green's matrix  $\mathcal{G}$  is obtained by a cyclic permutation of its first row vector  $\mathbf{a} \equiv (a_1, \dots, a_m)^T$ , which is defined term-wise by

$$a_1 \equiv R; \quad a_j = G_{j1} \equiv G(\mathbf{x}_j; \mathbf{x}_1), \quad j = 2, \dots, m. \quad (6.6.4)$$

We can numerically evaluate  $G_{j1}$  for  $j = 2, \dots, m$  and  $R$  by using (6.6.2) and (6.6.3), respectively. Since  $\mathcal{G}$  is a cyclic matrix, it has an eigenpair, corresponding to a synchronous perturbation, given by

$$\mathcal{G}\mathbf{e} = \omega_1 \mathbf{e}; \quad \mathbf{e} \equiv (1, \dots, 1)^T, \quad \omega_1 \equiv \sum_{j=1}^m a_j = R + \sum_{j=1}^m G_{ji}. \quad (6.6.5)$$

When  $D = \mathcal{O}(1)$ , the steady-state solution is determined by the solution to the nonlinear algebraic system (6.2.7) and (6.2.13). Since  $\mathbf{F}_j = \mathbf{F}$  for  $j = 1, \dots, m$ , and  $\mathbf{e}$  is an eigenvector of  $\mathcal{G}$  with eigenvalue  $\omega_1$ , we can look for a solution to (6.2.7) and (6.2.13) having a common source strength, so that  $\mathbf{S} = S_c \mathbf{e}$ ,  $\mathbf{u}_j = \mathbf{u}$  for all  $j = 1, \dots, m$ , and  $\mathbf{u}^1 = u_1 \mathbf{e}$ . In this way, we obtain from (6.2.7) and (6.2.13), that the steady-state problem is to solve the  $n+1$  dimensional nonlinear algebraic system for  $S_c$  and  $\mathbf{u} = (u_1, u_2, \dots, u_n)^T$  given by

$$\mathbf{F}(\mathbf{u}) + \frac{2\pi D}{\tau} S_c \mathbf{e} = \mathbf{0}; \quad S_c = -\beta u_1, \quad \beta \equiv \frac{d_2 \nu}{d_1 + 2\pi \nu d_1 \omega_1 + D\nu}, \quad (6.6.6)$$

where  $\nu \equiv -1/\log \epsilon$  and  $\omega_1$  is defined in (6.6.5). We remark that  $\omega_1$  depends on  $D$ ,  $r_0$ , and  $m$ .

To study the linear stability of this steady-state solution, we write the GCEP, given in (6.2.32), in the form

$$\mathcal{G}_\lambda \mathbf{c} = -\frac{1}{2\pi \nu} \left[ 1 + \frac{D\nu}{d_1} + \frac{2\pi \nu d_2 D}{d_1 \tau} \frac{M_{11}}{\det(\lambda I - J)} \right] \mathbf{c}, \quad (6.6.7)$$

6.6. *The Effect of the Spatial Configuration of the Small Cells: The  $D = \mathcal{O}(1)$  Regime*

---

where  $J$  is the Jacobian of  $\mathbf{F}$  evaluated at the steady-state. In terms of the matrix spectrum of  $\mathcal{G}_\lambda$ , written as

$$\mathcal{G}_\lambda \mathbf{v}_j = \omega_{\lambda,j} \mathbf{v}_j, \quad j = 1, \dots, m, \quad (6.6.8)$$

we conclude from (6.6.7) that the set of discrete eigenvalues  $\lambda$  of the linearization of the steady-state are the union of the roots of the  $m$  transcendental equations, written as  $\mathcal{F}_j(\lambda) = 0$ , where

$$\mathcal{F}_j(\lambda) \equiv \omega_{\lambda,j} + \frac{1}{2\pi\nu} \left(1 + \frac{D\nu}{d_1}\right) + \left(\frac{d_2 D}{d_1 \tau}\right) \frac{M_{11}}{\det(\lambda I - J)}, \quad j = 1, \dots, m. \quad (6.6.9)$$

Any such root of  $\mathcal{F}_j(\lambda) = 0$  with  $\text{Re}(\lambda) > 0$  leads to an instability of the steady-state solution on an  $\mathcal{O}(1)$  time-scale. If all such roots satisfy  $\text{Re}(\lambda) < 0$ , then the steady-state is linearly stable on an  $\mathcal{O}(1)$  time-scale.

To study the stability properties of the steady-state using (6.6.9), and identify any possible Hopf bifurcation values, we must first calculate the spectrum (6.6.8) of the cyclic and symmetric matrix  $\mathcal{G}_\lambda$ , whose entries are determined by the  $\lambda$ -dependent reduced-wave Green's function  $G_\lambda(\mathbf{x}; \boldsymbol{\xi})$ , with regular part  $R_\lambda(\boldsymbol{\xi})$ , as defined by (6.2.23). Since  $\mathcal{G}_\lambda$  is not a Hermitian matrix when  $\lambda$  is complex, its eigenvalues  $\omega_{\lambda,j}$  are in general complex-valued when  $\lambda$  is complex. Then, by replacing  $\theta_0$  in (6.6.2) and (6.6.3) with  $\theta_\lambda \equiv \sqrt{(1 + \tau\lambda)/D}$ , we readily obtain that

$$\begin{aligned} G_\lambda(\mathbf{x}; \boldsymbol{\xi}) &= \frac{1}{2\pi} K_0(\theta_\lambda |\mathbf{x} - \boldsymbol{\xi}|) \\ &\quad - \frac{1}{2\pi} \sum_{n=0}^{\infty} \sigma_n \cos(n(\psi - \psi_0)) \frac{K'_n(\theta_\lambda)}{I'_n(\theta_\lambda)} I_n(\theta_\lambda r) I_n(\theta_\lambda r_0); \\ &\quad \sigma_0 = 1, \quad \sigma_n = 2, \quad n \geq 1, \end{aligned} \quad (6.6.10)$$

with regular part

$$R_\lambda = \frac{1}{2\pi} \left[ \log 2 - \gamma_e + \frac{1}{2} \log D - \frac{1}{2} \log(1 + \tau\lambda) \right] - \frac{1}{2\pi} \sum_{n=0}^{\infty} \sigma_n \frac{K'_n(\theta_\lambda)}{I'_n(\theta_\lambda)} [I_n(\theta_\lambda r_0)]^2, \quad (6.6.11)$$

where we have specified the principal branch for  $\theta_\lambda$ . The Green's matrix  $\mathcal{G}_\lambda$  is obtained by a cyclic permutation of its first row  $\mathbf{a}_\lambda \equiv (a_{\lambda,1}, \dots, a_{\lambda,m})^T$ , which is defined term-wise by

$$a_{\lambda,1} \equiv R_\lambda; \quad a_{\lambda,j} = G_{\lambda,j1} \equiv G_\lambda(\mathbf{x}_j; \mathbf{x}_1), \quad j = 2, \dots, m. \quad (6.6.12)$$

6.6. *The Effect of the Spatial Configuration of the Small Cells: The  $D = \mathcal{O}(1)$  Regime*

---

Again we can numerically evaluate  $G_{\lambda,j1}$  for  $j = 2, \dots, m$  and  $R_\lambda$  by using (6.6.10) and (6.6.11), respectively.

Next, we must determine the full spectrum (6.6.8) of the cyclic and symmetric matrix  $\mathcal{G}_\lambda$ . For the  $m \times m$  cyclic matrix  $\mathcal{G}_\lambda$ , generated by permutations of the row vector  $\mathbf{a}_\lambda$ , it is well-known that its eigenvectors  $\mathbf{v}_j$  and eigenvalues  $\omega_{\lambda,j}$  are

$$\omega_{\lambda,j} = \sum_{n=0}^{m-1} a_{\lambda,n+1} e^{2\pi i(j-1)n/m}, \quad \mathbf{v}_j = (1, e^{2\pi i(j-1)/m}, \dots, e^{2\pi i(j-1)(m-1)/m})^T, \quad j = 1, \dots, m. \quad (6.6.13)$$

Since  $\mathcal{G}$  is also necessarily a symmetric matrix it follows that

$$a_{\lambda,j} = a_{\lambda,m+2-j}, \quad j = 2, \dots, \lceil m/2 \rceil, \quad (6.6.14)$$

where the ceiling function  $\lceil x \rceil$  is defined as the smallest integer not less than  $x$ . This relation can be used to simplify the expression (6.6.13) for  $\omega_{\lambda,j}$ , into the form as written below in (6.6.16). Moreover, as a result of (6.6.14), it readily follows that

$$\omega_{\lambda,j} = \omega_{\lambda,m+2-j}, \quad \text{for } j = 2, \dots, \lceil m/2 \rceil, \quad (6.6.15)$$

so that there are  $\lceil m/2 \rceil - 1$  eigenvalues of multiplicity two. For these multiple eigenvalues the two independent real-valued eigenfunctions are readily seen to be  $\text{Re}(\mathbf{v}_j) = (\mathbf{v}_j + \mathbf{v}_{m+2-j})/2$  and  $\text{Im}(\mathbf{v}_j) = (\mathbf{v}_j - \mathbf{v}_{m+2-j})/(2i)$ . In addition to  $\omega_1$ , we also observe that there is an additional eigenvalue of multiplicity one when  $m$  is even.

In this way, our result for the matrix spectrum of  $\mathcal{G}_\lambda$  is as follows: The synchronous eigenpair of  $\mathcal{G}_\lambda$  is

$$\omega_{\lambda,1} = \sum_{n=1}^m a_{\lambda,n}, \quad \mathbf{v}_1 = (1, \dots, 1)^T, \quad (6.6.16a)$$

while the other eigenvalues, corresponding to the asynchronous modes, are

$$\omega_{\lambda,j} = \sum_{n=0}^{m-1} \cos\left(\frac{2\pi(j-1)n}{m}\right) a_{\lambda,n+1}, \quad j = 2, \dots, m, \quad (6.6.16b)$$

where  $\omega_{\lambda,j} = \omega_{\lambda,m+2-j}$  for  $j = 2, \dots, \lceil m/2 \rceil$ . When  $m$  is even, we notice that there is an eigenvalue of multiplicity one given by  $\omega_{\lambda, \frac{m}{2}+1} =$

6.6. *The Effect of the Spatial Configuration of the Small Cells: The  $D = \mathcal{O}(1)$  Regime*

---

$\sum_{n=0}^{m-1} (-1)^n a_{n+1}$ . The corresponding eigenvectors for  $j = 2, \dots, \lceil m/2 \rceil$  can be written as

$$\begin{aligned} \mathbf{v}_j &= \left( 1, \cos\left(\frac{2\pi(j-1)}{m}\right), \dots, \cos\left(\frac{2\pi(j-1)(m-1)}{m}\right) \right)^T, \\ \mathbf{v}_{m+2-j} &= \left( 0, \sin\left(\frac{2\pi(j-1)}{m}\right), \dots, \sin\left(\frac{2\pi(j-1)(m-1)}{m}\right) \right)^T. \end{aligned} \quad (6.6.16c)$$

Finally, when  $m$  is even, there is an additional eigenvector given by  $\mathbf{v}_{\frac{m}{2}+1} = (1, -1, \dots, -1)^T$ .

With the eigenvalues  $\omega_{\lambda,j}$ , for  $j = 1, \dots, m$ , determined in this way, any Hopf bifurcation boundary in parameter space is obtained by substituting  $\lambda = i\lambda_I$  with  $\lambda_I > 0$  into (6.6.9), and requiring that the real and imaginary parts of the resulting expression vanish. This yields, for each  $j = 1, \dots, m$ , that

$$\begin{aligned} \operatorname{Re}(\omega_{\lambda,j}) + \frac{1}{2\pi\nu} \left( 1 + \frac{D\nu}{d_1} \right) + \frac{d_2 D}{d_1 \tau} \operatorname{Re} \left( \frac{M_{11}}{\det(\lambda I - J)} \right) &= 0, \\ \operatorname{Im}(\omega_{\lambda,j}) + \frac{d_2 D}{d_1 \tau} \operatorname{Im} \left( \frac{M_{11}}{\det(\lambda I - J)} \right) &= 0. \end{aligned} \quad (6.6.17)$$

Finally, we can use the winding number criterion of complex analysis on (6.6.9) to count the number of eigenvalues of the linearization when the parameters are off any Hopf bifurcation boundary. This criterion is formulated below in §6.6.1.

We remark that in the limit  $D \gg 1$ , we can use  $K_0(z) \sim -\log z$  together with  $I_0(z) \sim 1 + z^2/4$  as  $z \rightarrow 0$ , to estimate from the  $n = 0$  term in (6.6.10) and (6.6.11) that  $-(2\pi)^{-1} K'_0(\theta_\lambda)/I'_0(\theta_\lambda) \sim D/[\pi(1 + \tau\lambda)]$  as  $D \rightarrow \infty$ . Therefore, for  $D \rightarrow \infty$ , the Green's matrix  $\mathcal{G}_\lambda$  satisfies  $\mathcal{G}_\lambda \rightarrow Dm\mathcal{E}/[\pi(1 + \tau\lambda)]$ , where  $\mathcal{E} = \mathbf{e}\mathbf{e}^T/m$  and  $\mathbf{e} \equiv (1, \dots, 1)^T$ . This yields for  $D \gg 1$  that  $\omega_1 = Dm/[\pi(1 + \tau\lambda)]$  and  $\omega_j = \mathcal{O}(1)$  for  $j = 2, \dots, n$ . By substituting these expressions into (6.6.17), we can readily recover the spectral problems (6.3.20) and (6.3.21), considered in §6.3, associated with the regime  $D = \mathcal{O}(\nu^{-1})$ . Therefore, (6.6.17) provides a smooth transition to the leading-order spectral problems considered in §6.3 for  $D = \mathcal{O}(\nu^{-1})$ .

### 6.6.1 Example: The Sel'kov Model

We now use (6.6.17) to compute phase diagrams in the  $\tau$  versus  $D$  parameter space associated with  $m$  equally-spaced cells of radius  $\epsilon$  on a ring of radius

6.6. *The Effect of the Spatial Configuration of the Small Cells: The  $D = \mathcal{O}(1)$  Regime*

---

$r_0$ , with  $0 < r_0 < 1$ , concentric within the unit disk. For the intracellular dynamics we let  $n = 2$ , so that  $\mathbf{u} = (u_1, u_2)^T$ , and we consider the Sel'kov dynamics  $\mathbf{F} = (F(u_1, u_2), G(u_1, u_2))^T$  as given in (6.4.17). For this choice, (6.6.6) yields the steady-state solution  $(u_{1e}, u_{2e})^T$  for the coupled cell-bulk system given by

$$u_{1e} = \frac{\mu}{1 + 2\pi D\beta/\tau}, \quad u_{2e} = \frac{\mu}{\alpha + u_{1e}^2}, \quad (6.6.18a)$$

where  $\beta$  is defined in (6.6.6). Upon using (6.4.19) we calculate that

$$\begin{aligned} \det(J) &= \epsilon_0 \left( \alpha + u_{1e}^2 \right) > 0, \\ \operatorname{tr}(J) &= \frac{1}{\alpha + u_{1e}^2} \left[ 2u_{1e}\mu - (\alpha + u_{1e}^2) - \epsilon_0(\alpha + u_{1e}^2)^2 \right]. \end{aligned} \quad (6.6.18b)$$

In this subsection we fix the Sel'kov parameters  $\mu$ ,  $\alpha$ , and  $\epsilon_0$ , the permeabilities  $d_1$  and  $d_2$ , and the cell radius  $\epsilon$  as

$$\mu = 2, \quad \alpha = 0.9, \quad \epsilon_0 = 0.15, \quad d_1 = 0.8, \quad d_2 = 0.2, \quad \epsilon = 0.05. \quad (6.6.19)$$

With these values for  $\mu$ ,  $\alpha$ , and  $\epsilon_0$ , the intracellular dynamics has a stable steady-state when uncoupled from the bulk.

Then, to determine the Hopf bifurcation boundary for the coupled cell-bulk model we set  $M_{11} = \lambda - G_{u_2}^e$  in (6.6.17), and use  $G_{u_2}^e = -\det(J)$  as obtained from (6.4.19). By letting  $\lambda = i\lambda_I$  in the resulting expression, we conclude that any Hopf bifurcation boundary, for each mode  $j = 1, \dots, m$ , must satisfy

$$\begin{aligned} \operatorname{Re}(\omega_{\lambda,j}) + \frac{1}{2\pi\nu} \left( 1 + \frac{D\nu}{d_1} \right) - \left( \frac{d_2 D}{d_1 \tau} \right) \frac{\left[ \lambda_I^2 \operatorname{tr}(J) + \det(J) (\lambda_I^2 - \det(J)) \right]}{\left[ (\det(J) - \lambda_I^2)^2 + (\lambda_I \operatorname{tr}(J))^2 \right]} &= 0, \\ \operatorname{Im}(\omega_{\lambda,j}) + \left( \frac{d_2 D}{d_1 \tau} \right) \frac{\left[ \lambda_I (\det(J) - \lambda_I^2) + \det(J) \operatorname{tr}(J) \lambda_I \right]}{\left[ (\det(J) - \lambda_I^2)^2 + (\lambda_I \operatorname{tr}(J))^2 \right]} &= 0. \end{aligned} \quad (6.6.20)$$

For a specified value of  $D$ , we view (6.6.20) as a coupled system for the Hopf bifurcation value of  $\tau$  and the corresponding eigenvalue  $\lambda_I$ , which we solve by Newton's method.

For parameter values off of any Hopf bifurcation boundary, we can use the winding number criterion on  $\mathcal{F}_j(\lambda)$  in (6.6.9) to count the number of

6.6. *The Effect of the Spatial Configuration of the Small Cells: The  $D = \mathcal{O}(1)$  Regime*

---

unstable eigenvalues  $N_j$  of the linearization for the  $j$ -th mode. By using the argument principle, we obtain that the number  $N_j$  of roots of  $\mathcal{F}_j(\lambda) = 0$  in  $\text{Re}(\lambda) > 0$  is

$$N_j = \frac{1}{2\pi} [\arg \mathcal{F}_j]_{\Gamma} + P, \quad (6.6.21)$$

where  $P$  is the number of poles of  $\mathcal{F}_j(\lambda)$  in  $\text{Re}(\lambda) > 0$ , and the square bracket denotes the change in the argument of  $\mathcal{F}_j$  over the contour  $\Gamma$ . Here the closed contour  $\Gamma$  is the limit as  $\mathcal{R} \rightarrow \infty$  of the union of the imaginary axis, which can be decomposed as  $\Gamma_{I+} = i\lambda_I$  and  $\Gamma_{I-} = -i\lambda_I$ , for  $0 < \lambda_I < \mathcal{R}$ , and the semi-circle  $\Gamma_{\mathcal{R}}$  defined by  $|\lambda| = \mathcal{R}$  with  $|\arg(\lambda)| \leq \pi/2$ . Since  $\omega_{\lambda_j}$  is analytic in  $\text{Re}(\lambda) > 0$ , it follows that  $P$  is determined by the number of roots of  $\det(\lambda I - J) = 0$  in  $\text{Re}(\lambda) > 0$ . Since  $\det(J) > 0$ , as shown in (6.6.18b), we have that  $P = 2$  if  $\text{tr}(J) > 0$  and  $P = 0$  if  $\text{tr}(J) < 0$ . Next, we let  $\mathcal{R} \rightarrow \infty$  on  $\Gamma_{\mathcal{R}}$  and calculate  $[\arg \mathcal{F}_j]_{\Gamma_{\mathcal{R}}}$ . It is readily seen that the Green's matrix  $\mathcal{G}_{\lambda}$  tends to a multiple of a diagonal matrix on  $\Gamma_{\mathcal{R}}$  as  $\mathcal{R} \gg 1$ , of the form  $\mathcal{G}_{\lambda} \rightarrow R_{\lambda, \infty} I$ , where  $R_{\lambda, \infty}$  is the regular part of the free-space Green's function  $G_f(\mathbf{x}; \mathbf{x}_0) = (2\pi)^{-1} K_0(\theta_{\lambda} |\mathbf{x} - \mathbf{x}_0|)$  at  $\mathbf{x} = \mathbf{x}_0$ , given explicitly by the first term in the expression (6.6.11) for  $R_{\lambda}$ . Since  $\omega_{\lambda, j} \rightarrow R_{\lambda, \infty}$  for  $j = 1, \dots, m$ , we estimate on  $\Gamma_{\mathcal{R}}$  as  $\mathcal{R} \gg 1$  that

$$\mathcal{F}_j(\lambda) \sim -\frac{1}{2\pi} \log \sqrt{1 + \tau\lambda} + c_0 + \mathcal{O}(1/\lambda),$$

for some constant  $c_0$ . It follows that  $\mathcal{F}_j(\lambda) \sim O(\ln \mathcal{R}) - i/8$  as  $\mathcal{R} \rightarrow \infty$ , so that  $\lim_{\mathcal{R} \rightarrow \infty} [\arg \mathcal{F}_j]_{\Gamma_{\mathcal{R}}} = 0$ . Finally, since  $[\arg \mathcal{F}_j]_{\Gamma_{I+}} = [\arg \mathcal{F}_j]_{\Gamma_{I-}}$ , as a consequence of  $\mathcal{F}_j$  being real-valued when  $\lambda$  is real, we conclude from (6.6.21) that

$$N_j = \frac{1}{2\pi} [\arg \mathcal{F}_j]_{\Gamma_{I+}} + P, \quad P = \begin{cases} 2 & \text{if } \text{tr} J > 0 \\ 0 & \text{if } \text{tr} J < 0 \end{cases}. \quad (6.6.22)$$

By using (6.6.20) for the real and imaginary parts of  $\mathcal{F}_j$ ,  $[\arg \mathcal{F}_j]_{\Gamma_{I+}}$  is easily calculated numerically by a line sweep over  $0 < \lambda_I < \mathcal{R}$ . Then, by using (6.6.18b) to calculate  $\text{tr}(J)$ ,  $P$  is readily determined. In this way, (6.6.22) leads to a highly tractable numerical procedure to calculate  $N_j$ . This criterion was used for all the results below to identify regions in parameter space where instabilities occur away from any Hopf bifurcation boundary.

In Fig. 6.13 we plot the Hopf bifurcation boundaries when  $m = 2$  and  $r_0 = 0.25$ . From the left panel of this figure, the synchronous mode is unstable in the larger lobe shaped region, whereas the asynchronous mode is

6.6. *The Effect of the Spatial Configuration of the Small Cells: The  $D = \mathcal{O}(1)$  Regime*

---

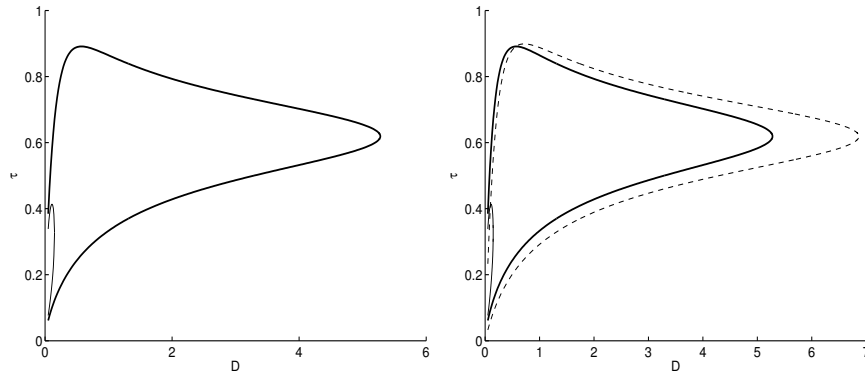


Figure 6.13: Hopf bifurcation boundaries in the  $\tau$  versus  $D$  plane for  $m = 2$ ,  $r_0 = 0.25$ , and with parameters as in (6.6.19), computed from (6.6.20). Left panel: the heavy solid curve and the solid curve are the Hopf bifurcation boundaries for the synchronous and asynchronous modes, respectively. Inside the respective lobes the corresponding mode is linearly unstable, as verified by the winding number criterion (6.6.22). Right panel: same plot except that we include the Hopf bifurcation boundary for the synchronous mode from the leading-order  $D = D_0/\nu \gg 1$  theory, computed from (6.3.20).

6.6. *The Effect of the Spatial Configuration of the Small Cells: The  $D = \mathcal{O}(1)$  Regime*

---

unstable only in the small lobe for small  $D$ , which is contained within the instability lobe for the synchronous mode. In the right panel of Fig. 6.13 we show the Hopf bifurcation boundary for the synchronous mode, as obtained from (6.3.20), corresponding to the leading-order  $D = D_0/\nu \gg 1$  theory. Since the instability lobe occurs for only moderate values of  $D$ , and  $\epsilon = 0.05$  is only moderately small, the leading-order theory from the  $D = D_0/\nu$  regime is, as expected, not particularly accurate in determining the Hopf bifurcation boundary. The fact that we have stability at a fixed  $D$  for  $\tau \gg 1$ , which corresponds to very fast intracellular dynamics, is expected since in this limit the intracellular dynamics becomes decoupled from the bulk diffusion. Alternatively, if  $\tau \ll 1$ , then for a fixed  $D$ , the intracellular reactions proceed too slowly to create any instability. Moreover, in contrast to the large region of instability for the synchronous mode as seen in Fig. 6.13, we observe that the lobe of instability for the asynchronous mode only occurs for small values of  $D$ , where the diffusive coupling, and communication, between the two cells is rather weak. Somewhat more paradoxically, we also observe that the synchronous lobe of instability is bounded in  $D$ . This issue is discussed in more detail below.

In Fig. 6.14 we show the effect of changing the ring radius  $r_0$  on the Hopf bifurcation boundaries. By varying  $r_0$ , we effectively are modulating the distance between the two cells. From this figure we observe that as  $r_0$  is decreased, the lobe of instability for the asynchronous mode decreases, implying, rather intuitively, that at closer distances the two cells are better able to synchronize their oscillations than when they are farther apart. We remark that results from the leading-order theory of §6.3 for the  $D = \mathcal{O}(\nu^{-1})$  regime would be independent of  $r_0$ . We further observe from this figure that a synchronous instability can be triggered from a more clustered spatial arrangement of the cells inside the domain. In particular, for  $D = 5$  and  $\tau = 0.6$ , we observe from Fig. 6.14 that we are outside the lobe of instability for  $r_0 = 0.5$ , but inside the lobe of instability for  $r_0 = 0.25$  and  $r_0 = 0.75$ . We remark that due to the Neumann boundary conditions the cells on the ring with  $r_0 = 0.75$  are close to two image cells outside the unit disk, which leads to a qualitatively similar clustering effect of these near-boundary cells as when they are on the small ring of radius  $r_0 = 0.25$ .

In Fig. 6.15 we plot the Hopf bifurcation boundaries when  $m = 3$  and  $r_0 = 0.5$ . For  $m = 3$ , we now observe that the region where the synchronous mode is unstable is unbounded in  $D$ . The lobe of instability for the asynchronous mode still exists only for small  $D$ , as shown in the right panel of Fig. 6.15. In this case, we observe that the Hopf bifurcation boundary for the synchronous mode, corresponding to the leading-order  $D = D_0/\nu \gg 1$

6.6. *The Effect of the Spatial Configuration of the Small Cells: The  $D = \mathcal{O}(1)$  Regime*

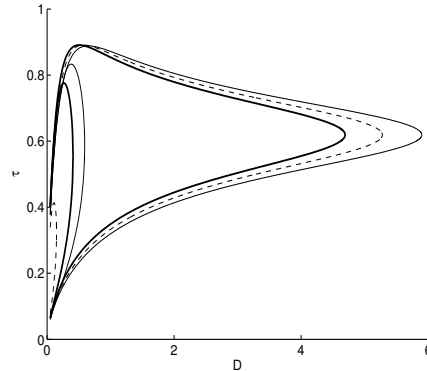


Figure 6.14: Hopf bifurcation boundaries for the synchronous mode (larger lobes) and the asynchronous mode (smaller lobes) in the  $\tau$  versus  $D$  plane for  $m = 2$  and for three values of  $r_0$ , with  $r_0 = 0.5$  (heavy solid curves),  $r_0 = 0.75$  (solid curves), and  $r_0 = 0.25$  (dashed curves). The other parameters are given in (6.6.19). We observe that as  $r_0$  decreases, where the two cells become more closely spaced, the lobe of instability for the asynchronous mode decreases.

theory and computed from (6.3.20), now agrees rather well with results computed from (6.6.20).

In the left panel of Fig. 6.16 we plot the Hopf bifurcation boundaries for the synchronous mode for  $m = 5$  when  $r_0 = 0.5$  (heavy solid curves) and for  $r_0 = 0.25$  (solid curves). We observe that for moderate values of  $D$ , the Hopf bifurcation values do depend significantly on the radius of the ring. The synchronous mode is unstable only in the infinite strip-like domain between these Hopf bifurcation boundaries. Therefore, only in some intermediate range of  $\tau$ , representing the ratio of the rates of the intracellular reaction and bulk decay, is the synchronous mode unstable. As expected, the two curves for different values of  $r_0$  coalesce as  $D$  increases, owing to the fact that the leading-order stability theory for  $D = D_0/\nu \gg 1$ , as obtained from (6.3.20), is independent of  $r_0$ . In the right panel of Fig. 6.16 we compare the Hopf bifurcation boundaries for the synchronous mode with  $r_0 = 0.5$  with that obtained from (6.3.20), corresponding to the leading-order theory in the  $D = D_0/\nu \gg 1$  regime. Rather curiously, we observe upon comparing the solid curves in the left and right panels in Fig. 6.16 that the Hopf bifurcation boundaries from the  $D = \mathcal{O}(1)$  theory when  $r_0 = 0.25$ , where the five cells are rather clustered near the origin, agree very closely with the leading

6.6. *The Effect of the Spatial Configuration of the Small Cells: The  $D = \mathcal{O}(1)$  Regime*

---

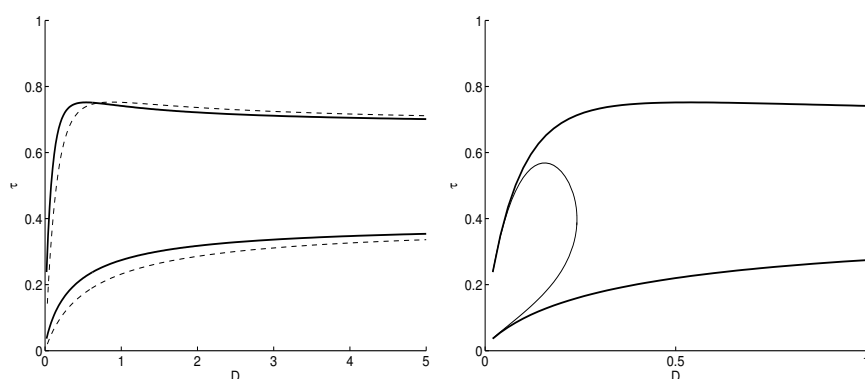


Figure 6.15: Left panel: Hopf bifurcation boundaries in the  $\tau$  versus  $D$  plane for the synchronous mode for  $m = 3$  equally-spaced cells on a ring of radius  $r_0 = 0.50$  (heavy solid curves), as computed from (6.6.20), with parameters as in (6.6.19). The dashed curve is the Hopf bifurcation boundary from the leading-order  $D = D_0/\nu$  theory computed from (6.3.20). Right panel: The Hopf bifurcation boundaries for the asynchronous mode (solid curve) and the synchronous mode (heavy solid curve) shown in a magnified region of  $D$ . The asynchronous mode is linearly unstable only inside this small lobe, which lies within the unstable region for the synchronous mode.

6.6. *The Effect of the Spatial Configuration of the Small Cells: The  $D = \mathcal{O}(1)$  Regime*

---

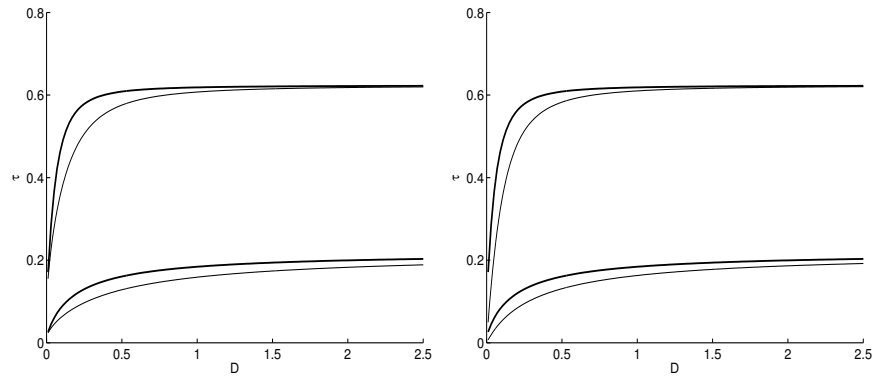


Figure 6.16: Left panel: Hopf bifurcation boundaries in the  $\tau$  versus  $D$  plane for the synchronous mode for  $m = 5$  equally-spaced cells on a ring of radius  $r_0 = 0.25$  (solid curves) and radius  $r_0 = 0.5$  (heavy solid curves) concentric with the unit disk, as computed from (6.6.20), with parameters (6.6.19). Right panel: Comparison of the Hopf bifurcation boundaries for the synchronous mode with  $r_0 = 0.5$  (heavy solid curves), as computed from (6.6.20), with that obtained from (6.3.20) for the leading-order  $D = D_0/\nu$  theory (solid curves). These curves agree well when  $D$  is large.

6.6. *The Effect of the Spatial Configuration of the Small Cells: The  $D = \mathcal{O}(1)$  Regime*

order theory from the  $D = D_0/\nu \gg 1$  regime. Since the clustering of cells is effectively equivalent to a system with a large diffusion coefficient, this result above indicates, rather intuitively, that stability thresholds for a clustered spatial arrangement of cells will be more closely approximated by results obtained from a large  $D$  approximation than for a non-clustered spatial arrangement of cells. In Fig. 6.17 we plot the Hopf bifurcation boundaries for the distinct asynchronous modes when  $m = 5$  for  $r_0 = 0.5$  (left panel) and  $r_0 = 0.75$  (right panel), as computed from (6.6.20) with  $j = 2, 5$  (larger lobe) and with  $j = 3, 4$  (smaller lobe). The asynchronous modes are only linearly unstable within these small lobes.

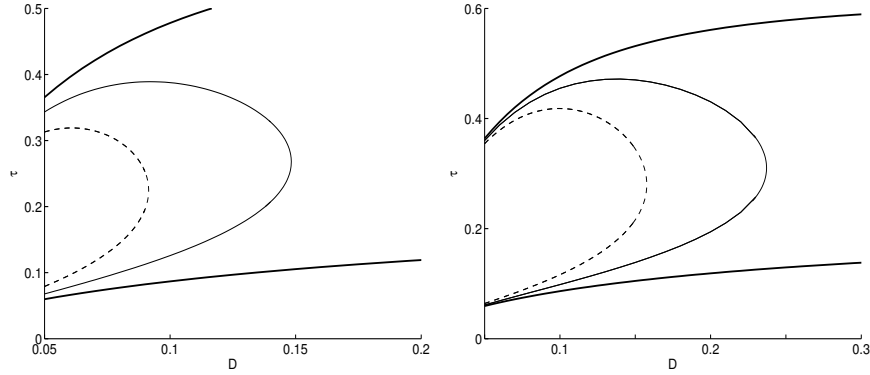


Figure 6.17: Hopf bifurcation boundaries for the two distinct asynchronous modes when  $m = 5$  for  $r_0 = 0.5$  (left panel) and  $r_0 = 0.75$  (right panel), as computed from (6.6.20) with  $j = 2, 5$  (larger solid curve lobe) and with  $j = 3, 4$  (smaller dashed curve lobe). The heavy solid curves are the Hopf bifurcation boundaries for the synchronous mode. The parameters are as in (6.6.19). The asynchronous mode for  $j = 2, 5$  and  $j = 3, 4$  is linearly unstable only inside the larger and smaller lobe, respectively.

To theoretically explain the observation that the instability region in the  $\tau$  versus  $D$  plane for the synchronous mode is bounded for  $m = 2$ , but unbounded for  $m \geq 3$ , we must first extend the large  $D$  analysis of §6.5 to the case of  $m$  small cells. We readily derive, assuming identical behavior in each of the  $m$  cells, that the reduced cell-bulk dynamics (6.5.16) for one cell must be replaced by

$$U'_0 = -\frac{1}{\tau} \left( 1 + \frac{2\pi m d_1}{|\Omega|} \right) U_0 + \frac{2\pi d_2 m}{\tau |\Omega|} u_1, \quad \mathbf{u}' = \mathbf{F}(\mathbf{u}) + \frac{2\pi}{\tau} [d_1 U_0 - d_2 u_1] \mathbf{e}_1, \quad (6.6.23)$$

when there are  $m$  cells. This indicates that the effective domain area is  $|\Omega|/m = \pi/m$  when there are  $m$  cells. Therefore, to examine the stability of the steady-state solution of (6.6.23) for the Sel'kov model, we need only replace  $|\Omega|$  with  $|\Omega|/m$  in the Routh-Hurwitz criteria for the cubic (6.5.27).

With this approach, in Fig. 6.18 we show that there are two Hopf bifurcation values of  $\tau$  for the steady-state solution of (6.6.23) when  $m = 3$  and  $m = 5$ . These values correspond to the horizontal asymptotes as  $D \rightarrow \infty$  in Fig. 6.15 for  $m = 3$  and in Fig. 6.16 for  $m = 5$ . The numerical results from XPPAUT [16] in Fig. 6.18 then reveal the existence of a stable periodic solution branch connecting these Hopf bifurcation points for  $m = 3$  and  $m = 5$ . A qualitatively similar picture holds for any  $m \geq 3$ . In contrast, for  $m = 2$ , we can verify numerically using (6.5.27), where we replace  $|\Omega|$  with  $|\Omega|/2$ , that the Routh-Hurwitz stability criteria  $p_1 > 0$ ,  $p_3 > 0$ , and  $p_1 p_2 > p_3$  hold for all  $\tau > 0$  when  $m = 2$  (and also  $m = 1$ ). Therefore, for  $m = 2$ , there are no Hopf bifurcation points in  $\tau$  for the steady-state solution of (6.6.23). This analysis suggests why there is a bounded lobe of instability for the synchronous mode when  $m = 2$ , as was shown in Fig. 6.13.

For the permeability values  $d_1 = 0.8$  and  $d_2 = 0.2$  used, we now suggest a qualitative reason for our observation that the lobe of instability for the synchronous mode is bounded in  $D$  only when  $m \leq m_c$ , where  $m_c$  is some integer threshold. We first observe that the diffusivity  $D$  serves a dual role. Although larger values of  $D$  allows for better communication between spatially segregated cells, suggesting that synchronization of their dynamics should be facilitated, it also has the competing effect of spatially homogenizing any perturbation in the diffusive signal. We suggest that only if the number of cells exceeds some threshold  $m_c$ , i.e. if some *quorum* is achieved, will the enhanced communication between the cells, resulting from a decrease in the effective domain area by  $|\Omega|/m$ , be sufficient to overcome the increased homogenizing effect of the diffusive signal at large values of  $D$ , and thereby lead to a synchronized time-periodic response.

Finally, fixing  $d_2 = 0.2$ , we use the Routh-Hurwitz stability criteria for the cubic (6.5.27) to determine how the quorum-sensing threshold  $m_c$  depends on the permeability  $d_1$ . Recall that if  $m > m_c$  there is a range of  $\tau$  for which the steady-state solution of (6.6.23) is destabilized due to Hopf bifurcations at some  $\tau_-$  and  $\tau_+$ , with a periodic solution branch existing on the range  $\tau_- < \tau < \tau_+$ . Our computations using the Routh-Hurwitz conditions yield for the unit disk that  $m_c = 3$  if  $d_1 = 0.5$ ,  $m_c = 4$  if  $d_1 = 0.4$ ,  $m_c = 6$  if  $d_1 = 0.3$ ,  $m_c = 9$  if  $d_1 = 0.2$ ,  $m_c = 12$  if  $d_1 = 0.15$ , and  $m_c = 19$  if  $d_1 = 0.1$ . We observe that by decreasing  $d_1$ , the number of cells required to attain a quorum increases rather steeply. This suggests that small changes

6.6. *The Effect of the Spatial Configuration of the Small Cells: The  $D = \mathcal{O}(1)$  Regime*

---

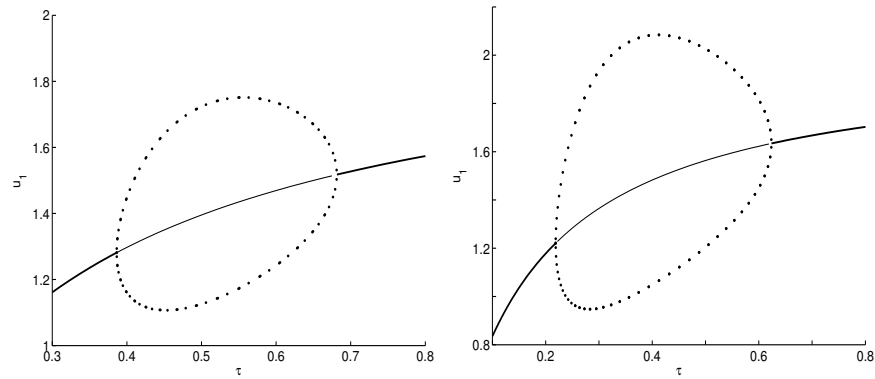


Figure 6.18: Global bifurcation diagram of  $u_{1\epsilon}$  versus  $\tau$  for the Sel'kov model (6.4.17) as computed using XPPAUT [16] from the ODE system (6.6.23) characterizing the limiting problem as  $D \rightarrow \infty$  with  $m$  small cells in the unit disk  $\Omega$ . Left panel:  $m = 3$ . Right panel:  $m = 5$ . The Sel'kov parameters are  $\mu = 2$ ,  $\alpha = 0.9$ , and  $\epsilon_0 = 0.15$ , while  $d_1 = 0.8$ , and  $d_2 = 0.2$ . The thick/thin solid line represents stable/unstable steady-state solutions, while the solid dots indicate a stable synchronous periodic solution in the cells. For  $m = 5$  (right panel), there are two Hopf bifurcation points at  $\tau = 0.2187$  and  $\tau = 0.6238$ . For  $m = 3$  (right panel), the two Hopf bifurcation points are at  $\tau = 0.3863$  and  $\tau = 0.6815$ . These points correspond to the horizontal asymptotes as  $D \rightarrow \infty$  in Fig. 6.16 for  $m = 5$  and in Fig. 6.15 for  $m = 3$ .

6.6. *The Effect of the Spatial Configuration of the Small Cells: The  $D = \mathcal{O}(1)$  Regime*

---

in the permeabilities can have a rather dramatic influence on increasing the number of cells needed to reach a quorum, and thereby initiate synchronous oscillations. For  $d_1 \leq 0.15$ , a new effect is observed in that there is a lower threshold value  $m_-$  of  $m$  needed to ensure that the synchronous lobe is bounded. In particular, we obtain for  $d_1 = 0.15$  and  $d_1 = 0.1$  that the synchronous lobe is bounded only for  $2 \leq m \leq 12$  and  $2 \leq m \leq 19$ , respectively, but is unbounded if  $m = 1$ . The explanation for the lower limit is that the steady-state can be unstable when  $d_1 = 0$  and  $d_2 = 0.2$  for some range of  $\tau$ . By ensuring  $p_1 p_2 = p_3$  at some  $\tau = \tau_c > 0$  with  $p_1 p_2 > p_3$  for  $\tau \neq \tau_c$ , together with  $p_1 > 0$  and  $p_3 > 0$ , in the Routh-Hurwitz criteria, in Fig. 6.19 we plot the numerically computed quorum-sensing threshold  $m_c$  and the lower threshold  $m_-$  as continuous functions of  $d_1$ .

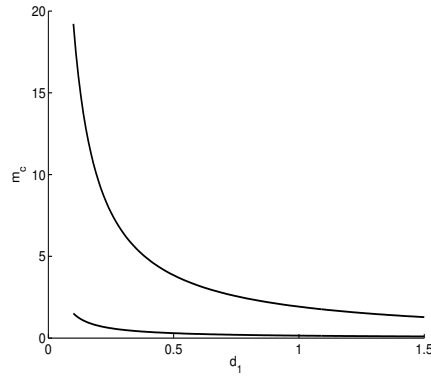


Figure 6.19: For  $d_2 = 0.2$ , and as  $d_1$  is varied, the instability lobe for the synchronous mode is bounded in  $D$  for any integer value  $m$  between the lower and upper curves. The domain is the unit disk, and the Sel'kov parameters are given in (6.6.19). The upper curve gives the quorum-sensing threshold for the number of cells  $m$  in the well-mixed  $D \gg \mathcal{O}(\nu^{-1})$  regime that are needed to initiate a collective synchronous oscillatory instability between the cells for some range of  $\tau$ .

Owing to the fact that the key parameter in the cubic (6.5.27) is  $|\Omega|/m$ , in order to determine thresholds for other domains we need only multiply the thresholds given above in Fig. 6.19 for the unit disk by the factor  $|\Omega|/\pi$ . The existence of this lower threshold  $m_-$  as  $d_1$  decreases explains the observation seen in Fig. 6.4 for  $d_1 = 0.1$  and  $d_2 = 0.2$  where one cell on a domain of area  $|\Omega| = 10$  lead to an unbounded lobe of instability for the synchronous mode. For this domain area, and by using the real-valued thresholds in

Fig. 6.19 for the unit disk together with our scaling law, we predict that there is a bounded lobe of instability for the synchronous mode only when  $5 \leq m \leq 61$ . Therefore, for  $m = 1$ , as in Fig. 6.4, we correctly predict that the lobe should be unbounded. In addition, for  $d_1 = 0.5$  and  $d_2 = 0.2$ , and with  $|\Omega| = 10$ , the lower threshold is slightly below unity, while the upper quorum-sensing threshold is  $m_c = 12$ . This confirms the bounded lobes of instability for the synchronous mode for  $m = 1, 2, 3$  as seen in Fig. 6.3.

## 6.7 Infinite Domain: Two Identical Cells

In the previous sections we studied the case where  $m$  small disjoint cells are located inside a bounded domain  $\Omega$ . For this case, we showed that the construction of the steady-state solution, and the analysis of the linear stability of this steady-state, simplifies considerably when  $D = \mathcal{O}(\nu^{-1}) \gg 1$ . For this large  $D$  regime, a stability analysis based on retaining leading-order terms in  $\nu$  was performed. The fact that the domain was bounded was essential to the large  $D$  analysis.

In this section, we consider the case where there are two small circular cells of a common radius  $\epsilon$  centered symmetrically at  $(x_0, 0)$  and  $(-x_0, 0)$  in the infinite plane. For this problem, we will construct a steady-state solution and we formulate the linear stability problem. We emphasize that our analysis below is not a leading-order-in- $\nu$  analysis, but incorporates all orders in  $\nu = -1/\log \epsilon$ . The geometry is shown in Fig. 6.20.

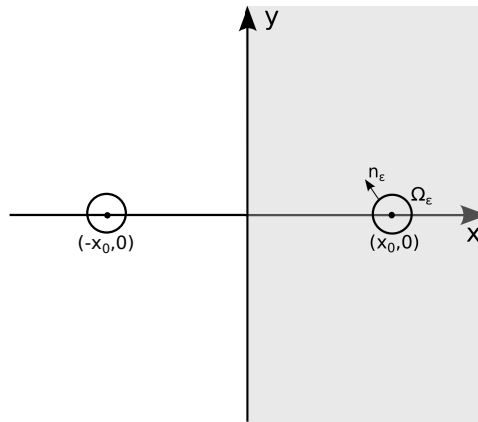


Figure 6.20: Schematic plot of the geometry of two cells on the infinite plane

To formulate our model, we take the two cells as the circular regions

### 6.7. Infinite Domain: Two Identical Cells

---

$\Omega_{\epsilon_{\pm}} = \{\mathbf{x} \mid |\mathbf{x} - (\pm \mathbf{x}_0)| \leq \epsilon\}$  of radius  $\epsilon$ . Let  $U(\mathbf{x}, t)$  represent the concentration of the signaling molecule in the bulk. Then, similar to (6.2.1), its spatial-temporal dynamics can be described by the PDE

$$\begin{aligned} \tau U_t &= \Delta U - U, & \mathbf{x} \in \mathbb{R}^2 \setminus \Omega_{\epsilon_{\pm}}; & & U \rightarrow 0 \quad \text{as} \quad |\mathbf{x}| \rightarrow \infty, \\ \epsilon \partial_{\mathbf{n}_{\epsilon}^+} U &= d_1 U - d_2 u_1^+, & \mathbf{x} \in \partial \Omega_{\epsilon_+}, & & \\ \epsilon \partial_{\mathbf{n}_{\epsilon}^-} U &= d_1 U - d_2 u_1^-, & \mathbf{x} \in \partial \Omega_{\epsilon_-}, & & \end{aligned} \quad (6.7.1a)$$

where  $\mathbf{n}_{\epsilon}^{\pm}$  denotes the outer normal to the cell  $\Omega_{\epsilon}^{\pm}$ , and so points into the bulk region.

Within each cell we assume, as before, that there are  $n$  dynamically interacting species. Assuming that the reaction kinetics are the same within each of the two cells, the cell dynamics are governed by

$$\frac{d\mathbf{u}^{\pm}}{dt} = \mathbf{F}(\mathbf{u}^{\pm}) + \frac{1}{\epsilon \tau} \int_{\partial \Omega_{\epsilon_{\pm}}} (d_1 U - d_2 u_1^{\pm}) ds \mathbf{e}_1, \quad (6.7.1b)$$

where  $\mathbf{u}^{\pm} = (u_1^{\pm}, \dots, u_n^{\pm})^T$  represents the concentration of the  $n$  species in the two cells  $\Omega_{\epsilon_{\pm}}$  and  $\mathbf{e}_1 \equiv (1, 0, \dots, 0)^T$ . In our formulation we assume that only one species, labeled by  $u_1^{\pm}$  inside the cell, is capable of being transported across the cell membrane into the bulk region.

To derive (6.7.1), which has unit diffusivity, starting from our original dimensional formulation (6.1.1), we proceed as follows: We introduce the dimensionless variables

$$t = k_R T, \quad \mathbf{x} = \mathbf{X}/L_B, \quad U = \frac{L_B^2}{\mu_c} \mathcal{U}, \quad \mathbf{u} = \frac{\boldsymbol{\mu}}{\mu_c}, \quad (6.7.2a)$$

where  $L_B$  is the diffusion length  $L_B \equiv \sqrt{D_B/k_B}$ . We assume that  $L/L_B \gg 1$ , where  $L$  is the radius of  $\Omega$ , so that effectively  $\Omega$  can be replaced by  $\mathbb{R}^2$ . In terms of the  $x$ -variable, the radius of the cells are  $\epsilon \equiv \sigma/L_B \ll 1$ . We then introduce  $\mathcal{O}(1)$  constants  $d_1$  and  $d_2$  defined by

$$\beta_1 \equiv (k_B L_B) \frac{d_1}{\epsilon}, \quad \beta_2 \equiv \left( \frac{k_B}{L_B} \right) \frac{d_2}{\epsilon}, \quad \epsilon \equiv \frac{\sigma}{L_B}, \quad L_B \equiv \sqrt{\frac{D_B}{k_B}}. \quad (6.7.2b)$$

In terms of (6.7.2), we readily derive (6.7.1), where  $\tau \equiv k_R/k_B$ . In (6.7.1), the key parameters are  $\tau$ , the half-distance  $d$  between the centers of the cells, and the permeability constants  $d_1$  and  $d_2$ .

We now study (6.7.1) in the limit  $\epsilon \rightarrow 0$ .

### 6.7.1 The Steady-State Solution

We now construct the steady-state solution to (6.7.1) when  $\epsilon \ll 1$ . Since the two cells have identical kinetics and coupling mechanisms, we seek a steady-state solution that is symmetric about the midplane  $x = 0$ . This steady-state solution satisfies

$$\begin{aligned} \Delta U - U &= 0, & x > 0 \setminus \Omega_\epsilon; & & U &\rightarrow 0 & \text{as } |\mathbf{x}| \rightarrow \infty, \\ \epsilon \partial_{n_\epsilon} U &= d_1 U - d_2 u_1, & \mathbf{x} \in \partial \Omega_\epsilon; & & U_x &= 0 & \text{on } x = 0, \end{aligned} \quad (6.7.3)$$

where  $\Omega_\epsilon$  denotes the circular disk of radius  $\epsilon$  centered at  $\mathbf{x}_0 \equiv (x_0, 0)$ . Here we have dropped the subscript '+' for convenience of notation. The Neumann boundary condition at  $x = 0$  arises from the symmetry assumption.

We use the method of matched asymptotic expansions to study (6.7.3) for  $\epsilon \ll 1$ . In the neighbourhood of the cell region  $\Omega_\epsilon$ , we introduce the local variables  $\mathbf{y} = \epsilon^{-1}(\mathbf{x} - \mathbf{x}_0)$  and  $U_0(\mathbf{y}) = U(\mathbf{x}_0 + \epsilon \mathbf{y})$ , and we let  $\rho = |\mathbf{y}|$ . In terms of these local variables, and neglecting algebraic terms in  $\epsilon$ , we obtain from (6.7.3) that  $U_0$  satisfies

$$\partial_{\rho\rho} U_0 + \rho^{-1} \partial_\rho U_0 = 0, \quad 1 < \rho < \infty, \quad (6.7.4a)$$

subject to the boundary condition

$$\frac{\partial U_0}{\partial \rho} = d_1 U_0 - d_2 u_1, \quad \rho = 1. \quad (6.7.4b)$$

We readily solve (6.7.4), in terms of the as yet unknown source strength  $S$ , to get

$$U_0 = S \log \rho + \chi, \quad \text{where} \quad \chi \equiv \frac{1}{d_1} (S + d_2 u_1). \quad (6.7.5)$$

Within the cell, the steady-state  $\mathbf{u}$  of the membrane dynamics satisfies

$$\mathbf{F}(\mathbf{u}) + \frac{1}{\epsilon\tau} \int_{\partial \Omega_\epsilon} (d_1 U_0 - d_2 u_1) ds \mathbf{e}_1 = 0. \quad (6.7.6)$$

By evaluating the integral over the perimeter, we readily find that

$$\mathbf{F}(\mathbf{u}) + \frac{2\pi S}{\tau} \mathbf{e}_1 = 0. \quad (6.7.7)$$

Next, we analyze the outer region. We match the far-field behavior of the inner solution (6.7.5) to the bulk solution, which yields a singularity

6.7. Infinite Domain: Two Identical Cells

---

condition for the bulk solution as  $\mathbf{x} \rightarrow \mathbf{x}_0$ . In this way, we obtain that the outer bulk solution must satisfy

$$\begin{aligned} \Delta U - U &= 0, & x > 0 \setminus \{\mathbf{x}_0\}; & & U \rightarrow 0 & \text{ as } |\mathbf{x}| \rightarrow \infty, \\ U_x &= 0 & \text{ on } x = 0, & & & (6.7.8) \\ U &\sim S \log |\mathbf{x} - \mathbf{x}_0| + S/\nu + \chi, & & & \text{ as } \mathbf{x} \rightarrow \mathbf{x}_0, \end{aligned}$$

where  $\chi$  is given in (6.7.5) and  $\nu \equiv -1/\log \epsilon$ .

To solve (6.7.8), we introduce the reduced-wave Green's function  $G(\mathbf{x}; \mathbf{x}_0)$  satisfying

$$\begin{aligned} \Delta G - G &= \delta(\mathbf{x} - \mathbf{x}_0), & x > 0; & & G \rightarrow 0 & \text{ as } |\mathbf{x}| \rightarrow \infty, \\ G_x &= 0 & \text{ on } x = 0. & & & (6.7.9) \end{aligned}$$

It is well-known that the free space Green's function  $G_f$  for this operator is

$$G_f(\mathbf{x}; \mathbf{x}_0) = \frac{1}{2\pi} (K_0(|\mathbf{x} - \mathbf{x}_0|)), \quad (6.7.10)$$

where  $K_0(z)$  is the modified Bessel function of the second kind of order zero. Then, by the method of images, the Green's function satisfying (6.7.9) is

$$G(\mathbf{x}; \mathbf{x}_0) = \frac{1}{2\pi} [K_0(|\mathbf{x} - \mathbf{x}_0|) + K_0(|\mathbf{x} - \mathbf{x}_0^*|)], \quad (6.7.11)$$

where  $\mathbf{x}^* \equiv (-x_0, 0)$ . We recall that as  $z \rightarrow 0$ ,  $K_0(z)$  has the local behavior

$$K_0(z) \sim -\log(z/2)(1+z^2/4+\mathcal{O}(z^4))+(-\gamma_e+(1-\gamma_e)z^2/4+\dots), \quad \text{as } z \rightarrow 0, \quad (6.7.12)$$

where  $\gamma_e$  is Euler's constant. This yields the singular behavior of the Green's function (6.7.11) as  $\mathbf{x} \rightarrow \mathbf{x}_0$  given by

$$G \sim -\frac{1}{2\pi} \log |\mathbf{x} - \mathbf{x}_0| + R + o(1), \quad \text{as } \mathbf{x} \rightarrow \mathbf{x}_0, \quad (6.7.13)$$

where the regular part  $R$  is

$$R = \frac{1}{2\pi} (\log 2 - \gamma_e + K_0(2d)), \quad (6.7.14)$$

and where  $2d \equiv |\mathbf{x}_0 - \mathbf{x}_0^*|$  is the distance between the centers of the two cells.

In terms of  $G(\mathbf{x}; \mathbf{x}_0)$ , the solution to (6.7.8) can be represented as

$$U = -2\pi S G(\mathbf{x}, \mathbf{x}_0) = -S [K_0(|\mathbf{x} - \mathbf{x}_0|) + K_0(|\mathbf{x} - \mathbf{x}_0^*|)].$$

Therefore, as  $\mathbf{x} \rightarrow \mathbf{x}_0$ , we have that

$$U \rightarrow S (\log |\mathbf{x} - \mathbf{x}_0| - \log 2 + \gamma_e - K_0(2d) + \dots) . \quad (6.7.15)$$

By matching the regular part of the singularity behavior in (6.7.8) with that in (6.7.15), we obtain that  $S$  satisfies

$$S (-\log 2 + \gamma_e - K_0(2d)) = \frac{S}{\nu} + \chi , \quad (6.7.16)$$

where  $\chi$  is defined in (6.7.5). Upon substituting for  $\chi$  in (6.7.16), and recalling (6.7.7), we obtain the following  $n+1$  dimensional nonlinear algebraic system for  $S$  and  $\mathbf{u} = (u_1, \dots, u_n)$ :

$$S \left( \frac{1}{\nu} + \frac{1}{d_1} + \log 2 - \gamma_e + K_0(2d) \right) = -\frac{d_2 u_1}{d_1} , \quad \mathbf{F}(\mathbf{u}) + \frac{2\pi S}{\tau} \mathbf{e}_1 = 0 , \quad (6.7.17)$$

where  $\nu \equiv -1/\log \epsilon$  and  $\gamma_e$  is Euler's constant. This completes the asymptotic approximation of the steady-state solution to (6.7.1) that is symmetric about the midplane  $x = 0$ .

### 6.7.2 Linear Stability Analysis

To formulate the linear stability problem, we first introduce the perturbations

$$U(\mathbf{x}, t) = U_e(\mathbf{x}) + e^{\lambda t} \Phi(\mathbf{x}) , \quad \mathbf{u}(t) = \mathbf{u}_e + e^{\lambda t} \boldsymbol{\phi} ,$$

into (6.7.1) and linearize. By symmetry, we will only consider the region  $x > 0$ , and will impose suitable boundary conditions on  $x = 0$  for  $\Phi$  as discussed below. This leads to

$$\begin{aligned} \Delta \Phi - (1 + \tau \lambda) \Phi &= 0, & x > 0 \setminus \Omega_\epsilon; & \quad \Phi \rightarrow 0 \quad \text{as} \quad |\mathbf{x}| \rightarrow \infty, \\ \epsilon \partial_{n_\epsilon} \Phi &= d_1 \Phi - d_2 \phi_1, & \mathbf{x} \in \partial \Omega_\epsilon, & \end{aligned} \quad (6.7.18a)$$

which is coupled to the linearized cell dynamics

$$\lambda \boldsymbol{\phi} = J \boldsymbol{\phi} + \frac{1}{\epsilon \tau} \int_{\partial \Omega_\epsilon} (d_1 \Phi - d_2 \phi_1) ds \mathbf{e}_1 \quad (6.7.18b)$$

Here  $J$  is the Jacobian of  $\mathbf{F}$  at the steady-state solution  $\mathbf{u} = \mathbf{u}_e$ , while  $\phi_1$  is the first element in the eigenvector  $\boldsymbol{\phi} = (\phi_1, \dots, \phi_n)^T$ .

To complete the formulation of the stability problem we must impose a boundary condition for  $\Phi$  on the midplane  $x = 0$ . There are two choices

for this boundary condition. The choice  $\Phi(0, y) = 0$  corresponds to an anti-phase synchronization of the two cells, while  $\Phi_x(0, y) = 0$  corresponds to an in-phase synchronization of the two cells. We will consider both types of perturbation in our analysis.

We now study (6.7.18) by the method of matched asymptotic expansions. In the inner region near the cell we introduce the local variables  $y = \epsilon^{-1}(\mathbf{x} - \mathbf{x}_0)$  and  $\Phi_0(\mathbf{y}) = \Phi(\mathbf{x}_0 + \epsilon\mathbf{y})$ . Upon neglecting algebraic terms in  $\epsilon$ , we look for a radially symmetric solution in terms of  $\rho = |y|$  to

$$\partial_{\rho\rho}\Phi + \rho^{-1}\partial_{\rho}\Phi = 0, \quad 1 < \rho < \infty; \quad \frac{\partial\Phi}{\partial\rho} = d_1\Phi - d_2\phi_1, \quad \rho = 1. \quad (6.7.19)$$

In terms of a constant  $C$  to be determined, the solution to (6.7.19) is

$$\Phi = C \log \rho + B, \quad \text{where} \quad B = \frac{1}{d_1} (C + d_2\phi_1). \quad (6.7.20)$$

By substituting (6.7.20) into (6.7.18b) we obtain that

$$(J - \lambda I)\phi + \frac{2\pi C}{\tau}\mathbf{e}_1 = 0. \quad (6.7.21)$$

Next, we formulate the outer problem by matching the far-field behavior of the inner solution (6.7.20) to the bulk solution, which yields a singularity condition for the outer solution as  $\mathbf{x} \rightarrow \mathbf{x}_0$ . This yields the outer problem

$$\begin{aligned} \Delta\Phi - \varphi_{\lambda}^2\Phi &= 0, \quad x > 0 \setminus \{\mathbf{x}_0\}; \quad \Phi \rightarrow 0 \quad \text{as} \quad |\mathbf{x}| \rightarrow \infty, \\ \Phi &\sim C \log |\mathbf{x} - \mathbf{x}_0| + \frac{C}{\nu} + B, \quad \text{as} \quad \mathbf{x} \rightarrow \mathbf{x}_0, \end{aligned} \quad (6.7.22a)$$

subject, for either symmetric (+) or asymmetric perturbations, to the boundary condition

$$\Phi = 0 \quad \text{on} \quad x = 0, \quad (-) \text{ (async)}, \quad \text{or} \quad \Phi_x = 0 \quad \text{on} \quad x = 0, \quad (+) \text{ (sync)}. \quad (6.7.22b)$$

Here  $B$  is defined in (6.7.20), and  $\varphi_{\lambda} \equiv \sqrt{1 + \tau\lambda}$ , where we have chosen the principal branch of the square root.

The solution to (6.7.22) is written in terms of the  $\lambda$ -dependent Green's function  $G_{\lambda}(\mathbf{x}, \mathbf{x}_0)$  as

$$\Phi = -2\pi C G_{\lambda}(\mathbf{x}, \mathbf{x}_0), \quad (6.7.23)$$

where  $G_{\lambda}(\mathbf{x}; \mathbf{x}_0)$  satisfies

$$\Delta G_{\lambda} - \varphi_{\lambda}^2 G_{\lambda} = -\delta(\mathbf{x} - \mathbf{x}_0), \quad x > 0; \quad G_{\lambda} \rightarrow 0 \quad \text{as} \quad |\mathbf{x}| \rightarrow \infty, \quad (6.7.24a)$$

6.7. Infinite Domain: Two Identical Cells

---

subject to either of the two possible boundary conditions

$$G_\lambda = 0 \quad \text{on} \quad x = 0, \quad (-), \quad \text{or} \quad G_{\lambda x} = 0 \quad \text{on} \quad x = 0, \quad (+). \quad (6.7.24b)$$

By the method of images, the solution to (6.7.24) is

$$G_\lambda(\mathbf{x}; \mathbf{x}_0) = \frac{1}{2\pi} \left( K_0(\varphi_\lambda |\mathbf{x} - \mathbf{x}_0|) \pm K_0(\varphi_\lambda |\mathbf{x} - \mathbf{x}_0^*|) \right), \quad (6.7.25)$$

for either the synchronous (+) or asynchronous (-) mode. As  $\mathbf{x} \rightarrow \mathbf{x}_0$  we obtain the local behavior

$$G_\lambda(\mathbf{x}; \mathbf{x}_0) \sim -\frac{1}{2\pi} \log |\mathbf{x} - \mathbf{x}_0| + \frac{1}{2\pi} \left( -\log \left( \frac{\varphi_\lambda}{2} \right) - \gamma_e \pm K_0(2d\varphi_\lambda) \right), \quad (6.7.26)$$

as  $\mathbf{x} \rightarrow \mathbf{x}_0$ ,

where  $\gamma_e$  is Euler's constant, and  $2d \equiv |\mathbf{x}_0 - \mathbf{x}_0^*|$  is the distance between the centers of the two cells. Upon using (6.7.26) in (6.7.23), we can calculate the local behavior of  $\Phi$  as  $\mathbf{x} \rightarrow \mathbf{x}_0$ . Then, we match this local behavior with the required singular behavior in (6.7.22a). This yields that

$$\frac{C}{\nu} + B = -C \left( -\log \left( \frac{\varphi_\lambda}{2} \right) - \gamma_e \pm K_0(2d\varphi_\lambda) \right). \quad (6.7.27)$$

Next, we substitute (6.7.20) for  $B$  into (6.7.27), and solve the resulting expression for  $C$  to obtain

$$C = \frac{d_2}{d_1 A_\lambda^\pm} \phi_1, \quad \text{where} \quad A_\lambda^\pm \equiv \log \left( \frac{\varphi_\lambda}{2} \right) + \gamma_e - (\pm) K_0(2d\varphi_\lambda) - \frac{1}{\nu} - \frac{1}{d_1}, \quad (6.7.28)$$

where the + and - signs denote the synchronous and asynchronous modes, respectively. Upon substituting (6.7.28) into (6.7.21), we readily derive that

$$\left[ (J_e - \lambda I) + \frac{2\pi}{\tau} \frac{d_2}{d_1 A_\lambda^\pm} \mathbf{e}_1 \mathbf{e}_1^T \right] \boldsymbol{\phi} = \mathbf{0}, \quad (6.7.29)$$

where  $\mathbf{e}_1 = (1, 0, \dots, 0)^T$ . We conclude that  $\lambda = \mathcal{O}(1)$  is an eigenvalue of the linearized problem (6.7.18) if and only if there is a nontrivial  $\boldsymbol{\phi}$  to (6.7.29).

To derive an explicit transcendental equation for  $\lambda$  we use the matrix determinant lemma  $\det(A + \mathbf{a}\mathbf{b}^T) = (1 + \mathbf{b}^T A^{-1} \mathbf{a}) \det(A)$ , to conclude that

### 6.7. Infinite Domain: Two Identical Cells

---

if  $\lambda$  is not an eigenvalue of  $J$  then there is a nontrivial solution to (6.7.29) if and only if

$$1 - \frac{2\pi}{\tau} \frac{d_2}{d_1 A_\lambda^\pm} e_1^T (\lambda I - J)^{-1} e_1 = 0.$$

Finally, by calculating  $(\lambda I - J)^{-1}$ , we conclude that  $\lambda$  is a discrete eigenvalue of the linearization if and only if  $\lambda$  is a root of  $Q_\pm(\lambda) = 0$ , where  $Q_\pm$  is defined by

$$Q_\pm(\lambda) = A_\lambda^\pm - \frac{2\pi d_2}{d_1 \tau} \frac{M_{11}}{\det(\lambda I - J)}. \quad (6.7.30a)$$

Here  $M_{11}$  is the cofactor of the element in the first row and first column of  $\lambda I - J$ , and  $A_\lambda^\pm$  is defined by

$$A_\lambda^\pm \equiv \log\left(\frac{\varphi_\lambda}{2}\right) + \gamma_e - (\pm)K_0(2d\varphi_\lambda) - \frac{1}{\nu} - \frac{1}{d_1}, \quad \varphi_\lambda \equiv \sqrt{1 + \tau\lambda}, \quad (6.7.30b)$$

where  $2d$  is the distance between the centers of the two cells,  $\nu = -1/\log \epsilon$ ,  $\gamma_e$  is Euler's constant, while the  $+$  and  $-$  signs indicate the synchronous and asynchronous modes, respectively. In (6.7.30a), the Jacobian of the membrane kinetics is evaluated at  $\mathbf{u}_e$ , where  $\mathbf{u}_e$  is obtained from the nonlinear algebraic system (6.7.17) associated with the steady-state solution.

Next we will use a winding number criterion to compute the roots of  $Q_\pm(\lambda)$  in  $\text{Re}(\lambda) > 0$ . By using the argument principle, we obtain that the number  $N$  of roots of  $Q_\pm(\lambda) = 0$  in  $\text{Re}(\lambda) > 0$  is

$$N = \frac{1}{2\pi} [\arg Q_\pm]_\Gamma + P, \quad (6.7.31)$$

where  $P$  is the number of poles of  $Q_\pm(\lambda)$  in  $\text{Re}(\lambda) > 0$ , and the square brackets denote the change in the argument of  $Q_\pm$  over the contour  $\Gamma$ . The closed contour  $\Gamma$  is the limit as  $R \rightarrow \infty$  of the union of the imaginary axis, which can be decomposed as  $\Gamma_{I+} = i\lambda_I$  and  $\Gamma_{I-} = -i\lambda_I$ , for  $0 < \lambda_I < R$ , and the semi-circle  $\Gamma_R$  defined by  $|\lambda| = R$  with  $|\arg(\lambda)| \leq \pi/2$ . Since  $A_\lambda^\pm$  is analytic in  $\text{Re}(\lambda) > 0$ , it follows that  $P$  is the number of roots of  $\det(\lambda I - J) = 0$  in  $\text{Re}(\lambda) > 0$ . Now if we let  $R \rightarrow \infty$  on  $\Gamma_R$ , we calculate using (6.7.30) that  $Q_\pm(\lambda) \sim O(\ln R) + i\pi/4$ , so that as  $R \rightarrow \infty$  we have  $[\arg Q_\pm]_{\Gamma_R} = 0$ . Further, since  $[\arg Q_\pm]_{\Gamma_{I+}} = [\arg Q_\pm]_{\Gamma_{I-}}$ , then (6.7.31) becomes

$$N = \frac{1}{\pi} [\arg Q_\pm]_{\Gamma_{I+}} + P, \quad (6.7.32)$$

where  $P$  is the number of roots of  $\det(\lambda I - J) = 0$  in  $\text{Re}(\lambda) > 0$ .

### 6.7. *Infinite Domain: Two Identical Cells*

---

With this framework we have formulated a hybrid asymptotic-numerical method to determine whether there can be any triggered oscillations due to Hopf bifurcations for the two-cell infinite line problem as parameters are varied. One future goal is to use this framework to compute phase diagrams in parameter space where different types of instabilities can occur for various specific reaction kinetics.

## Chapter 7

# Conclusion and Future Work

In this chapter we first give a brief summary of the main results presented in this thesis and then list a few open problems for possible directions of future work.

In general, on a one-dimensional spatial domain we have introduced and analyzed a class of models that couple two dynamically active compartments, either cell or membranes, separated spatially by a distance  $2L$ , through a linear bulk diffusion field. For this class of models, we have shown both analytically and numerically that bulk diffusion can trigger a stable synchronous oscillatory instability in the temporal dynamics associated with the two active compartments. Qualitatively, our results also show that oscillatory dynamics in the two compartments will only occur for some intermediate range of the compartment-bulk coupling strength and the parameter range where stable synchronous oscillations between the two compartments occur is much larger than that for asynchronous oscillations. This suggests that stable synchronized oscillations between two dynamically active compartments coupled by passive bulk diffusion can be a robust feature in coupled compartment-bulk dynamics.

For one particular form of local kinetics, we use center manifold and normal form theory to reduce the local dynamics of the model system to a normal form for a double Hopf bifurcation, which predicts the patterns of Hopf bifurcation and the stability of both synchronous and asynchronous modes near the double Hopf point. In the study of coupled oscillators, double Hopf bifurcations often appear in delay-coupled systems, e.g. [5, 69]. In our model, there is no explicit delay term, but the communication between the two oscillators is through spatial diffusion of a signalling chemical in the extracellular medium. For spatially separated cells, this can be a more realistic way to describe the connections among individuals and at the same time diffusion serves effectively as a time delay, reflecting the time needed for a chemical to change concentration at a distant location. In fact, diffusion can be explicitly represented as a distributed delay through the variation of constants formula [6], and this sometimes has practical advantages.

For the case of a single local component in each compartment, and in

the limit of  $L \rightarrow \infty$  we derive rigorous spectral results to characterize the possibility of Hopf bifurcations. Also, a weakly nonlinear theory is developed to predict the local branching behavior near the Hopf bifurcation point for finite  $L$ . In addition, we give a detailed theoretical analysis of the onset of oscillatory dynamics for a model system from [23] using asymptotic analysis together with bifurcation and stability theory.

In §6, we have formulated and studied a general class of coupled cell-bulk problems with the primary goal of establishing whether such a class of problems can lead to the initiation of oscillatory instabilities due to the coupling between the cell and bulk. Our analysis, formulated in an arbitrary bounded domain, relies on the assumption that the signalling compartments have a radius that is asymptotically small as compared to the length-scale of the domain. In this limit  $\epsilon \rightarrow 0$  of small cell radius we have used a singular perturbation approach to determine the steady-state solution and to formulate the eigenvalue problem associated with linearizing around the steady-state. In the limit for which the diffusivity  $D$  of the bulk is asymptotically large of order  $D = \mathcal{O}(\nu^{-1})$ , we have derived eigenvalue problems characterizing the possibility of either synchronous and asynchronous instabilities triggered by the cell-bulk coupling. Phase diagrams in parameter space, showing where oscillatory instabilities can be triggered, were calculated for a few specific choices of the intracellular kinetics. Our analysis shows that triggered oscillations are not in general possible when the intracellular dynamics has only one species. For the regime  $D \gg \mathcal{O}(\nu^{-1})$ , where the bulk can be effectively treated as a well-mixed system, for a one-cell geometry we have reduced the cell-bulk PDE system to a finite dimensional ODE system for the spatially constant bulk concentration field coupled to intracellular dynamics. This ODE system was shown to have triggered oscillations due to cell-bulk coupling, and global bifurcation diagrams were calculated for some specific reaction kinetics, showing that the branch of oscillatory solutions is globally stable. For the regime  $D = \mathcal{O}(1)$ , where the spatial configuration of cells is an important factor, we have determined phase-diagrams for the initiation of synchronous temporal instabilities associated with a ring pattern of cells inside the unit disk, showing that such instabilities can be triggered from a more clustered spatial arrangement of the cells inside the domain.

## 7.1 Future Work

This kind of compartment-bulk coupling model is relatively new and there are still many open problems that require further investigations. In the

following, we list a few possible directions for further work.

A biologically relevant direction related to our work in chapter §2 that warrants further investigation is to introduce different, more detailed, models for the coupling strength between the compartment and the bulk. It would be interesting to analyze triggered oscillations that result when the compartment-bulk coupling strength  $\beta$  varies dynamically in time, or is coupled to some slow dynamics, so as to create periodic bursts of synchronous oscillatory behavior, followed by intervals of quiescent behavior, in the two compartments. Such bursting and triggered dynamics have been well-studied in a purely ODE context (cf. [1], [2], [29], [49], see also the reference therein). A related, but rather challenging direction, would be to investigate the possibility of synchronized oscillations when  $\beta$  is allowed to switch stochastically in time between an ON and OFF state. Such stochastic switching behavior is a characteristic feature of channels in biological membranes. The resulting model is a stochastic hybrid system that consists of both continuous PDE-ODE dynamics, punctuated by discrete stochastic events. A mathematical analysis of a class of related stochastic hybrid system, whereby the boundary condition for a heat equation on a finite domain switches randomly between Dirichlet and Neumann, is analyzed in [43] and another example of switching boundary conditions is considered in [3].

Another direction is to consider more thoroughly the case of multi-species membrane dynamics in the one-dimensional system. More specifically, although a numerical winding number computation is readily implemented for multi-species membrane dynamics, there is a need to extend the theoretical spectral results in chapter §4 to the case of more than a single membrane-bound species. Furthermore, it would be interesting to extend the weakly nonlinear analysis in chapter §4 to the case of multiple membrane-bound species.

As a further extension to the studies in chapter §4 and chapter §5, it would be interesting to use numerical bifurcation software to give a detailed investigation of secondary instabilities arising from bifurcations of asymmetric steady-state solutions or either the synchronous or asynchronous periodic solution branch. Our preliminary results show that such secondary bifurcations can lead to more exotic dynamics such a quasi-periodic solutions or period-doubling behavior. In particular, it would be interesting to explore whether there can be any period-doubling route to chaotic dynamics such as was observed computationally in [56] for a related model consisting of two diffusing bulk species that are subject to nonlinear fluxes at fixed lattice sites.

In addition, It would also be worthwhile to study large-scale oscillations

by representing the bulk diffusion field in terms of a time-dependent Green's function with memory. Coupling to the membrane dynamics leads to a continuously distributed delay equation for the dynamically active membrane components.

An open direction relates to our assumption that the bulk diffusion field has a constant diffusivity and undergoes a linear bulk degradation. It would be worthwhile to extend our analysis to allow for either a nonlinear degradation of the signaling molecule in the bulk, a nonlinear diffusivity, or to allow for a sub-diffusive bulk diffusion process. Either of these three additional effects could be important in various biological applications. Particularly, for our study of the two-dimensional model in chapter §6, for the large  $D$  regime where  $D \gg \mathcal{O}(\nu^{-1})$ , it is possible to readily analyze the case where the bulk degradation is nonlinear, with possibly a Michaelis-Menton saturation of the bulk decay of the form  $\tau U_t = D\Delta U - \sigma_B(U)$ , where  $\sigma_B(U) = U/(1 + cU)$ . With this modification, we can readily derive in place of (6.5.16) that the coupled cell-bulk dynamics reduces to the finite-dimensional dynamics

$$U'_0 = -\frac{1}{\tau} \left( \sigma_B(U_0) + \frac{2\pi d_1}{|\Omega|} U_0 \right) + \frac{2\pi d_2}{\tau |\Omega|} u_1, \quad \mathbf{u}' = \mathbf{F}(\mathbf{u}) + \frac{2\pi}{\tau} [d_1 U_0 - d_2 u_1] \mathbf{e}_1. \quad (7.1.1)$$

It would be interesting to explore the effect of this nonlinear bulk decay on the possibility of Hopf bifurcations. In addition, in the large  $D$  regime, it is readily possible to derive an extended system of ODE's for the case where there are multiple, and not just one, small signalling compartment.

More far-reaching extensions of chapter §6 would be to derive amplitude equations characterizing the weakly nonlinear development of any oscillatory linear instability for the coupled cell-bulk model, and to analyze large-scale dynamics for the regime where  $D = \mathcal{O}(1)$  by first calculating the time-history dependent Green's function for the bulk diffusion process.

# Bibliography

- [1] S. M. Baer, T. Erneux, J. Rinzel, *The Slow Passage Through a Hopf bifurcation: Delay, Memory Effects, and Resonance*, SIAM J. Appl. Math., **49**(1), (1989), pp. 5571.
- [2] R. Bertram, M. J. Butte, T. Kiemel, A. Sherman, *Topological and Phenomenological Classification of Bursting Oscillations*, Bull. Math. Bio. **57**(3), (1995), pp. 413–439.
- [3] P. C. Bressloff, S. D. Lawley, *Escape From Subcellular Domains with Randomly Switching Boundaries*, preprint, (2015).
- [4] J. Buck, E. Buck, *Mechanism of Rhythmic Synchronous Flashing of Fireflies: Fireflies of Southeast Asia may use Anticipatory Time-Measuring in Synchronizing their Flashing*, Science, **159**(3821), (1968), pp. 1319–1327.
- [5] P. L. Buono, J. Bélair, *Restrictions and unfolding of double Hopf bifurcation in functional differential equations*, Journal of Differential Equations, **189**, (2003), pp. 234–266.
- [6] S. Busenberg, J. Mahaffy, *Interaction of spatial diffusion and delays in models of genetic control by repression*, Journal of Mathematical Biology, **22**, (1985), pp. 313–333.
- [7] S. N. Busenberg, J. M. Mahaffy, *The effects of dimension and size for a compartmental model of repression*, SIAM J. Appl. Math., **48**(4), (1988), pp. 882–903.
- [8] S. N. Busenberg, J. M. Mahaffy, *A compartmental reaction-diffusion cell cycle model*, Computers and Mathematics with Applications, **18**, (1989), pp. 883–892.
- [9] W. Chen, M. J. Ward, *The stability and dynamics of localized spot patterns in the two-dimensional Gray-Scott model*, SIAM J. Appl. Dyn. Sys., **10**(2), (2011), pp. 582–666.

## Bibliography

---

- [10] T. Chou, M. R. D’Orsogna, *Multistage Adsorption of Diffusing Macromolecules and Viruses*, J. Chem. Phys., **127**(1), J. Chem. Phys., (2007), 105101.
- [11] F. Chávez, R. Kapral, *Oscillatory and chaotic dynamics in compartmentalized geometries*, Phys. Rev. E., **65**, (2002), 056203.
- [12] W. Y. Chiang, Y. X. Li, P. Y. Lai, *Simple Models for Quorum Sensing: Nonlinear Dynamical Analysis*, Phys. Rev. E., **84**, (2011), 041921.
- [13] S. De Monte, F. d’Ovidio, S. Danø, P. G. Sørensen, *Dynamical quorum sensing: Population density encoded in cellular dynamics*, Proceedings of the National Academy of Sciences, **104**, (2007), pp. 18377–18381.
- [14] G. De Vries, A. Sherman, H. R. Zhu, *Diffusively coupled bursters: Effects of cell heterogeneity*, Bulletin of Mathematical Biology, **60**, (1998), pp. 1167–1200.
- [15] E. J. Doedel, A. R. Champneys, T. F. Fairgreave, Y. A. Kuznetsov, B. Sandstede, X. Wang, *AUTO97: Continuation and Bifurcation Software for Ordinary Differential Equations (with HomCont)*, Concordia University, Montreal, (1997).
- [16] G. B. Ermentrout, *Simulating, Analyzing, and Animating Dynamical Systems: A Guide to XPPAUT for Researchers and Students*, SIAM 2002, Philadelphia, USA.
- [17] P. A. Fletcher, Y. X. Li, *An Integrated Model of Electrical Spiking, Bursting, and Calcium Oscillations in GnRH Neurons*, Biophysical J., **96**(11), (2009), pp. 4514–4524.
- [18] B. Friedman, *Principles and Techniques of Applied Mathematics*, Applied Mathematics Series, John Wiley, New York, (1956), 315 pp.
- [19] A. Goldbeter, *Biochemical Oscillations and Cellular Rhythms: The Molecular Bases of Periodic and Chaotic Behaviour*, Cambridge U. Press, Cambridge, U.K. (1990), 632 pp.
- [20] M. Golubitsky, I. Stewart, *Nonlinear dynamics of networks: The groupoid formalism*, Bulletin of the American Mathematical Society, **43**, (2006), pp. 305–364.
- [21] D. Gonze, S. Bernard, C. Waltermann, A. Kramer, H. Herzel, *Spontaneous synchronization of coupled circadian oscillators*, Biophysical Journal, **89**, (2005), pp. 120–129.

## Bibliography

---

- [22] D. Gonze, N. Markadieu, A. Goldbeter, *Selection of in-phase or out-of-phase synchronization in a model based on global coupling of cells undergoing metabolic oscillations*, Chaos, **18**, (2008), pp. 037127.
- [23] A. Gomez-Marin, J. Garcia-Ojalvo, J. M. Sancho, *Self-Sustained Spatiotemporal Oscillations Induced by Membrane-Bulk Coupling*, Phys. Rev. Lett., **98**(16), (2007), 168303.
- [24] J. Gou, W. Y. Chiang, P. Y. Lai, M. J. Ward, Y. X. Li, *A Theory of Synchrony by Coupling Through a Diffusive Medium*, submitted, Physica D, (2016), (30 pages).
- [25] J. Gou, Y. X. Li, W. Nagata, *Interaction of In-Phase and Anti-Phase Synchronies in a Coupled Compartment-Bulk diffusion Model at a Double Hopf Bifurcations*, accepted subject to revision, IMA J. Appl. Math., (2016), (24 pages).
- [26] J. Gou, Y. X. Li, W. Nagata, M. J. Ward, *Synchronized Oscillatory Dynamics for a 1-D Model of Membrane Kinetics Coupled by Linear Bulk Diffusion*, SIAM J. Appl. Dyn. Sys. 14(4), (2015), pp. 2096-2137.
- [27] J. Gou, M. J. Ward, *Oscillatory Dynamics for a Coupled Membrane-Bulk Model with Fitzhugh-Nagumo Membrane Kinetics*, accepted, SIAM J. Appl. Math., (2016), ( 23 pages).
- [28] J. Gou, M. J. Ward, *An Asymptotic Analysis of a 2-D Model of Dynamically Active Compartments Coupled by Bulk Diffusion*, accepted, J. Nonlinear. Sci., (2016),(37 pages).
- [29] E. Izhikevich, *Dynamical Systems in Neuroscience: The Geometry of Excitability and Bursting*, MIT Press, Cambridge, MA, USA (2007).
- [30] B. Kazmierczak, T. Lipniacki, *Regulation of kinase activity by diffusion and feedback* Journal of theoretical biology **259**(2) (2009), pp. 291-296.
- [31] E. F. Keller, L. A. Segal, *Initiation of slime mold aggregation viewed as an instability*, Journal of Theoretical Biology, **26**, (1970), pp. 399–415.
- [32] A. Khadra, Y. X. Li, *A Model for the Pulsatile Secretion of Gonadotropin-Releasing Hormone from Synchronized Hypothalamic Neurons*, Biophysical J., **91**(1), (2006), pp. 74–83.
- [33] B. N. Kholodenko, *Cell-Signalling Dynamics in Time and Space*, Nat. Rev. Mol. Cell Biol., **7**, (2006), pp. 165–176.

## Bibliography

---

- [34] E. Knobil, *On the control of gonadotropin secretion in the rhesus monkey*, Recent Progress in Hormone Research, **30**, (1974), pp. 1–46.
- [35] L. Z. Krsmanovic, N. Mores, C. E. Navarro, K. K. Arora, K. J. Catt, *An Agonist-Induced Switch in G Protein Coupling of the Gonadotropin-Releasing Hormone Receptor Regulates Pulsatile Neuropeptide Secretion*, Proc. Natl. Acad. Sci. USA, **100**(5), (2003), pp. 2969–2974.
- [36] C. Kuehn, *A Mathematical Framework for Critical Transitions: Bifurcations, Fast/Slow systems and Stochastic Dynamics*, Physica D, **240**(12), (2011), pp. 1020–1035.
- [37] V. Kurella, J. Tzou, D. Coombs, M. J. Ward, *Asymptotic analysis of first passage time problems inspired by ecology*, Bull. of Math Biology, **77**(1), (2015), pp. 83–125.
- [38] D. Kulginov, V. P. Zhdanov, B. Kasemo, *Oscillatory surface reaction kinetics due to coupling of bistability and diffusion limitations*, The Journal of chemical physics, **106**(8), (1997), pp. 3117–3128.
- [39] Y. A. Kuznetsov, *Elements of Applied Bifurcation Theory*, Springer, (2004).
- [40] G. Martínez de la Escalera, A. L. H. Choi, R. I. Weiner, *Generation and Synchronization of Gonadotropin-Releasing Hormone (GnRH) Pulses: Intrinsic Properties of the GT1-1 GnRH Neuronal Cell Line* Proc. Natl. Acad. Sci. USA, **89**(5), (1992), pp. 1852–1855.
- [41] J. P. Lachaux, E. Rodriguez, J. Martinerie, F. J. Varela, *Measuring phase synchrony in brain signals*, Human Brain Mapping, **8**, (1999), pp. 194–208.
- [42] P. Y. Lai, *private communication*, (2013).
- [43] S. D. Lawley, J. C. Mattingly, M. C. Reed, *Stochastic Switching in Infinite Dimensions with Application to Random Parabolic PDE's*, to appear, SIAM J. Math. Analysis, (2015)
- [44] H. Levine, W. J. Rappel, *Membrane Bound Turing Patterns*, Phys. Rev. E., **72**, (2005), 061912.
- [45] C. Levy, D. Iron, *Dynamics and Stability of a Three-Dimensional Model of Cell Signal Transduction*, J. Math. Bio., **67**(6-7), (2013), pp. 1691–1728.

## Bibliography

---

- [46] C. Levy, D. Iron, *Dynamics and stability of a three-dimensional model of cell signal transduction with delay*, *Nonlinearity*, **28**(7), (2015), pp. 2515–2553.
- [47] Y. X. Li, A. Khadra, *Robust Synchrony and Rhythmogenesis in Endocrine Neurons via Autocrine Regulations in Vitro and in Vivo*, *Bull. Math. Biology*, **70**(8), (2008), pp. 2103–2125.
- [48] P. E. MacDonald, P. Rorsman, *Oscillations, intercellular coupling, and insulin secretion in pancreatic  $\beta$  cells*, *PLoS Biology*, **4**, (2006), pp. 167–171.
- [49] P. Mandel, T. Erneux, *The Slow Passage Through a Steady Bifurcation: Delay and Memory Effects*, *J. Stat. Physics*, **48**(5-6), (1987), pp. 1059–1070.
- [50] Maple 14, *Maplesoft, a division of Waterloo Maple Inc.*, Waterloo, Ontario.
- [51] M. K. McClintock, *Menstrual Synchrony and Suppression*, *Nature* **229**, (1971), pp. 244–245.
- [52] E. B. Merriam, T. I. Netoff, M. I. Banks, *Bistable network behavior of layer I interneurons in auditory cortex*, *The Journal of Neuroscience*, **25**, (2005), pp. 6175–6186.
- [53] M. B. Miller, B. L. Bassler, *Quorum sensing in bacteria*, *Annual Reviews in Microbiology*, **55**, (2001), pp. 165–199.
- [54] J. Müller, H. Uecker, *Approximating the Dynamics of Communicating Cells in a Diffusive Medium by ODEs - Homogenization with Localization*, *J. Math. Biol.*, **67**(5), (2013), pp. 1023–1065.
- [55] J. Müller, C. Kuttler, B. A. Hense, M. Rothballer, A. Hartmann, *Cell-Cell Communication by Quorum Sensing and Dimension-Reduction*, *J. Math. Biol.*, **53**(4), (2006), pp. 672–702.
- [56] F. Naqib, T. Quail, L. Musa, H. Vulpe, J. Nadeau, J. Lei, L. Glass, *Tunable Oscillations and Chaotic Dynamics in Systems with Localized Synthesis*, *Phys. Rev. E.*, **85**, (2012), 046210.
- [57] Y. Nec, M. J. Ward, *An Explicitly Solvable Nonlocal Eigenvalue Problem and the Stability of a Spike for a Sub-Diffusive Reaction-Diffusion System*, *Math. Modeling Natur. Phen.*, **8**(2), (2013), pp. 55–87.

- [58] J. Noorbakhsh, D. Schwab, A. Sgro, T. Gregor, P. Mehta, *Modeling oscillations and spiral waves in Dictyostelium populations*, Phys. Rev. E. **91**, 062711, (2015).
- [59] A. P. Peirce, H. Rabitz, *Effect of Defect Structures on Chemically Active Surfaces: A Continuum Approach*, Phys. Rev. B., **38**(3), (1998), pp. 1734–1753.
- [60] J. A. Pelesko, *Nonlinear Stability Considerations in Thermoelastic Contact*, ASME Journal Appl. Mech., **66**(1), (1999), pp. 109–116.
- [61] J. A. Pelesko, *Nonlinear Stability, Thermoelastic Contact, and the Barber Condition*, ASME Journal Appl. Mech., **68**(1), (2001), pp. 28–33.
- [62] P. Perlikowski, S. Yanchuk, O. V. Popovych, P. A. Tass, *Periodic patterns in a ring of delay-coupled oscillators*, Physical Review E, **82**, (2010), pp. 036208.
- [63] S. Pillay, M. J. Ward, A. Pierce, T. Kolokolnikov, *An asymptotic analysis of the mean first passage time for narrow escape problems: Part I: Two-dimensional domains*, SIAM Multiscale Modeling and Simulation, **8**(3), (2010), pp. 803–835.
- [64] H. Riecke, L. Kramer, *Surface-induced chemical oscillations and their influence on space- and time- periodic patterns*, J. Chem. Physics., **83**(8), (1985), pp. 3941–3947.
- [65] I. Rozada, S. Ruuth, M. J. Ward, *The stability of localized spot patterns for the Brusselator on the sphere*, SIADS, **13**(1), (2014), pp. 564–627.
- [66] M. J. Russel, G. M. Switz, K. Thompson, *Olfactory Influences on the Human Menstrual Cycle*, Pharm. Biochem. Behav., **13**(5), (1980), pp. 737–738.
- [67] S. Schroder, E. D. Herzog, I. Z. Kiss, *Transcription-based oscillator model for light-induced splitting as antiphase circadian gene expression in the suprachiasmatic nuclei*, Journal of Biological Rhythms, **27**, (2012), pp. 79–90.
- [68] I. Segota, L. Boulet, D. Franck, C. Franck, *Spontaneous emergence of large-scale cell cycle synchronization in amoeba colonies*, Physical Biology, **11**, (2014), pp. 036001.

- [69] L. P. Shayer, S. A. Campbell, *Stability, bifurcation, and multistability in a system of two coupled neurons with multiple time delays*, SIAM Journal on Applied Mathematics, **61**, (2000), pp. 673–700.
- [70] A. Sherman, *Anti-phase, asymmetric and aperiodic oscillations in excitable cells–I. Coupled bursters*, Bulletin of Mathematical Biology, **56**, (1994), pp. 811–835.
- [71] S. Y. Shvartsman, E. Schütz, R. Imbuhl, I. G. Kevrekidis, *Dynamics on Microcomposite Catalytic Surfaces: The Effect of Active Boundaries*, Phys. Rev. Lett., **83**, (1999), 2857.
- [72] K. Stern, M. K. McClintock, *Regulation of Ovulation by Human Pheromones*, Nature, **392**, (1998), pp. 177–179.
- [73] E. Terasawa, W. K. Schanhofer, K. L. Keen, L. Luchansky, *Intracellular Ca(2+) Oscillations in Luteinizing Hormone-Releasing Hormone Neurons Derived from the Embryonic Olfactory Placode of the Rhesus Monkey*, Jour. of Neuroscience, **19**(14), (1999), pp. 5898–5909.
- [74] B. Novak, J. J. Tyson. *Design principles of biochemical oscillators*, Nature reviews Molecular cell biology **9**(12), (2008), pp. 981-991.
- [75] F. Varela, J. P. Lachaux, E. Rodriguez, J. Martinerie, *The brainweb: Phase synchronization and large-scale integration*, Nature Reviews Neuroscience, **2**, (2001), pp. 229–239.
- [76] M. J. Ward, *Asymptotics for Strong Localized Perturbations: Theory and Applications*, online lecture notes for *Fourth Winter School on Applied Mathematics*, CityU of Hong Kong, (2010).
- [77] J. Wei, M. Winter, *Spikes for the two-dimensional Gierer-Meinhardt system: the weak coupling case*, J. Nonlinear Sci., **11**(6), (2001), pp. 415–458.
- [78] J. Wei, M. Winter, *Stationary multiple spots for reaction-diffusion systems*, J. Math. Biol., **57**(1), (2008), pp. 53–89.
- [79] M. J. Ward, J. Wei, *Hopf Bifurcations and Oscillatory Instabilities of Spike Solutions for the One-Dimensional Gierer-Meinhardt Model*, J. Nonlinear Science, **13**(2), (2003), pp. 209–264.
- [80] A. T. Winfree, *The Geometry of Biological Time*, Springer, New York, (2010).

## Appendix A

# Formulation of the PDE-ODE System for a Periodic Chain

In this appendix we will derive (2.3.1b) for the local dynamics for the case of one cell on  $[-L, L]$ , which occupies a narrow interval  $[-\epsilon, \epsilon]$  centered at the origin with  $0 < \epsilon \ll 1$ . Assume that the signaling molecule diffuses out of the cell at a certain rate. The local chemical species inside the cell, denoted by  $\mathbf{u} = (u_1, u_2, \dots, u_n)^T$ , are assumed to satisfy the following system

$$\begin{aligned} \mathbf{u}_t &= \epsilon D \mathbf{u}_{xx} + \mathbf{F}(\mathbf{u}), & -\epsilon < x < \epsilon, & \quad t > 0, \\ D \mathbf{u}_x(\epsilon, t) &= \mathbf{e}_1 G_1(C(\epsilon, t), u_1(\epsilon, t)), & D \mathbf{u}_x(-\epsilon, t) &= \mathbf{e}_1 G_2(C(-\epsilon, t), u_1(-\epsilon, t)), \end{aligned} \quad (\text{A.0.1})$$

where  $\epsilon \ll 1$  and  $\mathbf{e}_1 = (1, 0, \dots, 0)^T$ . Here for simplicity we assume that all local chemicals share the same diffusivity  $\epsilon D \ll 1$ , with  $D = \mathcal{O}(1)$ , which is asymptotically small as compared to the reaction rate of the kinetics.

We now derive a reduced model from (A.0.1) in the limit  $\epsilon \ll 1$  to obtain the approximate behavior of this system. To do so, we first introduce the local variable  $y = \epsilon^{-1}x$ , so that in terms of the  $y$  variable (A.0.1) becomes

$$\begin{aligned} \mathbf{u}_t &= \epsilon^{-1} D \mathbf{u}_{yy} + \mathbf{F}(\mathbf{u}), & -1 < y < 1, & \quad t > 0, \\ D \mathbf{u}_y(1, t) &= \epsilon \mathbf{e}_1 G_1(C(\epsilon, t), u_1(1, t)), & D \mathbf{u}_y(-1, t) &= \epsilon \mathbf{e}_1 G_2(C(-\epsilon, t), u_1(-1, t)). \end{aligned} \quad (\text{A.0.2})$$

We then expand the local species  $\mathbf{u}$  as

$$\mathbf{u} = \mathbf{u}^0 + \epsilon \mathbf{u}^1 + \dots \quad (\text{A.0.3})$$

Substituting this expansion into (A.0.2), and linearizing, we obtain to leading order that  $\mathbf{u}^0$  satisfies

$$\mathbf{u}_{yy}^0 = 0, \quad -1 < y < 1; \quad \mathbf{u}_y^0(\pm 1, t) = 0. \quad (\text{A.0.4})$$

The solution to (A.0.4), which is independent of the spatial variable  $y$ , is  $\mathbf{u}^0 = \mathbf{u}^0(t)$ . We then proceed to the next order to determine the equation

that  $\mathbf{u}^0$  satisfies. At the next order,  $\mathbf{u}^1$  satisfies

$$\begin{aligned} D\mathbf{u}_{yy}^1 &= \mathbf{u}_t^0 - \mathbf{F}(\mathbf{u}^0), \quad -1 < y < 1, \\ D\mathbf{u}_y^1(1, t) &= \mathbf{e}_1 G_1(C(\epsilon, t), u_1^0(t)), \quad D\mathbf{u}_y^1(-1, t) = \mathbf{e}_1 G_2(C(-\epsilon, t), u_1^0(t)), \end{aligned} \quad (\text{A.0.5})$$

where  $\mathbf{e}_1 = (1, 0, \dots, 0)^T$ , and  $u_1^0$  denotes the first component of  $\mathbf{u}^0$ . For this  $O(\epsilon)$  system, we invoke the divergence theorem to obtain that  $\int_{-1}^1 D\mathbf{u}_{yy}^1 dy = \int_{-1}^1 (\mathbf{u}_t^0 - \mathbf{F}(\mathbf{u}^0)) dy$ . Upon evaluating this expression, and using (A.0.5), we get

$$\begin{aligned} D\mathbf{u}_y^1(1, t) - D\mathbf{u}_y^1(-1, t) &= \mathbf{e}_1 \left( G_1(C(\epsilon, t), u_1^0(t)) - G_2(C(-\epsilon, t), u_1^0(t)) \right) \\ &= 2(\mathbf{u}_t^0 - \mathbf{F}(\mathbf{u}^0)). \end{aligned} \quad (\text{A.0.6})$$

Upon rewriting this equation we obtain a system of ODEs for  $\mathbf{u}^0$  given by

$$\mathbf{u}_t^0 = \mathbf{F}(\mathbf{u}^0) + \frac{\mathbf{e}_1}{2} \left[ G_1(C(\epsilon, t), u_1^0(t)) - G_2(C(-\epsilon, t), u_1^0(t)) \right]. \quad (\text{A.0.7})$$

Now letting the width of the cell approach 0, or equivalently  $\epsilon \rightarrow 0$ , we obtain the limiting system

$$\mathbf{u}_t^0 = \mathbf{F}(\mathbf{u}^0) + \frac{\mathbf{e}_1}{2} \left[ G_1(C(0^+, t), u_1^0(t)) - G_2(C(0^-, t), u_1^0(t)) \right]. \quad (\text{A.0.8})$$

If we consider the case of linear coupling for which  $G_1$  and  $G_2$  have the forms

$$G_1(C(0^+, t), u_1^0) = \kappa(C(0^+, t) - u_1^0), \quad G_2(C(0^-, t), u_1^0) = -\kappa(C(0^-, t) - u_1^0), \quad (\text{A.0.9})$$

then (A.0.8) becomes

$$\mathbf{u}_t^0 = \mathbf{F}(\mathbf{u}^0) + \mathbf{e}_1 \left[ \frac{\kappa}{2} (C(0^+, t) + C(0^-, t)) - \kappa u_1^0 \right]. \quad (\text{A.0.10})$$

This specifies ODEs for the time evolution of the leading order term for the local species inside the cell, and in this way approximately characterizing the local dynamics. In §2.3, we drop the superscript in  $\mathbf{u}^0$  and use (A.0.10) to describe the local dynamics inside each cell.

## Appendix B

# An Alternative PDE-ODE Formulation for a Periodic Chain

In this appendix we briefly discuss the implications of an alternative formulation of the periodic cell problem (2.3.1). In this simpler formulation, we assume that  $C(x, t)$  is continuous on the ring, but has jumps in the flux  $DC_x$  across each cell. This alternative formulation is

$$\begin{aligned} C_t &= DC_{xx} - kC, \quad t > 0, \quad x \in (-L, (2m-1)L), \\ &\quad \text{with } x \neq 2jL, \quad j = 0, \dots, m-1, \\ C(-L, t) &= C(2mL - L, t), \quad C_x(-L, t) = C_x(2mL - L, t), \\ [DC_x] \Big|_{x=2jL} &= 2\kappa [C(2jL, t) - u_{1j}], \quad j = 1, \dots, m, \end{aligned} \tag{B.0.1a}$$

where  $[u_x] \Big|_{x_0} \equiv u_x(x_0^+) - u_x(x_0^-)$ . This bulk field is then coupled to the internal cells dynamics by

$$\frac{d\mathbf{u}_j}{dt} = \mathbf{F}(\mathbf{u}_j) + \mathbf{e}_1 [\kappa C(2jL, t) - \kappa u_{1j}], \quad j = 0, \dots, m-1. \tag{B.0.1b}$$

For (B.0.1), we again obtain the symmetric steady-state solution as in §2.3.1. However, in contrast to the analysis in §2.3.2, in the linear stability analysis for (B.0.1) the perturbations in the bulk diffuson field must now be continuous across each cell. From an analysis similar to that in §2.3.2, we readily derive for the Sel'kov kinetics that the eigenvalue parameter  $\lambda$  satisfies (2.3.12a), where in place of (2.3.12b), we have

$$\Delta_\lambda \equiv -\frac{1}{\kappa} + \frac{1}{D\Omega_\lambda} \frac{\sinh(2\Omega_\lambda L)}{\text{Re}(z) - \cosh(2\Omega_\lambda L)}, \quad \text{Re}(z_l) = \cos\left(\frac{2\pi l}{m}\right), \tag{B.0.2}$$

where  $\Omega_\lambda$  is defined in (2.3.9). As a remark if we set  $z_l = 1$  (in-phase) and  $z_l = -1$  (anti-phase) in (B.0.2), we can readily show that (2.3.12a)

*Appendix B. An Alternative PDE-ODE Formulation for a Periodic Chain*

---

with (B.0.2) reduces, as expected, to the two-cell spectral problem (2.2.5) of §2.2.1 for either in-phase or anti-phase modes, respectively, upon setting  $\beta = \kappa$  in (2.2.5).

## Appendix C

# Calculation of Normal Form Coefficients

In this section, we describe the calculations to evaluate the four cubic coefficients  $G_{jklm}$ ,  $H_{jklm}$  in the normal form (3.3.2) that governs the dynamics near a double Hopf point. To evaluate the coefficients, it is sufficient to take parameters at the double Hopf point, thus  $\mu_1 = \mu_2 = 0$  and we have

$$\begin{aligned}\dot{\zeta}_1 &= i\omega_1\zeta_1 + G_{2100}\zeta_1^2\bar{\zeta}_1 + G_{1011}\zeta_1\zeta_2\bar{\zeta}_2 + O(\|(\zeta_1, \bar{\zeta}_1, \zeta_2, \bar{\zeta}_2)\|^5), \\ \dot{\zeta}_2 &= i\omega_2\zeta_2 + H_{1110}\zeta_1\bar{\zeta}_1\zeta_2 + H_{0021}\zeta_2^2\bar{\zeta}_2 + O(\|(\zeta_1, \bar{\zeta}_1, \zeta_2, \bar{\zeta}_2)\|^5).\end{aligned}\quad (\text{C.0.1})$$

At the double Hopf point, the nonlinear system (3.2.2)–(3.2.3), written as (3.3.1), is reduced to a system on a four-dimensional center manifold that is tangent, in the infinite-dimensional function space  $H$ , to the critical eigenspace  $T^c$ . Since this center manifold reduction is standard and follows closely the analogous procedure at a simple Hopf bifurcation described in detail for reaction-diffusion systems in the textbook [39], we give only a short description together with some details specific to our system. This center manifold system is further reduced to the normal form (C.0.1).

We first construct a projection  $P^c$  of the space  $H$ , onto the critical eigenspace  $T^c$ . This requires an inner product, and two adjoint eigenvectors. For a pair of complex vectors

$$p = \begin{bmatrix} \xi(x) \\ \chi_- \\ \vartheta_- \\ \chi_+ \\ \vartheta_+ \end{bmatrix}, \quad q = \begin{bmatrix} \eta(x) \\ \varphi_- \\ \psi_- \\ \varphi_+ \\ \psi_+ \end{bmatrix},$$

we define their inner product to be

$$\langle p, q \rangle = \int_{-L}^{+L} \overline{\xi(x)}\eta(x) dx + \bar{\chi}_-\varphi_- + \bar{\vartheta}_-\psi_- + \bar{\chi}_+\varphi_+ + \bar{\vartheta}_+\psi_+.$$

With respect to this inner product, the adjoint to the linear differential operator  $M$  is the linear differential operator  $M^*$ , given by

$$M^* \begin{bmatrix} \xi(x) \\ \chi_- \\ \vartheta_- \\ \chi_+ \\ \vartheta_+ \end{bmatrix} = \begin{bmatrix} D\xi''(x) - k\xi(x) \\ f_V\chi_- + \epsilon g_V\vartheta_- - \beta\chi_- + \kappa\xi(-L) \\ f_W\chi_- + \epsilon g_W\vartheta_- \\ f_V\chi_+ + \epsilon g_V\vartheta_+ - \beta\chi_+ + \kappa\xi(+L) \\ f_W\chi_+ + \epsilon g_W\vartheta_+ \end{bmatrix},$$

with adjoint boundary conditions

$$\begin{aligned} -D\xi(-L) &= \beta\chi_- - \kappa\xi(-L), \\ +D\xi(+L) &= \beta\chi_+ - \kappa\xi(+L). \end{aligned}$$

We solve for two adjoint eigenvectors

$$p_j = \begin{bmatrix} \xi_j(x) \\ \chi_{j,-} \\ \vartheta_{j,-} \\ \chi_{j,+} \\ \vartheta_{j,+} \end{bmatrix},$$

$j = 1, 2$ , satisfying

$$M^*p_1 = -i\omega_1 p_1, \quad M^*p_2 = -i\omega_2 p_2,$$

with normalizations such that

$$\langle p_1, q_1 \rangle = 1, \quad \langle p_2, q_2 \rangle = 1, \quad (\text{C.0.2})$$

where  $q_1, q_2$  are the eigenvectors given in Section 3.2. We note that the orthogonality conditions

$$\begin{aligned} \langle p_1, q_2 \rangle &= 0, & \langle p_1, \bar{q}_1 \rangle &= 0, & \langle p_1, \bar{q}_2 \rangle &= 0 \\ \langle p_2, q_1 \rangle &= 0, & \langle p_2, \bar{q}_1 \rangle &= 0, & \langle p_2, \bar{q}_2 \rangle &= 0, \end{aligned}$$

are automatically satisfied. We obtain

$$p_1 = a_1^0 \begin{bmatrix} \xi_{10} \sinh \Omega_3 x / \sinh \Omega_3 L \\ -1 \\ f_w / (i\omega_1 + \epsilon g_w) \\ 1 \\ -f_w / (i\omega_1 + \epsilon g_w) \end{bmatrix}, \quad p_2 = a_2^0 \begin{bmatrix} \xi_{20} \cosh \Omega_4 x / \cosh \Omega_4 L \\ 1 \\ -f_w / (i\omega_2 + \epsilon g_w) \\ 1 \\ -f_w / (i\omega_2 + \epsilon g_w) \end{bmatrix},$$

where the constants

$$a_1^0 = 0.250508 - i0.172379, \quad a_2^0 = 0.253847 - i0.181974,$$

are chosen so that the normalization conditions (C.0.2) hold, and

$$\Omega_3 = \sqrt{\frac{k-i\omega_1}{D}}, \quad \Omega_4 = \sqrt{\frac{i-i\omega_2}{D}}, \quad \xi_{10} = \frac{\beta}{\kappa + D\Omega_3 \coth \Omega_3 L}, \quad \xi_{20} = \frac{\beta}{\kappa + D\Omega_4 \tanh \Omega_4 L}.$$

We define the projection  $P^c$ , of  $H$  onto the critical eigenspace  $T^c$ , by

$$P^c X = z_1 q_1 + \bar{z}_1 \bar{q}_1 + z_2 q_2 + \bar{z}_2 \bar{q}_2,$$

for any  $X \in H$ , where  $z_1, z_2$  are complex numbers given by the inner products

$$z_1 = \langle p_1, X \rangle, \quad z_2 = \langle p_2, X \rangle.$$

Now we can use the projection  $P^c$  to split any vector  $X \in H$  into two parts

$$X = X^c + Y,$$

where the “center” part

$$X^c = P^c X = z_1 q_1 + \bar{z}_1 \bar{q}_1 + z_2 q_2 + \bar{z}_2 \bar{q}_2$$

belongs to the four-dimensional critical eigenspace  $T^c$  and the complementary part

$$Y = (I - P^c)X = X - \langle p_1, X \rangle q_1 - \langle \bar{p}_1, X \rangle \bar{q}_1 - \langle p_2, X \rangle q_2 - \langle \bar{p}_2, X \rangle \bar{q}_2,$$

where  $I$  denotes the identity operator, belongs to the infinite-dimensional stable subspace  $T^s$ . Correspondingly, the system (3.3.1) splits into two parts

$$\dot{X}^c = M X^c + \frac{1}{2} P^c B(X^c + Y, X^c + Y) + \frac{1}{6} P^c C(X^c + Y, X^c + Y, X^c + Y), \quad (\text{C.0.3})$$

$$\dot{Y} = MY + \frac{1}{2}(I - P^c)B(X^c + Y, X^c + Y) + \frac{1}{6}(I - P^c)C(X^c + Y, X^c + Y, X^c + Y). \quad (\text{C.0.4})$$

By center manifold theory, there is an invariant, exponentially attracting, four-dimensional local center manifold in  $H$  that is tangent to the critical eigenspace  $T^c$ , and the center manifold can be expanded in a Taylor series as

$$Y = Y(z_1, \bar{z}_1, z_2, \bar{z}_2) = \sum_{j+k+l+m=2} \frac{1}{j!k!l!m!} w_{jklm} z_1^j \bar{z}_1^k z_2^l \bar{z}_2^m + O(\|(z_1, \bar{z}_1, z_2, \bar{z}_2)\|^3). \quad (\text{C.0.5})$$

Substituting the expansion (C.0.5) into (C.0.3)–(C.0.4) and using the invariance of the center manifold, we collect terms of like powers and obtain nonhomogeneous linear boundary value problems for each of the ten coefficient vectors  $w_{jklm}$  at second order ( $j + k + l + m = 2$ ;  $j, k, l, m \geq 0$ ),

$$\begin{aligned} (2i\omega_1 I - M)w_{2000} &= (I - P^c)B(q_1, q_1), \\ -Mw_{1100} &= (I - P^c)B(q_1, \bar{q}_1), \\ (i\omega_1 I + i\omega_2 I - M)w_{1010} &= (I - P^c)B(q_1, q_2), \\ (i\omega_1 I - i\omega_2 I - M)w_{1001} &= (I - P^c)B(q_1, \bar{q}_2), \\ &\text{etc.} \end{aligned}$$

Using the explicit expressions (3.2.17) for  $q_1$  and  $q_2$ , we use matrix algebra and the method of undetermined coefficients, assisted by the mathematical software package Maple, to solve for the  $w_{jklm}$  that we require. It is helpful to use symmetry to reduce the number of explicit solutions needed.

Substituting (C.0.5) into each of the components of (C.0.3), we obtain a four-dimensional ordinary differential equation that gives the dynamics restricted to the invariant local center manifold,

$$\begin{aligned} \dot{z}_1 &= i\omega_1 z_1 + g(z_1, \bar{z}_1, z_2, \bar{z}_2), \\ \dot{z}_2 &= i\omega_2 z_2 + h(z_1, \bar{z}_1, z_2, \bar{z}_2). \end{aligned} \quad (\text{C.0.6})$$

Expanding in Taylor series

$$\begin{aligned} g(z_1, \bar{z}_1, z_2, \bar{z}_2) &= \sum_{j+k+l+m \geq 2} g_{jklm} z_1^j \bar{z}_1^k z_2^l \bar{z}_2^m, \\ h(z_1, \bar{z}_1, z_2, \bar{z}_2) &= \sum_{j+k+l+m \geq 2} h_{jklm} z_1^j \bar{z}_1^k z_2^l \bar{z}_2^m, \end{aligned}$$

the ten quadratic coefficients of the center manifold system (C.0.6) are given by

$$\begin{aligned} g_{2000} &= \frac{1}{2}\langle p_1, B(q_1, q_1) \rangle, \\ g_{1100} &= \langle p_1, B(q_1, \bar{q}_1) \rangle, \\ g_{1010} &= \langle p_1, B(q_1, q_2) \rangle, \\ g_{1001} &= \langle p_1, B(q_1, \bar{q}_2) \rangle, \\ &\text{etc.} \end{aligned}$$

Note that several of these coefficients vanish due to symmetry. We need explicitly only four of the cubic coefficients of the centre manifold system (C.0.6),

$$\begin{aligned} g_{2100} &= \langle p_1, B(q_1, w_{1100} + \frac{1}{2}B(\bar{q}_1, w_{2000}) + \frac{1}{2}C(q_1, q_1, \bar{q}_1)) \rangle, \\ g_{1011} &= \langle p_1, B(q_1, w_{0011}) + B(q_2, w_{1001}) + B(\bar{q}_2, w_{1010}) + C(q_1, q_2, \bar{q}_2) \rangle, \\ h_{1110} &= \langle p_2, B(q_2, w_{1100}) + B(q_1, w_{0110}) + B(\bar{q}_1, w_{1010}) + C(q_1, \bar{q}_1, q_2) \rangle, \\ h_{0021} &= \langle p_2, B(q_2, w_{0011}) + \frac{1}{2}B(\bar{q}_2, w_{0020}) + \frac{1}{2}C(q_2, q_2, \bar{q}_2) \rangle. \end{aligned}$$

Finally, a near-identity coordinate transformation of the form

$$z_1 = \zeta_1 + O(\|(\zeta_1, \bar{\zeta}_1, \zeta_2, \bar{\zeta}_2)\|^2), \quad z_2 = \zeta_2 + O(\|(\zeta_1, \bar{\zeta}_1, \zeta_2, \bar{\zeta}_2)\|^2),$$

takes the the center manifold system (C.0.6) into the normal form (C.0.1). The procedure to construct the coordinate transformation is lengthy but standard, and is described in textbooks. For example, see [39] for more details. In the end, there are formulas derived for the cubic coefficients in the normal form (C.0.1), in terms of the quadratic and cubic coefficients of the center manifold system (C.0.6): see equations (8.90)–(8.93) in [39]. We use Maple to evaluate these coefficients numerically, obtaining (3.3.3).

## Appendix D

# Two Specific Biological Models

### D.1 The Dictyostelium Model

The amoeba *Dictyostelium discoideum* is one of the most studied organism in biology. There are many stages in the life cycle of each such amoeba cell. When nutrient is readily available, they live as single cell organisms. However, when food becomes scarce, each cell starts to release cyclic AMP (cAMP) in order to attract other cells, and at the same time themselves are attracted by the cAMP signal emitted by others. This secretion results in an aggregation of individual amoeba to form aggregate centers [19]. This intercellular communication mechanism presents some similarities with the endocrine system in higher organisms. In [19] a two-variable model was proposed to describe the cAMP (cyclic adenosine monophosphate) oscillations in Dictyostelium cells. This minimal model was obtained from a reduction of a more elaborate model based on desensitization of the cAMP receptor which consists of variables representing molecules such as the active(R) and desensitized(D) forms of the receptor, free(C) and active form(E) of adenylate cyclase, intracellular( $P_i$ ) and extracellular(P) cAMP, and substrate ATP(S). In [19] this minimal model was used to analyze the bursting and birhythmicity observed in experiments with amoeba cells. The model is formulated as

$$\frac{d\rho_t}{dt} = f_2(\gamma) - \rho_t(f_1(\gamma) + f_2(\gamma)), \quad \frac{d\gamma}{dt} = \sigma^* \psi(\rho_t, \gamma) - k_e \gamma, \quad (\text{D.1.1a})$$

where

$$f_1(\gamma) \equiv \frac{k_1 + k_2 \gamma^2}{1 + \gamma^2}, \quad f_2(\gamma) \equiv \frac{k_1 L_1 + k_2 L_2 c_d^2 \gamma^2}{1 + c_d^2 \gamma^2},$$
$$\psi(\rho_t, \gamma) \equiv \frac{\alpha \left( \Lambda \theta + \frac{\epsilon \rho_t \gamma^2}{1 + \gamma^2} \right)}{(1 + \alpha \theta) + \left( \frac{\epsilon \rho_t \gamma^2}{1 + \gamma^2} \right) (1 + \alpha)}. \quad (\text{D.1.1b})$$

Here  $\rho_t$  is the total fraction of receptor in the active state,  $\alpha$  and  $\gamma$  denote the normalized concentration of intracellular ATP and extracellular cAMP,  $\theta$  is the ratio of Michaelis constants for the E and C forms of adenylate cyclase,  $\Lambda$  is the ratio of catalytic constants of forms C and E of adenylate cyclase,  $\epsilon$  is the coupling constant for activation of  $C$  by cAMP-receptor complex in active state,  $k_1$  is the rate constant for the modification step from R to D,  $L_1$  is the equilibrium ratio of the states R and D,  $k_2$  is the rate constant for modification step from  $R$  to  $D$  in the presence of cAMP,  $L_2$  is the corresponding equilibrium ratio,  $k_e$  is the ratio of maximum activity for extracellular phosphodiesterase and the Michaelis constant of extracellular phosphodiesterase for cAMP,  $c_d$  is the ratio of dissociation constants of cAMP-receptor complex in R and D states,  $\sigma^*$  is calculated as some combination of other constants. For a more detailed discussion of this model see [19] (pp. 195–258).

Since the cAMP molecules can diffuse in space, in our model we assume that the extracellular cAMP is also a function of location, so that  $\gamma = \gamma(x, t)$ . We assume that it can diffuse freely in space, with some bulk decay, but that all the reactions occur on the boundaries of amoeba cells. In this way, our model for cAMP, given a cell at  $x = 0$  and at  $x = 2L$ , and with  $\tau \equiv 1/k_e$  is

$$\begin{aligned} \tau \frac{d\gamma}{dt} &= D \frac{d^2\gamma}{dx^2} - \gamma, & t > 0, \quad 0 < x < L; \\ \gamma_x(L, t) &= 0, \quad D\gamma_x(0) = -\sigma^* \psi(\rho_t, \gamma(0, t)), & & (D.1.2) \\ \frac{d\rho_t}{dt} &= f_2(\gamma(0, t)) - \rho_t [f_1(\gamma(0, t)) + f_2(\gamma(0, t))] . \end{aligned}$$

## D.2 The GnRH Model

Gonadotropin-releasing hormone (GnRH) is a decapeptide secreted by GnRH neurons in the hypothalamus that regulates the reproductive function in mammals. There are about 800-2000 GnRH neurons scattered in a few areas of the hypothalamus. Each GnRH neuron releases GnRH to portal blood in an oscillatory profile with a period of several minutes and they synchronize to produce large GnRH pulses with a period ranging from twenty minutes to one hour. Experiments reveal that GnRH neurons express GnRH receptors. Based on these biological facts, a possible synchronization mechanism of GnRH neurons was proposed in [17, 32, 47]. In this model, it is assumed the the GnRH neurons are coupled through GnRH in the extracellular environment. This model was able to predict that oscillations occur over a one hour period. Assuming two neurons, one each at  $x = 0$  and at

## D.2. The GnRH Model

---

$x = 2L$ , this model system is

$$g_t = Dg_{xx} - g, \quad t > 0, \quad 0 < x < L; \quad g_x(L, t) = 0, \quad Dg_x(0) = -\sigma j, \quad (\text{D.2.1a})$$

with the three-component membrane dynamics

$$\alpha_t = \phi_\alpha \left( \frac{[g(0, t)]^{n_\alpha}}{k_\alpha^{n_\alpha} + [g(0, t)]^{n_\alpha}}, \alpha \right), \quad \alpha = \{s, q, i\}. \quad (\text{D.2.1b})$$

with coefficients  $n_s = 4$ ,  $n_q = 2$  and  $n_i = 2$ . In (D.2.1a),  $\sigma$  reflects the secretion efficiency, and the boundary flux is

$$j \equiv 1 + \beta \left( \frac{\iota + 1 + \zeta q}{\mu + 1 + \delta q} \right)^3 \left( \eta + \frac{s}{\omega + i} \right)^3, \quad (\text{D.2.1c})$$

(see [32, 47] for further details and definition of the parameters). In (D.2.1a),  $s$ ,  $q$  and  $i$  represent the concentration of three G-proteins,  $G_S$ ,  $G_Q$  and  $G_I$ , respectively. It is postulated that the release of GnRH is mediated through activation ( $G_S$ ,  $G_Q$ ) and inhibition ( $G_I$ ) of these proteins. With the assumption that the time scales of  $s$  and  $q$  are much faster than  $i$ , we use a quasi-steady state approximation to fix  $s$  and  $q$  at (approximately) their steady-state values. This leads to the following reduced coupled system

$$g_t = Dg_{xx} - g, \quad t > 0, \quad 0 < x < L; \quad g_x(L, t) = 0, \quad Dg_x(0) = G(g(0, t), i), \quad (\text{D.2.2a})$$

with the one-component membrane dynamics and boundary flux given by

$$\begin{aligned} i_t &= \epsilon \left( \frac{[g(0, t)]^2}{k_i^2 + [g(0, t)]^2} - i \right), \\ G(g(0, t), i) &= -\sigma \left[ 1 + \beta \left( \frac{\iota + 1 + \zeta q}{\mu + 1 + \delta q} \right)^3 \left( \eta + \frac{s}{\omega + i} \right)^3 \right], \end{aligned} \quad (\text{D.2.2b})$$

Here,  $s$  and  $q$ , which depend on  $g(0, t)$ , are given by

$$s = \frac{[g(0, t)]^4}{k_s^4 + [g(0, t)]^4}, \quad q = \frac{[g(0, t)]^2}{k_q^2 + [g(0, t)]^2}. \quad (\text{D.2.2c})$$